5th International Conference on Magnetic Resonance Microscopy

The Heidelberg Conference

September 5 - 9, 1999

German Cancer Research Center, Heidelberg, Germany

Conference Program

Groupement Ampère

division of spatially resolved magnetic resonance

Abstracts

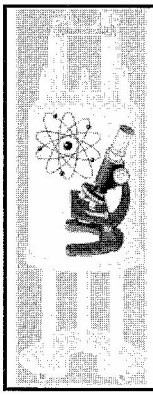

5th International Conference on Magnetic Resonance Microscopy Heidelberg, Germany, Sept. 5-9,1999

Local Organizer: Dr. William E. Hull, Central Spectroscopy Dept. (R0400)
German Cancer Research Center (DKFZ), Neuenheimer Feld 280,
D-69120 Heidelberg, Germany; w.hull@dkfz-heidelberg.de

Groupement Ampère

division of spatially resolved magnetic resonance

Dear Colleagues and Friends,

Welcome to the romantic city of Heidelberg for the 5th Meeting in the biennial series of international conferences on **Magnetic Resonance Microscopy** (ICMRM).

The German Cancer Research Center (DKFZ) and its Director, Prof. Harald zur Hausen, have provided us with modern conference facilities, including a 300-seat auditorium with an attractive foyer for Poster display and adjacent seminar rooms for exhibitions by MR vendors.

This multidisciplinary conference provides a congenial forum for discussion of the most recent advances in NMR and EPR techniques for imaging and localized spectroscopy and their applications in biology, medicine, materials and earth sciences at spatial resolutions ranging from microns to centimeters.

As you can see in the Table below, this year's meeting has statistics which are similar to those from previous meetings. The international flair of the conference remains, and the number of oral and poster presentations is sufficiently high to keep us thoroughly busy for the duration of the meeting.

	1991 Heidelberg	1993 Heidelberg	1995 Würzburg	1997 Albuquerque	1999 Heidelberg
Participants	183	173	217	156	**185**
Countries	20	23	23	18	**18**
Educational Lectures	5	6	0	7	**5**
Session Lectures	51	69	52	63	**68**
Posters	51	64	96	60	**87**

The next meeting in 2001 will be held in Cambridge, UK, and will be organized by Prof. Laurie Hall.

As your Local Organizer this year, I do hope you will have an enjoyable and scientifically stimulating visit in Heidelberg. In spite of all the work in store for us, we do have some social events on the program, including a wine tasting / poster viewing party on Monday evening and a special grand tour of Heidelberg castle on Wednesday where we will be able to enter areas not usually opened to the public. After the tour and a leisurely stroll around the grounds we will enjoy a Buffet Feast in the King's Hall (Königssaal) with good food and drink and hopefully some enjoyable music provided by your Local Organizer and perhaps a special guest as well.

As in the past this meeting has been organized as part of the activities of the

Division of Spatially Resolved Magnetic Resonance

of the *Groupement Ampère*, a renowned scientific society in the field of magnetic resonance.

The Division was founded in 1995 during the third scientific meeting on "Magnetic Resonance Microscopy". The purpose of the Division is to advance the subject of "Spatially Resolved Magnetic Resonance" by means of

- International Conferences organized biennially anywhere in the world,
- Symposia, Summer Schools and Workshops.

The main organs of the Division are:

- The *Executive Committee*
- The *Division Committee*
- The *General Meeting*.

The *General Meeting* has the final authority of the Division and takes place at the International Conferences of the Division. All participants of the conference are automatically members of the *General Meeting*.

The *Division Committee* is responsible for carrying out the business of the Division, including the scientific organization of the conference. The *Executive Committee* is responsible for the management, administration and finances of the Division.

During the last meeting in Heidelberg (1993) it was decided to call the series of "Magnetic Resonance Microscopy" Conferences the "Heidelberg Meetings", in honor of the city where the first meetings were held.

The current members of the Executive Committee (Division Office) are listed below.

Chair	P.C. Lauterbur (Urbana, USA)
Vice Chair	L.D. Hall (Cambridge, UK)
Secretary General	A. Haase (Würzburg, Germany)
Vice Secretary General	R. Botto (Argonne, USA)
Treasurer	R. Kimmich (Ulm, Germany)
Former Conference Chair	E. Fukushima (Albuquerque, USA)
Conference Chair	W.E. Hull (Heidelberg, Germany)
Former Division Chair	W. Kuhn (Blieskastel, Germany)
Advisors	L. Berliner (Columbus, USA)
	B. Blümich (Aachen, Germany)
Honorary Member	E.R. Andrew (Gainesville, USA)

The Division Committee has the following members:

J.L. Ackerman (USA)	R.L. Armstrong (Canada)	P.T. Callaghan (New Zealand)
A.N. Garroway (USA)	W. Halperin (USA)	A. Jasinski (Poland)
L.W. Jelinski (USA)	G.A. Johnson (USA)	P. Jonsen (UK)
R.A. Komoroski (USA)	K. Kose (Japan)	D. Le Bihan (France)
P. Mansfield (UK)	B. Maraviglia (I)	G.D. Mateescu (USA)
M.J. McCarthy (USA)	P.J. McDonald (UK)	D. Müller (Germany)
R.N. Muller (Belgium)	G.J. Nesbitt (NL)	T.G. Nunes (Portugal)
J.M. Pope (Australia)	D.J. Pusiol (Argentina)	S.K. Sarkar (USA)
H.W. Spiess (Germany)	J.H. Strange (UK)	S. Sukumar (USA)
M. Szayna (USA)	H. van As (NL)	H.M. Vieth (Germany)

All members of the Division Office and Division Committee contributed to the development of the Scientific Program and suggesting invited speakers for the 5th ICMRM, the Heidelberg Conference.

The final program was put together by Robert Botto, Axel Haase, and William E. Hull, with the valuable assistance of the following additional abstract reviewers:

John Strange	Gil Navon	Reinhard Surkau
Rainer Kimmich	Bruce Balcom	Peter Bluemler
Eiichi Fukushima	Paul Callaghan	Richard Bowtell
Markus von Kienlin	Miguel Martín-Landrove	Hellmut Merkle
Richard Ehman	Jim Pope	Dan Demco
Bernhard Bluemich		

The conference begins with a one-day Educational Session on Sunday, as described below, for which ca. 90 participants are registered. Then follows a 3.5 day scientific meeting comprising 12 sessions of Oral presentations and 5 Poster sessions. A total of 32 invited plenary lectures form the basis around which the meeting is constructed. From 125 submitted Abstracts a total of 36 were selected for oral presentation. We could have easily selected more but the time frame of the meeting forced us to limit the number of orals.

This year, for the first time, we introduced a Young Investigators Competition, whereby doctoral students and postdocs who were primarily responsible for their projects could submit a three-page Abstract for a more detailed judgement of their work. A total of ten competitors joined in the fun, and we selected six of these (4 postdocs and 2 predocs) to present their work as a 15-min Oral. As a special bonus their conference fees have been waived.

All Abstracts that reached us were in fact accepted for presentation, either as an Oral or as a Poster. This year we were also able to obtain financial support from the Deutsche Forschungsgemeinschaft (DFG) for a total of 14 scientists from eastern Europe and the Russian Federation. Thus, we were able to cover the fees and part of the travel and hotel costs for 9 members of the Russian Federation, three colleagues from Poland, and one each from the Czech Republic and Slovakia.

On the following pages you will find the detailed Program and time schedule for the meeting. All oral presentations and all poster contributions are listed here with corresponding code numbers for the Abstracts which are presented in the second part of this booklet. The Oral sessions were constructed on the basis of the basic topic categories Biology, Materials, Methods, Instrumentation, etc., whereby we have tried to bring closely related topics together in a logical way. Unfortunately, due to constraints on participation dates for several lecturers, it was not possible to achieve the ideal arrangement of topics. For example, it was planned to have Materials 1, Materials 2, and Diffusion & Flow as three major categories. However, departure dates forced us to mix members of the latter two categories together.

The Posters have also been organized according to main topic (see List following the Program) and further arranged to place related subjects close to together. The Program is organized with alternating oral and poster sessions in a way which we hope will stimulate Poster viewing and provide welcome relief from the strenuous Oral sessions. The Coffee Breaks coincide with the Poster Sessions and take place in the Foyer of the Communication Center.

Registration Desk

The desk in the Foyer of the Communication Center will be manned beginning Sunday morning at 9:00 h and through the conference. Here you will receive the conference materials and tote bag and hopefully be able to get useful information and help for any problems.

Oral Presentations

In addition to slides or overhead transparencies it is possible to use a so-called "beamer" to project directly from a Laptop PC using Powerpoint, for example. If you wish to use this facility please contact the Projectionist early on to familiarize yourself with the system and perform the required data transfers.

Poster Presentations

Posters should be mounted as soon as possible on the numbered Poster Boards, at the latest on Sunday evening during the reception. The number assigned to your Poster is given in a Table in this booklet. Double-sided tape and push-pins will be provided for mounting. Posters should be viewable throughout the entire conference but must be removed on Thursday afternoon after the last Session.

Lunches

The one-hour lunch break begins at 13:15 - 13:30 and inexpensive meals can be obtained in the DKFZ-Cafeteria located adjacent to the Conference site. The Personel have been notified that we will be coming at the indicated time and sufficient "extra" portions of the offered menus should be available.

Public Transportation

The DKFZ is unfortunately 1 - 2.5 km distant from most hotels, but the hotels we have chosen are generally quite close to Bus and Tram (Streetcar) connections (Haltestelle). For example, for Hotels in the Friedrich Ebert Anlage in the City Center, the Bus #33 (direction Sportzentrum) goes right by the door of these hotels and has a stop just in front of the DKFZ. The Tram Line #1 goes from Dossenheim through Bismarck Platz to the Hauptbahnhof and then over the bridge to Neuenheim. The first stop on the north side of the bridge is at the intersection of Jahn and Berliner Strasse and is the closest stop for the DKFZ (ca. 300 m walk). Tickets for a single ride cost cost about DM 2.80 I believe, can be bought from the driver and do not require exact change. Tickets are cheaper as a block of 5 and there is also a 24-h ticket, a week ticket and other such alternatives.

I wish you a successful conference and enjoyable stay in Heidelberg, sincerely, *Bill Hull*

5th Int. Conference on Magnetic Resonance Microscopy, German Cancer Research Center, Heidelberg

Sunday, Sept. 5, 1999

Educational Program

The one-day program provides five lectures by respected experts in the field of MR, which provide an overview of the basic aspects of MR imaging, now including EPR. The information and background needed to understand a variety of modern techniques and applications, many of which will be the subject of other presentations at the Scientific Sessions, will also be presented.

Participants in this Session will receive additional documentation (so-called handouts or course notes) provided by the lecturer. One-page summaries of each lecture can be found in the Abstracts section of this booklet (E1 - E5).

The Educational Session takes place in the main lecture theater of the Communication Center of the German Cancer Research Center (DKFZ). The detailed Program is listed below. Participants will be provided free of charge with a light lunch delivered by a catering service since the DKFZ Cafeteria is closed on weekends.

Following the lectures there will be an informal Reception in the Foyer with buffet-style refreshments, giving participants a chance to relax and mingle with friends and colleagues, to setup their poster presentations, and to get in the mood for the hard work coming up in the days ahead.

5th ICMRM Educational Session **Chairman: Robert E. Botto**

Sunday	Sept. 5, 1999		
	Lecturer	**Title**	**Abstract**
9:20	Greetings and Announcements		
9:30 - 11:00	**Bernhard Blümich** MARC, RWTH Aachen, GER	**Fourier Imaging: Spatial Resolution and Contrast**	**E1**
11:00 - 11:30	Coffee Break	Foyer of the Communication Center	
11:30 - 13:00	**Axel Haase** Univ. Würzburg, GER	**Biomedical NMR Imaging**	**E2**
13:00 - 14:00	Lunch Break	Foyer	
14:00 - 15:30	**Paul Callaghan** Massey University, New Zealand	***Q*-space and beyond**	**E3**
15:30 - 16:00	Coffee Break	Foyer	
16:00 - 17:30	**Gil Navon**, Tel Aviv, Israel	**Imaging of X-Nuclei**	**E4**
17:30 - 18:00	**Harold Swartz** Dartmouth Med. School, Hanover, USA	**EPR in Viable Systems**	**E5**
18:30 - 21:00	**Reception with Buffet**	**"Poster Hanging"**	

The detailed Program for the Scientific Sessions appears on the following pages.

5th Int. Conference on Magnetic Resonance Microscopy, German Cancer Research Center, Heidelberg

Scientific Program: Plenary Lectures (L) are 25 min; Contributed Orals (O) are 15 min; Presenter is in bold face.

Monday	Sept. 6, 1999		Title	Abstract
8:30 - 9:15	**Opening Session**			
8:30	Greetings and Announcements			
	Opening Lecture			
8:45 - 9:15	**Sir Peter Mansfield**	Univ. Nottingham, UK	From Solids to Humans by NMR	**L1**
9:15 - 10:45	**Oral Session 1**	**Materials 1**	**Chair: Peter Blümler (Canterbury, UK)**	
9:15	**Bruce J. Balcom**	Univ. New Brunswick, CAN	SPRITE MRI of Materials	**L2**
9:40	**J. Gelan**, P. Adriaensens, A. Pollaris and L. Storme	Limburg University, Diepenbeek, BEL	MRI Heterogeneities and End-User Properties of Polymer Materials	**L3**
10:05	D. M. Gregory and **R.E. Botto**	Argonne National Laboratory, USA	Probing Polymer Architecture by MRM	**O1**
10:20 - 10:35	**Farida Grinberg** and Rainer Kimmich	Univ. of Ulm, GER	The Dipolar Correlation Effect in Organized Liquids and Polymer Networks	**O2**
10:35 - 10:45	Discussion			
10:45 - 11:45	**Poster Session 1**	odd numbered posters		

Monday	Sept. 6			
11:45 - 13:15	**Oral Session 2**	**Commercial Applications**	**Chair: Robert Botto (Argonne Lab, USA)**	
11:45	**Sudeep Chandra**, Susanta K. Sarkar, Frank C. Barone, and Eliot H. Ohlstein	Smithkline Beecham Pharmaceuticals, USA	Learning from Carotid Arteries using High-Resolution in vivo MRI	**L4**
12:10	**Peter Blümler**	University of Kent at Canterbury, UK	Potentials of NMR Imaging in Process Engineering	**L5**
12:35	**Koji Saito**, Ikuo Komaki and Kennichi Hasegawa	Nippon Steel Corporation, JPN	*In-Situ* High-Temperature NMR Imaging Study of Coals	**O3**
12:50 - 13:15	**Lowell J. Burnett**	Quantum Magnetics, Inc., San Diego, USA	Explosives Detection	**L6**
13:15 - 13:30	Discussion			
13:30 - 14:30	**Lunch**			
14:30 - 16:45	**Oral Session 3**	**Biology 1**	**Chair: Geoffrey Hunter (Dundee, UK)**	
14:30	**Hellmut Merkle**, Nikos Logothetis, Seong-Gi Kim, et al.	University of Minnesota Medical School, USA	High-Field MR Investigations *in vivo*	**L7**
14:55	**Frank Wiesmann**	Univ. Würzburg, GER	High-Resolution MRI in Mice	**L8**
15:20	**Jan Ruff**, Frank Wiesmann, Axel Haase	Physikalisches Inst., Med. Universitätsklinik, Würzburg, GER	High-Resolution 3D NMR Imaging of the Mouse Heart	**O4**
15:35	**Felix W. Wehrli**	University of Pennsylvania Medical Center, Phila., USA	NMR Microscopy for the Study of Trabecular Bone Architecture and Mechanical Competence	**L9**
16:00	**Vikas Gulani**, John R. Gardner, Christopher P. Hess, Andrew G. Webb, M. Joan Dawson	University of Illinois, Urbana-Champaign, USA	Magnetic Resonance Microscopy of Morphological Alterations in Mouse Tibiae Following Hindlimb Suspension	**O5**

16:15	**Kazuya Ikoma**, Yoshiteru Seo, Hisatake Takamiya, Yoshiaki Kusaka	Kyoto Prefectural University of Medicine, JPN	^{1}H Double-Quantum Filtered NMR Imaging of Rabbit Leg Joints	**O6**
16:15 - 16:30	**Yoshiteru Seo**, Kazuya Ikoma, et al.	Kyoto Prefectural University of Medicine, JPN	Healing Process of Ruptured Achilles Tendon Assessed by ^{1}H Double-Quantum Filtered MRI	**O7**
16:30 - 16:45	Discussion			
16:45 - 17:15	**Coffee Break**			
17:15 - 19:15	**Oral Session 4**	**Methods**	**Chair: Teresa Nunes (Lisabon, POR)**	
17:15	**G. Guthausen**, A. Guthausen, et al.	RWTH Aachen, GER	Surface NMR via the NMR MOUSE	**L10**
17:40	**François Humbert** , Bernard Diter, et al.	Université Henri Poincaré, Nancy, FRA	Recent Progress in NMR Microscopy using B_1 Gradients	**O8**
17:55	**Gerhard Fink**, Andrea Schwaiger, Bernhard Blümich	RWTH Aachen, GER	Quantifying periodic cyclic motion by oscillating gradients in MRI	**O9**
18:10	**Robert A. Wind**	Pacific Northwest National Laboratory, USA	Prospects of Magnetic Resonance Microscopy combined with Dynamic Nuclear Polarization	**L11**
18:35	**A. Roch**, A. Ouakssim, R. N. Muller , P. Gillis	University of Mons-Hainaut, BEL	Proton Relaxometry as Tool for the Characterization of Superparamagnetic Nanosystems	**O10**
18:50 - 19:05	**R. Bowtell**, S. Gutteridge and C. Ramanathan	Univ. of Nottingham, UK	Imaging the Long-Range Dipolar Field in Structured Liquid State Samples	**O11**
19:05 - 19:15	Discussion			
19:30 - 21:30	**Poster Session 2**	viewing at your leisure	**Wine Tasting:** a selection of German wines served with a typical German "Abendbrot"	
19:30 - 20:30	Executive Committee Meeting			

Tuesday	Sept. 7			
8:30 - 10:00	**Oral Session 5**	**Instrumentation 1**	**Chair: Richard Bowtell (Nottingham, UK)**	
8:30	**Katsumi Kose**	Univ. Tsukuba, JPN	Portable MRI Systems	**L12**
8:55	**M. Rokitta**, E. Rommel, U. Zimmermann, A. Haase	Univ. Würzburg, GER	A Selfcontained Portable NMR Imager	**O12**
9:10	**Gerhard Roth**	Bruker Analytik GmbH, Karlsruhe, GER	High-Field NMR Magnets	**L13**
9:35 - 10:00	**Wolfgang U. Roffmann,** Dieter Gross, et al.	University of Queensland, Brisbane, AUS	Hardware Developments for *In-Vivo* MR Microscopy at Fields up to 17.6T	**L14**
10:00 - 10:10	Discussion			
10:10 - 11:10	**Poster Session 3**	even numbered posters		
11:10 - 13:00	**Oral Session 6**	**Instrumentation 2**	**Chair: Katsumi Kose (Tsukuba, JPN)**	
11:10	**Sarah E. Hurlston**, Steve A. Suddarth, G. Allan Johnson	Duke University Center for *In Vivo* Microscopy, USA	High-Temperature Superconducting Resonators: from Theory to Application	**L15**
11:35	**H. Douglas Morris**	Univ. of Illinois, Urbana, USA	Microsamples, Microcoils, Micromagnets – Where Will All This Smallness End?	**L16**
12:00	**Kevin R. Minard** and Robert A. Wind	Pacific Northwest National Laboratory, USA	Design and Analysis of Microcoils for Cellular Research in High Magnetic Fields with ^{1}H NMR	**O13**
12:15	**Seung-Cheol Lee**, Kiseong Kim, et al.	Korea Advanced Institute of Science and Technology, Taejon, KOR	Development of a high S/N 600 MHz NMR microscopy probe	**O14**
12:30	**R. Bowtell**, S. Crozier, B. Beck and S. Blackband	Univ. Nottingham, UK	Multi-Layer Transverse Gradient Coils	**O15**
12:45 - 13:00	**P.M. Glover**, P.S. Aptaker, J.R. Bowler, et al.	University of Surrey, UK	A High-Gradient Permanent Magnet for the Profiling of Planar Films and Coatings	**O16**
13:00 - 13:15	Discussion			

Tuesday	Sept. 7			
13:15 - 14:15	**Lunch**			
14:15 - 16:15	**Oral Session 7**	**Biology 2**	**Chair: William E. Hull (Heidelberg, GER)**	
14:15	**Richard L. Ehman**	Mayo Foundation, Rochester, MN, USA	Magnetic Resonance Elastography by Direct Visualization of Propagating Acoustic Waves	**L17**
14:40	**Denis Le Bihan**	SHFJ/CEA, Orsay, FRA	Looking at Tissue Structure and Function at the Microscopic Scale with Macroscopic Images	**L18**
14:55	**Peter Morris**, Richard Bowtell, et al.	Univ. Nottingham, UK	Single-Event fMRI in Motor Cortex and Other Brain Regions	**L19**
15:20	**A.C. Bageac**, M.L. Gray, M. Zhang, A.R. Poole, D. Burstein	Harvard Medical School, Boston, USA	Development of an MRI Surrogate for Immunohistochemical Staining of Collagen Damage in Cartilage	**O17**
15:35	**K. Potter**, J. Butler, W.E. Horton, and R.G.S. Spencer	National Institutes of Health, Bethesda, USA	Non-invasive Evaluation of Engineered Cartilage Tissue Using Proton NMR Microscopy	**O18**
15:50	**T.W.J. Scheenen**, A.M. Heemskerk, et al.	Wageningen University, NL	Xylem at Work: Embolism Induction and Refilling in Vessels of a Cucumber Plant	**O19**
15:50 - 16:00	Discussion			
16:00 - 17:00	**Poster Session 4**	odd numbered posters		

Tuesday	Sept. 7			
17:00 - 19:30	**Oral Session 8**	**X-Nuclei**	**Chair: Gil Navon (Tel Aviv, ISR)**	
17:00	I. L. Moudrakovski, ... and **J. A. Ripmeester**	National Research Council, Ottawa, CAN	^{129}Xe as a Probe for Localized Spectroscopy and Imaging	**L20**
17:25	Anselm Deninger, Balthasar Eberle, ... **Reinhard Surkau** et al.	Univ. Mainz, GER	^{3}He Lung MRI	**L21**
17:50	**Laurence W. Hedlund**, Gary P. Cofer, G. Allan Johnson	Duke University Medical Center, USA	Proton and Helium MR Microscopy of the Small Animal Lung	**O20**
18:05	**Bryan H. Suits**	Michigan Technological University, USA	NQR: What's the Same and What's Different?	**L22**
18:30	**Silvia Olt**, Eva Krötz, et al.	Univ. Würzburg, GER	^{23}Na- and ^{1}H-NMR Microimaging of Intact Plants for a Functional Study of Salt Stress	**O21**
18:45	**Dean O. Kuethe**, Arvind Caprihan, Volker C. Behr, et al.	Lovelace Respiratory Research Institute, Albuquerque, USA	Imaging SF_6 in Lungs as an Index to Gas Exchange: Something Useful?	**L23**
19:10 - 19:25	Michiko Narazaki, Kazuhiro Shimokawa and **Yoko Kanazawa**	Kyushu University, Nihon Schering K.K., Osaka, JPN	Characteristic Diagnosis of Hepatocellular Carcinoma by ^{19}F-MRSI of FDGal	**O22**
19:25 - 19:35	Discussion			
	Evening free for participants			
20:15 - 22:00	**Division Committee Dinner Meeting**	Restaurant to be arranged		

Wednesday	Sept. 8			
8:30 - 10:45	**Oral Session 9**	**Materials 2**	**Chair: B. Balcom (Fredericton, NB, CAN)**	
8:30	**John H. Strange** and Mike J. D. Mallett	Univ. Kent, UK	Broadline MRI of Porous Materials	**L24**
8:55	**M. Bencsik**, P. Mansfield and R. Bowtell	Univ. Nottingham, UK	Ultra-fast Fluid Flow Measurement in Porous Media by MRI: Correlation Studies in a Heterogeneous System	**O23**
9:10	**Teresa G. Nunes**	ICTPOL/IST, Lisabon, POR	Relevant Aspects of Polymer and Cement Science: A Stray-Field Imaging Approach	**L25**
9:35	Burkhard Geil, Gernot Laicher, **David C. Ailion**	Univ. Utah, USA	Restricted Water Self-Diffusion in Lung	**L26**
10:00	**Philip W. Kuchel**	Univ. Sydney, AUS	NMR Diffusion Coherence in Cells	**L27**
10:25 - 10:40	**S. Altobelli**, J. D. Seymour, L. Mondy	New Mexico Resonance, Sandia National Laboratories, USA	Settling in Concentrated Suspensions	**O24**
10:40 - 10:45	Discussion			
10:45 - 11:45	**Poster Session 5**	even numbered posters		

Wednesday	Sept. 8			
11:45 - 13:25	**Oral Session 10**	**EPR**	**Chair: Harold Swartz (Dartmouth, USA)**	
11:45	**Joost A. B. Lohman**	Bruker UK	Aspects of EPR Imaging	**L28**
12:10	**Murali Cherukuri Krishna**	NIH, Bethesda, USA	Time-Domain RF EPRI: Applications in Cancer Research	**L29**
12:35	**Sankaran Subramanian**	NIH, Bethesda, USA	Three-Dimensional Imaging of Small Animals Using Pulsed Radiofrequency EPR	**L30**
13:00 - 13:25	**Harold M. Swartz**	Dartmouth Med. School, USA	In Vivo EPR Spectroscopy for Measuring Oxygen in Tissues and Other Clinically Relevant Applications	**L31**
13:25 - 13:30	Discussion			
13:30 - 14:30	**Lunch**			
14:00 - 15:00	**New Executive Committee Meeting**			
15:30 - 16:00	**Bus Transport to Castle**		Buses will make stops at the Cancer Center and various Hotels to pick up participants	
16:00 - 18:30	**Castle Tours in groups of 30 persons (English and German will be offered)**			
18:30 - 19:00	**Gather in the King's Hall for an Aperitif (sparkling wine)**		A musical Aperitif will be offered by Denis Le Bihan at the Steinway	
19:00 - 21:00	**Festive Buffet Dinner**	(leisure dress)		
21:00 - 22:00	**After Dinner Music**		A selection of romantic piano pieces will be offered by William Hull	
22:00 - 22:30	**Bus Transport to Hotels**			

Thursday	Sept. 9			
8:30 - 9:00	**General Division Meeting**			
9:00 - 10:30	**Oral Session 11**	**Young Investigator Awards**	**Chair: Laurie D. Hall (Cambridge, UK)**	
9:00	**Tomoyuki Haishi**, Yoshimasa Matsuda, Takaaki Uematsu, Katsumi Kose	Univ.Tsukuba, JPN	Development of a compact MR Microscope using a 1.0 T Permanent Magnet	**O25**
9:15	**Stephen Dodd** and Chien Ho	Carnegie Mellon University, Pittsburgh, USA	Short Biplanar Gradient Coils for MR Microscopy Using Concentric Return Paths	**O26**
9:30	**Pablo J. Prado** and Bernhard Blümich	RWTH Aachen, GER	MRI with a Palm-Size Probe	**O27**
9:45	**B. A. Moffat** and J. M. Pope	Queensland University of Technology, AUS	Mapping the Refractive Index Distribution in Crystalline Lenses Using Transverse Relaxation (T_2) Imaging	**O28**
10:00	**Sally Harding**, Herbert Baumann	Univ. of Agricultural Sciences, Uppsala, SWE	Dynamic NMR imaging of chromatographic columns	**O29**
10:15 - 10:30	**Sederman, A.J.**, Gladden, L.F. and Manz, B	Univ. Cambridge, UK	MRI 3D Velocity Mapping in a Sphere Packing: Visualization and Velocity Propagators	**O30**
10:30 - 11:00	**Coffee Break**			

Thursday	Sept. 9			
11:00 - 13:00	**Oral Session 12**	**Materials 3**	**Chair: Rainer Kimmich (Ulm, GER)**	
11:00	**J. M. Pope** and B. A. Moffat	Queensland University of Technology, AUS	NMR Micro-Imaging of Water Diffusion in the Human Eye Lens	**L32**
11:25	**Henk Van As**, Ulrich Tallarek, Tom Scheenen	Wageningen Agricultural University, NL	Flow, diffusion and mass transfer studied by PFG-NMR	**O31**
11:40	**Michael J. McCarthy** and Kathryn L. McCarthy	University of California, Davis, USA	Measurement of Mixing Effectiveness for Suspension Flow in a Kenics Static Mixer	**O32**
11:55	**Bertram Manz**, Patrick B. Warren, et al.	Fraunhofer-Inst. für Biomed. Technik, GER	Flow and Dispersion in Porous Media	**O33**
12:10	**C. De Panfilis** and K.J. Packer	Univ. Nottingham, UK	Characterisation of Porous Media by NMR Imaging and Flow-Diffraction	**O34**
12:25	**Marion I. Menzel**, Song-I Han, et al.	RWTH Aachen, GER	NMR on Salt Water Ice	**O35**
12:40 - 12:55	E. Ciampi, U. Goerke, J.L. Keddie and **P.J. McDonald**	Univ. Surrey, UK	Lateral Transport of Water during Drying of Alkyd Emulsions	**O36**
12:55 - 13:10	Discussion			
13:10 - 14:00	**Lunch**		**Conference Ends**	
			Removal of Posters	

5th Int. Conference on Magnetic Resonance Microscopy, German Cancer Research Center, Heidelberg
Scientific Program: Poster Presentations arranged according to category and topic; Presenter is in bold face.

	Category: Biology		
Abstract	Authors	Affiliation	Title
P1	**W. Gründer**, G. Hanke, U. Reibetanz, A.Werner	Univ. Leipzig, GER	Determination of Structure and Biomechanical Properties of Joint Cartilage by Magic Angle Sensitive Dynamic NMR Microscopy
P2	**Hideyuki Aoshiba**,Yoshiaki Kusaka, Sinitiro Nakajima, et al.	Kyoto Univ. of Medicine, JPN	Matrix Strain and Water Redistribution Within the Intervertebral Disc Under Non-Axial Bending Stress
P3	**Osamu Uemura**, Yoshiaki Kusaka, Shin-ichiro Nakajima, Yoshiteru Seo	Meiji University of Oriental Medicine, Kyoto, JPN	Uneven Strain and Water Kinetics Within the Intervertebral Disc under Compression
P4	R. Haken and **B. Blümich**	RWTH Aachen, GER	Tendon Anisotropy by in vivo T_2 Relaxation with the NMR-MOUSE
P5	**Hisatake Takamiya**, Yoshiaki Kusaka, Yoshiteru Seo, Kazuya Ikoma, et al.	Kyoto Univ. of Medicine, JPN	T_2 Relaxation Anisotropy as a Non-Invasive Measure to Evaluate the Structural Repair of Injured Tendon Tissue
P6	**J. Tritt-Goc, N. Piślewski**, A. Kaflak-Hachulska, D. Chmielewski, et al.	Polish Academy of Sciences, Poznan	Proton Magnetic Resonance Microimaging of Human Trabecular Bone
P7	**Pavol Szomolanyi**, Vladimír Jellúš, Franco Vittur and Renato Toffanin'	Slovak Academy of Sciences, Bratislava	Short-TE projection reconstruction NMR microscopy of trabecular bone
P8	**Matthias Nahrendorf**, Frank Wiesmann, Karl-Heinz Hiller, et al.	Univ. Würzburg, GER	In vivo Assessment of Cardiac Remodeling after Myocardial Infarction in Rats by Cine-FLASH-Magnetic Resonance Imaging – Comparison of methods
P9	**M. Szayna**	NIH/National Institute on Aging, USA	An MRI View of Obesity?
P10	**Bence Csapó**, Josef Széles, Csilla Balássy, Markus Klarhöfer, et al.	Univ.Vienna, Med. School, AUT	In vitro high resolution NMR imaging of the human cervix at 3 T for detection of early cervical carcinoma
P11	**Josef Constantin Széles**, Markus Klarhöfer, Bence Csapó, et al.	Univ. Vienna, AUT	Phase Contrast Angiography and Flow Measurements in the Human Finger
P12	**B. A. Moffat**, I. W. Turner* and J. M. Pope	Queensland University of Technology, AUS	Diffusion Tensor Imaging of Human Eye Lenses

P13	G. Allan Johnson, **Laurence W. Hedlund,** Gary P. Cofer, Sally L. Gewalt	Duke Univ., USA	Rapid Phenotyping using Magnetic Resonance Microscopy
P14	Eric J. Ackerman, Gary R. Holtom, Paul D. Majors, **Kevin R. Minard**, and Robert A. Wind	Pacific Northwest National Laboratory, USA	Integrated Optical and Magnetic Resonance Microscopy for Cellular Research
P15	J.A. Chudek, I.E. Geoghegan, C. Lowe, **G. Hunter**, R.L. MacKay,et al.	Univ. Dundee (Scotland), UK	A Study of the Effect of Dietary Changes on the MRM characteristics of the Seven-spot Ladybird *Coccinellae septempunctata.*
P16	J.A. Chudek, C. Halpin, D.W. Hopkins, **G. Hunter**, J. Metcalfe and E.A. Webster	Univ. Dundee (Scotland), UK	T_2 and ^{1}H Density Maps as Probes of Changes in the Lignin Structure of the Stems of Genetically Modified Tobacco Plants
P17	Juan J. Gonzalez; .... and **Michael J. McCarthy**	Univ. California, Davis, USA	Detection and Monitoring of Internal Browning Development in Fuji Apples Using NMRI
P18	**Nobuaki Ishida**, Seiichiro Isobe, Mika Koizumi, et al.	National Food Research Institute, Tsukuba	Effect of Electric Field on Water Status in Germinating Morning Glory Seeds
P19	Bertram Manz and **Frank Volke**	Fraunhofer-Inst. Engineering (IBMT), GER	Dehydration Of Multilamellar Phospholipid Model Membranes Studied On-line With ^{1}H-NMR Microimaging
P20	**Olga V. Volobuyeva**, Genady A. Velikanov, et al.	Kazan State Univ., RUS	NMR Study of Water Permeability of Two Transport Channels in Plasmodesmata in Plant Cells
P21	**L. van der Weerd**, M.M.A.E. Claessens, H. Van As	Wageningen Univ., NL	Imaging Membrane Permeability in Plants during Osmotic Stress
P22	**N. Sorokina**, V. Oslopov	Kazan Institute of Biochemistry and Biophysics	Disturbance of the Ion Exchange at Membrane Pathology. A NMR Study
P23	**Saebomi Park**, Seung-Cheol Lee, et al.	Korea Basic Science Institute, Taejon, KOR	NMR Microscopy of Biological Samples at 600 MHz
P24	**M. Gussoni**, F. Greco, A.Vezzoli and L. Zetta	Università di Milano, IT	MRM Images from Biology and Materials Science
P25	**R. Giesen**, C. Chwatinski, D. E. Demco, B. Blümich,et al.	RWTH Aachen, GER	Applications of NMR Imaging to Biomaterials
P26	**A. Berg**, A. Ertl, E. Moser	Univ. Vienna, AUT	High-resolution quasi-3D gel dosimetry: applications using γ-knife collimators of different sizes

	Category: Diffusion & Flow		
P27	**François Humbert**, Michel Valtier, and Daniel Canet	Université Henri Poincaré, Nancy, FRA	Self-Diffusion Coefficient Maps and Visualization of the Restricted Diffusion in NMR Microscopy using B_1 Gradients
P28	**François Humbert**, Marie-Hélène Ropers, Marie-José Stébé, and Daniel Canet	Université Henri Poincaré, Nancy, FRA	Application of B_1 Gradients in NMR Microscopy: Structural and Dynamical Study of a Water-Nonionic Fluorinated Surfactant System
P29	**Bernd Simon** and Hartmut Oschkinat	Forschungsinstitut für Molekulare Pharmakologie, Berlin	Signal Attenuation by Self-Diffusion in Pulsed Field Gradient Heteronuclear Spectroscopy
P30	**K. V. Adams** and L. F. Gladden	Univ. Cambridge, UK	H_2O Self-Diffusion Within Cellulose Fibres Studied Using Pulsed Gradient Nuclear Magnetic Resonance
P31	**M.V. Skirda***, R.V. Archipov	Kazan Physical-Technical Institute, RUS	NMR Study of Self-diffusion in the Isotropic Phase of a Nematic Liquid Crystal
P32	**Irene Bartusseck**, Christian Heine, Song-I Han, Siegfried Stapf,et al.	RWTH Aachen, Germany	Chemical-shift Selective NMR and MRI Investigations of Diffusion and Transport in Multicomponent and Multiphase Systems
P33	**M. L. Johns** , A.J. Sederman , L.F. Gladden , A. Wilson , S. Davies	Univ. Cambridge, UK	Displacement Propagators as a Probe of the Effect of a Polymer Treatment on the Permeability of Rock
P34	**William M. Holmes**, Robin G.Graham and Ken J.Packer	Univ. Nottingham, UK	Diffusion in surface-wetting films in a two-phase saturated porous solid characterised by pulsed magnetic field gradient NMR
P35	**Oleg Opanasyuk**	Kazan State Univ., RUS	Molecular Mobility Of Liquids in ZSM-5 Zeolite
P36	**M. Iko Burgar**	CSIRO, AUS	Detection of Fluid Flow by Profile Imaging
P37	Alexandr L. Fiodorov, **Viatcheslav V. Frolov** and Konstantin V. Tiutiukin	St. Petersburg State University, RUS	NMR imaging of dead flow using a very low magnetic field
P38	**Song-I Han**, Christa Chwatinski, Siegfried Stapf, et al.	RWTH Aachen, GER	Imaging and Exchange NMR of Translational Motion
P39	**Marion I. Menzel**, Song-I Han, et al.	RWTH Aachen, GER	NMR on Salt Water Ice

	Category: Instrumentation		
P40	**P.A. de Jager**, T.W.J. Scheenen, and H. Van As	Wageningen Univ., NL	A Sensitive RF Coil for MRI Studies on Plant Stems
P41	**Wolfgang U. Roffmann,** Stuart Crozier, et al.	Univ. Queensland, Brisbane, AUS	The "TILT-Coil", a Novel RF Coil with 360 Degree Rotation
P42	**Ken-ichi Hasegawa** [1], Yoshiaki Yamakoshi [1], Koji Saito [2]	JEOL Ltd., JPN	High-Temperature Imaging Probe
P43	W. H. Wong, **Subramaniam Sukumar**, and Howard Hill	Varian NMR Systems, USA	Applications of the "MP-Q" Imaging Coil
P44	**J. Dechow**, A. Forchel, T. Lanz, A. Haase	Univ. Würzburg, GER	Fabrication of NMR microsensors for nanoliter sample volumes
P45	**J-C. Ginefri** [1], L. Darrasse [1], P. Crozat [2]	CNRS, Orsay, FRA	Resolution Improvement on *In-Vivo* Human Skin Microscopy using a superconducting receiver coil at 1.5 Tesla
P46	**D. Tomasi**	Univ. Nac.al de Gen. San Martin, Buenos Aires, ARG	Stream Function Optimization for Gradient Coil Design
P47	**Ralf Eymael**, Kidist Hailu, Anette Wiesmath, et al.	RWTH Aachen, GER	The NMR MOUSE: New Developments, Methods and Applications
P48	**Eiichi Fukushima** and Jasper A. Jackson	New Mexico Resonance, Albuquerque, USA	Unilateral Magnets for Remote NMR
P49	P. Kinchesh, A.A. Samoilenko, **A.R. Preston** and E.W. Randall	Univ. London, Queen Mary & Westfield College, UK	Development of a Large-Diameter (5-cm) STRAFI Probe and Preliminary Results
P50	**Tomoyuki Haishi**, Takaaki Uematsu, Yoshimasa Matsuda, et al.	Univ. Tsukuba, JPN	Development of an MR Microscope Using a Portable MRI unit and a Clinical Whole-Body Magnet

	Category: Materials		
P51	**Johannes Leisen**, Haskell W. Beckham	Georgia Inst. of Technology, USA	Quantitative Applications of Magnetic Resonance Microscopy for the Characterization of Moisture Distributions in Fibrous Substrates
P52	**Manfred Knörgen**, Horst Schneider, Karl-Friedrich Arndt, et al.	Univ. Halle-Wittenberg, GER	Investigation of Swelling and Diffusion in Organic and Non-Organic Materials by ^{1}H- and ^{2}H-NMR Imaging
P53	**Anne Pollaris**, Peter Adriaensens, Victor Litvinov, et al.	Limburg University, BEL	Magnetic Resonance Imaging Study of Water Ingress into Polyamide 4,6
P54	**G. Maddinelli** and A. Ferrando	Enitecnologie S.p.A., Milano, Italy	Diffusion of Solvents Inside Multi-Phase Polymer Systems
P55	**Liesbet Storme**, Peter Adriaensens , Victor Litvinov, et al.	Limburg Univ., BEL	Visualization of Tensile Stress Induced Material Response at a Crack Tip in Polymers under Critical Load by NMR Imaging
P56	**Peter Adriaensens**, Anne Pollaris, Jeffery White, et al.	Limburg Univ., BEL	Critical Analysis of Network Defects and Statistical Void Densities in Cross-linked Isobutylene-Based Elastomers by NMR Imaging.
P57	**Paul Denner**, Lutz Deutschbein, Sergui Zhukov, Bernd Walter	Ilmenau Technical Univ., GER	Analysis of Local and Coherent Segmental Mobility in Elastomeric Materials by NMR Techniques
P58	**Maciej Garbarczyk**, Farida Grinberg, Rainer Kimmich, et al.	A. Mickiewicz Univ., Poznan, POL	The NMR dipolar-correlation effect as a potential imaging contrast parameter for material properties of polymer networks
P59	**L. Gasper**, M. Schneider, D. E. Demco, and B. Blümich	RWTH Aachen, GER	NMR Dipolar Contrast Filters in Soft Matter
P60	**U. Goerke**, E. Crilly, P.J. McDonald, A.H.L. Chamberlain	Univ. Surrey; UK	Stray Field Imaging and Numerical Modelling of Water Ingress into Compacted Xanthan Powder
P61	Bryce MacMillan, Greg Ziegler, **Bruce Balcom**	Univ: New Brunswick, CAN	Visualization of Moisture Transfer During Starch Molding Using SPRITE

P62	**I.V. Koptyug,** R.Z. Sagdeev, L.Yu. Khitrina, and V.N. Parmon	Int. Tomography Center, Novosibirsk, RUS	Supported Catalysts and Sorbents: An NMR Microscopic Visualization of Active Components and Dynamic Processes
P63	**Siegfried Stapf**, Ken J. Packer, Pierre M. Adler	Univ. Nottingham, UK RWTH Aachen, GER	Rheoporometry - One- and Two-Dimensional *q*-Space Mapping of Fluids in Porous Media as a Tool to Probe Restricted Geometries
P64	**E.N. Vasina**, V.D. Skirda	Kazan State Univ., RUS	Determining an Angle Distribution of Pore Channels in Track Membranes by NMR PFG
P65	**Andreas Klemm**, Rainer Kimmich	Univ. Ulm; GER	Velocity Mapping in Percolation Model Objects: Detection of a New Power Law
P66	**Markus Weber**, Andreas Klemm, Rainer Kimmich	Univ. Ulm; GER	Free Convection in Porous Media: Simulation and NMR Experiment
P67	**T. Watanabe**, S. Matsukawa, and K. Gersonde	Tokyo Univ. Fisheries, JPN	Visualization of the Diffusion of Cu^{2+} Ions in Dextran/K^+ Gel and Dextran/Na^+ Viscous Sol Systems by NMR Microscopy
P68	Kathrin Hesse, **Günther Neue**	Univ. Dortmund, GER	Skin Effect Imaging of Small Spheroidal Particles
P69	**A.M.Zaripov**, G.G. Pimenov and A.V.Filippov	Kazan State Univ., RUS	Crystallization Kinetics of Flexible Chain Polymer Confined in Pores
P70	**Jadwiga Tritt-Goc** and **Narcyz Piślewski**	Polish Academy of Sciences, Poznan, POL	The Hardening of Portland Cement Paste and Freezing of Hardened White Cement Monitored by Single-Point Imaging
P71	John A. Chudek, Charles H. Lloyd, **Sheelagh N. Scrimgeour,** Geoffrey Hunter	Univ. Dundee (Scotland), UK	The Application of the FLASH - MOVIE to the Study of Polymerization of Visible Light Cured Dental Restorative Materials

	Category: Methods		
P72	Elisabeth de Castro Caparelli and **Dardo Gustavo Tomasi**	Univ. Nac. de San Martin, Buenos Aires, ARG	An Analytical Calculation of the Biot Savart Law
P73	**F. Bălibanu**, K. Hailu, R. Eymael, D.E. Demco and B. Blümich	RWTH Aachen, GER	Numerical Simulations of the Signal Response for the NMR-MOUSE
P74	**F. Vergeldt**, D. Hluskov, S. Melnikov, E.G. Novikov and H. Van As	Wageningen Agricultural Univ., NL	Modeling of Self-Diffusion and Relaxation Time NMR in Multi-Compartment Systems
P75	**Harvey H. Hensley**, John Haselgrove	Fox Chase Cancer Center, Phila, USA	The Effect of Finite Pixel Size and Signal-to-Noise Ratio on Quantitative Measurements in Magnetic Resonance Microscopy
P76	**Radomír Svoboda**	Brno Univ. Technology, SLV	Estimation of NMR Signal Frequency Using FIR Filters
P77	S.D. Beyea, **B.J. Balcom**, I.V. Mastikhin, et al.	Univ. New Brunswick	turboSPI: A New MRI Technique for Imaging of Heterogeneous Materials
P78	D. J. Goodyear and **B. J. Balcom**	Univ. New Brunswick, CAN	A Single-Point Approach to Spiral Scan Magnetic Resonance Imaging
P79	**C. Ramanathan**, S. Gutteridge and R. Bowtell	Univ Nottingham	Structural Investigations Using the Long-Range Dipolar Field in liquid-State NMR
P80	**T. G. Nunes**, E.W. Randall, G.Guillot	ICTPOL/IST, Lisabon, POR	^{1}H Stray-Field Magnetic Resonance Imaging of Water in Different Chemical Environments: Long Hahn-Echo Train Observations
P81	A.R. Preston, **E.W. Randall** and P. Kinchesh	Univ. London, Queen Mary & Westfield College, UK	Calibration of the Gradient of the Stray Magnetic Field by Multi-Nuclear STRAFI
P82	Jeffrey H. Walton, Juan J. Gonzalez, and **Michael J. McCarthy**	Univ. California, Davis, USA	Temperature Mapping via Chemical Shift Imaging

	Category: X-Nuclei		
P83	**Volker C. Behr**, Dean O. Kuethe	Univ. Würzburg, Lovelace Respiratory Research Inst., USA	Relaxation of fluorinated gases for lung imaging
P84	**A. R. Cross**, S. Breeze, I. Cameron, et al.	Carleton Univ., Ottawa, CAN	T_1 Measurements of Hyperpolarized Xenon at 85 Gauss
P85	**Igor L. Moudrakovski**, Anivis Sanchez, et al.	National Research Council, Ottawa, CAN	Application of Optically Polarized ^{129}Xe to Magnetic Resonance Imaging and Spectroscopy of Microporous Materials
P86	Jeffrey H. Walton, and **Michael J. McCarthy**	Univ. California, Davis, USA	Preliminary Investigations on ^{17}O Imaging to Study Moisture Distribution and Migration in Foods
P87	**M. Heidenreich**, W. Köckenberger, N. Chandrakumar, R. Bowtell, R. Kimmich	Univ. Ulm, GER	Indirectly detected ^{13}C NMR imaging

Abstracts for the Educational Session

E1

Fourier Imaging: Spatial Resolution and Contrast

Bernhard Blümich

Magnetic Resonance Center MARC, RWTH Aachen, D-52056 Aachen

NMR is known to the public because of its significance as a diagnostic imaging method in medicine. In competition with X-ray tomography, NMR imaging provides unique features which are unsurpassed by other imaging methods. Although the spatial resolution often is less than microscopic, the possibilities to achieve contrast in soft matter and to map functional processes in a noninvasive fashion are most striking. These features are also of benefit in materials science and other non-medical fields of research, process and quality control.

Following a short introduction to NMR the concepts of space encoding and spatial resolution are introduced along with k space, the space which is obtained by inverse Fourier transformation of functions in real space. Most NMR imaging experiments are carried out in Cartesian k space. These imaging methods are referred to as Fourier imaging. Different basic methods of Fourier imaging are reviewed for imaging of liquids and soft matter as well as for solid-state imaging of rigid matter, where special techniques are required to cope with strong nuclear spin interactions, which are absent in most liquids. Particular attention is paid to different ways of introducing contrast. The various techniques addressed in the lecture are illustrated with examples from non-medical NMR. The presentation concludes with a short overview of single-sided NMR for process and quality control.

Literature

P. T. Callaghan, *Principles of Nuclear Magnetic Resonance Microscopy*, Clarendon Press, Oxford, 1991.

R. Kimmich, *NMR Tomography, Diffusometry, Relaxometry*, Springer, Berlin, 1997.

M. T. Vlaardingerbroek, J. A. den Boer, *Magnetic Resonance Imaging*, Springer, Berlin, 1996.

B. Blümich, *NMR Imaging of Materials*, Clarendon Press, Oxford, in press.

B. Blümich, P. Blümler, R. Botto, E. Fukushima, *Spatially Resolved Magnetic Resonance*, Wiley-VCH, Weinheim, 1998.

B. Blümich, W. Kuhn, *Magnetic Resonance Microscopy*, VCH, Weinheim, 1992.

J. B. Miller, *Progr. Nucl. Magn. Reson. Spectrosc.* **33,** 273 (1998).

E2

Biomedical NMR Imaging

Axel Haase

Physics Institute, University of Würzburg, 97074 Würzburg, Germany

NMR imaging has tremendous clinical importance, but it is now well-established that this technique has great potential in all areas of medicine and biology. Compared to other imaging modalities, NMR is non-invasive and has no harmful side-effects. NMR imaging is applicable to human studies, large but also very small animals, embryos, organs and cell cultures. In addition, plant physiology is a further area for biomedical NMR imaging. However, it must be noted that other imaging techniques exhibit a higher spatial resolution (e.g. X-ray), have shorter measuring times (e.g. ultrasound) and provide a deeper investigation of the biochemistry of tissues (e.g. positron emission tomography). The great advantage of NMR compared to other imaging techniques is that many aspects of the live tissue can be investigated using one experiment: characterization of the anatomy, function and biochemistry of the tissue. NMR imaging is a so-called "one-stop-shop".

The lecture will be limited to ^{1}H-NMR imaging, other nuclei will be covered in another presentation. Furthermore, only some important applications of ^{1}H-NMR spectroscopy in combination with imaging will be presented.

The spatial resolution in biomedical NMR-imaging is poor compared to other methods although some parameters (NMR relaxation times, chemical shift or *J*-coupling) in NMR provide very local information on a nanometer scale. The typical volume of an image element (voxel) in (human) medical NMR imaging is 1 mm^3 while for small animals (and plants) it may reach 10^{-5} mm^3. This later regime is the area of "NMR microscopy" which is one of the major topics of this conference. This wide range in spatial resolution is only possible with major hardware changes. Medical NMR imaging is entirely performed using static magnetic field strengths of below 2.0 T and magnetic field gradients of up to 40 mT/m. NMR microscopy on small animals, organs, etc. needs high magnetic field strengths up to 17.5 T and gradient strengths of more than 1000 mT/m. The main limitation in biomedical NMR imaging is the limited signal/noise ratio (note: the NMR signal is linearly dependent on the voxel volume!), technological limits (maximum magnetic field strength and gradient strength is dependent on the present state of magnet technology!) and safety concerns.

The most important topic for the biomedical application of NMR imaging is the image contrast. There exists an intrinsic image contrast due to the interaction of NMR properties of the tissue, image sequences and scan parameters. For the beginner in this field, NMR image contrast is the most confusing issue. The NMR signal intensity depends on intrinsic parameters (e.g., relaxation times T_1, T_2, spin density, magnetic susceptibility, bulk flow, perfusion, oxygenation, temperature, etc.), on the type of NMR experiment (spin-echo, gradient-echo, stimulated-echo, and their timing parameters), and on the NMR instrument (magnetic field strength, radiofrequency coil, stability, etc.).The dependencies are well understood and should be kept in mind in all biomedical applications. In addition, it is important that true biological information can be obtained, when these parameters are measured quantitatively (e.g. perfusion, oxygenation, temperature, blood flow, etc.). Furthermore extrinsic contrast can be obtained using contrast media. Here abnormal perfusion and tissue-specific information can be detected, like the detection of the breakdown of the blood-brain barrier.

A prerequisite for all biomedical NMR imaging applications is the use of a fast imaging technique. For example, it is needed to "freeze" cardiac motion which can be as fast as 600 beats/min in mice. In many applications, three-dimensional image acquisition, determination of quantitative parameters and functional information is needed. In order to keep the total experimental time as short as possible, some kind of fast acquisition is applied. During the last two decades, a large number of fast NMR imaging techniques was described. The lecture will summarize the important advantages and disadvantages of the different methods. The improvement of fast imaging methods is still going on. Recently, a dramatic decrease of the image acquisition time could be achieved using new hardware developments, e.g. phased-array coil technology.

Dramatic improvements were described in biomedical NMR imaging in the area of flow imaging and applications to angiography and the determination of perfusion. The method and applications to animal studies will be demonstrated in the lecture.

These methods were first described and applied in animal studies and clinical examinations. However, NMR imaging is not only limited to this area. Several groups have successfully applied NMR imaging to the study of plant physiology and function. Important studies, techniques and experimental difficulties for NMR of plants will be summarized in this lecture.

E3

Q-space and beyond

Paul T. Callaghan

Institute of Fundamental Sciences, Physics, Massey University
Palmerston North, New Zealand

The use of pulsed magnetic field gradients in order to encode spin magnetization for position or positional displacement leads to a variety of spatial coherences in the spin phases, each coherence being manifest in a characteristic diffraction pattern, whether in k-space or q-space. These phenomena, which are sensitive to different temporal moments of the gradient waveform, range from the original Mansfield-Grannell position diffraction, through diffusive and flow diffraction, to diffraction patterns which arise due to dispersion in a heterogeneous velocity field. Each of these will be described and examples of their use given.

In fact the idea of applying single gradient pulses to phase encode for position, or double gradient pulses to phase encode for displacement, can be generalised to provide pulse sequences which are sensitive to other categories of motion. One approach is to use steady time-varying gradients which can then probe the frequency domain of motion. Another approach is to use the double PGSE sequence, which is especially effective in encoding for changes in motion. In particular the double Pulsed Gradient Spin Echo NMR experiment may be used to study stochastic processes in dispersive flow. We give a detailed analysis of this type of experiment, illustrated with the example of Poiseuille flow in a pipe.

1. Diffraction effects

1.1 Mansfield and k-space-position diffraction.
1.2 q-space and position correlation (diffusive) diffraction.
1.3 Interconnected porous media, diffusive and flow diffraction.
1.4 Finite pulse duration effects.
1.5 Dispersion and the gaussian limit.

2. PGSE NMR with generalised Gradient waveforms and restricted diffusion

2.1 Theoretical treatments - gaussian assumption.
2.2 Impulse-propagator formalism
2.3 Frequency Domain PGSE NMR

3. Dispersion and restricted diffusion

3.1 Stochastic fluctuations and dispersion
3.2 The double PGSE NMR experiment
3.3 Velocity correlation and stochastic displacement correlation
3.4 Taylor dispersion in pipe flow

E4

Imaging of X-Nuclei

Gil Navon

School of Chemistry, Tel Aviv University, Tel Aviv 69978, Israel.

The talk will review various aspects of MR imaging of nuclei other than protons ("X-nuclei"). The review will start with direct imaging of high sensitivity X-nuclei, i.e. hyperpolarized noble gases and fluorine. Then methods of indirect detection of X-nuclei will be described. In these methods, proton images reflecting the distribution of the X-nuclei are obtained. Finally, MRI and multiple-quantum filtered (MQF) MRI of quadrupolar nuclei will be described.

The best known case of X-nuclei imaging with sensitivity comparable to that of protons is the case of the hyperpolarized noble gases – ^{129}Xe and ^{3}He. The basic principles and few examples will briefly be described.

1. The relative sensitivity of ^{19}F is very close (83%) to that of protons. Fluorine is not a natural constituent of biological tissues. However it is present in many drugs. Consequently ^{19}F NMR and MRI are useful for the study of the pharmacokinetics and the spatial distribution of fluorine-containing drugs.
2. Indirect detection of X-nuclei: spin polarization induced NOE (SPINOE) and proton imaging of oxygen-17 (PRIMO).
3. Quadrupolar nuclei. Examples will be given for ^{23}Na and ^{2}H imaging. The method of double-quantum filtered (DQF) MRI will be described. In this technique a new contrast mechanism is obtained, utilizing the residual quadrupolar interaction resulted from the anisotropic motion of molecules in ordered biological tissues.

E5

EPR in Viable Systems

Harold M. Swartz

EPR Center for the Study of Viable Systems; Department of Radiology,
Dartmouth Medical School, Hanover, NH 03755

EPR (ESR) is a magnetic resonance technique that is similar in many ways to NMR, but is based on the magnetic properties of the electron rather than a nucleus. Because the magnetic moment of the electron is about 700 times larger than that of the proton, on a per spin basis EPR is considerably more sensitive. Because electrons usually are paired and therefore have no net magnetic moment, EPR features absolute specificity for species with *unpaired* electrons (paramagnetic species). The usual types of such molecules that are important in biomedical studies are free radicals (both naturally occurring and, especially, synthetic free radicals) and paramagnetic metals.

One of the most important and biologically useful aspects of EPR spectra is their sensitivity to the environment surrounding the unpaired electron. Like NMR this includes spectral splitting due to the presence of other magnetic species, especially nuclei with net magnetic moments. In addition, the EPR spectra, especially those spectra with hyperfine structure due to splittings from nuclei are changed significantly by many parameters of interest such as pH, molecular oxygen, charge, and motion of the molecule on which the unpaired electron is located. Many of these parameters are both important and difficult to measure by other means.

The three most important potential limiting factors for the use of EPR in biological systems are the typically short relaxation times of the unpaired electrons, the high frequency needed for high sensitivity, and the lack of naturally occurring high concentrations of paramagnetic species. When the biological sample is a living animal, additional problems may arise because of the presence of physiological motions.

Recently many of the potential technical limitations have been overcome and EPR studies of intact biological systems have become increasingly reported. The results indicate that this technique can provide very useful information that often is different or better than that obtainable by other techniques.

The presentation will review briefly the principles of EPR spectroscopy, consider in more detail the types of information and techniques that provide useful data, and then survey the areas in which EPR spectroscopy is being used successfully in experimental animals. The aim is to provide participants who have a background in NMR with sufficient information and orientation to obtain full benefit from the presentations in the regular sessions that use EPR techniques.

Abstracts for the Scientific Session

Plenary Lectures

L1

From Solids to Humans by NMR

Peter Mansfield

Magnetic Resonance Centre, University of Nottingham

As far as I am concerned, MRI started in the summer of 1972 when I first had the idea of imaging solids. This arose out of work that I had been actively engaged with in the development of multiple-pulse line-narrowing sequences for removing or reducing dipolar interactions in solids. At that time we had recently developed a class of reflection symmetry cycles using short 90° pulses with appropriate relative rf phases, and we were able to reveal hidden chemical shift interactions in a range of solids. Ulrich Häberlen was engaged in similar work in Heidelberg.

Our particular sequences, one of which was named the MREV-8 sequence (incidentally, it was named by the German group), were being used at Nottingham to look at chemical shift anisotropy in a range of fluorinated materials including Teflon. We quickly ran out of easily available materials, and this led me to think long and hard about other possible applications. It was at this point that I realised that, if the dipolar interaction could be removed, there may be the possibility of looking at structure in solids. As it transpired, I came to Heidelberg in the autumn of 1972 to work with Ulrich Häberlen on further developments of multipulse sequences and was, therefore, unable to continue the work in imaging myself. However, this was continued at Nottingham in my absence and later led to our independent publication on MRI in solids in 1973. In my view this is a classic example of a situation where fundamental scientific research in one area leads to an entirely new approach in a different area, and in the case of MRI this new direction created an entirely new industry.

Microscopy was always at the heart of my early thinking in MRI, and it is satisfying to see so many applications of high- and ultra-high-resolution MRI in solid and liquid systems, and especially in porous media. One of the major problems with high-resolution MRI is that echo-volumar imaging (EVI) may well be the direction that should be given some priority. We have been developing at Nottingham ultra-high-speed imaging techniques based on echo-planar imaging (EPI) but specifically for situations where susceptibility can interfere with image quality. For these techniques, which are related to solids imaging methods, a sequence of short 90° pulses is used, both to encode velocity in our case but also to do spatial encoding instead of using the traditional gradient modulation of EPI. However, there is a new class of EVI techniques which use 180° pulses instead of gradient modulation, and this class has been dubbed π-EVI or PEVI. PEVI has not been tried out so far in our laboratory, but it clearly has an advantage in terms of data acquisition rate and might well be the way forward in an area where imaging is inherently slow. π-EPI or PEPI has been tried out at Nottingham, and images showing detail in a porous vuggy dolomite have been produced.

Medical imaging is now a vast subject, and in the limited time available I can only select one or two topics which could have applications in both small- and large-scale imaging. The first of these is active magnetic screening. Since we introduced the concept in 1986, its major application has been in gradient coil design, but I wish to mention another so far unexploited area. The second is acoustic screening of gradient coils. This could have important ramifications at the microscopic level but especially so for human imaging since in many high-speed applications of imaging the sound level could exceed 130 dB.

L2

SPRITE Magnetic Resonance Imaging of Materials

Bruce J. Balcom

MRI Research Centre, Department of Physics, University of New Brunswick,
Fredericton, NB, Canada

A wide variety of physical systems which one may wish to visualize with MRI are difficult or impossible to image with traditional techniques due to very short transverse spin-spin relaxation times. The SPRITE method, and its derivatives, have proven to be a general and robust way of overcoming the difficulties inherent to imaging broad linewidth systems [1,2]. The methods are intuitively appealing because they do not require specialized hardware, the image contrast is easily controlled and understood and the techniques do not depend on the specific relaxation mechanism [3]. This lecture will cover the basis of the SPRITE technique as well as improvements in the basic methodology over the last two years. Material science applications including porous materials [4,5], rigid polymeric materials [6], and biopolymers will be chosen to illustrate the features of the basic techniques.

References

1. Balcom, B.J.; SPRITE Imaging of Short Relaxation Time Nuclei. In: *Spatially Resolved Magnetic Resonance: Methods. Materials, Medicine, Biology, Rheology, Geology, Ecology, Hardware.* Wiley-VCH, Weinheim, Germany, 1998.
2. Beyea, S.D., Balcom, B.J., *et al.*; Relaxation Time Mapping of Short-T_2* Nuclei with Single-Point Imaging (SPI) Methods. *J. Magn. Reson.* **135**, 156-164 (1998).
3. Prado, P.J., Balcom, B.J., *et al.*; Magnetic Resonance Imaging of Gases. A SPRITE Study. *J. Magn. Reson.* **137**, 324-332 (1999).
4. Beyea, S.D., Balcom, B.J., *et al.*; Magnetic Resonance Imaging and Moisture Content Profiles of Drying Concrete. *Cement and Concrete Research* **28**, 453-463 (1998).
5. Prado, P.J., Balcom, B.J., *et al.*; Spatially Resolved Relaxometry and Pore Size Distribution by Single Point MRI Methods. Porous Media Calorimetry. *J. Phys. D* **31**, 2040-2050 (1998).
6. Kennedy, C.B., Balcom, B.J., Mastikhin, I.V.; Three-Dimensional Magnetic Resonance Imaging of Rigid Polymeric Materials Using Single-Point Ramped Imaging with T_1 Enhancement (SPRITE). *Can. J. Chem.* **76**, 1753-1765 (1998).

L3

MRI Heterogeneities and End-User Properties of Polymer Materials

J. Gelan, P. Adriaensens, A. Pollaris and L. Storme

Institute for Materials Research, Limburg University, Building D, Department SBG
B-3590 Diepenbeek, Belgium

In a first contribution a MRI study of void distribution and of the heterogeneity of organic and anorganic cross-linkers of industrial rubbers will be presented. Using chemical shift selective imaging, separate rubber and solvent images of the same slices can be generated. Images of swollen as well of non-swollen rubbers will be discussed.

The next contribution will show how a combination of MRI and wideline NMR relaxometry, correlated to data from DSC and gravimetry, is used to obtain information about the water absorption mechanism of a high crystalline nylon, polyamide PA46, which deviates from more classical polyamides. Usefulness of simple spin-echo MRI sequences combined with the need for signal quantification will be shown.

The last contribution will demonstrate the use of MRI to study the crack-growth resistance of polymer materials under conditions of critical load. Acquisition of MRI images of such samples is made possible by the development of a dedicated stress calibrated device, fitting in the MRI probehead. Images of samples of two types of injection moulded materials, measured under constant load, will be shown and interpreted. As examples an ABS (acrylonitrile butadiene styrene) and a block copolymer PBT/PTMO (poly-butyleneterephtalate/poly-tetramethylene oxide) will be shown.

L4

Learning from Carotid Arteries using High-Resolution in vivo MRI

Sudeep Chandra, Susanta K. Sarkar, Frank C. Barone, and Eliot H. Ohlstein

SmithKline Beecham Pharmaceuticals, King of Prussia, PA, 19355, USA.

Introduction

Magnetic resonance imaging (MRI) provides the option to study anatomical changes *in vivo* in high resolution. Use of this tool in early phases of drug discovery research provides numerous benefits. For example, one can serially characterize experimental animal models *in vivo*, serially profile disease modifying interventions, and provide lead differentiation for future drug development. A wide spectrum of studies from pharmaceutical R&D laboratories[1-7] has demonstrated each one of these benefits. This presentation describes two specific applications of MR imaging to illustrate its utility in pharmacological testing of experimental agents in carotid artery disease.

Model 1

Vascular restenosis (renewed stenosis or lumen loss) after percutaneous transluminal angioplasty (PTCA) poses a formidable challenge for clinical management. Typically, a restenotic relapse occurs in a large patient population (~30-50%) in the clinic following PTCA or stent implantation. The carotid balloon angioplasty model[8] in the rat is often used as a primary *in vivo* screen for testing agents designed to alleviate this problem. In combination with *in vivo* high-resolution MRI (~100 x 100 μm in-plane) the feasibility to follow vascular lumen loss in the rat carotid artery has been demonstrated before[4,9,10]. In this study, the efficacy of a nonpeptide dual ET_A/ET_B receptor antagonist, *SB 217242*, (15 mg/kg, bid, po) to prevent such vascular stenosis was tested in the rat using MRI in conjunction with histological analyses (n = 11-12 in both treated/non-treated groups).

A cardiac-gated T_2-weighted pulse sequence (TR/TE = 4000/23 ms) was used with flow-tailored gradient pulses (1 G/cm) in a 4.7 T/40 cm Bruker Biospec spectrometer. Eighteen 1.5-mm slices were collected with an in-plane resolution of 120 x 120 μm over a FOV of 3 x 3 cm. The lumen volumes of carotid arteries were estimated serially at baseline, day 7 and day 14 after balloon catheter-induced denudation of the carotid arterial wall. Histomorphometric analysis was performed at day 14 after surgery to quantitate intimal hyperplasia.

Results

In comparison to vehicle-treated animals, a 20% protection (p<0.05) from reduction in lumen volume was obtained by using *SB 217242*. Histologic analyses indicated a 42% decrease (p<0.05) in the neointimal growth. The MRI lumen volumes had a significant correlation with the corresponding histologic indices. Protection from both lumen volume reduction and neointima formation could thus be demonstrated in this model by use of non-invasive imaging as an adjunct tool.

Model 2

In a second study, vascular compliance was studied in spontaneously hypertensive stroke-prone rats (SHRSP), which served as a control strain for severe hypertension. To quantitate the lack of blood vessel compliance in these animals, high-resolution cardiac-gated MR angiograms (first-order gradient moment nulled gradient-echo sequence with TR/TE = 1800/11 ms; 256 x 256 pixels; FOV = 3 x 3 cm; three 1.5-mm slices) were acquired on a 4.7 T/40-cm Bruker spectrometer with a

home-built 9-strut half-birdcage RF transceiver. These images allowed direct visualization of arterial lumen cross-sections *in vivo*.

Normalized over blood pressure, a distensibility index (D)[11] was calculated for spontaneously hypertensive stroke-prone (SHRSP; n = 4), and normotensive (WKY; n = 4) strains of rats. The antihypertensive agent *Eprosartan* (60 mg/kg/day; chronic dosing for 18 weeks) was tested for its efficacy to increase the distensibility index in this experimental model of hypertension.

Results

A significant (p<0.01) reduction in vessel distensibility (p<0.01) was obtained for the SHRSP animals both on normal diet (D = 0.42 ± 0.04 %/mm of Hg) as well as on high-salt/high-fat diet (D = 0.29 ± 0.04) as compared to the WKY (D = 1.1 ± 0.04) controls. Treatment with *Eprosartan* significantly (D = 0.80 ± 0.01) reversed this loss in distensibility (p<0.01) in the SHRSP group on high-salt/high-fat diet. These data indicate that MRI can characterize these contractile components of blood vessels *in vivo* and that these measures can yield valuable information on *in vivo* efficacy of vasoactive agents.

With the advent of high-throughput combinatorial chemistry, early *in vivo* testing will become increasingly important in the selection of drug candidates from diverse chemical leads. MR imaging can add value to this effort by allowing serial monitoring of surrogate markers of disease in small animal models.

References

1. Rudin *et al.*, *TIPS* **12**, 416-421 (1991).
2. Sarkar *et al.*, *Magn. Reson. Med.* **7**, 117-124 (1988).
3. Sauter and Rudin, *Stroke* **17**, 1228-1234 (1986).
4. Cook *et al.*, *Blood Pressure* **2**, 322-331 (1993).
5. Waterton *et al.*, *Magn. Reson. Med.* **28**, 84-86 (1992).
6. Kapadia *et al.*, *Proc. Int. Soc. Magn. Reson. Med.* **3**, 475 & 1187 (1995).
7. Chandra *et al.*, *Pharmacology* **58**, 292-299 (1999).
8. Clowes *et al.*, *Lab. Invest.* **49**, 208-215 (1983).
9. Summers *et al.*, *Magn. Reson. Med.* **33**, 785-789 (1995).
10. Chandra *et al.*, *Circulation* **97**, 2252-2258 (1998).
11. Behling *et al.*, *Nature* **341**, 321-323 (1989).

L5

Potentials of NMR Imaging in Process Engineering

Peter Blümler

School of Physical Sciences, University of Kent at Canterbury, UK

Since the eighties MRI has grown continuously in terms of developments and applications. In contrast to the early expectations and visions its impact in non-clinical applications has been considerably low or only very specific. As pointed out by many researchers this is mainly due to its high costs and low spatial resolution when compared to competing techniques. On the other hand the unique and diverse contrast generation schemes seemed to justify its application in dedicated fields (e.g. materials science) and its non-invasive nature was at least a benefit if not a prerequisite (as in the biomedical sciences). However the discrepancy between the potentials of the technique and widespread use as a standard analytical tool is obvious.

The aim of this paper is to discuss the prerequisites of problems suitable for spatially resolved magnetic resonance with an emphasis on possible industrial exploitation. It will be shown, that non-invasiveness is imperative in that respect, which divides spatially determined problems into two different classes. The first deals with such applications that do not necessarily require non-invasive or simultaneous investigations of the entire sample and can be solved by local probing or sensing. Examples range from stop-flow measurements in combinatorial chemistry to low-field NMR and mobile scanners for quality control [1]. The second class requires the investigation of the entire system and will be discussed in greater detail.

Such considerations show that the applications which will greatly benefit from non-clinical MRI investigations are those which study processes, which can be described by spatial differential equations of various quantities. Typically such equations can only be solved by knowing all spatial boundary conditions (including material inhomogeneities) and therefore require investigations of the entire system. A possible classification based on the general transport equations and system properties will be given.

This class of problem is typical of process engineering, and pioneering MRI-investigations were performed by various groups [2]. Despite the fact that strategies exist to detect the quantities of interest (e.g. velocity, concentration, temperature) independently, in real systems complications arise in their mutual interdependence and their detection in space and time. Different attempts in approaching this problem as well as the accessible time and space scales will be discussed.

References

[1] P.J. Prado, B. Blümich, B.J. Balcom: *Spectroscopy in Process Analysis*, J. M. Chalmers (ed.), to be published by Sheffield Academic Press, January, 2000.

[2] L.F. Gladden and P. Alexander: Applications of nuclear magnetic resonance imaging in process engineering, *Meas. Sci. Technol.* **7**, 423-435 (1996);
S.J. Gibbs and L.D. Hall: What roles are there for magnetic resonance imaging in process tomography?, *Meas Sci. Technol.* **7**, 827-837 (1996).

L6

Explosives Detection

Lowell J. Burnett

Quantum Magnetics, Inc., 7740 Kenamar Court, San Diego, CA 92121 USA
Department of Physics, San Diego State University, San Diego, California 92182 USA

The ideal explosives detection system scans items and responds quickly, exhibiting a high probability of detection and a low rate of false alarms. With high chemical specificity and generally adequate sensitivity, magnetic resonance is an ideal technology base for explosives detection systems.

There are three major explosives detection applications: (1) scanning sealed and unsealed bottles for the presence of liquid explosives and flammables; (2) scanning mail, packages, and luggage for the presence of terrorist explosives; and, (3) military and humanitarian demining. Examples of each of these three applications, along with the physical basis for the detection process, will be presented.

L7

High-Field MR Investigations *in vivo*

Hellmut Merkle[1], Nikos Logothetis[2], Seong-Gi Kim[1],
Michael Garwood[1], Kamil Ugurbil[1]

[1]Center for Magnetic Resonance Research, Department of Radiology,
University of Minnesota Medical School, Minneapolis, Minnesota.

[2]Max Planck Institute for Biological Cybernetics, Tuebingen, Germany

Introduction

It is well established that high field MR enables increased sensitivity and spectral resolution. There is a trend toward utilization of high field magnetic fields not only in research but also in clinical environments, e.g. for diagnostic imaging, (dynamic) in vivo spectroscopy and/or functional magnetic resonance imaging (fMRI), which is now successfully established in nonhuman primates as well [1]. The development of novel hard- and software is critical to maximize its usefulness in research applications. In this contribution, we report on this developments and on results obtained from experiments on humans and animals at magnetic flux densities between 4 and 9.4 Tesla.

Methods

We used a 4.7 Tesla MR system with a 40 cm diameter vertical bore shielded magnet, (Bruker), a 4.7 Tesla, horizontal bore magnet system (Varian) with a homemade 11 cm diameter gradient insert, a 4 Tesla 90 cm human system (Oxford magnet, Siemens gradient system, Varian console), a 7 Tesla 90 cm human system (Magnex, Varian, PCI, Dressler, CPC, RRI).

We utilized all homemade radio frequency (rf) coils (except a Bruker birdcage coil) that were customized and optimized for sensitivity at the area of interest or for homogeneity. These included adapted transceive- as well as electronically decoupled transmit/receive coil systems.

Results

A variety of experimental setups will be described and result will be shown which includes studies on human brain and breast. Due to the sensitivity advantage of high fields and small coils, detailed anatomical images were obtained (e.g. 0.25 x 0.25 x 0.5 mm on monkey visual cortex using segmented EPI).

Literature

N.K. Logothetis *et al., Nature Neuroscience* 2(6):255-262 (1999).

L8

High-Resolution MRI of Mice

Frank Wiesmann, MD
University of Wuerzburg, Germany

Introduction

The animal model of the mouse is gaining increasing popularity and importance in the field of basic research. The main reasons for this gradual move from larger animal models to the mouse is its well known genome, and the possibility of distinct genetic modulation, such as gene overexpression, mutation and knock-out. This allows to investigate the consequences of such genetic changes under well-defined and characterized conditions.

While these transgenic mouse models appear in great number in all fields of basic research, there is currently still a lack of dedicated tools to study the resulting phenotype in these animals. Particularly when one is interested in the follow-up of morphological and functional changes of the cardiovascular system, a non-invasive imaging modality with high temporal and spatial resolution is required.

Methods

MR imaging is able to meet the requirements of the murine cardiovascular physiology: Working at high speed, MR microimaging allows for a time-resolved visualization of the cardiac motion at heart rates of 500 to 600 beats per minute (corresponding to a cardiac cycle length of 100 to 120 ms). To avoid image artefacts from flow and breathing motion, the shortest possible echo time is preferable. A further challenge for MRI is the small size of the mouse heart, which lies 2 to 3 orders of magnitude below the human heart. Therefore, highest temporal resolution is crucial for detailed visualization of the cardiac structures and, what is even more important, for quantitative analysis. To achieve microscopic image resolution (defined as in-plane pixel size < 100 µm) with sufficient signal to noise ratio, the use of dedicated microscopy gradient systems at high field strength is recommended. For cardiac gating, a reliable EKG signal must be derived from the mouse paws.

Quantification of left ventricular function and mass

Magnetic resonance imaging has proved to be highly accurate and reproducible in the assessment of cardiac morphology and function, both in animal studies and in man. Whereas visualization of the murine heart by conventional (slow) MRI techniques has been reported [1, 2], we were recently able to demonstrate the application of a faster MRI method for assessment of LV volumes and mass in adult mice [3], where data acquisition with high temporal resolution and microscopic spatial resolution is achievable. This allows not only high accuracy of LV volume and mass quantification but also high reproducibility and, hence, reliability of measurements (intra- and interobserver variability of 5% mean).

Cardiac characterization of new-born and young mice

Cardiovascular transgenic mouse models with an early phenotype or even premature death require non-invasive imaging methods that allow for accurate visualization of cardiac morphology and function. Thus, an important issue was to test the feasibility of magnetic resonance imaging (MRI) to characterize cardiac function and mass in new-born, juvenile and adult mice [4]. We therefore studied mice from 7 age groups (3 days to 4 months after birth) by MRI under Isoflurane anesthesia. MRI revealed cardiac anatomy in mice from all age groups with high temporal and spatial resolution. There was close correlation between MRI-determined and autopsy left ventricular (LV) mass (r=0.95). The increase of LV mass (range 9.6 mg to 101.3 mg), cardiac output (range 1.1 ml/min to 14.3 ml/min) and stroke volume (range 3.2 µl to 40.2 µl) with age could be quantified by MRI measurements. Ejection fraction and cardiac index did not change with ageing. However, LV mass index decreased with increasing age ($p<0.01$).These findings are consistent with the human cardiovascular postnatal physiology and demonstrate the potential of MR microimaging when applied in transgenic mouse models.

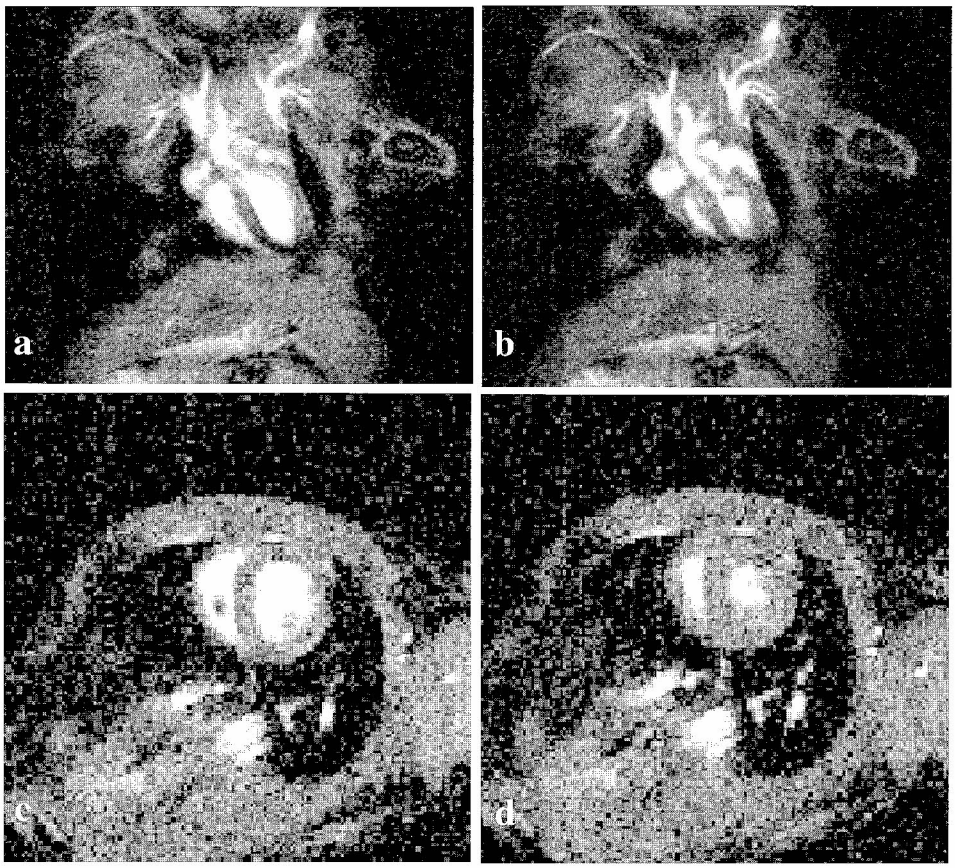

Fig. 1. End-diastolic (a) and end-systolic (b) cine MR images in a coronal view, acquired in a new-born mouse (78 μm pixels, 500 μm slice, 8.6 ms per cine frame); (c,d) are the corresponding short axis views.

Future directions

The potential of MRI in mice will not end with the quantification of LV volumes and mass and the assessment of global ventricular function. There is a variety of alternative applications of cardiovascular MRI which might give new insights into the underlying pathomechanisms in gene-targeted mice, such as MR tagging for regional wall motion analysis [5] or visualization of atherosclerotic plaques [6] among many others.

References:

1. Siri FM, Jelicks LA, Leinwand LA, Gardin JM: *Am. J. Physiol.* **272**, H2394-2402 (1997).
2. Slawson SE, Roman BB, Williams DS, Koretsky AP: *Magn. Reson. Med.* **39**, 980-987 (1998).
3. Ruff J, Wiesmann F, Hiller KH, Rommel E, Neubauer S, Haase A, et al.: *Magn. Reson. Med.* **40**, 43-48 (1998).
4. Wiesmann F, Ruff J, Hiller KH, Rommel E, Haase A, Neubauer S: *Circulation* **98**(17), I-857 (Suppl) (1998).
5. Henson R, Song SK, Ackerman JJH, Wickline SA, Lorenz CH: *Proc. Int. Soc. Magn. Reson. Med.* **5**, 883 (1997).
6. Fayad ZA, Fallon JT, Shinna M, Wehrli S, Dansky HM, Fuster V, et al: *Circulation* **98**, 1541-1547 (1998).

L9

NMR Microscopy for the Study of Trabecular Bone Architecture and Mechanical Competence

Felix W. Wehrli

Laboratory for Structural NMR Imaging, University of Pennsylvania Medical Center, Philadelphia, PA, USA

Wir wollen nicht nur wissen wie die Natur ist (und wie ihre Vorgänge ablaufen), sondern wir wollen auch nach Möglichkeit das vielleicht utopisch und anmassend erscheinende Ziel erreichen, zu wissen warum die Natur so und nicht anders ist (A. Einstein, Zürich, 1929).

Like its companion connective tissues, bone is a composite material consisting of a collagenous matrix which becomes mineralized with calcium hydroxy apatite. One of this tissue's most remarkable features is its capacity to renew itself through what is termed 'remodeling', which implies the interplay of bone resorption by osteoclasts and bone deposition by osteoblasts, the bone forming cells. Though incompletely understood, this process is believed to repair fatigue fractures and provides a means to adapt the skeleton to changes in loading. Remodeling is regulated by the direction, frequency and magnitude of the stresses to which the bone is subjected (Wolff's Law), presumably mediated by osteocytes acting as piezoelectric pressure transducers. Most of the axial skeleton (e.g. vertebrae, ribs) and the appendicular skeleton near the joints consist primarily of trabecular (TB) or cancellous bone. This type of bone, while similar in ultrastructure to cortical bone (which provides the shell of our bones), consists of a lattice of interconnected plates and struts. Such an organization ensures maximum strength at minimum weight.

In the normal adult skeleton, homeostasis ensures maintenance of bone mass; that is the rate of bone resorption is exactly balanced by the rate of bone deposition. Homeostasis is at least in part regulated hormonally, therefore, the relatively sudden loss in bone mass in women around age 50 has been associated with the rapid decrease in estrogen levels following menopause. Osteoporosis comprises a variety of disorders and etiologies which share, as a common feature, a net loss in bone mass. The resulting decreased mechanical competence causes fractures of the vertebrae, hip, wrist, and humerus. Low bone mass is a risk factor for osteoporosis and the occurrence of fractures, which led to bone densitometry for screening subjects at risk [1]. However, there is now compelling evidence that bone mineral density alone does not determine TB resistance to fracture [2]. Just as the strength of engineering materials is governed by the materials' intrinsic properties, mass density and spatial arrangement, it is plausible that TB architecture plays a role in determining the propensity to fracture. Intuition suggests that a well-connected network is stronger than one in which trabeculae have been disconnected by excessive osteoclastic resorption. Therefore, the quantification of microarchitecture is paramount to understanding and predicting TB network strength.

Although bone has been imaged directly by both proton and ^{31}P NMR, the spatial resolution achievable in this manner is limited. ^{31}P NMR imaging, on the other hand, has the potential to provide information on the chemical makeup of the bone's mineral phase and thus addresses questions regarding possible age and disease-related changes in the intrinsic material properties. Direct proton NMR imaging may be of some interest as well. The constituent imaged in this case is collagen-bound water (T_1 ~ 200 ms; T_2 <0.5 ms) and thus, in principal, these protons are amenable to imaging. Its feasibility has recently been demonstrated by such techniques as single and multi-point mapping [3,4] or projection-reconstruction imaging [5].

More widely applicable, however, in terms of achieving a resolution sufficient to visualize and quantify TB architecture, is imaging of the bone marrow [6,7] or its substitutes [8]. Since marrow is usually homogeneous within the volume of interest (although it can consist of hematopoetic and yellow marrow, which have different spectral and relaxation characteristics), we are essentially dealing with a system of discrete binary tomography, greatly simplifying processing and analysis of the images. One complication that affects the imaging strategy is the bone's diamagnetism relative to marrow. Bone is more diamagnetic by 0.2 ppm (cgs) relative to bone marrow [9,10]. The discontinuity in magnetic susceptibility leads to local gradients near the bone marrow interface which, in turn, cause intravoxel spin dephasing in gradient echo images [6] (except at extremely short echo times). The problem obviously is exacerbated at high magnetic fields at which most of the *in vitro* specimen work is being conducted, therefore a spin-echo pulse sequence is indicated. In the work performed in the author's laboratory, a partial flip-angle 3D spin-echo technique has proven optimal [6]. For in vitro microscopy at high field, removing the bone marrow and substituting it with saline, eliminates inclusions of air in the marrow spaces. Further, doping it with 1 mM Gd(DTPA) reduces T_1 to about 300 ms and thus enhances SNR.

The resolution necessary to resolve bone microstructure depends on TB thickness, which is species dependent. It is on the order of 100-150 μm in humans but only 50-70 μm in small animals such as rats. Depending on specimen size, an isotropic resolution on the order of 40-80 μm is easily achievable at 9.4 T in one hour scan time, affording SNR~10. For a voxel size comparable to TB thickness, the signal intensity histogram is typically bimodal and the images can easily be binarized by setting a threshold at the midpoint of the marrow and background peak [11]. In vivo at 1.5 T, the highest resolution achieved in the distal radius of the wrist is 137x137x350 μm [12]. At this resolution, partial volume blurring causes the two peaks of the intensity histogram to coalesce, in which case no objective criteria for binarization

are available. One approach developed in the author's laboratory is based upon histogram deconvolution, the output of which is a noiseless bone volume fraction (BVF) map [13].

Finally, the 3D BVF maps can be analyzed by probing the distribution of the bone by means of spatial autocorrelation analysis, with the TB network being treated as a quasi-regular lattice. The second maximum of the spatial autocorrelation function (ACF) therefore is a measure of intertrabecular spacing. Since trabecular bone is typically highly anisotropic, a parameter called 'tubularity' has been defined as the normalized ACF between slices (assuming the images have been acquired in the direction transverse to the principal fabric axis). In recent work it was found that a polynomial model involving only two AC parameters, could explain 90% of the variance of Young's modulus for uniaxial loading, in contrast to BVF, which accounted for only 57% of the bone stiffness [14]. Another successful approach for characterizing trabecular network architecture relies on digital topology, which examines the 3x3x3 neighborhood of each bone voxel of the digitized image, from which a unique topological class can be assigned to each voxel [15]. For example, voxels can be distinguished as being part of a surface, curve, or junction. It has been shown that in this manner bone erosion can be quantified and followed during disease progression since, as bone becomes eroded, plates are converted to rods and rods are thinned and eventually become disrupted. Topologically, this conversion manifests in a decrease in the surface/curve ratio (Figure 1).

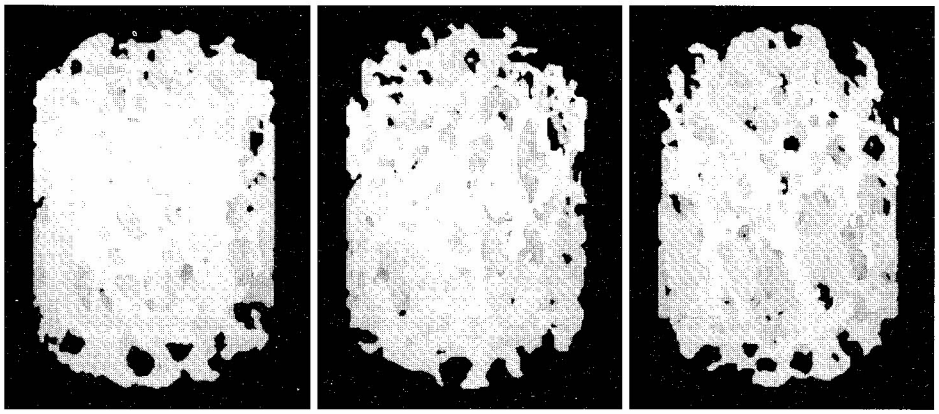

A B C

Fig. 1. "Virtual bone biopsies" derived from in vivo MR images of the distal radius. **A**: male, age 30; **B**: female, age 33; **C**: female, age 67, osteopenic. The surface/curve ratios are 11.9, 11.4 and 6.9, commensurate with a more plate-like connected network in the younger subjects.

In summary, NMR microscopy provides a unique tool for visualizing and quantifying the 3D architecture of TB noninvasively in humans and laboratory animals to explore the associations between architecture and function of this important connective tissue. Finally, recent progress in image acquisition and processing methodology, along with advances in the treatment of metabolic bone disease, will permit the study of patients longitudinally as a means to evaluate the effectiveness of therapy.

References

1. H. W. Wahner and I. Fogelman, *The evaluation of osteoporosis: dual energy X-ray absorptiometry in clinical practice*, University Press, Cambridge (1994).
2. A. M. Parfitt, *Bone* **13**, S41 (1992).
3. S. Gravina and D. G. Cory, *J. Magn. Reson.* **104**, 53 (1994).
4. Z. H. Cho and Y. M. Ro, *Magn. Reson. Med.* **32**, 258 (1994).
5. Y. Wu, D. A. Chesler, M. J. Glimcher, L. Garrido, J. Wang, H. J. Jiang, and J. L. Ackerman, *Proc. Natl. Acad. Sci. USA* **96**, 1574 (1999).
6. J. Ma, F. W. Wehrli, and H. K. Song, *Magn. Reson. Med.* **35**, 903 (1996).
7. C. L. Gordon, C. E. Webber, N. Christoforou, and C. Nahmias, *Med. Phys.* **24**, 585 (1997).
8. F. W. Wehrli, J. C. Ford, H. W. Chung, S. L. Wehrli, J. L. Williams, M. J. Grimm, S. D. Kugelmass, and H. Jara, *Calcif. Tissue Int.* **53(Suppl 1)**, S162 (1993).
9. J. A. Hopkins and F. W. Wehrli, *Magn. Reson. Med.* **37**, 494 (1997).
10. S. N. Hwang and F. W. Wehrli, *J. Magn. Reson.* **139**, 35 (1999).
11. H. W. Chung, F. W. Wehrli, J. L. Williams, S. D. Kugelmass, and S. L. Wehrli, *J. Bone Miner. Res.* **10**, 803 (1995).
12. H. K. Song and F. W. Wehrli, *Magn. Reson. Med.* **41**, 947 (1999).
13. S. N. Hwang and F. W. Wehrli, *Int. J. Im. Syst. Technol.* **10**, 186 (1999).
14. S. N. Hwang, F. W. Wehrli, and J. L. Williams, *Med. Phys.* **24**, 1255 (1997).
15. P. K. Saha, B. R. Gomberg, and F. W. Wehrli, *Int. J. Im. Syst. Technol.* in press, (1999).

L10

Surface NMR via the NMR MOUSE

G. Guthausen[1], A. Guthausen[2], K. Hailu, R. Eymael, and B. Blümich
Institut für Technische und Makromolekulare Chemie,
RWTH Aachen, Worringer Weg 1, 52054 Aachen,
[1]Institut für Mechanische Verfahrenstechnik und Mechanik,
Am Fasanengarten, 76128 Karlsruhe, Germany
[2]Bruker Analytik, Silberstreifen, 76287 Rheinstetten

The NMR-MOUSE [1] is a device for convenient characterization of surface-near volume elements of arbitrarily shaped soft samples via NMR relaxation measurements. The system is small, portable, and easy to handle in industrial environments. As the NMR relaxation rates in first order do not depend on the magnetic field homogeneity, large magnetic field gradients are no hindrance in this context. Different realizations of the underlying concept of single-sided NMR can be found in literature [2,3], the most convenient being in oil well logging [2]. In contrast to these applications of NMR relaxation measurements on porous media in inhomogeneous fields, use of the NMR-MOUSE has been made primarily in the characterization of soft materials. It was already found by ^{1}H-NMR in homogeneous magnetic fields that especially the transverse relaxation rate T_2 and the $T_{1\rho}$ relaxation often reflect material properties as for example the cross-link density in elastomers (for example [4]). The NMR relaxation rates are sensitive to molecular fluctuations in different time windows, for example T_1 is mainly caused by fluctuations with correlation times in the range of the inverse Larmor frequency, which amounts to about 8 x 10^{-9} s in the case of the NMR-MOUSE. In contrast, the transverse relaxation times are caused by molecular fluctuations on the time scale of the experiment (about 10^{-5} to 10^{-2} s) and strongly depend on the refocusing properties of the applied pulse sequence. As elastomers are poly-disperse macromolecular systems with wide distributions of correlation times of molecular motion, it is quite obvious that the dipolar coupling is strongly modulated and, depending on temperature, it strongly influences NMR relaxation. For a given polymer, the relaxation reflects the molecular mobility at the measurement temperature and therefore give information about the material properties. Thus, the NMR-MOUSE is able to monitor materials properties, which are influenced by the molecular motions which modulate the dipolar coupling [5,6].

Because the transverse relaxation depends on the refocusing properties of the pulse sequence applied, a solid echo, for example, allows the refocusing of the static dipolar coupling of a spin pair, whereas in a Hahn-echo sequence the dipolar coupling leads to a magnetization decay. In the case of the NMR-MOUSE, the polarizing magnetic field B_0 and the rf field B_1, are strongly inhomogeneous and therefore the measurement conditions deviate strongly from what is known from NMR in homogeneous fields, and pulse sequences have to be reexamined. Questions arise concerning the refocusing properties of π-pulses, whether differences can be found for example in solid and Hahn echoes with respect to the dipolar coupling of ^{1}H. As most of the materials investigated show a large number of protons, this question is of great importance concerning the possibility of materials characterization. Furthermore, can the gradients be used for spatial resolution or for diffusion and velocity measurements?

The experimental realization of the NMR-MOUSE will be outlined, pulse sequences implemented so far are discussed. Finally possible areas of application of the NMR-MOUSE are presented.

References

[1] Eidmann, G. *et al.*, *J. Magn. Res.* **A 122**, 104 (1996).

[2] Kleinberg, R. L., *NMR well Logging*, In: *Encyclopedia of NMR, Vol. 8*, D. M. Grant and R. K. Harris (eds.), p. 4960 (1996) and references therein.

[3] Matzkanin, G. A., in: *Nondestructive Characterization of Materials*, P. Höller, V. Hauck, C. O. Rund and R. E. Green (eds.), Springer Berlin (1989).

[4] Blümler, P. *et al.*, Review, *NMR Imaging of Elastomers.* In: *Rubber Chem. Techn.*, **70**, 468 (1997) and references therein.

[5] Guthausen, A. *et al.*, *J. Magn. Reson.* **130**, 1 (1998).

[6] Zimmer, G. *et al., Solid State NMR* **12**, 183 (1998).

L11

Prospects of Magnetic Resonance Microscopy Combined with Dynamic Nuclear Polarization

Robert A. Wind

Pacific Northwest National Laboratory, P.O. Box 999, MS K8-98, Richland, WA 99352, USA

The NMR sensitivity is one of the key parameters determining the ultimate spatial resolution that can be achieved in NMR microscopic imaging and localized spectroscopy. One approach to improve the sensitivity is to use large external fields, but this method has its limitations and is expensive. It is well known that the field-dependence of the sensitivity is determined by the factor $M\{\omega_o\ Q/(F\ \Delta f)\}^{1/2} = M\ H(\omega_o)$, where M is the nuclear magnetization, ω_o is the nuclear Larmor frequency, Q is the quality factor of the NMR resonant circuit, F is the noise factor of the receiver, and Δf is the NMR line width. In low fields, where $Q \sim (\omega_o)^{1/2}$, $F \approx 1$, and Δf is field-independent, the sensitivity is proportional to $(\omega_o)^{7/4}$. However, in large fields Q becomes more or less field-independent or can even decrease as a result of increased capacitive and/or sample losses; Δf often increases proportional to the field strength as a result of susceptibility broadenings; and F may increase. The result is that the factor $H(\omega_o)$ becomes only weakly field-dependent, and the sensitivity increase in large fields is mainly due to increased M values.

An alternative approach of increasing the NMR sensitivity is the use of Dynamic Nuclear Polarization (DNP), which can be applied in materials containing both magnetic nuclei and unpaired electrons [1, 2]. In DNP a polarization transfer between the electron and nuclear spin systems is obtained by irradiating at or near the electron Larmor frequency, resulting in an enhanced nuclear polarization. Although DNP can been applied in both solids and liquids, we shall restrict ourselves to DNP in liquids, where DNP is obtained by saturating the EPR signal. This phenomenon is called the Overhauser effect [1-7]. Here the polarization transfer is governed by relaxation transitions, arising from the electron-nuclear scalar and dipolar interactions, rendered time dependent by the molecular motions in the liquids. The resulting Overhauser enhancement factor of the nuclear polarization, E_{OV}, is given by

$$E_{OV} = 1 - \rho f s A\ \gamma_e / \gamma_n \qquad [1]$$

In Eq. [1], ρ is the coupling factor, determined by the strengths of the electron-nuclear scalar and dipolar interactions and by the spectral density functions characterizing the thermal motions in the liquids; f is the leakage factor, given by $f = 1\text{-}T_1/T_{10}$, where T_1 and T_{10} are the nuclear relaxation times in the presence and absence of the radical; s is the saturation factor, given by $s = 1\text{–}P_e/P_{eo}$, where P_e and P_{eo} denote the saturated and unsaturated electron polarizations; A takes into account the possibility that only part of the EPR spectrum can be saturated; and γ_e and γ_n are the electron and nuclear gyromagnetic ratios. The maximum values of f, s, and A are unity, whereas in low fields the coupling factor ρ varies between +1 for pure scalar interactions and -1/2 for pure dipolar interactions, resulting in positive respectively negative Overhauser enhancements (γ_e<0). Table 1 shows examples of enhancement factors, measured at room temperature in different fields and for different nuclei. It follows that large polarization enhancements can be obtained.

Table 1. Experimental Overhauser Enhancements at Room Temperature.

Nucleus	Molecule	Solvent	Radical	Field (T)	E_{OV}-1 (s = f = 1)	Ref.
^1H	-	toluene	BDPA	0.01	-330	8
^1H	-	toluene	BDPA	0.3	-130	8
^1H	-	toluene	BDPA	1.4	-40	8
^1H	-	water	TAM [a]	0.01	-270	9
^1H	-	water	TAM	1.4	-12	10
^{19}F	cyclo-C_6F_{10}	benzene	GALV	0.008	-262	7
^{19}F	-	C_6F_5OH	TEMPO	0.008	+270	7
^{31}P	-	$(CH_3O)_2POD$	DTBN	0.008	+1200	7
^{31}P	-	$(CH_3O)_3PO$	CTNO	0.008	-648	7
^{31}P	-	TIP [b]	BDPA	0.018	+540	5
^{31}P	-	TIP	BDPA	0.3	+650	5
^{31}P	-	TIP	BDPA	1.4	+440	5

[a] TAM = Trirarylmethyl-based radical provided by Nycomed (Sweden); [b] TIP = tri-isopropyl phosphite.

With respect to combining DNP with MR microscopy (MRM) the following remarks can be made:

- The product of its thermal equilibrium value and the Overhauser enhancement gives the overall DNP-enhanced nuclear magnetization M_{OV}. Hence, in order to obtain the maximum NMR sensitivity, the factor $B_{OV} \cdot E_{OV}$ must be maximized, where B_{OV} is the external field used for DNP. It will be shown that for aqueous samples, where the Overhauser enhancement decreases rapidly with increasing field, M_{OV} is predicted to become maximal in an external field of 0.3 T, corresponding to an electron Larmor frequency of 9 GHz. In contrast, for organic solvents, where the Overhauser enhancement decreases considerably more slowly with increasing field, B_{OV} should be made as large as possible.
- Problems with DNP in larger fields for dielectric lossy solvents like water are the small penetration depth of the microwaves necessary to saturate the EPR line (e.g., at 9 GHz the penetration depth is ~4 mm), and the associated sample heating. However, for DNP-MRM this need not to be a serious problem, as small samples, with sizes of 1 mm or less, are often required to obtain a large spatial resolution, and special DNP probes can be made which substantially reduce the electrical component of the microwave field in the sample.
- DNP can result in considerable increases in the NMR sensitivity, especially in non-aqueous samples. For instance, if we consider the DNP enhancements in Table 1, obtained at 1.4 T, it follows that for benzene doped with BDPA the ^{1}H DNP-enhanced polarization is equal to the thermal equilibrium polarization in an external field of 56 T, whereas for TIP doped with BDPA with DNP a ^{31}P polarization is obtained that would have required a magnet of 616 T without DNP! And even for aqueous samples the results are promising: It is predicted that at the optimal field of 0.3 T the ^{1}H DNP enhancement in water doped with TAM is about 100, so that without DNP a field of 30 T would have been required to get the same polarization, higher than the largest available high-resolution magnet available to date.
- The DNP enhancements can be further improved if the correlation times, characterizing the molecular motions that are responsible for the Overhauser effect, can be reduced, i.e. if the viscosity of the solvent can be reduced. This can be achieved, e.g., by increasing the temperature or by using supercritical fluids.
- Performing the actual NMR experiments in a larger external field than the field required for optimal DNP results can further increase the DNP-NMR sensitivity. This can be achieved, e.g., by shuttling the sample from the low DNP field into the large NMR field, or by field cycling. However, as susceptibility broadenings are reduced in low fields, the optimal field for NMR may not differ that much from the optimal field for DNP.

We conclude that DNP has the potential to push the NMR sensitivity to values that can not be achieved without this technique. As a result, MRS can be performed on voxels that can be an order of magnitude smaller than without DNP, and images can be obtained with a spatial resolution that approaches the 1 micron limit in favorable cases. In fact, for imaging the low-viscosity samples required for DNP the diffusion-induced broadening may become the resolution-limiting factor, and special imaging techniques like constant-time imaging and very large gradients, several kG/cm or more, need be used to reduce this resolution below that imposed by the sensitivity.

Acknowledgment.

Pacific Northwest National Laboratory is a multiprogram laboratory operated by Battelle Memorial Institute for the U.S. Department of Energy under Contract DE-AC06-76RLO 1830.

References.

1. A. Abragam, The Principles of Nuclear Magnetism, Clarendon Press, Oxford 1961.
2. R.A. Wind, M.J. Duijvestijn, C. van der Lugt, A. Manenschijn, and J. Vriend, *Progr. in NMR Spectrosc.* **17**, 33-67 (1985).
3. A.W. Overhauser, *Phys. Rev.* **92**, 411-415 (1953).
4. K.H. Hausser and D. Stehlik, In: *Advances in Magnetic Resonance* (J.S. Waugh, Ed.), vol.3, pp 79-139, Academic Press, New York (1968).
5. J. Trommel, Thesis, Delft University of Technology, Delft, the Netherlands (1978).
6. W. Muller-Warmuth and K. Meise-Gresch, In: *Advances in Magnetic Resonance* (J.S. Waugh, Ed.), vol. 11, pp 79-139, Academic press, New York (1983).
7. R.D. Bates, Jr., *Magn. Reson. Review* **16**, 237-291 (1993).
8. G.J Kruger, W. Muller-Warmuth, and R. van Steenwinkel, *Z. Naturforsch.* **21a**, 1224 (1966).
9. J.H. Ardenkjaer-Larsen, I. Laursen, I. Leunbach, G. Ehnholm, L.-G. Wistrand, J.S. Petersson, and K. Golman, *J. Magn. Reson.* **133**, 1-12 (1998).
10. R.A. Wind and J.H. Ardenkjaer-Larsen, *J. Magn. Reson.*, submitted.

Portable MRI Systems

Katsumi Kose
Institute of Applied Physics, University of Tsukuba, Tsukuba City 305-8573, Japan

Introduction

MRI is a very useful tool for nondestructive investigation of unknown objects, as we have seen from many papers published in this area. In the (near) future, MRI should be widely used as one of analytical tools like optical microscopes. In such a situation, MRI should be **compact, low-cost, portable, and simple to use**.

Portable MRI Units

A typical MRI system can be divided into two subsystems: electric and magnetic subsystems. The magnetic subsystem should be designed for objects to be imaged but the design of the electric subsystem can be common to all of the MRI systems, though the power units (RF transmitter and gradient drivers) should depend on the object size. Here we call the electric subsystem "**MRI unit**". Recent development of electronics and computer technology has enabled us to make the MRI unit very compact and even portable.

The right figure shows our standard portable MRI unit (total weight: ~80 kg, size: 54 cm (W) x 77 cm (H) x 60 cm (D)) developed for several MRI applications. This unit consists of a TFT liquid crystal display, PC, RF modulator & detector, 3-channel gradient driver, and RF transmitter (top to bottom). All of the digital units are assembled in the PC: a commercial DSP board for the MRI pulse programmer (100 ns time resolution) [1] and ADC board for the data acquisition system [2,3]. Another compatible digital control unit has been developed using a note PC and a PC card to ISA bus extension box. Because the total weight of this unit is about 8 kg and small enough, a more compact system can be built. The RF transmitter and gradient drivers can be made much smaller. Now we have developed a more compact MRI power unit (45 cm (W) x 15 cm (H) x 40 cm (D)) which consists of a 50 W wide-band (300 kHz to 300 MHz) RF power amplifier (Thamway Corp. Japan) and three channel gradient drivers (±10 V, ±5 A each, home built).

Portable MRI Systems

We have developed several portable or compact MRI systems using the portable MRI unit described above.

The first application is an MR microscope using a magnetic field of a clinical MRI in which the MRI unit is working independently of the clinical MRI [4]. To operate the independent MRI unit in a clinical MRI room, the MRI unit has been developed to be compact and portable. By using this system, 2D images with 50 μm square in-plane pixels and 3D images with 150 to 200 μm cube voxels were successfully obtained within a practical imaging time.

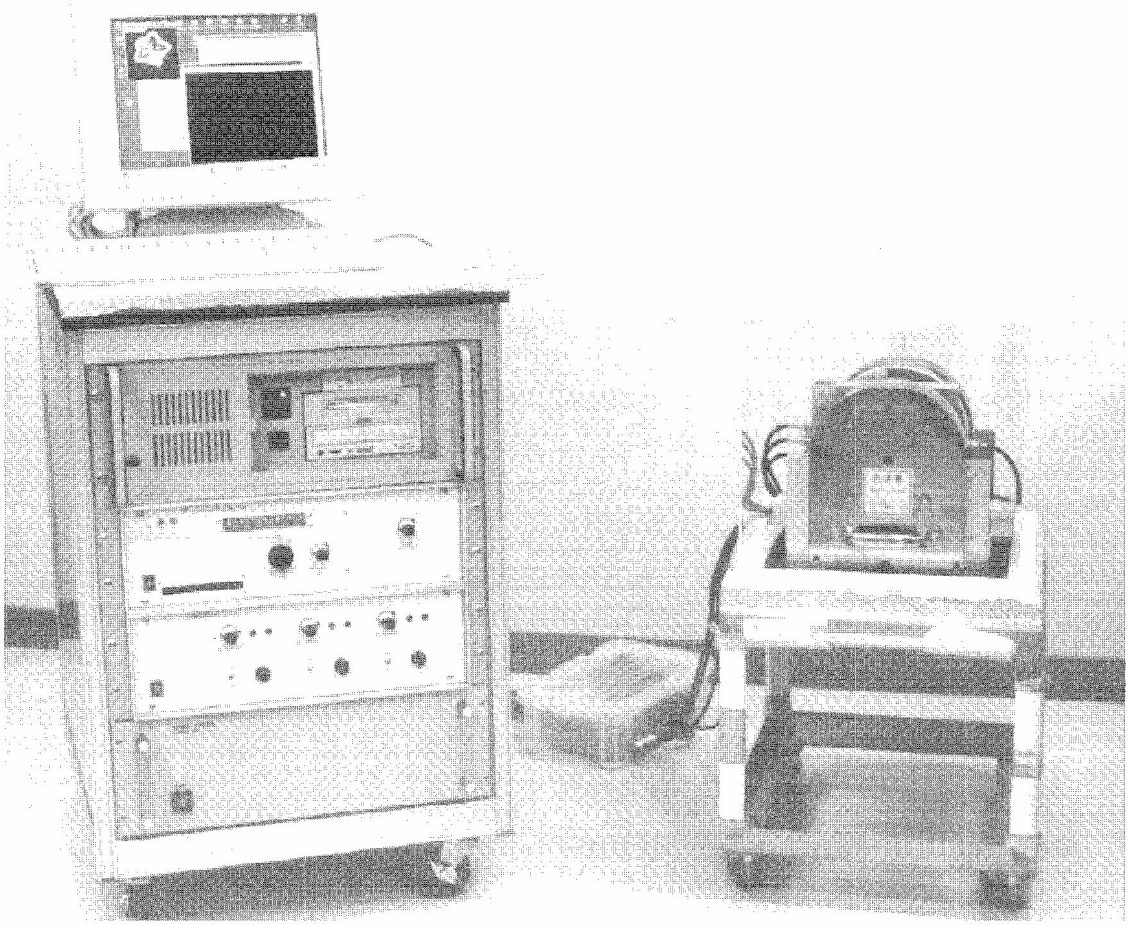

The second application is a compact MR microscope using a 1.0 T permanent magnet (gap: 61 mm, homogeneity: 12 ppm over 20 mm dsv, magnet size: 62 cm (W) x 75 cm (H) x 75 cm (D), weight: 1,350 kg) which can be installed within a 1 m^2 space [5]. Now this magnet is too heavy for portable use but if more efficient permanent magnets are developed or lower field permanent magnets are used, real portable MRI systems can be constructed. The right figure shows a set-up of a portable MRI system in which a movable 0.3 T permanent magnet (gap: 80 mm, homogeneity: 60 ppm over 30 mm dsv, magnet size: 26 cm (W) x 27 cm (H) x 20 cm (D), weight: 57 kg) is used.

Conclusion

For portable MRI systems, compactness and mobility of the MRI unit and magnet is essential. At present, **effective combination of "commercially available" electronics units** (good performance, high integration, reasonable price) and **sophisticated permanent magnet design technology** developed for medical MRI systems have enabled us to make portable MRI systems. I believe portable MRI systems will explore a lot of MRI applications in various fields.

I acknowledge Drs. Anno and Yoshioka at Institute of Clinical Medicine, and Messrs. Haishi, Adachi, Uemastu, and Matsuda in my laboratory for cooperative work, and Messrs. Nakanishi, Okada, and Aoki at Sumitomo Special Metals Company for developments of permanent magnets.

References

1. Kose, T. Haishi, In: *Spatially Resolved Magnetic Resonance*, Wiley-VCH, pp.703-709 (1998).
2. K. Kose, T. Haishi, A. Caprihan, E. Fukushima, *J. Magn. Reson.* **124**, 35-41 (1997).
3. T. Haishi and K. Kose, *J. Magn. Reson.* **134**, 138-141. (1998).
4. K. Kose, T. Haishi, N. Adaci, I. Anno, *Proc. Int. Soc. Magn. Reson. Med.* **6**, 1924 (1998).
5. T. Haishi, Y. Matsuda, T. Uematsu, K. Kose, *Proc. Int. Soc. Magn. Reson. Med.* **7**, 2035 (1999).

L13

High-Field NMR Magnets

Dr. Gerhard Roth

BRUKER ANALYTIK GMBH, 76189 Karlsruhe, Germany

NMR magnet technology at very high fields has made considerable progress over the past decade. After some slower development in the late 80's and early 90's, magnet technology has made faster progress again with the introduction of the first 750 MHz and 800 MHz magnets. This progress is based on new developments in the NMR magnet design and construction, on advances in superconducting wire technology, as well as on the new supercooled cryostat concept.

One precondition for the construction of very high-field magnets is the availability of suitable high-field superconductors. These superconductors are especially designed to fulfill the needs of the NMR magnet design with respect to parameters such as critical current density at high fields, stability, safety in the case of a quench and wire geometry to withstand the very high forces within the magnet.

The new advanced cooling concept for NMR magnets allows to increase the available critical current density and the critical magnetic field of a given superconductor even further, thus being the key method for the construction of superconducting magnets at ultra high fields. All newer high-field NMR projects worldwide make use of this supercooling method that was pioneered by Bruker.

The next steps in high-field magnet development will be the design and construction of 900 and 1000 MHz high-resolution NMR magnets. Whereas the materials used for the 900 MHz will still be in the range of metallic superconductors, magnets operating at 1000 MHz or even higher fields will require the successful development of high-performance oxide superconductors.

Hardware Developments for *In-Vivo* MR Microscopy at Fields up to 17.6T

Wolfgang U. Roffmann, *Dieter Gross, Stuart Crozier, Stephen Wilson, Kurt Luescher David M. Doddrell, *Volker Lehmann and *Klaus Zick

Centre for Magnetic Resonance, The University of Queensland, Brisbane, Australia
*Bruker Analytik, Germany

Introduction

Recent advances in magnet technology have made it possible to produce magnets for very high field NMR experiments (with ^{1}H frequency up to 800 MHz). Most of these magnets are used for NMR spectroscopy in liquids and solids with the room temperature bore oriented vertically. They take advantage of the improved SNR and dispersion associated with the gain in magnet field strength. The room temperature bore size (usually <60 mm) of these magnets is the limiting factor to use them for in-vivo microimaging or spectroscopy. Further advances in magnet technology have seen the development of very high field vertical bore magnets (with ^{1}H frequency up to 750 MHz) with bore sizes of up to 89 mm (termed wide-bore (WB)) which make it possible to perform in-vivo experimentation.

The demands on the equipment to perform in-vivo experiments are quite different to those of high-resolution experiments and consideration has to be given to the construction and performance requirements of such equipment.

In this presentation we will discuss some of the engineering issues involved in performing in-vivo experiments in high field vertical bore magnets:

RF Coils and Animal Handling Systems

In-vivo microscopy experiments in vertical bore magnets demand a different approach to coil design and animal handling. The RF coil should be tailored to the experiment with special consideration for the animal under investigation and the region of interest. A "one coil does it all" approach does not present the best solution.

We have developed an Animal Handling System AHS with interchangeable RF coil attachments. The RF Coil attachments are integrated into the AHS from the start of the design process and provide flexibility [Fig. 1].

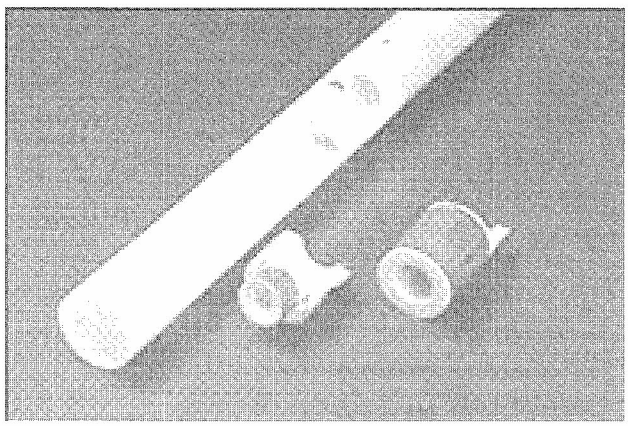

Fig. 1. Animal Handling System with "Tilt-Coil" and Mouse Brain attachments.

We have also developed a "whole-body" mouse probe with integrated Animal Handling System [Fig. 2].

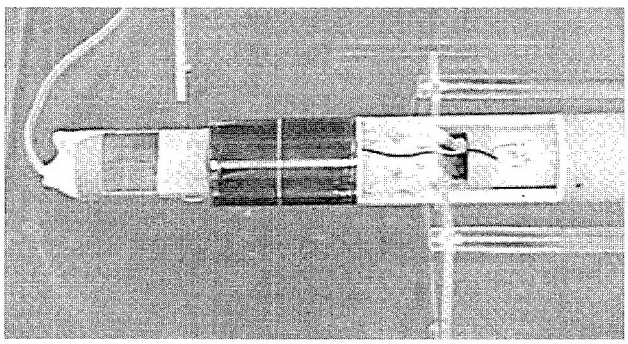

Fig. 2. The "whole-body" mouse probe.

The Animal Handling System is a vital and integral part of the design for in-vivo experiments in vertical high-field magnets.

The system must provide:

- Reliable and humane positioning and restraining of the animal.
- Reliable anesthesia delivery.
- Physiological monitoring and gating.

Fig. 3 shows a sagittal slice of the mouse brain acquired at 17.6 T using the mouse head resonator shown in Fig. 1.

Fig. 3. RARE mouse brain image at 17.6 T

Acknowledgements

We would like to acknowledge the help from the people of the CMR workshop, especially Simon Teed, Gavin Hinds and Nick Mills. We would also like to thank Dr. Toni Keller from Bruker Analytik for the use of the WB 750 spectrometer and Dr. Ian Brereton (CMR) for helpful discussions.

Support for this work is acknowledged from SPIN Systems Qld Pty Ltd under an AusIndustry Start Grant.

High-Temperature Superconducting Resonators: from Theory to Application

Sarah E. Hurlston, Steve A. Suddarth, G. Allan Johnson
Duke University Center for *In Vivo* Microscopy, Durham NC, USA 27710

Introduction

The use of high temperature superconducting (HTS) receiver coils for attaining increased sensitivity has been widely reported for both low-field magnetic resonance imaging (1-3) and for magnetic resonance microscopy (MRM) (4-6). The reported SNR gains attained from HTS coils have varied over a wide range, from a low of 1.8 X (1) to a high of 34 X (7). We present data that helps to explain these variations and emphasizes some of the important considerations in SNR comparisons. In addition, we provide examples for specific coil designs with emphasis on operating concerns that have significant impact on the SNR in a given experiment.

Methods

Images and electrical data have been acquired using two HTS volume probes that utilize Helmholtz coil pairs (Conductus Inc., Sunnyvale CA). The first of these probes is designed to accommodate samples of up to 5 mm in diameter, while the second can hold samples up to 10 mm in diameter. The coils in the Helmholtz pair are inductively coupled to one another and to two simple loops, one used for fine control of the resonant frequency and a second for matching the coils to the 50 Ω line. Two copper volume probes, a Helmholtz pair, and a single-turn solenoid were used for reference to the 5-mm- and 10-mm-bore diameter HTS probes, respectively. The 5-mm Helmholtz was designed to give a comparison for geometry identical to that of the HTS coil. The solenoid was chosen to give a comparison of an HTS coil to the best possible geometry for the copper coil. The Q values for all coils were measured using a HP4195 network/spectrum analyzer.

All imaging experiments were performed on a 9.4 T microscopic imaging system controlled by a Bruker Omega console. The experiments can be divided into two categories: phantom imaging studies for understanding the mechanisms that influence SNR and *in vitro* imaging experiments designed to demonstrate the utility of the probes in microscopic imaging studies. All imaging experiments have been performed using either spin-echo or GRASS sequences modified for use in microscopic imaging studies.

Results and Discussion

Coils were analyzed based on their loaded and unloaded Q values, effective noise temperature, calculated B_1 per unit current, and inductance. A summary of the results is presented in Table 1 (8):

Table 1

Parameter	5-mm HTS Probe	5-mm Copper Helmholtz	10-mm HTS Probe	10-mm Copper Solenoid
Unloaded Q	18,000	160	8,700	155
Loaded Q	16,000	150	6,900	145
Noise Temp.	77 K	300 K	150 K	300 K
B_1 per Ampere	1.03	1.10	0.38	0.58
Estimated SNR	12	1	1.6	1
Measured SNR	7	1	2.2	1

The SNR values for each HTS coil are normalized with respect to the appropriate copper reference coil, so that the number reported for the HTS coils represents the gain in SNR over the copper coil. For the 10-mm HTS probe, the agreement between the predicted and measured values was well within the expected measurement error. The error between predicted and measured SNR values for the 5-mm HTS probe were substantially larger. Further analysis indicated that the noise temperature

measured using the hot/cold resistor method was not consistent with the noise temperature measured from the image data (8) due to compromised noise performance of the preamplifier over part of the imaging bandwidth. Because the noise temperature of this probe is lower while its Q is much higher, matching to the preamplifier is more critical. Additional enhancements to the matching network are underway.

The differential in the SNR gain from the two HTS probes highlights the strong influence of filling factor on any given coil comparison. For the 5-mm Helmholtz coils, the ratio of the B_1 per Ampere for the HTS and copper coils is 0.94. The B_1 per Ampere for the HTS Helmholtz is only 0.66 times that of the copper solenoid. This means that when an optimal copper coil is compared to the HTS probe, the SNR advantage is reduced. Present designs for HTS coils are constrained to Helmholtz configurations because the HTS material must be deposited on flat surfaces. Thus, HTS coils must be designed carefully to compensate for the loss in filling factor due to geometry and thermal isolation constraints.

In vitro studies add an additional level of complexity over carefully controlled phantom studies. To attain high-resolution images of samples typically examined in MRM, long scan times are frequently required even with the SNR advantage provided by the HTS coils. Two sources of instability, temperature fluctuation and mechanical vibration from support equipment, have been analyzed. Simple design modifications have allowed us to keep frequency shift to within ±10 kHz over scan times of up to 10 hours. We present additional design enhancements that have allowed us to carefully control sample temperature without reduction in filling factor or addition of unnecessary heat load.

References

1. van Heteren JG, James TW, Bourne LC. *Magn. Reson. Med.* **32**, 396-400 (1994).
2. Okada H, Hasegawa T, van Hetern JG et al. *J. Magn. Reson., Ser. B* **107**, 158-164 (1995).
3. Hall AS, Alford NM, Button TW et al. *Magn. Reson. Med.* **20**, 340-343 (1991).
4. Black RD, Early TA, Roemer PB et al. *Science* **259**, 793-795 (1993).
5. Miller JR, Hurlston SE, Face DW et al. *Magn. Reson. Med.* **41**, 72-79 (1999).
6. Odoj F, von Kienlin M Haase. *Proc. Int. Soc. Magn. Reson. Med.* **5**, 173 (1997).
7. Black RD, Early TA, Johnson GA. *J. Magn. Reson. A* **113**, 74-80 (1995).
8. Hurlston SE, Brey WW, Suddarth SA, et al. *Magn. Reson. Med.* **41**, 1032-1038 (1999).

Acknowledgements

Research support by a grant from NIH NCRR (#P41 RR05959). The authors would like to thank Rich Withers and Rob Nast from Bruker Institute (Fremont, CA) and Bill Brey from Conductus, Inc. (Sunnyvale, CA) for technical assistance and advice, and Elaine Fitzsimons for editorial service.

L16

Micro-samples, Micro-coils, Micro-magnets: Where will all this smallness end?

Doug Morris [1,4], Peter G. Gorkov [1], Andrew B. Harris [1], Jeffery Tsao [1], Kevin Moser [2], John Georgiadis [2], Andrew Webb [3,4], Paul C. Lauterbur [1,4]

University of Illinois

[1] Biomedical Magnetic Resonance Laboratory, [2] Dept. of Mechanical Engineering, [3] Dept. of Electrical Engineering, and [4] Beckman Institute
Urbana IL 61801 USA

A continuing goal of any microscopic technique is the increase of resolution or resolving power to view progressively smaller objects in higher detail. In NMR spectroscopy this goal is detecting and analyzing small amounts of material whether it is complex organic compounds, biomolecules, or solids. For NMR imaging this is manifest by producing higher resolution images of small objects containing generally aqueous solutions. Both goals require significant increases in SNR per unit volume to offset the reduction in the number of spins generating signal. Few means for boosting SNR are available. Some that are includes increasing the B_0 field, increasing the number of spins, or increasing the filling factor of the RF coil. Recently investigators have used the last option by means of very small RF coils, or microcoils, for increasing the per unit volume signal power [1].

The SNR gains from microcoils follow the well know inverse coil diameter relation until feature sizes of the coil become similar to the RF skin depth of the conducting metal. The Figure 1 shows the change in SNR functionality from 1/d to $1/d^{1/2}$ at a feature size of 300 μm for a coil resonating at 300 MHz.

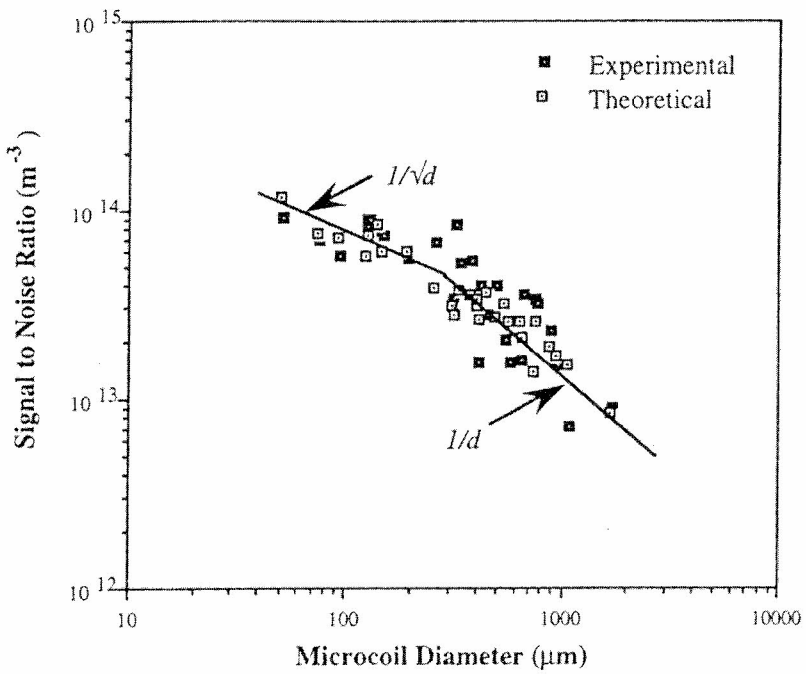

Figure 1. SNR per unit volume versus solenoidal RF coil diameter.

Webb and colleagues have shown the utility of microcoils for standard NMR spectroscopy for some mass limited samples, generally in the case of biomolecules and neuropeptides [2-4]. The NMR imaging applications to date have been single cell or small tissue samples [5].

The success of the microcoil applications for small samples suggests a question. If one has reduced the size of the sample and the apparatus detecting the excited magnetization does one need a magnet that will accommodate a sample of 10^4 large volume? In NMR spectroscopy, there is no substitute for spectral dispersion for resolving features, and compressing a superconducting high field magnet into 1/100th the space is not practical due mainly to cryogenic engineering constraints.

NMR imaging is not so tightly coupled to higher polarizing fields. At first glance this may not be apparent. The goal of microscopic NMR imaging is the 3D resolution of an image and the SNR of a pixel is related to the volume of that pixel. Thus the SNR of a 3D image follows the isotropic pixel volume as the inverse cube root of the resolution. We can simplify the relationship between polarizing magnetic field and pixel size to the following approximations:

$$\text{SNR} \propto \omega_0^{7/4} \text{ (solenoid RF coil)} \qquad \text{Isotropic resolution} \propto \omega_0^{-7/12}$$

Figure 2 displays this B_0 relation over a range of 0.5 to 11.7 T normalized to a 4.7 T field. The top curve graphs the relation of isotropic resolution vs. B_0. A second curve estimates the effect of T_1 dependence upon the SNR as one

changes the main field. The T_1 estimate is based on the Gortner relation for spin-lattice relaxation with polarizing field strength.

High-resolution 3D NMR images may be acquired in a reasonable time with B_0 fields as low as 1 T. This is easily in the range of permanent magnet materials and makes possible a class of micromagnets. We have built a prototype of such a magnet and are investigating its properties and stability [6].

The miniaturization of NMR equipment makes possible a new class of experiments where by embedded imaging systems can be combined with other measurements or imaging methods, such as optical microscopy. These combined methods and progress to date will be discussed [7].

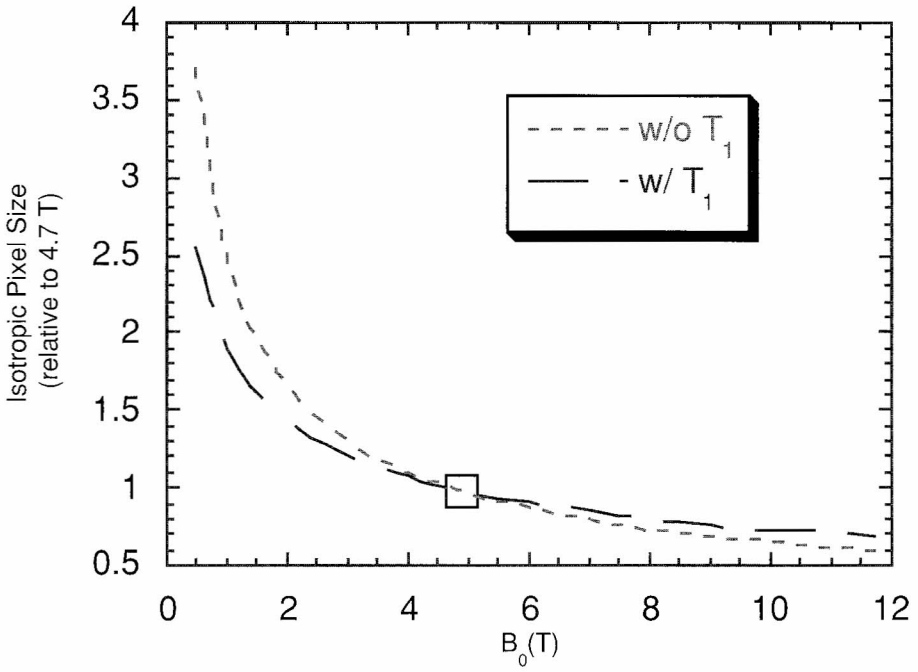

Fig. 2. Isotropic resolution of an image vs. B_0.

References

1. Peck, T.L.; Magin, R.L.; Lauterbur, P.C.; Design and Analysis of Microcoils for NMR Microscopy, *J. Magn. Reson. B*, **108**, 114-124 (1995).
2. Olson, D.L.; Peck, T.L.; Webb, A.G.; Magin, R.L.; Sweedler, J.V.; High resolution microcoil 1H-NMR for mass-limited nanoliter-volume samples, *Science* **270**, 1967-70 (1995),
3. Wu,N.; Peck, T.L.; Webb, A.G.; Magin, R. L.; Sweedler, J.V.; Nanoliter volume sample cells for ^{1}H-NMR: application to on-line detection in capillary electrophoresis. *J. Am. Chem. Soc.* **116**, 7929 (1994).
4. Subramanian, R.; Sweedler, J.V.; Webb, A.G.; Rapid two dimensional inverse detected heteronuclear correlation experiments with < 100 nanomole samples using solenoidal microcoil NMR probes. *J. Am. Chem. Soc.* **121**, 2333-2334 (1999).
5. Grant, S.; Plant, D.; Gibbs, S.; Aiken, N.R.; Webb, A.; Mareci,T.H.; Blackband, S.J.; Spatially Localized ^{1}H Spectroscopy on Isolated Single Neurons; *Proc. Int. Soc. Magn. Reson. Med.* **7**, 32 (1999).
6. Gorkov, P.G.; Morris, H.D.; Georgiadis, J.; Moser, K.; Development of a Small Permanent Magnet for Biomedical MRI, 40th Experimental NMR Conference (ENC), Orlando FL, Feb. 28 – Mar. 5, 1999.
7. Gorkov, P.G.; Harris, A.B.; Tsao, J.; Konda, S.; Morris, H.D.; Wiener, E.C.; Lauterbur, P.C.; Dual Observation of Histological Samples with Magnetic Resonance and Optical Microscopy, *Proc. Int. Soc. Magn. Reson. Med.* **7**, 2121 (1999).

L17

Magnetic Resonance Elastography by Direct Visualization of Propagating Acoustic Waves

Richard L. Ehman, M.D.
Mayo Foundation, Rochester, MN, USA

Introduction

Malignant tumors and other tissue abnormalities are often characterized by marked changes in tissue mechanical properties. This accounts for the efficacy of palpation as a clinical tool for detecting cancer in accessible regions of the body. Indeed, most tumors of the thyroid, breast, and prostate are still first detected by this centuries-old diagnostic technique. Unfortunately, small or inaccessible lesions cannot be detected by touch, and conventional diagnostic imaging methods such as ultrasound, computed tomography, and magnetic resonance imaging do not provide information that is in any way analogous.

In engineering terms, palpation assesses the tendency of tissue to resist deformation, a physical property called elastic modulus. The elastic moduli of various human tissues are known to vary over a wide range. Most of the physical properties depicted by conventional medical imaging modalities are distributed over a much smaller range. For instance, the x-ray attenuation coefficients of various soft tissues assessed in CT imaging vary by only by a factor of about 2. In contrast, the elastic moduli of soft tissues vary by factors of as much as 10,000. In addition, the elastic modulus of tumors may differ from surrounding tissues by a factor of 20.

The major goal of this work is to develop and validate a technique for quantitatively imaging the viscoelastic mechanical properties of tissues in vivo. We call the technique magnetic resonance elastography (MRE). Our overall hypothesis is that magnetic resonance elastography can be successfully implemented as a clinical tool and that it will be useful for detecting and characterizing focal and diffuse disease processes that may be difficult to investigate by other methods.

Methods

In general, estimating elasticity involves the following steps: (1) causing a known static or cyclic mechanical stress within the medium, (2) measuring the deformation of the medium in response to this stress, and (3) computing the elastic modulus of the medium from the measurements. MRE uses harmonic low frequency transverse acoustic waves (10 Hz - 1.1 kHz) as the source of external mechanical stress. The acoustic waves cause tiny cyclic displacements (on the order of tenths of microns) as they propagate. With mechanical waves, the calculation of regional elastic modulus is simplified, because it can be computed directly from the local wavelength, rather than requiring estimation of the regional static stress distribution.

The MRE method consists of three major elements: (1) a system for generating mechanical waves within the object to be imaged, (2) a sensitive NMR-based method for imaging mechanical waves in tissue, and (3) an analysis algorithm for converting images depicting propagating waves into qualitative or quantitative maps of elasticity. Acoustic shear waves are generated within the object by a surface-mounted electromechanical driver, a piezoelectric device, or radiation pressure from a modulated ultrasound beam. Mechanical waves are imaged using a modified phase-contrast MRI technique. An oscillating, motion-sensitizing field gradient is applied synchronously with acoustic mechanical waves that are generated inside the imaged object. The cyclic motion of the spins in the presence of these motion-sensitizing gradients causes a measurable phase shift in the received NMR signal. The phase shift is proportional the displacement amplitude and the number of the cyclic motion-sensitizing gradients. Thus, extreme sensitivity to small amplitude synchronous motion can be achieved by accumulating phase shifts over multiple cycles of mechanical excitation and the motion-sensitizing gradient waveform. From the measured phase shift in each voxel, it is possible to estimate the amplitude of displacement of each voxel in the reconstructed image. This displacement map yields a snapshot of the mechanical waves propagating within the object. The cyclic motion-sensitizing gradients can be superimposed along any desired axis, and therefore it is possible to estimate all components of the strain dyadic non-invasively. The wave images are then processed to generate shear modulus images, using spatial filtering to calculate local wavelength or other methods such as inverse scattering algorithms.

Results and Discussion

Experimental results, obtained with a 1.5 T whole body MR imager, show that the MRE technique can image acoustic shear waves with displacement amplitudes of less than 100 nanometers in tissues. MRE-derived measurements of the shear modulus of tissue-simulating gel specimens correlated well with independent mechanical testing results. A series of phantom studies demonstrated that the technique can delineate tumor-simulating inclusions with diameters as small as 2 mm.

Studies of organ and tissue specimens have provided quantiative elastograms depicting the shear modulus of kidney, liver, muscle, and adipose tissue. Our measurements demonstrate that the viscoelastic properties of some tissues are isotropic, while other tissues such muscle is highly anistropic. Studies of human pathologic specimens have demonstrated the feasibility of delineating breast and prostate tumors with the technique.

Subsequent experiments have assessed the feasibilty of applying MRE in vivo. To date, we have successfully acquired MRE images of skeletal muscle, breast, and brain in human volunteers and patients. The studies of skeletal muscle demonstrate that the observed shear modulus is directly proportional to muscle loading. The results suggest that MRE may be a useful tool for assessing the funtional properties and tension distribution within muscle in vivo. Studies of volunteers and patients have demonstrated the feasibility of imaging normal breast anatomy with MRE and delineating breast cancer. These results provide motivation for exploring the capacity of MRE to detect and characterize breast tumors, particularly in premenopausal women. Preliminary MRE studies of the brain in volunteers have provided quantitative images of brain elasticity, demonstrating for instance that white matter has a higher shear modulus than gray matter. These are the first in vivo measurements of the viscoelastic properties of human brain tissue *in vivo* and may be of interest in the study of traumatic brain injury, neurooncology, and neurosurgical simulation.

Conclusions

The findings indicate that the MR Elastography can be used as a quantitative tool for mapping the viscoelastic properties of tissue in vivo. The technique allows measurement of *shear modulus*, *shear viscosity*, and the *anisotropy* of these properties, as new tissue characterization parameters. Preliminary studies of MRE as a clinical diagnostic method, have shown that it can be used to non-invasively "palpate" regions of the body that are beyond the reach of the physician's hand and that it is capable of delineating lesions that are too small to detect by touch. The technology may find additional applications in the fields of acoustics and materials science.

References

1. Muthupillai R, Lomas DJ, Rossman PJ, et al. Magnetic Resonance Elastography by Direct Visualization of Acoustic Strain Waves. *Science* 269: 1854-1857 (1995).
2. Muthupillai R, Rossman PJ, Lomas DJ, et al. Magnetic Resonance Imaging by of Transverse Acoustic Strain Waves. *Magn. Reson. Med.* 36:266-274 (1996).
3. Muthupillai R, Ehman RL. Magnetic resonance elastography. *Nature Medicine* 2:601-603 (1996).
4. Manduca A, Muthupillai R, Rossman PJ, et al. Image Processing for Magnetic Resonance Elastography. *SPIE International Symposium on Medical Imaging 1996*. Newport Beach, CA: Society of Photo-Optical Engineers, pp. 616-623 (1996).
5. Smith J, Muthupillai R, Greenleaf JF, et. al. Tissue Characterization with MR Elastography. *RSNA Sci. Program.* 194 (1996).
6. Dresner MA, Rose GH, Rossman PJ, et al. Functional MR elastography of human skeletal muscle. *Proc. Int. Soc. Magn. Reson. Med.* 6: 493 (1998).
7. Wu T, Felmlee JP, Rossman PJ, et al. MR imaging of low frequency shear waves generated by focused ultrasound radiation force. *Proc. Int. Soc. Magn. Reson. Med.* 6: 693 (1998).
8. Kruse SA, Dresner MA, Rossman PJ, et al. "Palpation of the brain" using magnetic resonance elastography." *Proc. Int. Soc. Magn. Reson. Med.* 7: 258 (1999).
9. Wu T, Felmlee JP, Riederer SJ, Ehman RL. MR elastography of focused ultrasound induced thermal lesions. *Proc. Int. Soc. Magn. Reson. Med.* 7: 403 (1999).
10. Lawrence AJ, Rossman PJ, et al.. Assessment of breast cancer by magnetic resonance elastography. *Proc. Int. Soc. Magn. Reson. Med.* 7: 525 (1999).
11. Dresner MA, Rossman PJ, Kruse SA, Ehman RL. MR elastography of the prostate. *Proc. Int. Soc. Magn. Reson. Med.* 7: 526 (1999).

L18

Looking at Tissue Structure and Function at the Microscopic Scale with Macroscopic Images

Denis Le Bihan
SHFJ/CEA, Orsay, France

Although the effects of diffusion on the NMR signal have been analyzed long ago, the coupling of the NMR imaging principles with those of diffusion NMR measurements methods has been developed mainly during the last decade. Taking typical values for water diffusion and diffusion time achievable on conventional MRI equipment (e.g., $D \approx 10^{-3} mm^2/s$ and $T_d \approx 20ms$), free water molecules diffuse over distances on the order of 6 μm, which is about the size of many tissue structures. NMR, because of its noninvasive nature, is especially suited to probing the molecular dynamics and structural information of biological systems, as well as transport processes. The recent combination of such principles with NMR imaging (MRI) thus represents a spectacular and somewhat unpredicted development in the field of biomedical sciences. Measuring molecular displacements in biological tissues *in vivo* may have enormous interest, from the determination of the molecular organization in tissues to the emergency management of stroke patients, or the monitoring of laser surgery.

Despite the intrinsic sensitivity of diffusion MRI to motion artifacts, it has been demonstrated that, with care in the experimental settings and proper hardware (shielded or small dedicated gradient coils), water molecular diffusion can be measured *in vivo* with MRI with fairly good accuracy and reproducibility, especially in the brain. Motion artifacts can be significantly reduced using echo-planar imaging (EPI). With EPI many images can be acquired in short time intervals, allowing greater accuracy in the measurements. Also, diffusion measurements can now be achieved in other organs than in the brain, such as the kidneys or the heart.

Diffusion measurements may provide useful information on tissue microstructure and function, at a scale significantly smaller than the voxel size. Recently, it has been shown that, using appropriate algorithms, the entire diffusion tensor can be determined *in vivo*, including in the human brain. The interest of diffusion *tensor* measurements, instead of simple *coefficient* measurements, is emphasized by the finding that diffusion could be anisotropic in some tissues, such as brain white matter and muscle. This anisotropy is related to the tissue microstructure which is also anisotropic, although the exact mechanisms are still unclear. For instance, the role of restricted diffusion by the myelin sheath has been suggested for anisotropic diffusion in brain white matter. However, restricted diffusion effects have not been clearly demonstrated yet and diffusion anisotropy can be detected well before white matter fibers have been myelinated.

Another recently developed field is the measurement of diffusion of important metabolites *in vivo*. Most diffusion studies have been based on water diffusion for obvious reasons of technical easiness. However, with proper spectroscopic encoding schemes, diffusion coefficients of some brain metabolites have been determined. These measurements may help us to understand how metabolites are compartmentalized.

In the field of Functional Magnetic Resonance Imaging (fMRI) recent data suggest that diffusion MRI visualizes dynamic tissue changes associated with large neuronal activation and space orientation of large bundles of myelinated axons in the white matter. FMRI has appeared as a new tool which is very powerful for cognitive neuroscience, offering the potential to look at the dynamics of cerebral processes underlying cognition, noninvasively and on an individual basis. Still, the real understanding of brain function requires direct access to the functional unit made of the

neuron, so that one may look at the transient temporal relationships that exist between largely distributed groups of hundreds or thousands of neurons. Furthermore, communication pathways between networks must be identified to establish connectivity maps at the individual scale, taking into account individual variability resulting from genetic factors and cerebral plasticity. In this respect, MRI of molecular diffusion is especially helpful to detect changes in tissue microstructure, such as changes in cell geometry associated with neuronal function and to map out fiber tracts connecting activated regions.

Reference

Le Bihan, D. (Ed.) *Magnetic Resonance Imaging of Diffusion and Perfusion: Applications to Functional Imaging*. Lippincott-Raven Press, New York, 1995.

L19

Single-Event fMRI in Motor Cortex and Other Brain Regions

Peter Morris, Richard Bowtell, Steve Butterworth, Stuart Clare,
Miles Humberstone and Guy Sawle
MR Centre, School of Physics & Astronomy, University of Nottingham, Nottingham UK.

Introduction

The first functional magnetic resonance imaging (fMRI) studies used experimental paradigms of the type developed in earlier positron emission tomography (PET) work. Such epoch-based designs severely restrict the application of fMRI and we (Humberstone *et al.*, 1995) and others introduced single event fMRI methods that enabled us to study individual motor events and simple cognitive paradigms. New methods of statistical analysis are required for such experiments, especially when the activation timecourse is unknown and correlation methods are not readily applicable.

Method

Complete three-dimensional activation data are collected as sets of 12 contiguous slices every 1-3s. They are superimposed on a reference image obtained using an inversion recovery EPI sequence with the T1 selected so as to null grey matter. Such white matter reference sets are a great aid to correct localisation of the cerebral anatomy. As they are collected using the same EPI technique as the activation data, both data sets will be subject to the same susceptibility-induced distortion, thus eliminating possible misregistration artefacts. Single event activation data are analyzed using a modification of an analysis of variance (ANOVA) technique (Clare *et al.*, in press).

Results and Discussion

We have studied a simple 'go, no-go' paradigm in which subjects were asked to push a button once with their right thumb in response to a figure '5' shown on an LED display (go), but to do nothing in response to presentation of a '2' (no go). When the 'go, no-go' responses are compared, an anterior portion of the supplementary motor area (SMA) is seen to be active in both cases, whereas a more posterior region is active only in the 'go' response. This suggests a hierarchical subdivision of the (SMA) into regions responsible for movement decision making and execution (Humberstone *et al*, 1997). Subsequently, by studying dynamic behavioural profiles – an opportunity afforded by the rapidity with which fMRI studies can be executed – we have shown this pre-supplementary area is underactive during motor tasks in subjects with Parkinson's Disease, and that this may be responsible for their bradykinesia. In sharp contrast, the same studies reveal an overactivation of the primary motor (contra- and ipsilateral) and sensory cortex (contralateral). We believe that this reflects diffuse disinhibition of these regions and is the cortical mechanism responsible for rigidity in Parkinson's disease.

A rather different picture emerges in dystonic patients performing the same task, where, in the 'go' condition, there is lower peak activity in the primary motor cortex and SMA proper, but an increased activity in the pre-SMA. It is not yet clear whether this is part of the pathology of dystonia, or a 'normal' response to pathology elsewhere.

In the 'go, no-go' experiment, there is a delay of several seconds following the button push before activity is detected. This is due to the latency of the haemodynamic response which is related to the

transit time of the blood through the capillary network. This delay clearly hampers the interpretation of temporal data. However, if the time-course of the haemodynamic response is known, its effect can be removed by deconvolution (Hykin *et al.*, 1996). By using our ANOVA method to identify active regions, and deconvolution of the haemodynamic response function, we have been able to achieve a precise match between the discrete cognitive elements in a short-term memory test (Sternberg paradigm) and the activation responses.

Conclusions

Single-event fMRI provides a powerful tool to study cognitive processing and will have tremendous impact on psychology and psychiatry. The main limitation is the latency and protracted nature of the haemodynamic response which can be partly countered by simple deconvolution assuming a uniform response function. A more sophisticated approach would be to map the haemodynamic response function and this is best carried out using echo volumar imaging EVI (Mansfield *et al.*, 1995) which generates images of the brain within a few tens of ms, eliminating the significant delays inherent in the multislice approach.

References

Clare S, Humberstone M, Hykin J, *et al.*, *Magn. Reson. Med.* (in press).

Humberstone M, Barlow M, Clare S, *et al.*, *Proc. Int. Soc. Magn. Reson. Med.* **3**, 858 (1995).

Humberstone M, Sawle GV, Clare S, *et al.*, *Annals of Neurology* **42**(4), 632-637 (1997).

Hykin J, Clare S, Bowtell R, *et al.*, *MAGMA suppl v*4 (2) p. 180 (1996).

Mansfield P, Coxon R, Hykin J, *J. CAT*, **19**(6), 847-852 (1995).

L20

^{129}Xe as a Probe for Localized Spectroscopy and Imaging

I. L. Moudrakovski, S. Breeze, S. Lang, A. Nossov,
A. Sanchez, C. I. Ratcliffe and **J. A. Ripmeester**

Steacie Institute for Molecular Sciences, National Research Council of Canada
Ottawa, Ontario K1A 0R6, Canada

It has been about 20 years since it was first recognized that the chemical shift of xenon sorbed into voids in solids could be used as a tool to learn about the geometry of the void space[1]. Early efforts involved mainly the establishment of correlations of the chemical shifts with pore size, pore shape, and as probes of intrazeolitic sorbents and metal clusters[2] Eventually it was realized that it was extremely important to include the role of dynamics, as the chemical shift is a population-weighted average over all accessible sites both inside and outside the particles of the material under study. This introduces a sensitivity of the spectra to particle size and sample morphology[3] A fundamental understanding of the chemical shifts of xenon in small voids in terms of the xenon - cage wall potential and xenon atom dynamics was developed only in the last few years[4].

The sensitivity of the average chemical shift to the microscopic void space in materials and the relatively high mobility of the xenon atom presents unique opportunities to study dynamic processes over a wide set of length scales so that intersite[5] interphase[6]and interparticle[7]diffusion can be studied, with information on diffusion constants and domain sizes becoming available

The large chemical shift dispersion of xenon make imaging with chemical shift contrast an attractive possibility. In the last few years several reports have been published on imaging with xenon gas, although only one with chemical shift contrast[8]. For this, as well as other demanding applications such as the study of processes requiring time resolution, some of the limitations of working with xenon become quite apparent: general sensitivity issues, requiring work at high gas pressure, and potentially long data acquisition times because of inefficient relaxation.

The development of technology to produce hyperpolarized (HP) xenon[9]gas by optical pumping, with vastly improved sensitivity over thermally polarized xenon, solves some of these problems. Of course, these developments have benefited a great deal from the interest and efforts directed at the development of clinical imaging with HP xenon, for instance, of human lungs.[10] Batch mode production of hyperpolarized xenon allows time-resolved NMR or MRI, the former with continuous observation of processes using short rf pulses, the latter in a "stopped-flow" mode. The continuous production of hyperpolarized xenon[11] in a flow system has allowed further developments, namely the recording of NMR spectra or MRI images of the gas flowing through porous materials, all at a Xe partial pressure of ~ 7 torr. The NMR spectra of zeolites recorded this way are characteristic of those obtained under essentially infinite dilution conditions, with the additional observation of defect sites present only at low concentrations. In the case of MRI on model catalyst beds it has been possible to produce chemical shift resolved images in a reasonable length of time.

References

1. Ripmeester, J. A., *J. Am. Chem. Soc.* **104**, 289 (1982);
   Ripmeester, J. A., Ratcliffe, C. I., and Tse, J. S., *J. Chem. Soc., Farad. Trans.* 1 **84**, 3731 (1988);
   Ito, T., and Fraissard, J. *J. Chem. Phys.* 76, 5225 (1982).
2. Ratcliffe, C. I., *Ann. Rep. NMR Spectr.* **36**, 123 (1998).
3. Ripmeester, J. A., and Ratcliffe, C. I., *Anal. Chim. Acta* **283** 1103 (1992).
4. Jameson, C. J., Jameson, A. K., Lim, H. M., Baello, B. I., *J. Chem. Phys.* **100**, 5977 (1994);
   Jameson, C. J., Lim, H.-M., *J. Chem. Phys.* **103**, 3885 (1995).
5. Larsen, R. G., Shore, J., Scmidt-Rohr, K., Emsley, L, Long, H., Pines, A., Janicke, M., Chmelka, B. F., *Chem. Phys. Lett.*, **214**, 220 (1993);
   Jameson, A. K., Jameson, C. J., Gerald II, R. E., *J. Chem. Phys.* **101**, 1775 (1994);
   Moudrakovski, I. L., Ratcliffe, C. I., Ripmeester, J. A., *J. Am. Chem. Soc.*, **120**, 3123 (1998).
6. Tomaselli, M., Meier, B. H., Robyr, P., Suter, U. W., Ernst, R. R., *Chem. Phys. Lett.* 205, 145 (1993).
7. I. L. Moudrakovski, C. I. Ratcliffe and J. A. Ripmeester, *Applied Magnetic Resonance* **8**, 385 (1995); I. L. Moudrakovski, C. I. Ratcliffe and J. A. Ripmeester, *Zeolites, A Refined Tool for Designing Catalytic Sites.* L. Bonneviot and S. Kaliaguine, (Eds.) Elsevier, 1995, pp. 243-250.
8. Gregory, D.M., Gerald II, R.E., Botto, R.E., *J. Magn. Res.*, **131**, 327-335 (1998).
9. Grover, B.C. *Phys. Rev. Lett.* **40**, 391(1978); Happer, W., Miron, E.; Schaefer, S.; Schreiber, D.; van Wingaarden, W.A.; Zeng, X. *Phys. Rev. A*, **29**, 3092 (1984).
10. Albert, M.S.; Cates, G.D.; Driehuys, B.; Happer, W.; Saam, B.; Springer, C.S.; Wishnia, A. *Nature*, **370**, 188(1994);
    Mugler III, J.; Driehuys, B.; Brookeman, J. et al, *Magn. Res. Med.*, **37**, 809-815 (1997).
11. Driehuys, B., Cates, G.D., Miron, E., K. Sauer, Walter, D.K.; Happer, W. Appl. *Phys. Lett.*, **69**, 1668-1670 (1996).

L21

^{3}He Lung MRI

Anselm Deninger MS, Balthasar Eberle MD[2], Michael Ebert MS, Gordon Hanisch MS[1], Werner Heil PhD, Tino Großmann MS, Hans-Ulrich Kauczor MD[1], Ernst Otten PHD, Klaus Markstaller MD[2], Jörg Schmiedeskamp MS, Wolfgang Schreiber PhD[1], **Reinhard Surkau** PhD, Manfred Thelen MD[1], Norbert Weiler MD[2]

Depts. of Physics, [1]Radiology and [2]Anesthesiology, Johannes Gutenberg-Universität, D-55099 Mainz, Germany

Introduction / Purpose. Ventilated air space in the lung cannot be visualized by ^{1}H MR as physicians would like in order to assess diseases and plan treatments. The signal-to-noise ratio (SNR) is poor because of low proton density and short T_2* relaxation times due to susceptibility effects. Attempts have been made to increase lung tissue ^{1}H SNR using inhaled molecular oxygen as contrast agent, and T_1-weighted single-shot RARE [1]. Contrast enhancement due to increased oxygenation occurs in ventilated regions, but also in tissue with high blood flow, thus yielding little in overall contrast. Recent improvements of overall lung contrast and enhanced visualization of lung parenchyma have been demonstrated by simultaneous suppression of signal contributions from muscle and fat [2].

MRI of lung ventilation with high spatial and temporal resolution became feasible by employing hyperpolarized noble gases with spin I = ½ such as ^{3}He and ^{129}Xe. When these gaseous tracers are imaged during and after inhalation, the dynamics of their distribution in the lung, and thereby ventilation, becomes immediately apparent. Compared to proton density in tissues, the low density of these MRI tracer gases requires polarization degrees which are magnitudes of orders higher than Boltzmann equilibrium. This non-renewability of polarization has to be considered in MR sequence programming. On the other hand the hyperpolarization enables to perform very fast imaging, using small flip angles. One needs not to await Boltzmann polarization build-up, so dynamical studies become feasible.

Hyperpolarization is achieved by so called Optical Pumping, which has been investigated in noble gases for nearly four decades using spin exchange scattering (SE) [3] or metastability exchange scattering (ME) [4]. Since powerful resonant laser light became available for Optical Pumping larger quantities of ^{3}He-gas could be operated [5,6]. The original interest was the development of dense spin-polarized targets for fundamental research in physics [7]. As a spin-off the possibility of MRI of lungs filled with hyperpolarized ^{129}Xenon was demonstrated in 1994 [8]. Later, ^{3}He was used for MRI in a guinea pig [9] and humans [10-12].

Methods : Optical Pumping of noble gases is a two-step process. First an intermediary gas is polarized, for instance an alkali-atom for SE (mostly rubidium) or metastable ^{3}He (^{3}He*) for ME. By absorbing light, which is circularly polarized along a weak holding field of about 0.8 mT, angular momentum is gained in the intermediary system. This angular momentum is then transferred to the ^{3}He-nucleus. The SE method has the advantage to operate in sealed cells at a pressure of several bar, while ME takes place in a discharge plasma at 1 mbar pressure. A polarization-preserving compression technique is needed after polarizing. The advantage of ME is the ability to polarize larger quantities of ^{3}He to higher polarization degrees.

For that purpose we have built a ^{3}He polarizer and compressor. The gas is polarized with the help of two home made LNA-lasers [13], which emit resonant light at λ = 1083 nm ^{3}He* transitions at 6 - 10 W output power. Thereafter a two-stage piston pump compresses the gas by nearly a factor of 10000 into a storage glass cell [14]. The storage cells can be closed by glass stopcocks and disflanged from the polarizer after filling. A small holding field maintains magnetization during transportation.

For gas administration inside the MR scanner a home-built applicator device is used. A predefined ^{3}He gas quantity is inserted as a "bolus" into the breath of a living subject at a predefined position. Bolus application can be performed during spontaneous breathing or during mechanical ventilation with conventional respirator machines.

At Mainz images are produced with a clinical 1.5 T MR unit (Siemens Medical Systems, Erlangen, Germany). We use 2D or 3D FLASH sequences adapted for several different types of studies (TR/TE/α = 2 - 11 ms / 0.7 - 4.2 ms / 1° - 3°, matrix size: 32*64 - 128*81, measurement time: 65 ms - 1 s per image, FOV: 320 - 340 mm). Morphologic images are taken with 1 cm slice thickness, dynamic scans with 4 cm slice thickness or as projection images. For these experiments about 200 - 300 ml of ^{3}He are used for each breathing cycle. Dynamic scans are performed to investigate in- and exhalation in real-time mode, and to study longitudinal relaxation phenomena inside the alveolar space.

Within the lung, irreversible loss of the ^{3}He non-equilibrium polarization occurs predominantly by RF pulses, relaxation due to molecular oxygen [15] and wall contact. Further relaxation sources, namely by ^{3}He dipolar coupling [16] and by magnetic field gradients [17] may be neglected under the given conditions. We model the dynamics of hyperpolarization by rate equations [18]. A double-aquisition method is used to separate flip angle depolarization from other relaxation sources. Thick partitions covering the entire ventilated volume are imaged to ensure homogenous excitation of all ^{3}He spins in the lung.

In animal experiments approved by the University´s Animal Care Committee, bronchoalveolar wall relaxation is studied in porcine lungs after cardiac arrest has been induced in the animal (27 kg), and oxygen has been washed out by administering pure nitrogen for 15 minutes prior to imaging. Also, the relationship between endexpiratory oxygen partial pressure, as measured by respiratory gas analysis, and ^{3}He-MRI-determined O_2 partial pressures (pO_2) within the lungs is studied in live animals ventilated with various inspiratory O_2 fractions. Furthermore, in experiments on three

human volunteers approved by the University's Ethics Committee, the time course of P_{O2} during short periods (10 - 35 s) of breathholding is investigated.

Results. Storage glass cells are filled achieving 50 % polarization at an average flow of 0.5 bar liters /hour. Increasing the flow to 1 bar liter per hour still yields 40 % polarization - sufficient for ventilation measurements. Polarization losses inside the cell are mainly due to wall relaxation. With caesium coating relaxation times up to T_1 = 176 h have been observed [20]. Cells for medical application from special "Supremax" glass with low iron content (provided by Schott Glaswerke, Mainz) and no coating show relaxation times of up to 110 h. At the scanner itself, a fast transfer of the cell through its stray field causes no significant polarization loss, nor does bolus application of ^{3}He gas into the study subject. Bolus volumes (20 to 500 cm^3) are delivered with an accuracy of 5 cm^3.

Morphologic ^{3}He MR images acquired at 1.5 T from lungs of healthy volunteers show homogeneous signal over the entire lung; pulmonary vessels appear as structures without signal (pixel size 1.4 mm^2 and 10 mm slice thickness). On patients with COPD and emphysema, signal imhomogeneities with a patchy pattern in both lungs or even ventilation defects were observed. On dynamic scans, evolution of ^{3}He inhalation is clearly seen, with a peak signal intensity in the trachea of about 3 times that of the alveolar space [21].

In the oxygen-depleted porcine lung, relaxation times, corrected for flip angle depolarization, of up to 4.3 minutes were measured. In the ventilated animal series, a significant correlation between MR-determined O_2 concentrations and end-expiratory values was demonstrated [19]. Thus, *in vivo*, paramagnetic molecular oxygen is the predominant relaxation effect within the lung, and ^{3}He MRI can be used to measure it non-invasively.

In the experiments on human volunteers, intrapulmonary oxygen concentrations as well as their time course could be quantified with high regional and temporal resolution. The temporal evolution of pO_2 was found to be linear, hence $pO_2(t) = P_0 - R\ t$. Values of P_0 ranged from 105 to 190 mb and R from 0 to 4 mb/s. Low values of P_0 were correlated with low rates R, whereas high P_0 corresponded to steep slopes (correlation coefficient 0.87). The flip angle could be calibrated simultaneously with an accuracy of better than 1%.

Discussion. Due to physical characteristics, compression of ME-optically pumped ^{3}He gas is at present the most productive method with highest output polarization. The latter is desirable because it allows to minimize the inspired gas tracer amount, in order to maintain alveolar gas composition as normal as possible for lung function imaging. Besides the high technical challenge of polarization, preservation, compression and storage, this method enables to separate gas production and application spatially and temporally, and thus offers a flexible way of hyperpolarized ^{3}He supply. Compared to ventilation scintigraphy, the present gold standard for lung ventilation imaging, ^{3}He MR images provide significantly higher spatial and temporal resolution. However, due to the ^{3}He high relaxivity and diffusivity [22 - 24], ventilation images may also have to be interpreted differently.

To quantitate local ventilation in the lung, determination of regional inspiratory and expiratory signal kinetics may help. Peak ^{3}He signal is typically delayed in lung parenchyma with respect to the trachea. Differences in regional inspiratory and expiratory time constants are visible in patients or smokers [21]. Oxygen concentrations may be analyzed as direct measure of alveolocapillary gas exchange. Its linear decrease during breathhold in full-thickness regions of interest may be caused by several mechanisms: perfusion-driven oxygen uptake into the blood, progressive mixing of low-oxygen alveolar gas with high-oxygen deadspace gas in the volume of interest, or both in variable degrees. The apparent correlation of p_0 with the decrease rate R could indicate the local matching of ventilation and perfusion, but could also reflect the relative contributions of alveolar space and peripheral anatomical deadspace to a volume of interest.

Conclusion. The tremendous signal gain that can be achieved using hyperpolarized noble gases opens the door to a large number of previously unimaginable NMR experiments. Current polarization techniques for ^{3}He are sufficiently mature to permit the routine use of hyperpolarized ^{3}He experiments requiring several liters of gas. The major emphasis to date has been on medical applications, where scientifically interesting and significant results have been produced. To a lesser extent hyperpolarized gases MRI are also used for material science applications.

References

1. V.M. Mai, et.al.; *Proc. Int. Soc. Magn. Reson. Med.* **7**, 137 (1999).
2. V.M. Mai, et.al.; *Proc. Int. Soc. Magn. Reson. Med.* **7**, 519 (1999).
3. M.A. Bouchiat, T.R. Carver, C.M. Varnum; *Phys. Rev. Lett.* **5**, 373-375 (1960).
4. F.D. Colegrove, L.D. Schearer, K. Walters; *Phys. Rev.* **132,** 2561-2572 (1963).
5. T.E. Chupp, M.E. Wagshul, K.P. Coulter, et.al.; *Phys. Rev. C* **36**, 2244-2251 (1987).
6. G. Eckert, W. Heil, et.al.; *Nucl. Inst. & Meth. A* **320,** 53-65 (1992).
7. M. Meyerhoff, et.al.; *Phys. Lett. B* **327,** 201-207 (1994).
8. M.S. Albert, et.al.; *Nature* **137**, 199-201 (1994).
9. H. Middleton, et.al.; *Magn. Reson. Med.* **33**, 271-275 (1995).
10. M. Ebert, et.al.; *Lancet* **347**, 1297-1299 (1996).
11. H.U. Kauczor, et.al.; *Radiology* **201**, 564-568 (1996).
12. H.-U. Kauczor, et.al.; *J. Magn. Reson. Imaging* **7**, 538-543 (1997).
13. C.G. Aminoff, et.al.; *Optics Commun.* **86**, 99-105 (1991).
14. R. Surkau et.al.; *Nuc. Instr. & Meth. A* **384**, 444-450 (1997).
15. B. Saam, W. Happer and H. Middleton; *Phys. Rev. A* **52**, 862-865 (1995).
16. N.R. Newbury, et.al.; *Phys. Rev. A* **48:6**, 4411-4420 (1993).
17. G.D. Cates, S.R. Schaefer, and W. Happer; *Phys. Rev. A* **37** , 2877-2885 (1988).
18. A.J. Deninger et.al.; *J. Magn. Reson.*, submitted (1999).
19. Eberle B. et al.; *J. Appl. Physiology*, submitted (1999).
20. W. Heil, et.al.; *Physica B* **267 – 268**, 328-335 (1999).
21. W.G. Schreiber, et al.; *Eur. Radiol.* **9**, B28 (1999).
22. M. Bock; *Magn. Reson. Med.* **38**, 890-895 (1997).
23. B. Saam, et.al.; *Proc. Int. Soc. Magn. Reson. Med.* **7**, 136 (1999).
24. X.J. Chen, et.al.; *Proc. Int. Soc. Magn. Reson. Med.* **7**, 130 (1999).

L22

NQR: What's the Same and What's Different?

Bryan H. Suits

Physics Department, Michigan Technological University, Houghton, MI, 49931, USA

The basic physics behind nuclear quadrupole resonance (NQR) is the same as that of nuclear magnetic resonance (NMR). Simple pulsed experiments, such as the observation of a free induction decay using a single RF pulse or an echo using two pulses, are performed identically to the corresponding NMR (wide-line) experiments except no large static magnetic field is applied. In this talk the significant differences between NQR and NMR which show up in other situations are examined with an emphasis on the complications which arise for NQR imaging measurements of powder or polycrystalline materials.

For NMR, a large external magnetic field is applied which defines an axis. The eigenstates of the Zeeman interaction, quantized along the applied field, form a simple basis set. For NQR, the nuclear levels are split by electric field gradients within the material which are part of the electronic structure of the material. Hence the orientation and strength of those fields are determined by the sample, and not the experimenter. In a powder, all orientations are simultaneously present. The quadrupole interaction is described by a traceless, second-rank tensor with an orientation which can be described using a principal axes system. In the general case, it is often inconvenient to think in terms of a single quantization axis for NQR.

For pulsed NMR measurements, the applied RF field is most effective if applied on resonance and in a plane perpendicular to the static applied field. For a pulsed NQR measurement, the applied RF field is most effective if on resonance and in a plane perpendicular to a particular principal axis – which axis depends on the transition being observed. For simple measurements using powder samples one will then necessarily observe behavior similar to that of an NMR experiment but with an extremely inhomogeneous RF field. For more complicated experiments, such as double resonance, the relative orientations of the two applied fields needs to be carefully considered for maximum effectiveness.

In an NMR experiment, an RF pulse is applied and during the pulse, the nuclear magnetization can be envisioned as rotating about the effective field. Only one sense of circular polarization for the RF pulse is effective to rotate the spins leading to the natural use of the „rotating reference frame." In free precession, the nuclear magnetization precesses about the externally applied magnetic field in only the same sense, giving rise to a signal which can be regarding as being circularly polarized. For NQR, there is no net nuclear magnetization in thermal equilibrium, and hence seemingly nothing for the pulse to rotate, and yet a free induction decay is readily observed. To some extent, this can be understood by considering the motion to be a superposition of two circular motions in opposite senses, which allows one to keep the rotating frame formalism. However, the rotating frame approach for NQR is limited and can lead to errors in one's intuition when applied in general. For NQR, transitions are induced by linearly polarized RF pulses and the response is linearly polarized along the same direction. In powders, this leads to the interesting result that the observed NQR response will have the same polarization as that of the RF excitation.

The response to small applied magnetic fields, such as the gradient fields used for NMR imaging, is completely different for NMR and NQR measurements. For an NMR imaging measurement, only the components of the gradient field along the large static magnetic field need be considered, leading to a description using the "x-, y-, and z-gradients." Whether, for example, one uses a reversed Helmholtz coil (a Maxwell pair) or a Golay saddle coil to produce a particular gradient will have no fundamental

effect on the imaging method. Image reconstruction based on a Fourier transform naturally follows for NMR imaging. However, for NQR of powder samples, the full gradient field must be considered and a simple description in terms of x-, y-, and z-gradients is not possible.[1,2] In addition, the coil configuration can make a significant difference, and the algorithm to produce an image from measured values will be necessarily more complicated.

Furthermore, for NQR the effect of a small static magnetic field on the nuclear energy levels is often quite inconvenient, and depends on the particular transition being observed. For a spin-1 nucleus, such as ^{14}N, a small static magnetic field will not change the transition frequencies in first order, making imaging based on static magnetic fields useless. For NQR using a spin-3/2 nucleus, a small magnetic field will create a complicated powder pattern, rather than a simple frequency shift. Though some methods have been proposed for spin-3/2 nuclei using static gradients, one is naturally lead to consider „rotating frame" imaging techniques using RF field gradients which will be more universally applicable for NQR imaging. Despite the dire situation presented above for NQR imaging, appropriate imaging methods can be developed. A method based on RF gradients will be shown as an example.[2] While significantly more inconvenient than for NMR imaging, perhaps to the point of being impractical for routine use in many situations, careful thought about the differences between NQR and NMR can lead to appropriate NQR imaging methods.

1. B. H. Suits and G. Y. Plude, *J. Magn. Reson.* **A117**, 84 (1995).
2. S. V. Swaminathan and B. H. Suits, *J. Magn. Reson.* **138**, 123 (1999).

Imaging SF_6 in Lungs as an Index to Gas Exchange: Something Useful?

Dean O. Kuethe, Arvind Caprihan[1], Volker C. Behr[2], Stephanie Begay[3], Jack A. Loeppky, Eiichi Fukushima[1], H. Michael Gach[4], Irving J. Lowe[5]

Lovelace Respiratory Research Institute, Albuquerque, USA
[1]New Mexico Resonance, Albuquerque, USA
[2]Bayerische Julius-Maximilians-Universität Würzburg, Germany
[3]Diné College, Shiprock, USA
[4]G. E. Medical Systems, Milwaukee, USA
[5]University of Pittsburgh, USA

Several labs image gases in lungs with NMR (1, 2, 8, 9, 12, 14, 16). Nonetheless, physicians want to know if we are going to come up with anything of practical use. We have little chance of competing with X-ray CT for imaging lung anatomy. It produces inexpensive images with submillimeter resolution. Our prospects are much better for making improvements in imaging how lungs function. There is desire for improvements over images of ventilation and blood perfusion made using radioactive tracers, especially if the new methods are within the monetary grasp of middle class people.

The rapid relaxation of some inert fluorinated gases (7, 11, 13, 15, 17), *e.g.*, SF_6, C_2F_6, and CF_4, facilitates imaging by allowing extensive signal averaging. In addition, it is ideal for spin-density imaging, which allows us to measure the fraction of inert gas in lungs. We exploit this feature to image obstructed ventilation. When a mammal breathes an O_2-rich gas mixture with an inert insoluble gas, like SF_6, blood removes the O_2 from alveoli but leaves the SF_6 behind. In regions where the ventilation is poor and the oxygen is not replenished, the SF_6 becomes concentrated (3, 4, 5, 6). The SF_6 in poorly ventilated regions can be four times as concentrated as in well ventilated regions, and provide wonderful contrast in images. Conversely, if the inhaled mixture is mostly SF_6, the concentrating effect is minimal, which allows us to obtain a reference image with nearly uniform SF_6 concentration. We use the reference image to correct for other causes of brightness variation, like B_1 inhomogeneity or differing gas-to-tissue ratios for different pixels.

We demonstrated this technique by imaging the lungs of rats when their left bronchi were partially obstructed with a glass bead containing a narrow gas passage. The image of the obstructed left lung was brighter than the that of the unobstructed right lung. In images made from the quotient of the obstruction-detecting image and the reference image, the pixel values can range from zero to one. The left lung's pixels had a higher mean and standard deviation (0.49 ± 0.10) than the unobstructed right lung (0.34 ± 0.049). The right lung's pixel standard deviation is very similar to the measurement error in the quotient image, calculated from the signal-to-noise ratios of the parent images. Much of the variation in the obstructed lung was due to variation in alveolar gas concentration.

Although we did not measure the ventilation-to-perfusion ratios by an independent means, the known physiology of gas exchange gives us a strong indication that they were in a clinically relevant range. Our images are full three-dimensional images of the lungs owing to our method of projection imaging with free induction decays (9, 10). Because humans are larger than rats, the increased signal-to noise ratio will allow one to obtain 64-cubed pixel images of similar quality in under half an hour. Such images would be much better than ones made with radioactive tracers.

A graph of lung volume *vs.* time during various patterns of breathing, can be a quick and inexpensive "pulmonary function" adjunct to the imaging procedure. When the inhaled mixture is

primarily SF_6, the NMR signal is proportional to the volume of gas in the lungs. There is enough signal in the raw FIDs to get a measurement of lung volume every 30 ms. A measurement that is easy by this method but otherwise difficult is the volume of gas remaining after full exhalation. This "residual volume" is commonly used to evaluate obstructive lung disease.

SF_6 is less soluble than N_2 and similarly inert, so we are fond of saying it is safer to breathe than N_2. It is affordable and also easy to recover because it condenses more readily than respiratory gases. The modifications necessary for a clinical MRI system to implement SF_6 imaging are minor, especially if they are part of the original manufacture and not a later modification. As with most talks whose titles pose a question, the authors think the answer is "Yes."

References

1. Albert, M. S., *et al. Nature* **370**:199-201 (1994)
2. Bachert, P., *et al. Magn. Reson. Med.* **36**:192-196 (1996)
3. Canfield, R. E. and H. Rahn. *J. Appl. Physiol.* **10**:165-172 (1957)
4. Farhi, L. E. *Resp. Physiol.* **3**:1-11 (1967)
5. Farhi, L. E. and A. J. Olszowka. *Respir. Physiol.* **5**:53-67 (1968)
6. Fenn, W. O., H. Rahn, and A. B. Otis. *Am. J. Physiol.* **146**:637-653 (1946)
7. Finney, R. J., M. Wolfe, and J. Jonas. *J. Chem. Phys.* **67**:4004-4011 (1977)
8. Kauczor, H., *et al. J. Magn. Reson. Imag.* **7**:538-543 (1997)
9. Kuethe, D. O., *et al. Magn. Reson. Med.* **39**:85-88 (1998)
10. Kuethe, D. O., *et al. J. Magn. Reson.* **139**:18-25 (1999).
11. Lizak, M. J., M. S. Conradi, and C. G. Fry. *J. Magn. Reson.* **95**:548-557 (1991)
12. Middleton, H., *et al. Magn. Reson. Med.* **33**:271-275 (1995)
13. Mohanty, S. and H. J. Bernstein. *J. Chem. Phys.* **53**:461-462 (1970)
14. Mugler, J. P., III, *et al. J. Magn. Reson. Anal.* (accepted, 1999).
15. Revokatov, O. P. and S. V. Parfenov. *JETP Lett.* **15**:103-105 (1972)
16. Rinck, P. A., S. B. Petersen, and P. C. Lauterbur. *Fortschr. Röntgenstr.* **140**:239-243 (1984)
17. Wolfe, M., E. Arndt, and J. Jonas. *J. Chem. Phys.* **67**:4012-4018 (1977)

L24

Broadline MRI of Porous Materials

John H. Strange and Mike J. D. Mallett
Physics Laboratory, University of Kent, Canterbury, Kent CT2 7NR UK

Introduction

Many modern materials of technological interest exhibit broad nuclear magnetic resonance (NMR) lines. Structural and support materials, polymeric materials and viscous fluids, in addition to typical solids, have reduced molecular motion so that an averaging of local magnetic interactions to produce line narrowing does not occur. Heterogeneous materials containing fluids in which motional narrowing is to be expected also often exhibit broad lines due to spatial susceptibility variation. This is commonly the case for liquids absorbed into porous structures or multiphase systems, particularly those containing a vapour component. Imaging of such materials becomes difficult because the natural linewidth must be dominated by spatially encoding magnetic field gradients. Unless artificial line-narrowing techniques can be employed – as is possible with some rigid solids – large magnetic field gradients are required. Various approaches are possible. Conventional imaging methods employing Fourier encoding but using small sample volumes with large switched gradients have been successfully employed for linewidths of a few kHz. Broader line systems may be imaged with more efficient use of power using large oscillating field gradient methods [1]. Utilisation of the very large static gradients in the peripheral field of a powerful magnet has led to a number of imaging and material mapping methods, e.g., STRAFI [2] and the NMR MOUSE [3], which are both capable of good spatial discrimination in very broad-line systems. Some recent examples of the applications of broad-line MRI techniques will be presented, drawing examples from food and bioproducts, natural mineralogy and porous construction materials.

Experimental Methods and Results

An example of the application of these methods to a biophysical problem is the recent experiments to image bacterial colonies in-situ. The bacteria used in some water purification processes are often supported on carbon filters that contain paramagnetic centres. Bacteria in soils are also in an environment of varied magnetic susceptibility. In both cases the NMR proton linewidth is typically of order 10 kHz. Using the bounded diffusion of fluid within bacteria as an NMR filter and combining this with broad-line imaging methods it has been shown [4] that it is possible to image bacterial colonies in concentrations of order 10^9 cells ml^{-1} in the presence of nutrient solution. Similar techniques are potentially applicable to a wide range of bio-materials including food products.

Other organic heterogeneous materials that frequently appear in food systems consist of a mixture of water, air, organic products and ice. These multiphase systems typically exhibit susceptibility-broadened NMR lines and again require broad-line techniques together with good temperature control for reliable study. Three-dimensional Fourier transform imaging techniques using large switched gradients have permitted a study of the air/ice distribution as a function of temperature and the time evolution of such a system as well as void/porosity connectivity.

Inorganic porous materials such as natural rock, sandstones and artificial cementitious structures have somewhat similar characteristics when flooded with fluids. The porosity and spatial pore size distribution in reservoir rocks is the subject of an on-going study using NMR cryoporometry combined with MRI techniques [5]. Rocks which are of interest to the petroleum industry typically contain large numbers of para- and ferro-magnetic centres. Nmr imaging techniques on such samples at high magnetic fields are limited by line broadening due to fluid diffusion in the large internal susceptibility gradients. The NMR linewidth for such samples can typically be 1-10 kHz. Suitably large switched gradients combined with cryoporometric techniques can yield information about the spatial pore size distribution within such rock samples.

Fluid ingress into porous media is of wide interest and has often been a subject of MRI investigation. One of the most important technical areas of application is in the behaviour of water in construction materials such as cement and concrete.

Cement is notorious for its impurity content of metal ions that produce large local field variation with consequent broadening of the NMR lines of absorbed water. NMR STRAFI techniques have been applied to record concentration profiles as a function of ingress time in an attempt to understand the mechanisms of capillary imbibition in ordinary Portland cement [6]. The kinetics have been studied both experimentally and theoretically. The water profiles follow a $t^{1/2}$ law and thus a master curve using the Boltzmann transformation can be constructed. The distribution of pore sizes within the samples was also measured by NMR using the technique of cryoporometry and a prominent peak in this distribution was found at about 10 nm. A computer model for the pore structure was developed consisting of interconnected pores with a size distribution based on the cryoporometric results. Simulation of the water imbibition kinetics fitted to the detailed NMR data provide a useful demonstration of the physical insight that can be gained from a quantitative assessment of fluid transport in this complex but technologically important class of materials.

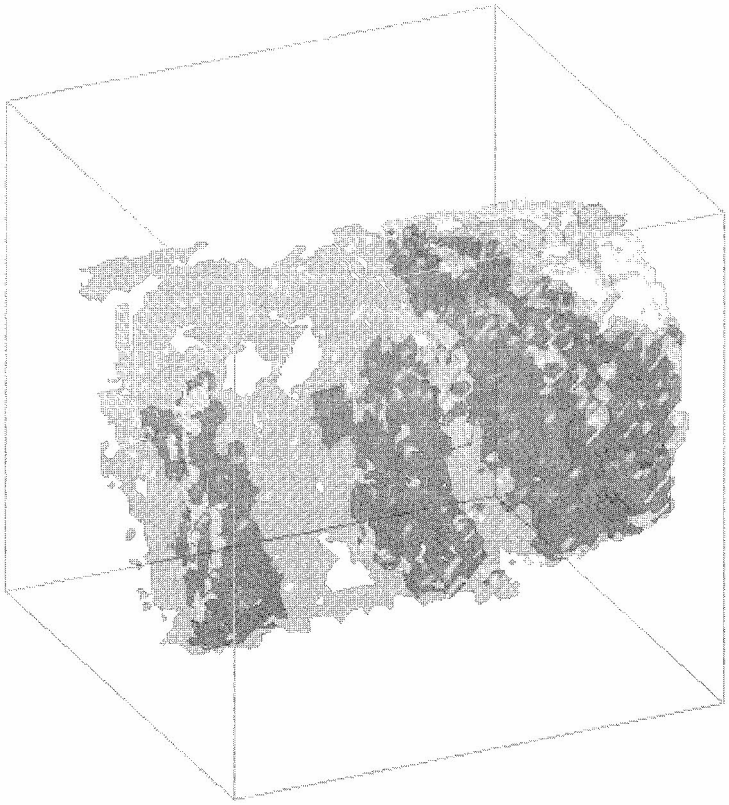

Fig. 1. 3D rendering of saturated sandstone core sample at 268K. Fluid in the large pores has frozen revealing the small pore stucture.

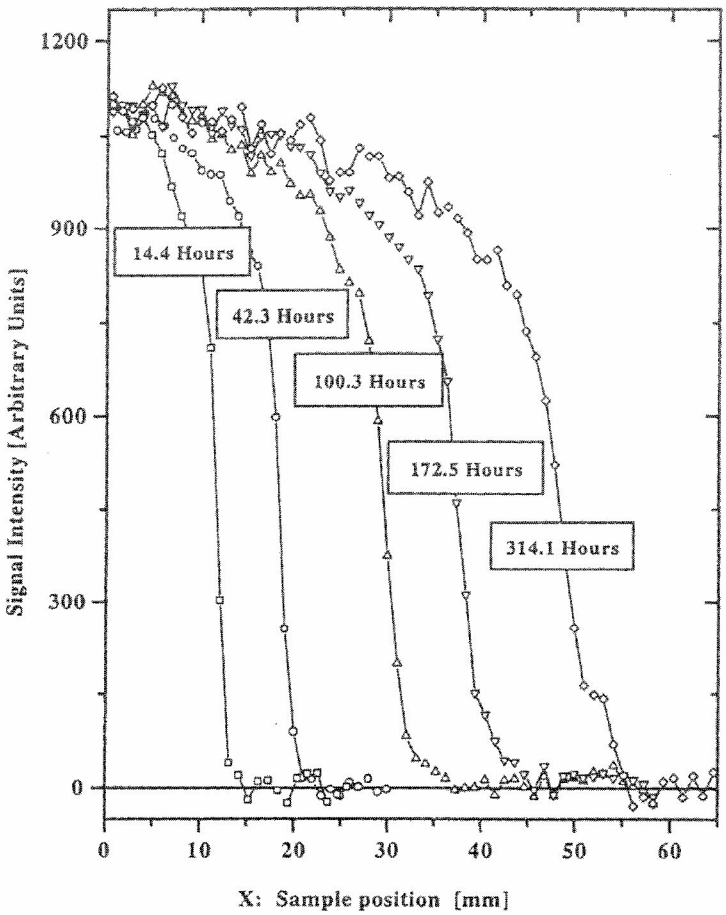

Fig. 2. Time-resolved 1D STRAFI images of water ingress into ordinary Portland cement.

The addition of pozzolanic binders and industrial waste products such as pulverised fuel ash are known to reduce the permeability of cement. The above experiments have been extended to a study of cement structure, using cryoporometry, and water penetration, by broad-line imaging in an attempt to understand the relationships between the changes in pore microstructures brought about in the cement as a result of additives and different water/cement ratios used in sample preparation and the transport of water. The NMR results demonstrate that the changes in permeability that can be produced in the method of preparation of cementitious materials can be related to the changes that are produced in the pore structure on a nano-metre scale.

Conclusion. Multiphase systems are common in materials science. Much can be learnt from an NMR/MRI study of their structure and dynamical behaviour but frequently broadline techniques must be adopted.

1. Mallett, M.J.D., Codd, S.L., Halse, M.R., Green, T.A.P., and Strange, J.H., *J. Magn. Reson. A* **119,** 105-110 (1996).
2. Samoilenko, A..,Artemov, A.,Yu, D. and Sibel'dina, L.A., *JETP*, **47**, 417-419 (1988).
3. Eidmann, G., Savelsberg, R. Blümler, P. and Blümich, B., *J. Magn. Reson. A* **122** 104-109 (1996).
4. Carlton, K.J., Halse M.R. and Strange, J.H., *J. Magn. Reson.* to be published.
5. Strange, J.H. and Webber, J.B.W., *Meas. Sci. Technol.* **8**, 551-561 (1997).
6. Leventis, A.,Verganelakis, D.A., Halse, M.R.,Webber, J.B.and Strange, J.H., *Transport in Porous Media* **1417**, 1-15 (1999).

L25

Relevant Aspects of Polymer and Cement Science: A *Stray-Field* Imaging Approach

Teresa G. Nunes

ICTPOL/IST, Departamento de Engenharia de Materiais, Lisboa, Portugal

Polymethylmethacrylate and related **polymers** are employed in the vast majority of clinical dental materials; for example, they are used as adhesion promoters of dentin to the final restorative material. The physical properties of visible-light cured adhesives depend on various parameters:

- the presence of unreacted methacrylate groups (UnG) in the final product, which has deleterious effects on the mechanical properties and dimensional stability and, consequently, is of considerable concern;
- polymerisation shrinkage (PS), which is also of critical importance [1] since it may cause, for instance, adhesive or cohesive failures, and is usually determined as *total volumetric change*, from dilatometric or density measurements; however, PS is highly anisotropic because light-cured systems contract towards the surface that is exposed to the light source;
- the influence of oxygen, a radical inhibitor; visible light penetrates better than UV and greater depths can be polymerised using longer times but the effect of oxygen must be taken into account.

Spatially resolved data on the photo polymerisation of the dentin/enamel bonding resin incorporated in the ALL-Bond 2 adhesive (Bisco) were obtained using ^{1}H stray-field magnetic resonance imaging (STRAFI-MRI) technique [2], which enables the observation of materials with a wide range of T_2s. Resin samples, in a cylindrical glass container (with 1 cm diameter and 0.4 cm height), not sealed, were irradiated from the top over periods of 2 s until a total of 60 s was reached.

Mono-exponential functions were fit to the experimental data obtained from different slices of the samples and the spatially resolved reaction rates were obtained. Slices close to the bottom of the sample polymerised about three times faster than slices close to the resin surface; the inhibitor effect of oxygen was clearly dominant, in comparison with the attenuation of the visible-light transmission. The PS along the cylinder axis was measured (~10%). The spatial distribution of UnG was obtained from 3D images (Figure).

The hydration of Portland **cement** pastes was studied by STRAFI-MR 1D Imaging and a spatial dependence of the kinetics was reported [*e.g.* 3]. In fact, the setting of the pastes depends on different parameters, like the initial water to cement ratio, R (w/w), or the particle size of the powder (G). For example, Portland cement of Type I with a particle size < 90 mμ has a compressive strength of 18 MPa, 2 days after the preparation of the paste, while a cement with a particle size < 45 mμ reaches a compressive strength of 36 MPa, after the same period of time, following the paste preparation. The influence of R, in the range 0.24-0.48, was achieved by STRAFI-MR 1D Imaging; the experimental data obtained from the pastes were fit to mono-exponential functions and the highest spatial variation of rate constants was obtained from the paste with R equal to 0.36 (a slice at the bottom of the container was found to hydrate about two times faster than a slice 5 mm distant). As an extension of these studies, results will be presented on the influence of G on the kinetics of the hydration of pastes with R equal to 0.4, obtained using the same technique and a similar protocol. Additionally, ^{2}H, with long-echo train acquisition [4], and ^{27}Al STRAFI one-slice observations will be presented on the hydration of the finest powdered cement.

In conclusion, STRAFI-MRI proved to be a very powerful technique to image rigid materials with strong magnetic susceptibility inhomogeneities.

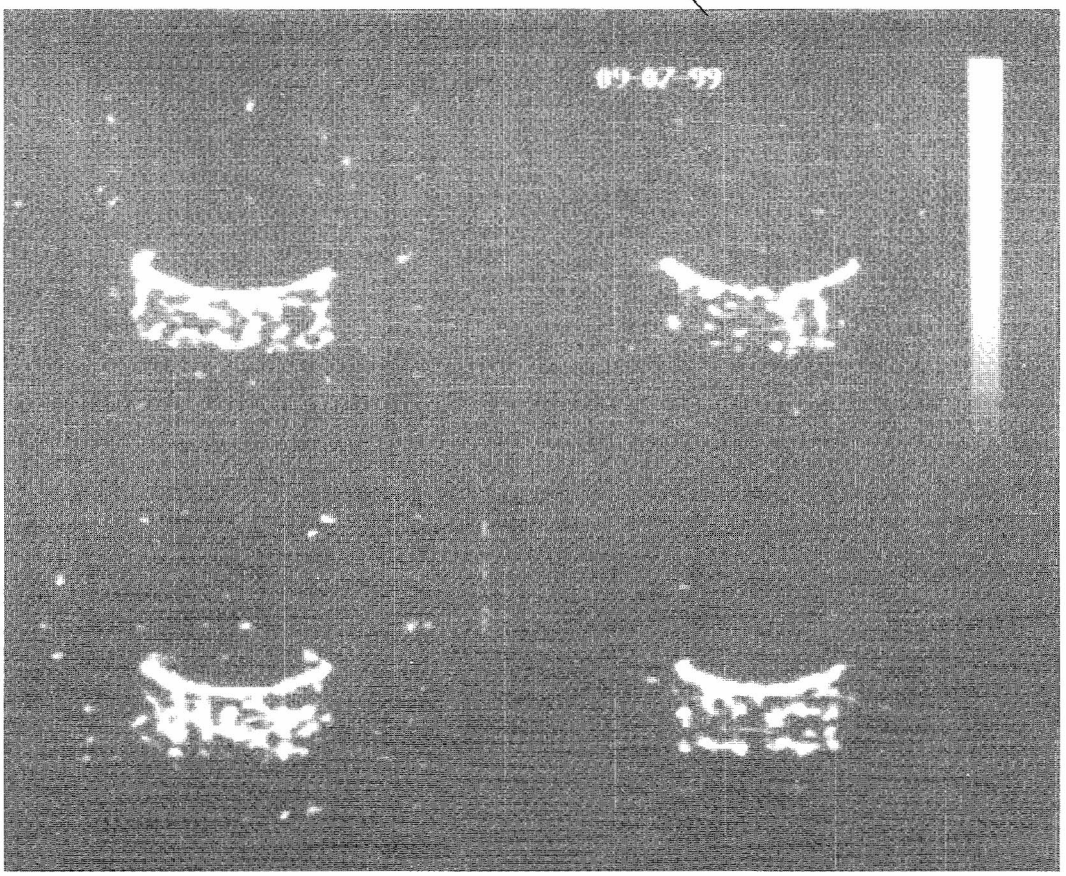

Figure. Four 2D slices, out of 128 slices obtained for the back-projection reconstruction of a 3D image, acquired from a light-cured resin (shear bond strength ~ 30 MPa). The spatial distribution of UnG is observed; in particular, a surface layer, with a thickness of about 500 mμ, is clearly detected.

Supported, in part, by the PRAXIS XXI program (PSAU/C/SAU/131/96).

References

1. Davidson C.L., in: "*Posterior Composite Resin Dental Restorative Materials*", Vanherle G., Smith D. C., (Eds.). Amsterdam: P. Szulc, pp. 61-5 (1985).
2. Samoilenko A.A., Artemov D.Yu and Sibeldina L.A., *JETP Lett.*, **47**, 417 (1988).
3. Nunes T., Bodart P. and Randall E.W., in: *"Spatially Resolved Magnetic Resonance: Methods, Materials, Medicine, Biology, Rheology, Geology, Ecology, Hardware"* P. Blumler, B. Blumich, R. Botto, E. Fukushima (Eds.), Wiley-VCH, 287-292 (1998); Nunes T., Bodart, P. and Randall, E.W., in: *"Nuclear Magnetic Resonance Spectroscopy of Cement-Based Materials"*, P. Colombet, A.-R. Grimmer, H. Zanni, P. Sozzani (Eds.), Springer, 411- 416 (1998).
4. Randall E.W., Nunes T. G., Guillot G. and Bodart P., *Solid State NMR* (in press).

L26

Restricted Water Self-Diffusion in Lung

Burkhard Geil**, Gernot Laicher*, **David C. Ailion***

*Department of Physics, University of Utah, 115 South 1400 East, Salt Lake City, UT 84112, USA
**Fachbereich Experimentelle Physik III, Universität Dortmund, Dortmund, Germany

Introduction

NMR has been a useful technique for studying diffusion. Typically, free unrestricted diffusion results in a Hahn echo decay time constant having an exponential dependence on the cube of the echo time or a stimulated echo decay time constant with an exponential dependence on the first power of the diffusion time. Furthermore, free diffusion is characterized by a mean squared displacement that increases linearly with time and a diffusion coefficient that is, accordingly, independent of time. Restricted diffusion, however, is characterized by a mean squared displacement that, at sufficiently long times, is independent of time and, hence, a diffusion coefficient that is time-dependent. Here we will describe the application of both pulsed and static magnetic field gradient techniques to determining the microscopic nature of water diffusion in lung.

The structure of lung tissue is very different from that of other organ tissues, notably due to the presence of large numbers of air-filled alveoli which significantly influence its NMR properties. These air-filled spaces distort the external magnetic field in the nearby lung tissue and give rise to substantial internal magnetic field gradients and corresponding inhomogeneous line-broadening [1]. Water self -diffusion across these internal gradients causes a rapid Hahn echo decay.

Direct measurements of the water self-diffusion coefficient in lung tissue using external magnetic field gradient (static and pulsed) methods have shown that diffusion in lung tissue results in spin-echo decays that deviate strongly from a single exponential decay [2, 3], which would be expected for normal free homogeneous diffusion. Such deviations from single-exponentiality are typically explained by heterogeneous diffusion (i.e., the presence of several different diffusion coefficients) and/or by restricted diffusion (i.e., a non-gaussian propagator due to the presence of impenetrable restricting barriers). Heterogeneous diffusion can be distinguished in principle from restricted diffusion by measuring the time dependence of the apparent diffusion coefficients. For purely free diffusion (either heterogeneous or homogeneous), there should be no time-dependence of the measured diffusion coefficients, whereas the apparent diffusion coefficients for restricted diffusion should be highly time-dependent. In particular, for diffusion times that are much shorter than the time required for the molecules to reach the restricting barriers, the diffusion coefficient is time-independent but, for times larger than the time required to reach these barriers, the apparent diffusion coefficient declines with a characteristic 1/t dependence, where t is the diffusion time [3]. Measurement of the time at which the diffusion coefficient changes from time-independent to time-dependent allows one to estimate the separation of the barriers and thus the effective size of the restricting region [3].

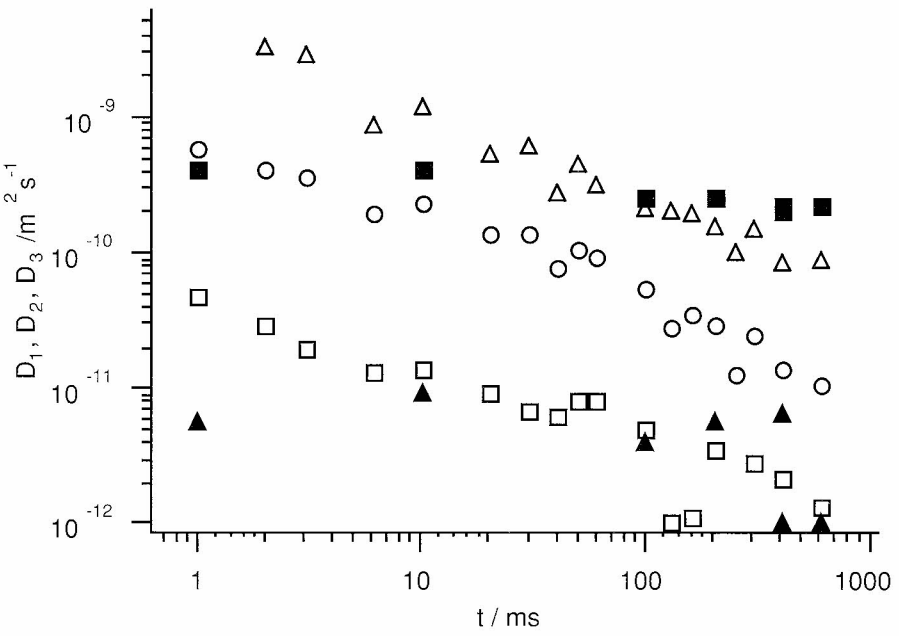

Fig. 1: Diffusion coefficients for normal rat lung (open symbols) and homogenized rat lung (filled symbols) vs diffusion time.

Methods

The high static gradient measurements were performed using a stimulated echo sequence in an anti-Helmholtz magnet, which provided magnetic field gradients of order 30 T/m [3]. Homogenization of the rat lungs was performed by grinding excised lungs in a Dounce homogenizer.

Results

Our measurements (Fig. 1) of the time dependence of the apparent diffusion coefficients in rat lung indicate that both diffusion heterogeneity and restrictions are present, the former even in the absence of air/tissue interfaces. This conclusion is supported by measurements of the time dependence of the diffusion coefficients in homogenized excised rat lung tissue over the same range in which the excised lung fragments exhibited the previously described crossover from free to

restricted behavior. We found that the diffusion coefficients now are independent of time and exhibit no crossover behavior. This implies that the homogenization procedure removes all restricting barriers, such as the cell walls and the alveolar structure, as expected for this procedure. The resulting echo decay is now purely biexponential and must be described by two diffusion coefficients. Thus, we can conclude that (1) diffusion in homogenized rat lung tissue appears to be heterogeneous and, (2) the restricting barriers (cell and/or alveolar walls) play a significant role in water diffusion in normal lung tissue. A comparison between homogenized and intact rat lung echo decays clearly shows differences which can be attributed to the presence of restricting barriers that are removed by the homogenization procedure.

On the other hand, for nonhomogenized rat lung we find that the echo decay depends strongly on the diffusion time. We have analyzed this time dependence by fitting the echo decay curves with a multiexponential (multiple apparent diffusion coefficients) decay and found that three components are necessary to fit the data (Figs.1 and 2). Each of these three magnetizations is characterized by a different diffusion coefficient whose time dependence can be measured separately. The apparent diffusion coefficient in the 1/t region is given by $D = \langle a^2 \rangle / 6t$, where a is of order of the size of the restricted space.

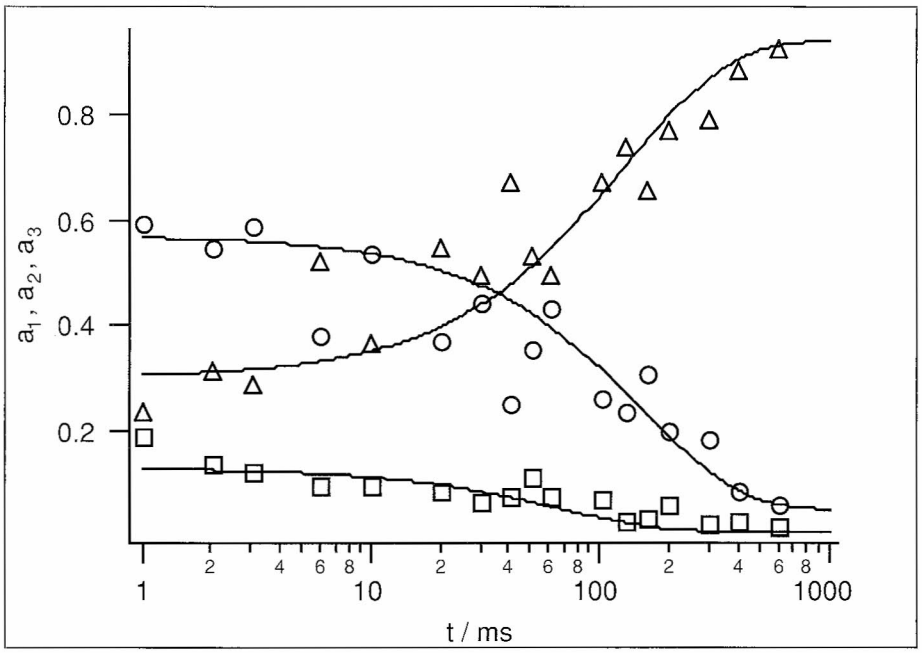

Fig. 2: Relative magnetization of the three components as a function of diffusion time.

Fig. 1 indicates that each of the three components corresponds to a restricting compartment with a different size. This is evident from the fact that, in the time regime where all components exhibit the 1/t dependence, the diffusion coefficients are different for all three components. In particular, the spins which appear to diffuse most slowly in the short time regime are undoubtedly restricted to the smallest compartments, whereas the most rapidly diffusing are restricted to the largest spatial compartment.

Another feature which we have observed is that the magnetizations associated with the three components depend on the diffusion time. Fig. 2 shows how the magnetization of one component increases with increasing diffusion time at the expense of another component. Such behavior indicates that exchange between these two components takes place.

Conclusions

We have shown that water diffusion in rat lung is heterogeneous and characterized by three components, each having a different diffusion coefficient. Furthermore, we have shown that the diffusion is restricted, with the more slowly diffusing water molecules confined to smaller restricting spaces. Homogenizing the lungs removes the barriers, and results in unrestricted but heterogeneous diffusion.

Acknowledgements

The authors would like to thank Prof. Dr. Franz Fujara for allowing us to use his high static gradient equipment in Dortmund, Prof. Antonio G. Cutillo (University of Utah) for useful discussions about the homogenization procedure, and Dr. Frank Wehner for providing us with rat lungs in Dortmund. One of the authors (B.G.) was supported by a Lynen Fellowship from the Alexander von Humboldt Stiftung.

References

[1] Ailion DC. Lung and Mediastinum: A discussion of the relevant NMR physics. In: *Encyclopedia of Nuclear Magnetic Resonance, Vol. 5*, Grant DM, Harris RK (Eds.), Wiley, Chichester, 1996; pp. 2867-2873.

[2] Laicher G, Ailion DC, Cutillo AG. Water self-diffusion measurements in excised rat lungs. *J. Magn. Reson.* B **111**: 243-253 (1996).

[3] Geil B, Ailion DC, Laicher G, Fujara F, Cutillo AG. Translational diffusion of water in lung tissue. In: *Spatially Resolved Magnetic Resonance*. Blümich B, Blümler B, Botto RE, Fukushima E. (Eds.), Wiley-VCH, Weinheim, 1998; pp. 323-335.

NMR Diffusion Coherence in Cells

Philip W. Kuchel

Department of Biochemistry, University of Sydney, New South Wales, 2006, Australia

NMR q-space plots derived from water diffusing in a suspension of erythrocytes display reproducible and characteristic coherence features ([1-3]; e.g., Fig. 1).

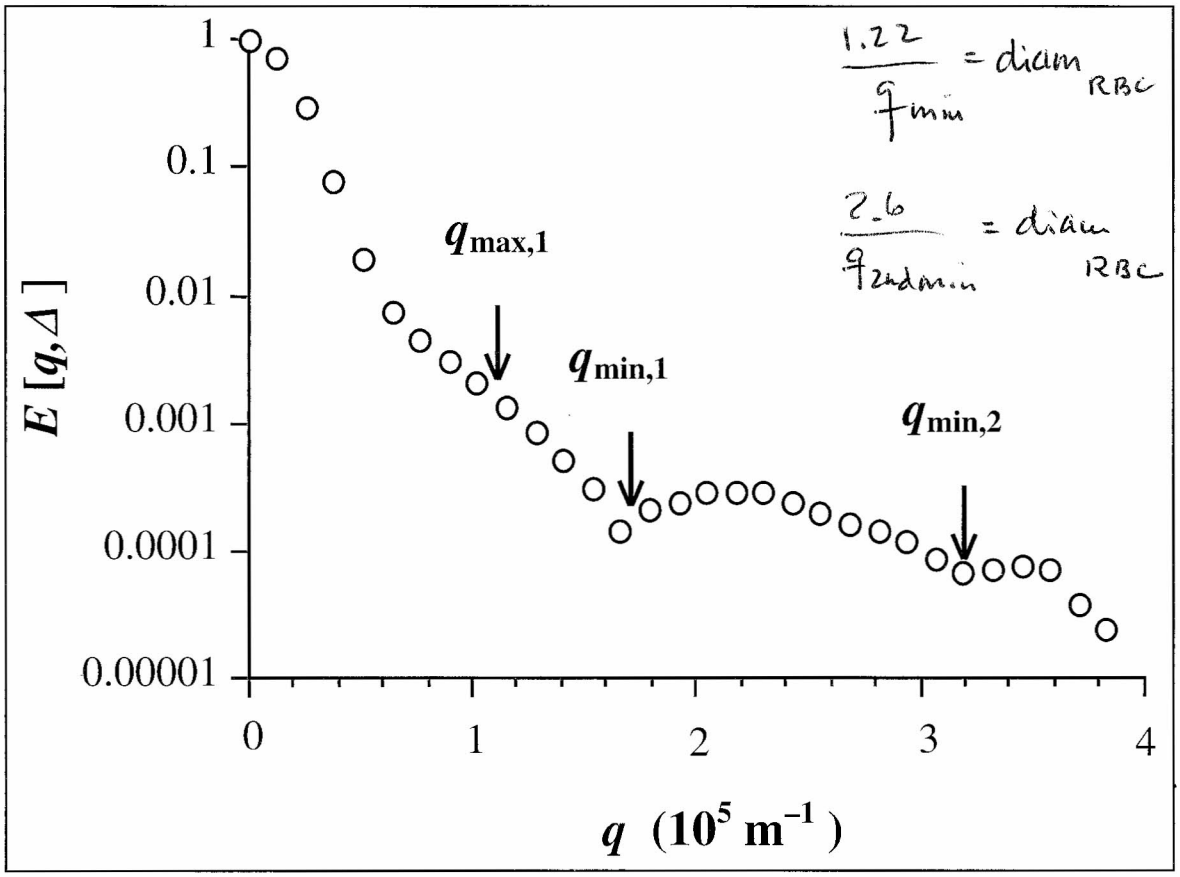

Fig. 1. ^{1}H NMR q-space plot of water in a suspension of fresh human red cells [3].

We determined which water populations, inside and outside the cells, give rise to the various features in these plots [3]. The experimental strategy was to use choline and choline phosphate which are virtually membrane impermeant on the time scale of the experiment. The former compound was incorporated into erythrocytes by a lysis-resealing method and the latter was simply added to the suspensions. Dimethyl sulfoxide (DMSO) readily but more slowly exchanges across the erythrocyte membranes than water and it also yielded q-space plots that were similar to those of water, but the differences were able to be accounted for on the basis of its slower membrane transport. Random walk simulations using a Monte Carlo procedure, together with a model of an array of biconcave discocytes, helped verify the interpretations of the assignment of the features of the plots to molecules diffusing in the two regions. Also, the simulations revealed how the presence or absence of transmembrane exchange affects the form of q-space plots.

Experiments were also conducted on cell suspensions that contained different shapes/forms of erythrocytes prepared by manipulating the conditions of the suspension medium, such as osmolality and pH, and altering metabolism to affect the ATP concentration [2]. Abnormal red cells from patients with hereditary stomatocytosis and megaloblastic anemia were also studied thus enabling assessment of the practical application of this 'new' technique. The results clearly showed that NMR diffusion-coherence is sensitive to small changes in the mean dimensions of the cells and that a 'characteristic' q-space plot/profile could be ascribed to each erythrocyte form. It was also found that the homogeneity of the cell shape and/or size is an important factor affecting the intensity of the diffusion-coherence peaks [2].

Under some circumstances the position of the coherence peaks will vary with the rate of molecular exchange across the membranes [4]. Thus, in a quest for a quantitative approach to the interpretation of such data we addressed the 'inverse problem' that entails the estimate of the permeability coefficient of membranes from q-space experiments. The developed theory provides predictions of q-space plots from molecules diffusing in a simple system of parallel semi-permeable membranes arranged with separations that alternate between two different values; this was designed to (loosely) mimic the intra- and extracellular compartments in a suspension of cells or a tissue. The development of the theory was facilitated by symbolic computation, and the analysis of synthetic data was shown to be achievable by the use of a three-layer back-propagation artificial neural network [4].

References

1. Kuchel, P. W., Coy, A. and Stilbs, P (1997) NMR "diffusion-diffraction" of water revealing alignment of erythrocytes in a magnetic field and their dimensions and membrane transport characteristics. *Magn. Reson. Med.* **37**, 637-643.
2. Torres, A. M., Michniewicz, R. J., Chapman, B. E., Young, G. A. R., and Kuchel, P. W. (1998) Characterisation of erythrocyte shapes and sizes by NMR diffusion-diffraction of water: correlations with electron micrographs. *Magn. Reson. Imag.* **16**, 423-434.
3. Torres, A. M., Taurins, A. T., Regan, D. G., Chapman, B. E., and Kuchel, P. W. (1999) Assignment of coherence features in NMR q-space plots to particular diffusion modes in erythrocyte suspensions. *J. Magn. Reson.* **138**, 135-143.
4. Kuchel, P. W., and Durrant, C. J. (1999) Permeability coefficients from NMR q-space data: models with unevenly spaced semi-permeable parallel membranes. *J. Magn. Reson.* in press.

L28

Aspects of EPR Imaging

Joost A. B. Lohman

Bruker UK Limited, Banner Lane, Coventry CV4 9GH, United Kingdom

Although EPR spectroscopy has never seen the wide range of applications that has made NMR spectroscopy the most powerful analytical tool to date, the study of free radicals can provide unique answers to many questions. With improvements in the versatility and the sensitivity of the experiments as is provided by developments such as pulsed FT EPR and instrumentation for W-Band spectroscopy, the technique is becoming ever more popular. The prospect of using imaging techniques to obtain spatially resolved spin density and EPR spectroscopic information is an exciting dimension that has been explored by a number of researchers in recent years.[1]

In this contribution, the principles of EPRI will be reviewed, with emphasis on instrument design. Particular attention will be given to the differences between EPRI and the more established technique of NMR imaging and their impact on the technology. The focus of the discussion will be the equipment needed for L-Band (1 GHz) EPRI* which is aimed at the study of relatively large and conductive objects such as biomedical and *in vivo* samples.

1. G.R. Eaton, S.S. Eaton and K. Ohno (Eds.), *EPR Imaging and In Vivo EPR*, CRC Press (1991).

* highest freq for in-vivo (400G)

Sample size

$T_2 \cong 1\,\mu s$

$L * \frac{di}{dt} \sim 10^5 V$ for grad switching.

3cm ? 30cm

$\lambda = \sqrt{\varepsilon^{-1}} \lambda_{vacuum}$

↑ dielectric constant

80 in water

Pulse excitation bandwidth of 300MHz or greater is needed.

No slice selection in CW → need to do full scans for each dimension.

birdcage loads less than resonator.

Time-Domain RF EPRI: Applications in Cancer Research

Murali C. Krishna, James B. Mitchell and Sankaran Subramanian

Radiation Biology Branch, National Cancer Institute,
NIH, Bethesda, MD 220892, USA

Introduction

Magnetic resonance imaging (MRI) is a powerful technique in diagnostic radiology used in delineating soft tissue morphology non-invasively to aid in the detection of pathological conditions in humans, utilizing tissue water protons as the endogenous NMR probes. Current efforts are being directed to augment MRI with functional imaging capabilities so as to gain physiological and pathophysiological information on the tissue or lesion being examined. Such capabilities will greatly enhance cancer detection capabilities by exploiting the putative metabolic differences between normal and malignant tissue. In addition to MRI, positron emission tomography (PET) and electron paramagnetic resonance imaging (EPRI) methods are being evaluated for such applications. EPRI is a magnetic resonance technique similar to NMR, but probes paramagnetic species, i.e., species containing unpaired electrons spins. By probing such species and their interactions with magnetic and radiofrequency fields, as in MRI, it is possible, in principle, to perform whole-body EPRI on living subjects including humans. However, the major limitation for the application of EPRI in human studies stems from the lack of endogenous paramagnetic probes in vivo at detectable levels . With the recent availability of non-toxic, water-soluble spin probes with desirable spectral properties for imaging, EPRI has become feasible for in vivo applications [1, 2]. Since the spectral features of the spin probes are extremely sensitive to conditions of the local environment, such as tissue pO_2, viscosity, etc.

Methods

Spectrometer. The spectrometer operates at a magnetic field of 10.0 mT, corresponding to a nominal EPR frequency of 300 MHz. RF pulses of 70 ns duration were generated by high-speed RF gates and delivered to the sample housed in the resonator after suitable amplification [3]. The spectral coverage afforded by these pulses was > 8 MHz. The transmit and receive arm were separated by a diplexor with an isolation of 30 dB. The induction signals centered around 300 MHz were mixed with another RF signal at 350 MHz. The intermediate frequency of 50 MHz was isolated by suitable band-pass filters and fed to the data acquisition system.

The sampler is capable of digitizing the induction signals at a rate of 1 GHz with 8-bit amplitude resolution [4]. High-speed summation hardware is integrated with the digitizer so that it is possible to sample and sum an FID of 2K points every 4 microseconds.

Resonator. An overcoupled parallel-coil resonator with a diameter of 25 mm and length of 50 mm was used in the EPRI experiments [5]. These dimensions were adequate for accommodating an experimental animal such as a mouse for imaging studies. The loaded Q of these resonators was adjusted to 25 by overcoupling to achieve the band width necessary for imaging studies. A resonator ring down time of 350 - 500 ns was noted for an input RF power of 80 W.

Spin probe. A tri-aryl methyl spin probe was used for EPRI. The spin probes are water soluble and have oxygen-dependent line widths ranging between 25 - 250 mG.

Magnet/gradient coils. The main magnetic field was provided by an electromagnet (30 cm id). The field homogeneity was found to be better than 10 ppm in the active volume of a 5-cm cube.

Gradients used for imaging experiments were provided by a shielded three-axis gradient coil system, capable of providing a maximum of 5 mT/m over a 5 cm diameter sphere with a uniformity of better than 1%.

Image reconstruction. The FIDs were treated with appropriate window functions and further processed with resolution enhancing filters. The FIDs were zero-filled up to 64K points and Fourier transformed. Image reconstruction was performed by filtered back-projection methods.

Results and Discussion

Results from phantom objects containing approximately 10^{17} spins of stable paramagnetic probes with single narrow EPR resonances provide three-dimensional spatial images with resolution better than 2 mm. When the spin probe was administered to mice, the spin probe accumulation was temporally observed in the thoracic, abdominal and pelvic regions. A three-dimensional image (from 144 projections) from a live mouse was collected in 5 minutes. With the aid of fiducial markers for orientation, it was found that the spin probe accumulation in organs such as liver, kidney and bladder.

Differences in the oxygen status between liver and kidney were observed with the EPR images obtained from mice administered with the spin probe by employing a convolution difference treatment of the time-domain signals prior to image reconstruction. The results from these studies suggest that, with the use of stable paramagnetic spin probes and time-domain RF EPR, it is possible to perform in vivo imaging on living animals and also to obtain important spatially resolved physiologic information.

Conclusion

The results obtained from this study indicate that *in vivo* time-domain EPRI at radiofrequencies is feasible with suitable spin probes and efficient data acquisition systems. The EPRI images provide spatially resolved physiological information such as pO_2. Such information, when coregistered with anatomic images, will greatly aid oxygen-dependent cancer therapies, such as radiation therapy of solid tumors.

10mT magnet

References

1. Murugesan, R., Cook, JA., Devasahayam, N., *et al.*, *Magn. Reson. Med.* **38**, 409-414 (1997).
2. Bourg, J., Krishna, M. C., Mitchell, J. B., *et al.*, *J. Magn. Reson.* **102**, 112-115 (1993).
3. Murugesan, R., Afeworki, M., Cook, J. A., *et al.*, *Rev. Sci. Instr.* **69**, 1869-1876 (1998).
4. Subramanian, S., Murugesan, R., Devasahayam, N., *et al.*, *J. Magn. Reson.* **137**, 379-388 (1999).
5. Devasahayam, N., Murugesan, R., Cook, J. A., *et al.*, *J. Magn. Reson.* (submitted).

200 - 1200MHz.

parameters		
10–100 μs	τ_p	4μs Hiso/ fast
0.3 – 1 μs	τ_{dead}	Q ~ 20
1 – 4 μs	T_2	

250MHz - 500MHz (8bit) digitizing rate

L30

Three-Dimensional Imaging of Small Animals Using Pulsed Radiofrequency EPR

Sankaran Subramanian, James B. Mitchell and Murali C. Krishna

Radiation Biology Branch, National Cancer Institute,
NIH, Bethesda, MD 220892, USA

Introduction

Magnetic resonance spectroscopy of the nuclei spin and that of the unpaired electron, namely NMR and EPR, were discovered more or less at the same time. NMR developed rapidly, in leaps and bounds, evolving from a physicist's tool for looking at nuclear moments, to a chemist's tool for elucidating molecular structure, to a multidimensional spectroscopic technique helping biochemists to unravel the complex three-dimensional structures of macromolecules, and most recently to a radiologist's tool for performing *in vivo* diagnostic and functional imaging of the human body and a microimaging tool for studying diffusion and related phenomena. While EPR spectroscopy has played a major role in the study of paramagnetic compounds, metals in enzymes, photosynthesis, radiation-induced free-radical reactions, etc., the development in the imaging arena has been rather slow. EPR imaging of live animals requires a sufficient concentration of free radicals in the tissue being examined, but in biological systems the concentration of endogenous free radicals is extremely low (mercifully so!), and even when they are present, the radicals are very short lived. In other words, unless stable, non-toxic free radicals are introduced exogenously into the animal there is nothing to image. An additional problem is that for historic and sensitivity reasons EPR experiments have, until recently, been carried out mostly at microwave frequencies, where the penetration of the electromagnetic radiation is less than one mm and, therefore, unsuitable for *in vivo* studies. The recent availability of stable non-toxic narrow-line EPR probes based on the triarylmethyl (trityl) radical [1] and the introduction of the L-band radiofrequency regime for EPR [2, 3] mean that useful functional *in vivo* EPR imaging can be done with small animals and, perhaps in the near future, on larger species as well. At the National Institutes of Health we have embarked on the design and development of *in vivo* imaging at RF frequencies using pulsed EPR. Our preliminary results are quite promising [4]. Here we present a description of our 300 MHz RF FT-EPR Spectrometer/Imager and some of our recent results in three-dimensional imaging of the mouse and some applications of time-domain imaging to obtain physiologic information. Since most EPR probes have line widths which depend on the partial pressure of oxygen, EPR imaging may have far reaching applications in the evaluation and monitoring of pO_2 *in vivo* and, therefore, prove quite useful for studying tumor oxygenation and hypoxia which are very important in oncology and radiation therapy.

Methods

Spectrometer. Pulsed RF EPR spectroscopy is a challenge in instrumentation. The spin-spin relaxation times T_2 of even narrow line probes such as the trityl radical, with imaging gradients of 5mT/m, is only 500 ns, and the FID decays into the noise level in about 2-3 µs. This necessitates the use of ultra-fast switches, fast-recovery preamplifiers, low-Q resonators and fast digitizers. Since we lose a considerable portion of the FID in the dead time, fast signal averaging is mandatory for achieving a good S/N ratio. Our pulsed spectrometer operates at 300 MHz in a single-channel mode. We use 90 le n in enin B_1 field of 1.5 G, which provides a uniform excitation bandwidth of ca. 8 MHz. Taking into account of insertion losses, this requires RF pulses of 80 Watts. To minimize the dead time and prevent excessive receiver pre-amplifier overload, we dampen the Q of our resonator to a value of 20 by overcoupling (and, if needed, with additional resistive damping). The actual conversion efficiency (from RF power to B_1 field) is, therefore, quite

500 Ms/s ADC 4 channels (ALTEC?) ← key

250K fids/sec (4K each)! **L30** phase cycle to reduce ringing.

low. With extremely fast GaAs FET switches, a home-made transmit/receive diplexer, and a fast recovery (50 ns) preamplifier, we have reduced the dead time down to ca. 400 ns. We detect our signals by mixing the induction signals with a local oscillator frequency of 350 MHz (derived from the same source as the transmit frequency to maintain phase coherence) so that the IF on resonance is at 50 MHz. With this high IF there is no need to deal with negative frequencies and, consequently, no need for quadrature detection and the attendent CYCLOPS phase cycling, making the spectrometer design quite simple. The dead time is still relatively long so that off-resonance signals are subject to a large first-order frequency-dependent phase rotation, and there is no simple way of correcting the spectra for pure absorption phase. Therefore, we work with the magnitude-mode spectrum after suitable weighting of the time-domain signals to give frequency-domain line shapes which are not too different from absorption-mode line shapes and which produce images of acceptable quality. In order to achieve rapid signal accumulation and high S/N under the conditions of a very short T_1, we use a custom-built signal averager with a sampling frequency of 1 GHz. The parallel architecture of the summation hardware allows 230,000 FIDs of 4K size to be summed in just 1 s, i.e., almost in real time.

Image data acquisition & processing. Since the FIDs decay within a few microseconds, we cannot use pulsed field gradients and slice selection as in MRI to perform direct Fourier imaging. The image data collection is, therefore, done under constant gradients using volume excitations, and the resulting projections are employed to construct 2D or 3D images using standard filtered back projection schemes, as used in X-ray CT, PET, or some MRI studies of rigid solids. The rotation of the gradients, the automation of data acquisition and subsequent image processing are done using a Silicon Graphics Indigo2 workstation with programs written in C++ and in Matlab®. The 3D image rendering is done using the program Voxelview® written for the Silicon Graphics computer. A 2D image with 18 projections can be acquired in 30 s while a 3D image with 144 projections can be obtained in under 4 min.

Results

We have performed all the imaging experiments on phantoms and animals (only mice) using exclusively the trityl radical which has a line width of ~200 mG without B_0 gradients. With the aid of surgically implanted fiducial markers containing the trityl radical, we have performed imaging of several mice, following *i.v.* administration of the trityl spin probe, and have obtained images of internal organs such as the liver, kidneys, bladder, etc. It was also possible to study changes in the signal intensity of individual liver lobes when they were subjected to ischemia and reperfusion, paving the way for a modality of EPR oxymetry and delineation of ischemic tissue. T_2* discrimination could be used to distinguish differences in oxygen partial pressure (pO_2), and we hope to use this method to interrogate tumor oxygenation status and hypoxia.

Conclusions

One can envisage applications of RF EPR spectroscopy and imaging for *in vivo* monitoring of the pharmacokinetics of exogenously introduced redox-sensitive free-radical probes such as nitroxides, for determining redox status and heterogeneity of tissue vasculature, for measuring pO_2 *in vivo*, and possibly, *in vivo* spin trapping of NO. Our recent results and possible future directions such as echo detection schemes will be discussed.

References

1. Golman K, *et al.*, *Acta. Radiol.* **39**, 10 (1998).
2. Kuppusamy P, *et al.*, *Proc. Natl. Acad. Sci. USA* **91**, 3388 (1994).
3. Murugesan R, *et al.*, *Rev. Sci. Instr.* **69**, 1869 (1998).
4. Murugesan R, *et al.*, *Magn. Reson. Med.* **38**, 409 (1997).

Sensitivity remains fairly constant as frequency comes down because of increase in _____ and reduction in penetration problems.

Nosense in QD because too much phase info is lost by the time the signal is recorded.

L31

In Vivo EPR Spectroscopy for Measuring Oxygen in Tissues and Other Clinically Relevant Applications

Harold M. Swartz

EPR Center for the Study of Viable Systems; Department of Radiology,
Dartmouth Medical School, Hanover, NH 03755

Introduction

While there are ample reasons for the development and use of in vivo EPR techniques for strictly experimental applications, there are also some very attractive potential clinical applications. In this presentation the rationale, status, and future prospects for clinical applications will be summarized.

Results and Discussion

The area with the most obvious immediate and effective clinical use appears to be oximetry, where EPR almost uniquely can make repeated accurate measures of pO_2 which can provide clinicians with information that can impact directly on diagnosis and therapy, especially for Oncology and Peripheral Vascular Disease. In this approach an oxygen-sensitive stable, particulate, paramagnetic material is placed at the site where the oxygen measurement is desired. It then can be queried as frequently as desired. In some tissues (e.g. CNS) the material remains responsive for periods of a year or more. It is also feasible to implant several different particles at distances of a few millimeters and then to resolve the oxygen-dependent spectra from all of them using magnetic field gradients to separate out the spectra and locate them anatomically.

A closely related area of potential widespread applications is the use of EPR to measure nitric oxide. Nitric oxide can be measured by use of dithiocarbamates and related substances, which bind the nitric oxide and form a stable characteristic paramagnetic material. While this approach is especially sensitive in biopsy samples that can be studied at optimal EPR frequencies, recent studies have shown the feasibility of obtaining useful data on nitric oxide in vivo.

Another area of potential extensive early applications is in pharmacology and pathophysiology where the unique capabilities of in vivo EPR to detect and characterize free radicals may be applied immediately to measure free radical intermediates from drugs and oxidative processes. Results in vivo have been obtained both with direct measurements of free radical intermediates of drugs and with "spin trapping" of more reactive free radicals. It is noteworthy that the latter studies have been recently extended to include the hydroxyl radical.

The sensitivity of EPR spectra of stable free radicals such as nitroxides to the immediate environment (e.g. pH, motion, charge) has already resulted in some very productive applications in pharmacology and these are likely to expand substantially in the near future. These again are parameters that are very difficult to measure in vivo with other techniques.

There are some challenging obstacles to clinical and experimental uses of EPR. These are especially the non-resonant loss of the microwave radiation in tissues and the presence of physiological motions. Another challenging area is the development of stable paramagnetic materials that can be used safely and effectively in human subjects. Finally, there are some developments that are required to make it physically convenient to carry out EPR measurements in large subjects such as people. Reasonable progress in all of these areas has been made and some measurements in human subjects are underway. The development of resonators appears to be an especially important aspect of the progress that is occurring.

Conclusion

There is a reasonable basis to conclude that *in vivo* EPR will emerge as an effective experimental *and* clinical tool early in the next millennium!

L32

NMR Micro-Imaging of Water Diffusion in the Human Eye Lens

J. M. Pope and B. A. Moffat

Centre For Medical and Health Physics, School of Physical Sciences,
Queensland University of Technology, GPO Box 2434, QLD, Australia, 4001

Introduction. The lens of the eye is a unique tissue. It is transparent, flexible and possesses a high refractive index. By changing its shape and refractive index distribution, the focal power of the eye is changed, (accommodation), enabling it to focus objects at varying distances. Most of the lens cells have no organelles which minimises light scattering. The cells also contain a high concentration (> 30%) of proteins (crystallins) and there is very little extra-cellular water, resulting in the high refractive index.

Lens fibre cells are not shed, but new cells are laid over existing cells, so the lens increases in size throughout life. Cells in the centre of the lens contain protein molecules (crystallins) that are as old as the individual. Transport of water, containing antioxidant species (such as glutathione), from the outer cortex of the lens to the lens nucleus is therefore vital for protecting and maintaining the structure of the crystallins, because the lens nucleus (being metabolically inactive) is unable to produce them. A deficiency in this transport may be responsible for the onset of eye conditions such as presbyopia (lens stiffening and loss of accommodation with age) and senile cataract. However very little is known about the details of the transport processes involved and the causes of both presbyopia and nuclear cataract as yet remain unclear. In this study, we have used NMR micro-imaging to observe age-related changes in both the kinetics of water transport in human eye lenses and the distribution of protein concentration that is responsible for variations in refractive index.

Methods. Human lenses obtained from the Queensland Eye Bank were imaged at 34.5 °C in artificial aqueous humour (AAH) containing nutrients and metabolites similar to those that are present *in vivo*. ^{1}H NMR imaging was performed on a Bruker MSL200 micro-imaging system using a 15-mm diameter 'birdcage' resonator and shielded gradient coils.

Results. Long-range transport of water (over time-scales of hours) was studied by replacement of H_2O based AAH with deuterium oxide (D_2O) based AAH. Spin-echo images were repeated at 20-minute intervals and the decrease in signal intensity from regions of interest in the lenses (corresponding to a decrease in concentration of H_2O within the lens) was recorded over a 24-hour period. A statistically significant correlation ($p < 0.001$) was found between the rate of NMR signal loss from the lens nuclei and increasing age of the lenses [1].

Short-range diffusion was studied using a modified pulsed field gradient spin echo (PFGSE) sequence to generate maps of the diffusion tensor for water (H_2O) diffusion in the lenses. The orientation of the principal axes and magnitude of the principal components for water diffusion within the lens were calculated based on the method of Coremans et al. [2]. A new approach to displaying diffusion ellipsoid results using a modified Matlab "quiver plot " has been developed which facilitates correlation of the results with the known lens morphology. The results show that the direction of most rapid diffusion is parallel to the axes of the lens fibre cells. Diffusion of water in the outer cortex of the lens is relatively rapid and highly anisotropic, while in the inner cortex of the lens, surrounding the nucleus, there appears to be an effective barrier to diffusion, consistent with the observations for long range diffusion described above.

Lens refractive index is known to be a linear function of crystallin concentration [3]. The water proton transverse (spin-spin) relaxation rate $R_2 = 1/T_2$ has previously been shown to correlate well

with protein concentration in solutions of bovine serum albumin [4]. T_2 was measured for lens protein homogenates using a standard Carr Purcell Meiboom Gill (CPMG) pulse sequence. An Abbe refractometer was used to measure the refractive index of the same homogenates as a function of protein concentration. Combining these measurements yielded a calibration for refractive index as a function of transverse relaxation rate R_2. Maps of transverse relaxation rate for intact human lenses were acquired using a modified CPMG pulse sequence and converted to maps of refractive index using this calibration. Initial results indicate that there are substantial changes in refractive index distribution as well as size and shape for human eye lenses as a function of age. There appears to be an increase in thickness of the anterior cortex region with age and the gradient of refractive index is higher in the posterior cortex than the anterior cortex.

Conclusions. The results show that as lenses age, there is a reduction in the rate at which water and presumably also water soluble low molecular weight metabolites, can enter the cells of the lens nucleus via the epithelium and cortex. A decrease in the rate of transport of water, nutrients and anti-oxidants (e.g. glutathione) would be expected to lead to progressive oxidative damage to lenses with age. This may ultimately contribute to crosslinking of crystallins, giving rise to stiffening of the lens in presbyopia and and precipitation of proteins in senile nuclear cataract.

Presbyopia occurs in almost all humans between the ages of 40 and 50 years. It is believed to arise from a decrease in lens power and elasticity with age. Paradoxically, the observed increase in lens thickness and curvature with age should, on its own, result in an *increase* in power. We are therefore currently engaged in modelling the observed age-dependent changes in lens shape and refractive index gradient to determine whether these can explain this 'lens paradox'. The possibility exists of extending these measurements to observe changes in lens shape and refractive index gradient during accommodation *in vivo*, using a clinical MR scanner.

References

[1] Moffat, B.A., Landman, K.A., Truscott, R.J.W., Sweeney M.H.J. and Pope, J.M., *Experimental Eye Research* (in press).

[2] Coremans, J., Luypaert, R., Verhelle, F., Stadnik, T., and Osteaux, M., *Magn. Reson. Imaging* **12**, 443-454 (1994).

[3] Pierscionek, B., Smith, G. and Augusteyn, R. C., *Vision Research* **27,** 1539-41 (1987)

[4] Hills, B. P., Takacs, S. F. and Belton, P. S., *Molecular Physics* **67,** 903-18 (1989).

Abstracts for the Scientific Session

Contributed Papers

Selected for Oral Presentation

O1

Probing Polymer Architecture by MRM

D. M. Gregory and **R. E. Botto**
Chemistry Division, Argonne National Laboratory, Argonne, IL 60439

Introduction

Time-resolved MRM investigations of a well-characterized suite of cross-linked polymers have yielded information on the dynamics of the solvent transport and mechanical relaxation of the networks. Network response parameters were then used to assess the macroscopic properties and cross-link densities of polymers with the degree of curing. We will discuss how this approach may be utilized to better define the thermodynamic relationships governing network relaxation and polymer architecture.

Results and Discussion

Imaging of Protonated Solvent. Time-resolved imaging of cyclohexane penetration into the polymers suggested anomalous swelling behavior. The data were fit to a generalized function, $x = k + v \bullet t^n$, where k = a constant and v = front velocity. For the suite of samples, the value calculated for exponent n ranged from 0.75 - 0.87, which implied the dynamics of swelling are intermediate between Fickian (n = 0.5) and case II (n = 1). Velocities of the solvent front correlated well cross-link density, where velocities increased with lower cross-link density. In diffusion-weighted images, pixel intensity of imbibed solvent was greatest just behind the solvent front. A direct correlation was found between intensity of pixels in the diffusion-weighted images and magnitude of the diffusion coefficients. Moreover, gradation in the diffusion coefficients was perceptible across the swollen samples. Because the diffusion coefficient is a measure of mean free path, this distance is short for solvent molecules near the solvent front and gradually increases with distance behind the front. This implies that the polymer network continues to expand well after free spaces have been filled with solvent.

Imaging in Deuterated Solvent. By acquiring proton images of the rubber samples during swelling in deuterated cyclohexane, we were able to observe changes in the polymer directly. T_2 maps created from the data show a gradation in T_2 values with the shortest T_2's occurring near the solvent front. This parameter reflects changes in polymer chain motion, i.e. the frequency of chain motion increases gradually from the solvent front. We also monitored the change in T_2 vs. time for an area of polymer at a constant distance from the outside edge of the sample. The data fit well to a simple exponential function. The 'rate' of change in T_2 for protons in the polymers was slower for samples with higher cross-link density. Final T_2 values showed the same trend; samples with higher cross-linking exhibited lower final T_2.

Relation to Mechanical Models. It is tempting to try to find analogies between the swelling process that we observe and the mechanical processes commonly measured in polymer systems. We draw analogy between changes in the motional correlation times of the network and strain relaxation in stress-strain experiments. In a stress-strain experiment, a constant mechanical stress is applied, and the strain required is measured. In a swelling experiment, a constant osmotic stress is exerted in the presence of solvent at and beyond the solvent front, and the segmental motion of the polymer chains is measured. In both cases, the strain decreases or relaxes over time. A simple Maxwell model predicts the relaxation rate is given by a single exponential function. As we have shown, network relaxation rates measured by T_2 and diffusion-weighted MRM decrease with higher cross-link density of the polymer network.

We have attempted to compute strain rates from solvent front velocities and network relaxation rates, assuming pure Newtonian viscous behavior. To a first-order approximation, the strain rate can be related to the osmotic stress, i.e., the chemical potential of the solvent in equilibrium with the polymer, by applying Flory-Rehner (F-R) theory, from which parameters such as the number averaged molecular weight between cross-links may be estimated.

Acknowledgments

This work was performed under the auspices of the Division of Chemical Sciences, Office of Basic Energy Sciences, U. S. Department of Energy under Contract No. W-31-109-ENG-38.

O2

The Dipolar Correlation Effect in Organized Liquids and Polymer Networks

F. Grinberg and R. Kimmich

Sektion Kernresonanzspektroskopie, Universität Ulm,
Albert-Einstein-Allee 11, 89069 Ulm, Germany

We used the dipolar-correlation effect [1, 2] (DCE) on the stimulated echo produced by the sequence of three 90° pulses in order to study ultraslow correlated molecular motions and ordering phenomena in various complex liquids such as liquid crystals, colloids and elastomers. The DCE as an echo attenuation mechanism in these systems originates from modulations of residual (unaveraged) dipolar couplings by ultraslow molecular motions with correlation times $>> 10^{-5}$ s. In liquid crystals, the DCE is proved to be indicative for orientational director fluctuations and the macroscopic order parameter. Experimental examples are given for some nematics and lyotropic mixtures.

In elastomers, the DCE is associated with ultraslow chain relaxation modes affected by topological constraints (intermolecular excluded-volume effects and chemical cross-links). Synthetic poly-(styrene-butadiene) elastomers and natural rubbers (NR) in dry and swollen states were studied. Both elastomers reveal a strong dependence of the DCE on the cross-link density. The quantitative parameter evaluated from attenuation curves was the mean squared fluctuation of the dipolar coupling constant, $<\delta\Omega_d^2>$. On this basis the DCE of dry and swollen rubber is suggested as a method for the determination of cross-link densities [3]. We also demonstrate "DCE-imaging" of natural rubber objects resulting in maps of $<\delta\Omega_d^2>$ which may be useful in materials science.

Acknowledgements

We thank Dr. E. Fischer, M. Garbarczyk, and M. Heidenreich for DCE experiments with rubber and Dr. W. Kuhn for fruitful discussions.

References

1. Kimmich, R. *NMR: Tomography, Diffusometry, Relaxometry*, Springer-Verlag, Heidelberg, 1997.
2. Grinberg, F. and Kimmich, R., *J. Chem. Phys.* **103**, 365 (1995).
3. Grinberg F., Garbarczyk M., Kimmich R., and Kuhn W., *J. Chem. Phys.*, submitted.

O3

In-Situ High-Temperature NMR Imaging Study of Coals

Koji Saito [a], Ikuo Komaki [a] and Kennichi Hasegawa [b]

[a] Nippon Steel Corporation, Advanced Technology Research Laboratories,
20-1 Shintomi Futtsu City, Chiba, 293-8511, JAPAN

[b] JEOL, Ltd.

Introduction

Thermally induced changes in coals are interest from the standpoints of both fundamental and applied research for iron-making process [1]. Furthermore, for very inhomogeneous coals, there is a fascination in the study about the influence of thermal dynamical changes. To monitor the dynamical changes in coals with temperature, an *in-situ* method must be used, because it is well-known that the properties of coals change dramatically in high temperature range (from 350 to 550 °C) [2]. A relatively new technique which is demonstrating great potential in the area of coal research is nuclear magnetic resonance imaging microscopy (NMR microimaging) [3]. However highly advanced technique and experimental setup are needed in the case of coals because of the line broadening effects due to the strong dipole-dipole interaction among protons with the rigid macromolecular network. In addition, the application of NMR microimaging to coal without solvent swelling method has so far been limited by typical low resolution and has just given unclear images, resulting from the influence of various magnetic in coals. Therefore, in this paper, we at first are demonstrating 3D-Single-Point-Imaging (SPI) which has shown to be successful for studying short relaxation time systems and which is free from distortions due to susceptibility variations for coals. And we have carried out the first systematic *in-situ* high-temperature NMR microimaging study of coals between 25 and 500 °C with our newly developed high temperature microimaging probe with systems in order to clarify the behavior of mobile component at high temperature in heterogeneous coal specimens[4].

Methods

The samples used in this study were Witbank coal and Goonyella coal. ^{1}H NMR images were recorded using a JEOL ⟨-400 NMR system (9.45 T) with microimaging accessory. Details of new hardware and probe that were designed, developed, and implemented to improve the reliability and performance are described elsewhere. *In-situ* 3D-SPI sequence was applied to observe the spatial change of the specimen at various temperatures. Two dimensional projection method in modified 3D-SPI sequence was used to reduce the measurement time. The time to echo was 80 ⌠sec, the recycle delay time was 10 ms, and the gradient strength was 79 G/cm for X axis and 94 G/cm for Y axis respectively. The data matrix size was 128 x 128, and the number of signals accumulated was 16. The data acquisition required about 8 min. The rate of heating was 3 °C/min. that is the same as that of the industrial coking process.

Results and Discussion

It is well-known that coals start to soften and melt at about 400 an d then, to cake and carbonize at more than 450 °C. In the case of Goonyella coal at 25 °C it was found that the distribution of mobile component was very heterogeneous like the distribution of *macerals* in the coal which was cut with the thickness of 100 ⌠m. The obtained images show that as the temperature became higher, the mobile component increased and its distribution became more homogeneous but remained heterogeneity. It means that coal starts to soften and melt, and then the existent rate of mobile component is increasing dramatically. It is very interesting that the softening and melting areas are moving from the one side to the other side in these images slightly like diffusion phenomenon. Therefore, it is likely that the stretching of the mobile component occurs since some immobile component changes into some mobile component by heating process. At the same time some mobile component parts which have good fluidity initially melts and moves with a slow diffusion to another areas. When the temperature was over 450 °C, the resolidification started ; the mobile component decreased and at last there was a few mobile parts in 475 °C because of the resolidification means that some mobile component converts to some immobile component and the carbonization means that the amount of proton in coal extremely decreases. On the other hand, it is surprised that there shows areas some unsoftened area which has low mobility corresponding to inert area, even at the maximum mobility temperature for Witbank coal. It is likely that low rank coals for coking like Witbank has some inert area which is difficult to soften, melt and move to another areas with diffusion at its maximum mobility temperature in its specimen.

Conclusion.

It is clear that *in-situ* variable-temperature NMR imaging method, which is based on Single-Point Imaging, is very powerful to investigate and clarify the thermal change of coal. Another interesting experiments for various coals are in progress with developing new imaging techniques in order to get information T_1 mapping.

Acknowledgement. We are grateful to Prof. Dr.B. Bluemich (RWTH-Aachen), Dr. P. Bluemler (RWTH-Aachen) and Dr. R.E. Botto (Argonne National Laboratory) for their helpful discussion and suggestions.

References

1. Scott, D.H. *Developments Affecting Metallurgical Uses of Coal ; IEACR*/74; IEA Coal Research: London, (1994)
2. Brown, H.R. and Waters, P.L. *Fuel* , **45**, 41 (1966)
3. French, D.C., Dieckman, S.L. and Botto, R.E. *Energy Fuels*, **7**, 90 (1993)
4. Saito, K., Komaki, I. and Hasegawa, K. *Fuel* 1999 (in press)

O4

High-Resolution 3D NMR Imaging of the Mouse Heart

Jan Ruff, Frank Wiesmann[#], Axel Haase

Physikalisches Institut and Medizinische Universitätsklinik[#], 97074 Würzburg

Introduction

In the recent years, it was shown that *In Vivo* NMR Imaging of the mouse heart is a reliable tool for functional cardiac studies in spite of the small size of the heart and its ultrafast heart rate [1,2]. The purpose of this work was to investigate high resolution imaging in three dimensions to depict microstructures and coronary arteries (ca. 160 µm diam.) of the mouse heart.

Methods

Mice with body mass less than 16 g were explored on a 7 T Bruker BIOSPEC spectrometer equipped with microscopy gradient system (maximum field strength 870 mT/m). During the experiment, the mouse was anesthetized with 1.5 vol% isoflurane and kept normothermic with a warming pad.

3D images were acquired with an echocardiogram triggered segmented FLASH sequence (8 phase-steps per R-R interval) [3]. Shortest possible echo time (1.5 ms) and repetition time (4.6 ms) were realized to reduce flow and motion artifacts. To retain the inflow contrast of fast FLASH sequences, a multiple thin slab (block thickness 3.2 mm) technique was employed [4]. Six to seven overlapping slabs were sufficient to acquire the entire heart within a total experiment time of less than 1 hour. Typical 4-8 averages led to sufficient signal-to-noise ratio. To damp signal of large structures, especially the myocardium, raw data were filtered with an gaussian high-pass filter.

Results

We obtained a nominal resolution of 100 µm in plane and 200 µm in the second phase direction. With a diastolic acquisition window of 37 ms we could acquire excellent heart images. Figure **a** illustrates a single short axis slice of the 3D data set: the aortic valve, the left coronary artery as well as the right coronary artery can be seen. Figure **b** represents a surface visualization of the heart and its coronary arteries.

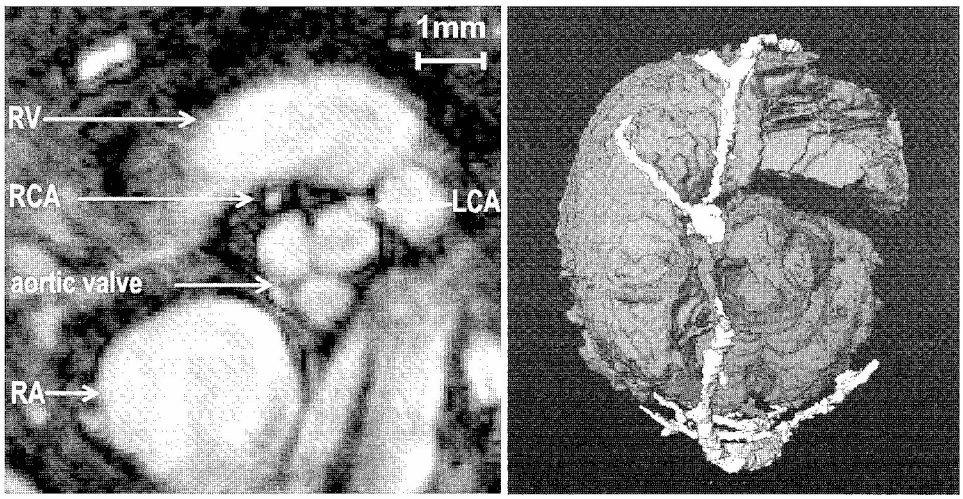

a) **b)**

a) Short axis view of aortic root (RA = right atrium, RV = right ventricle, LCA = left coronary artery, RCA = right coronary artery).

b) Surface visualization of left and right ventricle and coronary arteries.

Conclusion

Cardiac 3D high resolution NMR imaging of the living mouse offers high quality images reconstructable in any orientation to study anatomic microstructures such as coronary arteries or heart valves.

References

[1] Slawson SE *et al.*, *Magn. Reson. Med.* **39**, 980-987 (1998).
[2] Ruff J *et al.*, *Magn. Reson. Med.* **40,** 43-48 (1998).
[3] Atkinson DJ *et al*, *Radiology*, **178,** 357-360 (1991).
[4] Parker DL *et al. Magn. Reson. Med.* **17**, 434:451 (1991).

Magnetic Resonance Microscopy of Morphological Alterations in Mouse Tibiae Following Hindlimb Suspension

Vikas Gulani, John R. Gardner, Christopher P. Hess, Andrew G. Webb, M. Joan Dawson

University of Illinois, Urbana-Champaign, Illinois, USA

Introduction

A major concern for long-term spaceflight is the effect of micro-gravity conditions upon bone growth and existing bone structure. This micro-gravity environment has been shown to produce a calcium deficit and loss of bone mass in humans and rats (1). In order to study these phenomena, an animal model has been developed in which ground-based rat hindlimb-suspension (HS) produces changes in bone structure similar to those seen in spaceflight experiments (2-4). Recently, the Space Studies Board of the National Research Council's Committee on Space Biology and Medicine recommended the future use of mice over rats because they are much smaller (allowing greater numbers of experimental animals to be flown in space) and genetically homogenous strains, mutants, and transgenic animals are readily available (5).

The shortcomings of traditional microscopy (destructive, time-consuming, and costly) have led several investigators to explore the use of magnetic resonance (MR) microscopy to assess bone morphology. MR microscopy has been utilized to examine the structure of trabecular bone *in vitro* (6,7). Using a 400 MHz spectrometer equipped with a micro-imaging probe, the structure of trabecular bone from human radius has been imaged with an isotropic resolution of 78 x 78 x 78 μm (8). In this work, we applied MR microscopy to the study of the trabecular structure in the tibial metaphysis of HS mice.

Materials and Methods

Animal Model. The mice (FVB strain) used in these experiments were randomly assigned to either the control (C) (n=8) or HS (n=5) group. Mice underwent HS for four weeks as previously described (9). Following HS, the mice were sacrificed and the right tibiae were removed. Tibiae were prepared for analysis by extracting lipid in diethyl ether, after which tibiae were placed in water and the marrow evacuated under vacuum.

Imaging Protocol. All experiments were carried out on a Varian Unity-500 Spectrometer (500 MHz, 51 mm bore) equipped with a 5 mm Doty Scientific micro-imaging probe. A slab-selective 3-D spin-echo pulse sequence was used to image the excised bones (256 x 128 x 64 data matrix, 5 mm x 5 mm x 3.8 mm field of view, 3.6 mm slab, TR=2.3 s, TE=13 ms, NEX=2). The image resolution was 19.5 x 39 x 57 μm.

Image Analysis. After initial processing, the region containing the metaphysial trabecular bone of the proximal tibia was identified. Within each of the chosen slabs, a rectangular region of interest (ROI) enclosing the trabecular network was selected for analysis. Binary segmentation into bone and water phases was accomplished via analysis of the image intensity histogram. Four parameters were calculated from the segmented images: apparent trabecular bone volume fraction (BVF), apparent trabecular thickness (TbTh), apparent trabecular spacing (TbSp) and apparent trabecular number (TbN) (6). The two-tailed Student's *t*-test was used to compare the calculated parameters from C and HS animals.

Results and Discussion

The Figure depicts single inverted intensity images from the 3-D data sets collected for C (a) and HS (b) mice tibiae. The differences in trabecular bone morphology

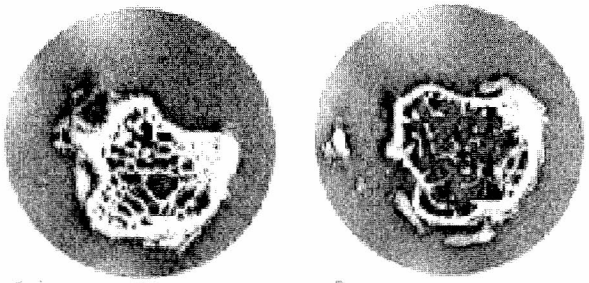

(a) (b)

following four weeks of HS were qualitatively apparent even without extensive analysis. Quantitative analysis confirmed the differences between C and HS bone. BVF was 48.5% lower in HS tibiae than observed for C tibiae (p=0.01). TbN was reduced by 40.0% (p<0.0005) and TbSp was increased by 86.8% (p<0.002) in HS tibiae. The changes in TbTh did not meet our criterion for statistical significance (p<0.05).

The voxel volume of approximately 4.33 x 10^4 μm^3 in this study represents an order of magnitude improvement over that previously reported for trabecular bone (8). Also, it is the first study to employ MR microscopy to examine HS rodents, and the first to quantify changes in bone structure for the relatively new murine model (9, 10) using any modality. The experiments clearly demonstrate that four weeks of HS produces a marked loss of trabecular bone volume and alterations in trabecular architecture comparable to those observed in rat spaceflight experiments (2-4) and that these changes can be successfully examined using MR microscopy.

References

1. Morey-Holton, et al., *Handbook of Physiology-Environmental Physiology*, Oxford University Press (1996).
2. Globus, et al., *Endocrinology* **114**:2264-2270 (1984).
3. Wronski TJ, et al., *Avait. Space. Environ. Med.* **58**:63-68
4. Vico L, et al., *Avait. Space Environ. Med.* **62**:26-31 (1987).
5. Space Science Board, NRC, *A strategy for research in space biology and medicine in the new century*, National Academy Press (1999).
6. Majumdar S, et al., *Bone* **17**:417-430 (1995).
7. Link TM, et al., *J. Bone Min. Res.* **13**:122-132 (1998).
8. Hwang SN, et al., *Med. Phys.* **24**:1255-1261 (1997).
9. McCarthy JJ, et al., *Am. J. Physiol.* **272**:R1552-R1561 (1997).
10. Simske SJ, et al., *J. Matter. Sci (Mater Med)* **2**:43-50 (1991).

Acknowledgments: Dr. Richard Tsika (University of Missouri), NIMH 5F30MH11041-05, PHS 5P41RR05964, DCCA 92-82144, NIH SIG 1S10RR06293, Servants United Foundation

O6

^{1}H Double-Quantum Filtered NMR Imaging of Rabbit Leg Joints

Kazuya Ikoma*, Yoshiteru Seo*, Hisatake Takamiya**, Yoshiaki Kusaka**

Department of Physiology* and Orthopaedic Surgery**, Kyoto Prefectural University of Medicine, Kyoto, Japan

Introduction

By conventional magnetic resonance imaging (MRI) technique, intact tendon, ligament, and meniscus can not be visualized directly. This is because these tissues have "bound water" which interact with collagen fibers, and thus have very short relaxation time. Therefore, we have used gadolinium diethylenetriaminopentaacetic acid (Gd-DTPA) as contrast agent and evaluated the anatomical shape, but we can not evaluate the degeneration and the regeneration of tendon, ligament, and meniscus.

Double quantum filtered (DQF) spectroscopy is the sensitive technique by which the anisotropic motion of quadrupolar nuclei can be revealed. The detection of anisotropic motion of water molecules has been reported by the ^{2}H DQF measurement of various biological tissues such as cartilage, tendon, skin, brain, and blood vessel. Recently, ^{1}H DQF spectroscopy in biological tissues has been detected, which depends on dipolar interaction of water molecules with ordered structures. Because ^{1}H DQF NMR technique allows selective acquisition of the water interacting with ordered structures, its application to imaging enables us direct visualization of invisible tissues with bound water such as tendon, ligament, and meniscus. Here we report ^{1}H DQF NMR signals and images of rabbit variable tissues.

Materials and Methods

Japanese white rabbits (2.5-3.0kg) were anesthetized with sodium pentobarbital (50mg/kg body weight i.p.). Achilles tendons, anterior cruciate ligaments, menisci, skin, and vastus lateralis muscles were isolated. A knee and a foot were cut off, and the knee joint was isolated with the joint capsule of the knee. All tissues without meniscus and skin were positioned with its long axis parallel to the magnetic field. Meniscus was positioned with its articular surface vertical to the magnetic field. NMR measurements and H-1 imaging were carried out on AMX-300wb Bruker NMR spectrometer (7.05 T) with 10 mm or 25 mm H-1 RF coil. ^{1}H DQF spectra were measured using the conventional DQF pulse sequence. In the DQF NMR imaging, the slice selective gradients were applied with the first 90° pulse. The phase and the frequency encoding gradients were applied after the last 90° pulse. All the examinations were done at 25°C.

Results and Discussion

We have measured joint tissues by changing the creation time, and found that all the tissues can be characterized by using creation time dependency of the ^{1}H DQF signal intensities. The difference of the creation time of each tissues comes from the degree of the structural anisotropy of the collagen fibers. Therefore, ^{1}H DQF NMR imaging of the rabbit foot and knee joint was measured by changing the creation time. As a control, imaging of the rabbit foot was measured by the gradient field echo pulse sequence (GE, TR 500 ms, TE 4.4 ms, Flip angle 22.5°). Tendons, ligaments, and bones were demonstrated very low signal intensity compared to the surrounding tissues. Muscles and subcutaneous tissues were depicted as areas as highlighted intensity. In the ^{1}H DQF image, at the creation time of 0.4 ms, the extensor digitorum superficialis tendon (EDST), the flexor digitorum profundus tendon (FDPT), and the flexor digitorum superficialis tendon (FDST), were depicted as areas as the highest signal intensity. Signals from the other tissues including bone, skin, and subcutaneous tissue were not detected on the ^{1}H DQF NMR image. When the creation time was 0.6 ms, signals from tendon tissues were slightly decreased, but signals from intermetatarsal ligaments, subcutaneous tissue, and skin were detected.

Thus this ^{1}H DQF imaging technique was able to visualize selectively invisible tissues such as tendon, ligament, and meniscus by using creation time dependency of the ^{1}H DQF signal intensities. The rapture and defect of tendon, ligament, and meniscus would be detected more easily by using this imaging technique. Moreover, the creation time dependency of the ^{1}H DQF signal intensities strongly related the ordered structure. We could evaluate the degeneration and the regeneration of tendon, ligament, and meniscus.

Conclusion

We visualized joints of rabbit by using ^{1}H DQF NMR imaging. We could visualize intact tendon, ligament, and meniscus which could not be visualized directly thus far. This technique would be the new technique by which we could use for the evaluation of the degeneration and the regeneration of these tissues.

References

1. L. Tsoref et al. *Magn. Reson. Med.* **39**, 11 (1998).
2. L. Tsoref et al. *Magn. Reson. Med.* **40**, 720 (1998).

O7

Healing Process of Ruptured Achilles Tendon Assessed by ^{1}H Double-Quantum Filtered MRI

Yoshiteru Seo[1], Kazuya Ikoma,[1] Hisatake Takamiya[2], Yoshiaki Kusaka[2], Liat Tsoref [3], Uzi Eliav[4], Hadassah Shinar[4], Gil Navon[4]

Departments of [1]Physiology and [2]Orthopedic Surgery,
Kyoto Prefectural University of Medicine, Kyoto, Japan,

[3]Schools of Physics and [4]Chemistry, Tel Aviv University, Tel Aviv, Israel

Introduction. The rupture of Achilles tendon is a very common incident in the daily and sports activities. Rehabilitation lasts at least several months and, in some cases, even more than a year. Unfortunately, there is a lack of objective scale of the tendon's chronic phase of healing since standard MRI techniques and ultrasonography give very little information. We have recently demonstrated that ^{1}H double quantum filtered (DQF) spectroscopy (1) as well as MRI (2) is a sensitive method for monitoring water molecules associated with ordered structures. We have applied DQF MRS and MRI techniques to ruptured Achilles tendon and have detected changes in order structure of water during healing process of the Achilles tendon.

Materials and Methods. The right Achilles tendon of male Japanese white rabbits (2.5 Kg) was severed sharply and transversely 1cm above its calcaneal insertion (tenotomy). The tendon was dissected under deep anesthesia, and was inserted in an NMR tube and the longitudinal axis of the tendon was aligned parallel to the static magnetic field. ^{1}H DQF spectra were obtained with a conventional pulse sequence and were measured as a function of the creation time, τ. DQF images were obtained according to an established technique (2) with the slice selection. All experiments were done at 25^{0}C.

Results and Discussion. The ^{1}H DQF spectra of the regenerated part of the Achilles tendons were measured as a function of the creation time. For the intact Achilles tendon, a maximal signal is obtained at τ of 0.4 ms. Three weeks after the tenotomy, the DQF signal was quite small and τ_{max} was 1.6 ms. The value of τ_{max} shortened gradually from 6 to 18 weeks after the tenotomy. Even 18 weeks after the tenotomy, the DQF signal intensity was a half of the intact tendon and τ_{max} was significant longer (0.7 ms) than the intact tendon.

Healing process was monitored by the conventional gradient echo (GE) imaging and DQF imaging. In the GE imaging, regenerated part of the tendon enlarged and highlighted at 3 weeks, then reducing its size and brightness. Thirteen weeks after tenotomy, the GE imaging become quite similar to the intact tendon. In the DQF imaging at τ of 0.4 ms, intact tendons were highlighted. three weeks after the tenotomy, no significant signal was detected in the regenerated part of the tendon. Eighteen weeks after the tenotomy, the regenerated part of the Achilles tendon and a thin layer of the subcutaneous tissue were also depicted at τ of 0.4 ms. In the DQF imaging at τ of 1 ms, the regenerated Achilles tendon was depicted as highlighted while the intact tendons were not observed. Even the longer creation time (2.0 ms), a part of the regenerated Achilles tendon gave the positive signal. These results suggest that regenerated part of the tendon consists of macroscopically inhomogeneous tissues.

Conclusions. ^{1}H DQF NMR and DQF MRI can be used to follow the progressive alignment and organization of the collagen fibrils accompanying the healing process of Achilles tendon. Therefore, ^{1}H DQF imaging is a very promising sensitive technique for examining structural disorders in tendons in vivo.

References

1. L. Tsoref et al. *MRM* **39**,11,1998.
2. L. Tsoref et al. *MRM* **40**,720,1998.

O8

Recent Progress in NMR Microscopy using B_1 Gradients

François Humbert [1], Bernard Diter [2], Michel Valtier [2],
Alain Retournard [2] and Daniel Canet [2]

[1] LCPE, UMR 9992, CNRS, Université Henri Poincaré, Nancy I
405, rue de Vandoeuvre, 54600 Villers-lès-Nancy, France
[2] Laboratoire de Méthodologie RMN, UPRESA 7042
Université H. Poincaré, B.P. 239, Vandoeuvre-lès-Nancy Cedex, France

Twenty years after the pioneering work of Hoult (1) who introduced the idea of spatial encoding using a radio-frequency field gradient (B_1 gradient), what is the current status of the B_1 gradients NMR microscopy?

We report some progress made in this field over the last three years. Undeniably, the major technical advance, which has opened new prospects, has been the development of probes delivering relatively large constant B_1 gradients, up to 100 G/cm, (2) and operating at frequencies ranging from 10 to 300 MHz. At first, this advance enabled us to achieve in microimaging an in-plane spatial resolution in the order of a few microns (2). Using these new probes combined with different methodological refinements, the range of measurable diffusion coefficients has significantly been extended (3). The study of numerous types of diffusion processes ranging from rapid diffusion in the gas phase (1 cm^2/s) to very slow diffusion (8 10^{-9} cm^2/s) in e.g. surfactants systems can be considered. Moreover, a whole array of image contrast schemes is now available. In particular, high quality maps of longitudinal relaxation time T_1 (4) and of diffusion coefficient (5, 6) can be obtained. A few examples of application both in the materials science and in biology illustrate these different features. Of course, this technique presents limitations and some difficulties still have to be overcome. However, the presented results, and especially those concerning the restricted diffusion at interfaces liquid-solid, prove that the B_1 gradients technique certainly represents more than a simple alternative to the conventional technique using B_0 gradients because of its key advantage which is its quasi-immunity to background gradients.

References

1. Hoult D. I., *J. Magn. Reson.* **33**, 183 (1979).
2. Humbert F., Diter B., and Canet D., *J. Magn. Reson.* **A123**, 242 (1996).
3. Humbert F., Valtier M., Retournard A. and Canet D., *J. Magn. Reson.* **134**, 245 1998).
4. Humbert F., Collenne E., Valtier M., and Canet D., *J. Magn. Reson.* **138**, 164 (1999).
5. Humbert F., Valtier M., and Canet D., *Chem. Phys. Lett.* **302,** 1 (1999).
6. Valtier M., Humbert F., and Canet D., *J. Magn. Reson.* in press (1999).

O9

Quantifying periodic cyclic motion by oscillating gradients in MRI

Gerhard Fink, Andrea Schwaiger, Bernhard Blümich
Institute for Technical and Macromolecular Chemistry, RWTH Aachen
Worringer Weg 1, 52056 Aachen, Germany

The elastic properties of soft matter can be probed by mapping propagating waves [1,2]. By exploiting cyclic periodic motion more sensitivity towards small displacements is obtained. A spin warp technique has been used to acquire 2D projections of propagating waves in a phantom. Application of an oscillating stress on the phantom results in propagating waves that can be visualized by introducing synchronous oscillating gradients into the imaging pulse sequence [3]. The phantom consists of a gelatine (7% m/m). A spiral coil incorporated into the gel starts vibrating when driven in the B_0 field by an alternating current. By triggering the nmr experiment to the excitation phase the same phase is recovered for a given voxel in successive scans. Any spin moving synchronous and colinearly with the oscillating gradients accumulates a phase shift relative to the static spins (see eq. 1), and the resulting total signal amplitude obtained after a two-dimensional Fourier transformation will diminish. Regions of motion are recognised in the projection by a reduced signal per voxel. Applying the oscillating gradients symmetrically in the dephasing and in the rephasing period of the spin echo sequence corrects for gradient imperfections. Furthermore it filters out effects of even harmonics of motion. The resulting effect of the interaction between gradients and oscillating spins can readily be calculated [4]. Assuming sinusoidal excitation and gradients at the given frequency the resulting phase of the signal Φ is given by equation (1).

$$\Phi = \frac{1}{2}\gamma\, G_{oscil}\, \xi \cos(k\,x + \phi)\, n\, t_{period} \qquad (1)$$

A different gradient shape will change the geometric factor (here ½). Extending the total encoding time to n periods of duration t_{period} will result in an enhanced sensitivity for cyclic motion. Furthermore the terms for amplitude $\xi\, cos(k\, x0+\phi)$ and gradient $n\, t_{period}\, G_{oscil}$ (proportional to a k-space variable) in equation (1) can be interpreted as Fourier pairs. Carrying out the experiment in a 3d manner by stepping the amplitude of the oscillating gradient will encode the modulated amplitude of motion $\xi(x) = \xi\, cos(k\, x0+\phi)$. After a 3D Fourier transformation the signal produced by static spins is concentrated at amplitude zero and the amplitude is determined on an absolute scale. Figure 1 shows a slice of the 3D data set representing amplitude $\xi(x)$ versus x direction. It reveals the fast damping of the wave travelling into the phantom. The grey scale marks the number of spins involved in the motion of a given amplitude. The low signal intensity at the edges of the image is due to the in homogeneous excitation of the birdcage resonator. Extracting the most abundant amplitude for each position in the sample results in a pure amplitude representation of the wave. Here the spin density is no longer involved and reflections at the sample boundaries become clearly visible.

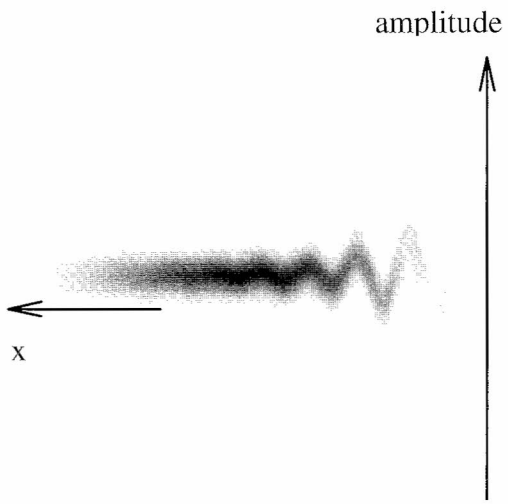

Fig. 1. Oscillation amplitude monitored by ^{1}H nmr imaging along the direction of wave propagation - The field of view is 7 cm in x direction and 200 μm in amplitude direction.

References

[1] Muthupillai R., *et al.*, Magnetic Resonance Imaging of Transverse Acoustic Strain Waves *Magn. Reson. Med.* **36**, 266-274 (1996).

[2] Muthupillai R., *et al.*, Magnetic Resonance Elastography by Direct Visualization of Propagating Acoustic Strain Waves *Science* **269**, 1854-1857 (1995).

[3] Cottrell S.P., *et al.*, *Meas. Sci. Technol.* **1**, 624 (1990).

[4] Lewa C.J., Elasto-Magnetic Resonance Spectroscopy *Europhysics Letters* **35**, 73-76 (1996).

[5] Chenevert T.L., *et al.*, Elasticity Reconstructive Imaging by Means of Stimulated Echo MRI *Magn. Reson. Med.* **39**, 482-490 (1998).

O10

Proton Relaxometry as Tool for the Characterization of Superparamagnetic Nanosystems

A. Roch [1], A. Ouakssim [1], R. N. Muller [1], P. Gillis [2]

[1] NMR Laboratory, Organic Chemistry Department

[2] Biological Physics, University of Mons-Hainaut, B-7000 Belgium

Introduction. Superparamagnetic colloids are suspensions of nanocrystals (r<10nm) made of single ferromagnetic domains. The field of applications of these materials is constantly increasing. In medicine, they are used as therapeutic agents in the context of hyperthermia[1] as well as contrast agents for Magnetic Resonance Imaging (MRI)[2]. Evaluating and understanding the performances of these magnetic nanomaterials as contrast agent for MRI was made possible by establishing a theory of the magnetic interactions of superparamagnetic compounds with water protons[3]. This new theory allows to understand the main characteristics of the NMRD profiles (i.e. the field dependence of the proton relaxation rate) and provides information about the superparamagnetic crystals namely their average radius r, their specific magnetization M_s, their Néel relaxation time τ_N and the magnitude of the anisotropy energy Ea.

Theory. Curie relaxation[4] plays a central role in our theory[3] ; it is based on the existence of two different time scales in the problem, allowing to consider separately the effect of water diffusion amongst the field inhomogeneities created by the mean magnetic moment of the magnetic particle, and the effect of the fluctuations of the magnetic moment itself. This separation accounts quite well for the high field part of the NMRD profiles ($B_o > 0.02$ T).

However, the NMRD profiles show a slight low field dispersion (below 1 MHz) for so-called Ultra Small Particles of Iron Oxide (USPIO, with a diameter smaller than 15 nm for magnetite crystals), a dispersion which completely disappears for relatively larger particles (Small Particles of Iron Oxide, SPIO). This difference can only be understood thanks to the crystal's anisotropy energy. The anisotropy field forces the particle magnetic moment to align on so-called axes of easy magnetization ; when anisotropy energy is large compared with thermal energy, it even locks the moment on one of the easy directions, possibly preventing it from precessing around the external field. The fluctuations are then due to the magnetic moment flipping from one easy direction to another, and they are characterized by the Néel correlation time. Accounting for the anisotropy energy implies to substitute for the unique electron transition frequency (characteristic of the Zeeman interaction) a wide transition frequency distribution, which generally peaks on values close to the highest frequency within this distribution. Furthermore, the thermodynamic probability of occupation of the crystal magnetic states are also strongly dependent on the anisotropy energy.

Results and Discussion. Our theoretical predictions match perfectly the NMRD profiles of colloidal suspensions of magnetite (Fe_3O_4) coated with dextran, and give:

the average size (r): at high magnetic field, the inflection point corresponds to the condition $\omega_I.\tau_D \sim 1$ with $\tau_D = r^2/D$ where r and D are the average size of the superparamagnetic crystals and the relative diffusion coefficient, respectively.

the Néel relaxation time (τ_N): the relaxation rate at very low field R_0 is proportional to a « zero magnetic field » correlation time. If $\tau_N << \tau_D$, τ_{CO} can be assimilated to τ_N and thus, R_0 allows to determine the value of τ_N.

the specific magnetization (Ms): using the value of τ_N and τ_D previously given and the maximum of the relaxation rate R_{max}, M_s can be obtained from the equation $M_s \sim C.(R_{max}/\tau_C)^{1/2}$ where C is a constant and τ_C , the global correlation time depends on τ_N and τ_D.

the crystal anisotropy energy (Ea): the absence or but very small dispersion at low field means a very high anisotropy energy. To verify this assumption, cobalt ferrites with a high anisotropy energy were synthesized. The low field dispersion observed for very small magnetite crystals disappears for those Co doped ferrite crystals of similar size which confirms our theoretical approach[5].

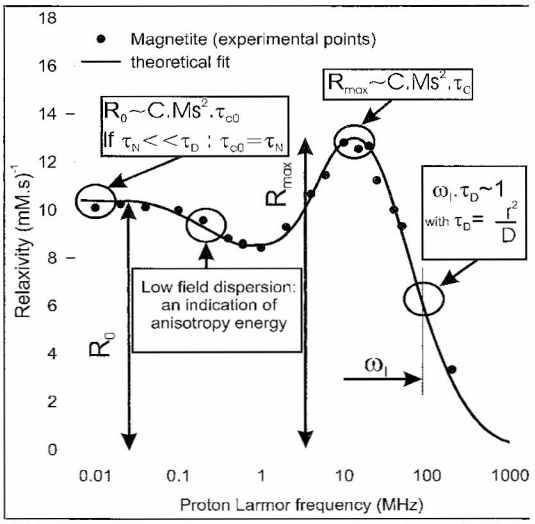

NMRD profile of magnetite particles in colloidal solution, the parameters given by the fitting are r=4.4nm, $M_s = 2.07\ 10^5$ A.m^{-1}, $\tau_N \sim 10^{-8}$s.

It is worth stressing that all these parameters can be precisely determined from the analysis of NMRD profiles as long as the size dispersion of the crystals is very small. Simplified analytical expressions for the NMRD profiles, in very good agreement with these theoretical predictions, were used[3] in order to avoid the very long numerical calculation required by the full theory.

1. Hilger I., Andra W., Bahring R., Daum A., Kaiser W.A. *Invest. Radiol.* **32**: 705-712 (1997).
2. Muller R.N., *Encyclopedia of NMR*, John Wiley, New York. 1438-1444 (1996).
3. Roch A, Muller RN, Gillis P, *J. Chem. Phys.* **110**: 5403-5411 (1999).
4. Gueron M, *J. Magn. Reson.* **19**: 58-66 (1975).
5. Roch A, Gillis P, Ouakssim A, Muller RN, *J. Magnetism and Magnetic Materials* **201**(1-3): 77-79 (1999).

O11

Imaging the Long-Range Dipolar Field in Structured Liquid State Samples

R. Bowtell, S. Gutteridge and C. Ramanathan

Magnetic Resonance Centre, School of Physics and Astronomy, University of Nottingham, University Park, Nottingham, NG7 2RD, UK

Introduction

The dipolar magnetic field generated by the nuclear magnetisation is generally neglected in NMR experiments. In highly polarised samples this field can however have a significant effect on the evolution of the magnetisation giving rise to multiple spin echoes[1,2] and unexpected multiple quantum coherences[3,4] between spins which are found in different molecules. These effects are most strongly manifested when spatially modulated transverse magnetisation evolves in the presence of similarly modulated longitudinal magnetisation. Such modulation can be produced by the application of RF[6] or magnetic field gradients[1-5]. Previously it has been shown that signals generated in this way are sensitive to the sample structure, since the dipolar field experienced at a particular location is mainly dependent upon the amount of magnetisation found within one 'wavelength' of the modulation[4,5]. By varying this modulation through manipulation of gradient pulse areas, structures can be probed at different length scales. In the previous work, measurements were made of the average structure, by recording the signal amplitude from the whole sample as a function of modulation[5]. Here we directly demonstrate the spatial sensitivity of the dipolar signal, by using it to form images of simply structured phantoms.

Methods

Images were produced using variants of the CRAZED sequence[3]. A conventional analysis of this sequence would suggest that no signal would be formed after the application of the second gradient pulse, because the pulse areas are in the ratio of 1:2. The action of the dipolar field generated by the modulated z-magnetisation however refocuses a fraction of the transverse magnetisation, to generate a signal that initially grows with time, T. This corresponds to double quantum coherence in the quantum picture of dipolar field effects[3,4]. In the situation where $\mu_0\gamma M_0 T << 1$, it can be shown that the amplitude of the signal is proportional to the magnitude of the z-component of the dipolar field, B_{dz}, multiplied by the equilibrium magnetisation, M_0. By adding an imaging module at the end of the sequence, it is possible to directly generate an image of this field distribution. This sequence was applied to a phantom consisting of a water filled 10 mm od NMR tube, using varying levels of modulation. The dependence of the signal on M_0 means that it is only possible to measure a signal from regions containing magnetisation. To allow more flexibility in measuring the field pattern we also therefore investigated samples containing two spin species, whose magnetisation could be independently manipulated by minor modification of the CRAZED sequence.

128 x 128 images (.09 x .09 x 6 mm^3 voxel size) were generated at 11.7 T, using modulations with spatial frequencies ($k_m=\gamma G\tau$) in the range 0.8 - 16 mm^{-1} (corresponding to wavelengths of ~ 0.4 - 8 mm). The evolution time, T, was 100 ms and TR values of > 6 s were used to avoid the formation of stimulated echoes. The expected dipolar field pattern was also simulated using expressions based on the Fourier transform of the magnetisation distribution[1,5].

Results and Discussion

The images of the simple tube of water are in good agreement with the simulations. At high values of k_m the dipolar field pattern is uniform inside the tube and follows the distribution of magnetisation, since on the pixel length scale B_d is just a function of the local magnetisation[1]. As k_m is reduced the signal in a region of width $\propto k_m^{-1}$ at the outer circumference of the sample is attenuated. This is a consequence of the changes in structure occurring within the length scale of the modulation in this region, as a result of proximity to the sample edge. Figure 1 shows images of the dipolar field pattern (k_m = 1.2 [A] and 4.8 [B] mm^{-1}) in a phantom consisting of a 5 mm NMR tube containing acetone, inside a 10 mm tube containing water. The sequence has been applied such that only longitudinal water magnetisation and transverse acetone magnetisation are present during the evolution period. The image thus mainly shows the field generated in the inner tube by magnetisation in the outer tube. It can be seen that this field is largest at the circumference of the inner tube in a region whose width decreases with k_m (~ 0.9 k_m^{-1}). Some residual water signal (shifted as a result of the chemical shift difference) remains, allowing visualisation of the outer tube.

Conclusions

We have directly measured the spatial variation of the dipolar field pattern generated in structured liquid state samples for the first time. The results are in good agreement with simulations, thus providing verification of the Fourier space expressions for the dipolar field[1,5] and of the structural sensitivity of measurements made using this signal.

Fig. 1

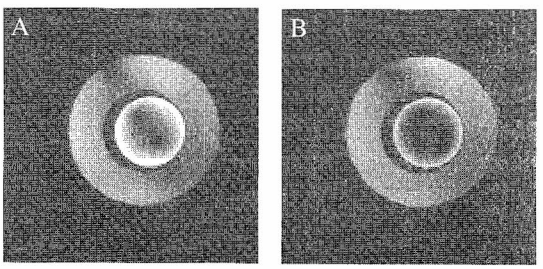

References

1) Deville G., Bernier M., Delrieux J.M., *Phys. Rev. B* **19**, 5666 (1979).

2) Bowtell, R., Bowley R.M., Glover P., *J. Magn. Reson.* **88**, 643 (1990).

3) Warren W. S., Richter W., Andreotti A.H., Farmer B.T., *Science* **262**, 2005 (1993).

4) Richter W., Lee S., Warren W.S., He Q., *Science* **267**, 654 (1995).

5) Bowtell R., Robyr P., *Phys. Rev. Lett.* **76**, 4971 (1996).

6) Jeerschow A., *Chem. Phys. Lett.*, **296** 466 (1998).

O12

A Self-Contained Portable NMR Imager

M. Rokitta, E. Rommel, U. Zimmermann*, A. Haase
Physikalisches Institut and *Lehrstuhl für Biotechnologie der Universität,
Am Hubland, D-97074 Würzburg, Germany

Introduction. To overcome the drawbacks of NMR regarding weight and expensiveness of the equipment we developed a portable NMR imager. The heaviest part of the instrument is a permanent magnet of 52 kg which can easily be transported. This opens a variety of applications for NMR imaging which are not bound to a laboratory. The portability of the system can be proven by an imaging experiment during the talk.

Methods. The instrument is based on a Minispec NMS 120 (Bruker, Karlsruhe) NMR spectrometer without imaging gradient hardware.The magnet (material: AlNiCo, B = 0.47 T, $\Delta B/B = 10^{-5}$, m = 52 kg) has a "C"-geometry and provides open access to the top, bottom and front. The gap is 19 mm which leaves a usable space of around 10 mm inside the RF-coil. We designed a set of 3 biplanar gradient coils (1, 2) and 3 gradient amplifiers which are capable of 5 A output current. The achievable gradient stregth is approx. 200 mT/m in each direction. In addition the gradient coils are used as linear shims. The thickness of all three gradients including an RF shield is below 2 mm on each side of the magnet gap. A solenoid coil is used as RF transmitter/receiver coil. In the experiments described here it had a length and diameter of 7 mm respectively. For experiments on the stems of living plants, the RF coil has to be wound directly round the stem. The maximum usable space inside the RF coil can be approx. 10 mm. The proton resonance frequency is 20 MHz. The imaging sequence which is actually used is a spin-echo experiment with an echo time of 6 ms and an acquisition time of 6 ms. Due to limitations of the Minispec electronics the minimum repetition time is 5 s. T_1 weighted images are so far realized by inversion-recovery spin-echo imaging. Real and imaginary parts of the echoes have to be acquired in separate experiments because of software restrictions.

Results. Fig. 1 shows a spin density weighted image of a phantom (a) and a T_1-weighted image (TIR = 200 ms) of a plant stem (castor bean) (b). The phantom was made of two concentric glass tubes filled with water with inner diameters of 5.5 mm and 1.25 mm. The plant stem had an outer diameter of 5.5 mm. The nominal in plane resolution (x-z-plane) was 78 µm / 63 µm (Fig. 1 a / b). A slice selection gradient was not applied. The slice thickness is therefore determined by the length of the RF-coil (7 mm). The wall of the inner glass capillary (fig. 1 a) has a thickness of 120 µm. It can be clearly resolved in the image. In fig. 1 b) different types of tissue can be distinguished: cortex, xylem (dark ring) and pith parenchyma.

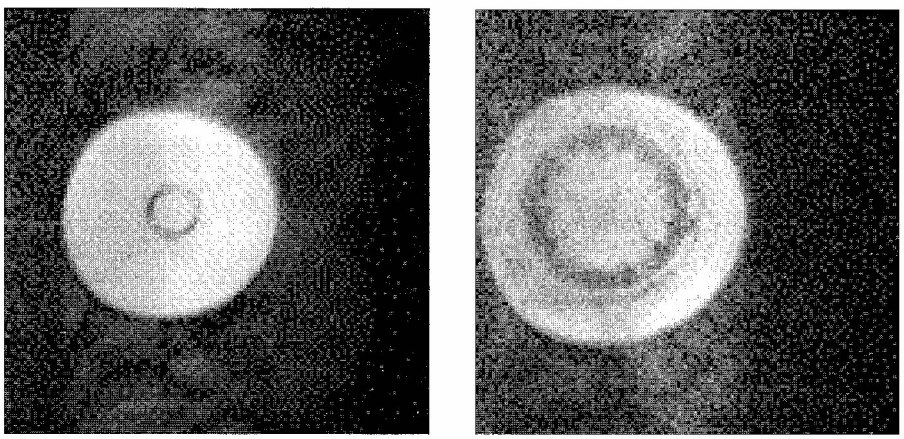

a) b)

Fig. 1: spin-echo images of (**a**) a phantom built of two concentric glass tubes (spin density weighted) and (**b**) the stem of a castor bean plant (T_1-weighted, TIR = 200 ms). The wall thickness of the inner glass capillary (a) is 120 µm.

Conclusion. The portable NMR imager provides good image quality with a very low weight and effort for the equipment. Current limitations such as the minimum TR of 5 s and the separate acquisition of the real and imaginary part of the signal will be solved soon by further electronic improvement.

References

[1] I. Frollo, *Rev. Sci. Instrum.* **60**, 3442 (1989)

[2] Y. Xia, K. R. Jeffrey, P. T. Callaghan, *Magn. Reson. Imag.* **10**, 411 (1992)

O13

Design and Analysis of Microcoils for Cellular Research in High Magnetic Fields with ^{1}H NMR

Kevin R. Minard and Robert A. Wind

Pacific Northwest National Laboratory, P.O. Box 999, MS K8-98, Richland, WA 99352, USA

Introduction: Over the years, considerable interest has been expressed in using proton MR microscopy for examining both the morphology and chemical composition of cellular systems in health and disease. However, because of the method's inherent insensitivity, applications have thus far been limited to large single cells such as the *Xenopus laevis* oocyte, or multicellular colonies in the form of individual tumor spheroids. In either case, sample size dictates the use of microcoils with diameters no smaller than about a millimeter. In solenoids of this size, NMR sensitivity is significantly degraded at high frequencies by radio frequency (RF) induced losses in the electrolytic media required for maintaining cell viability. In this study, the variation of such losses with coil design is considered and the impact on NMR sensitivity in high magnetic fields is assessed in both theory and experiment.

Methods: To reduce the total number of variables characterizing microcoil geometry, it is shown that homogeneity requirements for quantitative microscopy unambiguously define a coil's length-to-diameter ratio. Consequently, when the inner diameter of a single layer solenoid is fixed by sample size, NMR sensitivity generally depends on only two coil parameters; namely, the diameter of coil wire and the total number of turns. To illustrate how ^{1}H NMR sensitivity depends on the latter, several coils were constructed keeping all parameters constant except the total number of turns – which varied from 4 to 12 in steps of 2. Both skin and proximity effects on unloaded coil resistance were then measured between 10 and 350 MHz using a Hewlett Packard impedance analyzer (HP 4396A/option 010) in conjunction with a Coil Craft test fixture (RDL-A). The measured values of unloaded coil resistance agreed with the early theoretical predictions of Medhurst [1] and Butterworth [2] within 4%; thereby, establishing the accuracy of the impedance measurements. The frequency dependence of RF-induced sample losses was then measured by subtracting measurements of unloaded coil resistance from similar measurements performed on coils loaded with phosphate buffered saline (PBS) solution. Numerical fitting of frequency dependent RF-induced sample losses over the measurement range was then used to extrapolate losses to higher frequencies. Finally, information regarding sample loss behavior was combined with theoretical values of unloaded coil resistance and capacitor performance data (provided by manufacturers) in a *Mathematica* program. This was, in turn, used to predict relative NMR sensitivity for different coils at different frequencies. Sensitivity predictions were then compared directly with experimental data obtained at 500 and 750 MHz.

Results: With a coil length-to-diameter ratio of about two, good RF field homogeneity ensures that measurements of metabolite concentrations in tumor spheroids are accurate to within 10% even when using PRESS for micro-localized proton spectroscopy. For coils with this length-to-diameter ratio, and an inner diameter of 1 millimeter, impedance measurements confirmed the ω^2 dependence predicted for RF-induced losses in conducting samples [3]. In addition, computer calculations showed that NMR sensitivity above 500 MHz varied significantly with the number of turns – being characterized by a well defined maximum that shifted to lower turns at higher frequencies. NMR measurements at 750 MHz confirmed computer predictions and showed that NMR sensitivity could vary by ~ 20% depending on the number of turns. Importantly, more significant variations were predicted at higher fields.

Conclusions: To examine the frequency-dependence of proton NMR sensitivity, predicted values of relative sensitivity for loaded coils constructed with the optimal number of turns was plotted as a function of frequency between 500 and 1250 MHz. Data was then fit to a power law. The results showed that capacitor and sample losses conspire to reduce the frequency dependence of NMR sensitivity in this range from $\omega^{1.75}$ under ideal circumstances to ~ $\omega^{1.26}$. Moreover, we have observed experimentally that the NMR line-width in multicellular tumor spheroids is inhomogeneously broadened and increases linearly with field from 500 to 750 MHz. Under such circumstances, NMR sensitivity is further reduced by $\omega^{-0.5}$; thereby, resulting in a sub-linear frequency dependence of only ~ $\omega^{0.76}$. Therefore it is concluded that a relatively moderate frequency of 500 MHz is a good compromise between overall cost and performance for cellular research using proton NMR microscopy.

References:

[1] R.G. Medhurst, *Wireless Engineer* **24**, (March 1947).

[2] S. Butterworth, *Wireless Engineer*, **3**, (May 1926 pp.203 *et seq*).

[3] D.G. Gadian and F.N.H Robinson, *J. Magn. Reson.* **34**, 449-455 (1979).

O14

Development of a high S/N 600 MHz NMR microscopy probe

Seung-Cheol Lee[1], Kiseong Kim[1], Jeonghan Yi[2], Saebomi Park[3], Chaejoon Cheong[3], Soonchil Lee[1]

[1]Department of Physics, Korea Advanced Institute of Science and Technology, Taejon 305-701, Korea
[2]Department of Biomedical Engineering, Kon Kuk University, Choongju 380-701, Korea
[3]Magnetic Resonance Team, Korea Basic Science Institute, Taejon 305-333, Korea

The commercial Bruker 600 MHz NMR microimaging probe gives high S/N and resolution images resulting from 14.1 T magnetic field. While the probe is suitable for general purpose microimaging with rf coil diameters from 2 mm to 10 mm, for imaging small size samples with better resolution several improvements are possible:

- The gradient strength(200 G/ cm) has to be increased for ~2 um resolution imaging.
- The rf coil diameter(2 mm) has to be made smaller to get higher S/N[1]
- The distance between rf coil and tuning capacitors is large (about 2 cm for the commercial 2 mm coil) and degrades Q-factors; the distance should be minimized.

We developed a new improved microimaging probe in 14.1 T. The features are:

- Strong field gradient (~800 G/ cm in 40 A) with water cooling
  ; the accessible bore diameter is 13 mm. Aluminum powder was mixed to the epoxy resin to increase thermal conductivity and cooling efficiency of the gradient coil.
- Microcoils (diameter 0.5 mm and below)
  ; Optimum number of turns and wire diameters were searched for each coil diameter.
- Sample tubes which use just the inner diameters of the rf coils were developed to increase filling factors; acrylic resin surrounds the rf coil.
- The tuning capacitors are connected to the rf coil as close as possible to get high Q-factors.
- We located the preamplifier close to the rf coil to minimize the S/N degradation arising from coaxial line loss and the impedance mismatch loss. The directional coupler was constructed using PIN diodes(MA4PH237, MACOM) and a 1/4 λ coaxial line. The low noise preamplifier (AFSM2-00500100, MITEQ) with noise figure below 0.7 dB was used.

The high resolution images obtained with the improved probe will be presented. The voxel size of these images is less than that of any images reported so far.

References:

[1] Peck. T. L., Magin. R. L. and Lauterbur, *J. Magn. Reson.* Series B. 109, 114-124 (1995)

O15

Multi-Layer Transverse Gradient Coils

R. Bowtell [1], S. Crozier [2], B. Beck [3] and S. Blackband [3]

[1] University of Nottingham, Nottingham, UK, [2] University of Queensland, Brisbane, Queensland, Australia

[3] University of Florida, Gainesville, Florida, USA

Introduction

Very large magnetic field gradients are required in a variety of NMR experiments. NMR microscopy[1] and pulsed gradient spin echo (PGSE)[2] experiments can particularly benefit from the availability of switchable gradients of more than 10 Tm^{-1} strength. Access to such gradients is usually limited by the rapid increase in gradient coil resistance (R) with efficiency (η), which results from the reduction in usable wire diameter as the number of turns in a single layer cylindrical gradient coil increases ($R \propto \eta^3$). Similar effects occur in coils constructed by cutting wire patterns in conducting layers, because of the loss of conducting material with increasing numbers of cuts. Adopting a multi-layer approach to coil design[3], in which the coil windings are allowed to spread out in the radial direction, gives a more favourable scaling law[3], which allows larger gradients to be achieved at a given resistance and power dissipation. Previously we have applied this approach to the generation of axial magnetic field gradients[3]. Here we extend this work to the design and construction of transverse field gradient coils.

Theory

A multi-layer cylindrical coil confined between radii a and b ($a < b$) can be described by a current distribution $j(\phi,\rho,z)$. If j has only azimuthal and axial components, the magnetic field in the region $\rho < a$ is given by

$$B_z(\rho,\phi,z) = -\frac{\mu_0}{2\pi}\int_a^b d\rho'\rho' \sum_{m=-\infty}^{\infty}\int_{-\infty}^{\infty} k\,dk\; j_\phi^m(\rho',k)e^{ikz}e^{im\phi} \times K_m'(k\rho')I_m(k\rho)$$

where $j_\phi^m(\rho,k)$ is the Fourier transform of the azimuthal component of j, with respect to ϕ and z. In transverse coils only the terms with $m = \pm 1$ are important. Expressions for the inductance, L, and power, P, dissipated by the current distribution can also be derived . To design a coil, the current distribution is divided into a number of equally spaced layers and is composed from a number of axial varying harmonics in each layer. An optimal coil can be designed using the above equations by determining the harmonic weightings, which minimise a weighted combination of P, L and the field deviation from linearity[4], calculated over a grid of points defining the desired homogeneous region.

Results

The above methods have been used to design an unscreened transverse gradient coil with 10 mm inner diameter, which gives an internal region within which the field deviates from linearity by less than 5 % consisting of a right cylinder of 6.5 mm diameter. The first coil layer was located at a radius of 5.65 mm. and subsequent layers were placed at 0.6 mm intervals in the radius. Figure 1 shows the calculated variation of the optimum coil efficiency with the number of layers for two different types of coil of fixed resistance (1.5 Ω). The lower curve corresponds to wire wound coils (wire diameter of 300 μm). The upper curve corresponds to coils composed of "fingerprint" patterns cut into 300 μm thickness copper, with a 100 μm cut thickness. In both cases it can be seen that significant gains in coil efficiency at fixed resistance can be achieved by increasing the number of layers. The "cut" based coils have higher efficiency than those composed of discrete wires. For both types of coil the inductance increases with the number of layers.

A two-layer, wire-wound, coil has been built to test the feasibility of constructing and operating multi-layer transverse gradient coils. The first and second layers carry a total of 56 and 44 turns respectively, of 300 μm diameter copper wire. The coil has a resistance of 1.1 Ω, an inductance of 21 μH and an efficiency of 0.41 $Tm^{-1}A^{-1}$, all values being in good agreement with those calculated in the design process. The coil was constructed by cutting grooves into the surface of two concentric cylinders. Wires were laid in the grooves and then set in place using epoxy resin. The coil has been shown to perform as expected up to gradient strengths of 10 Tm^{-1}.

Conclusions

Multi-layer transverse gradient coils offer improvements in achievable gradient strengths in the regime where performance is limited by the coil resistance. A two-layer prototype coil has been constructed and tested.

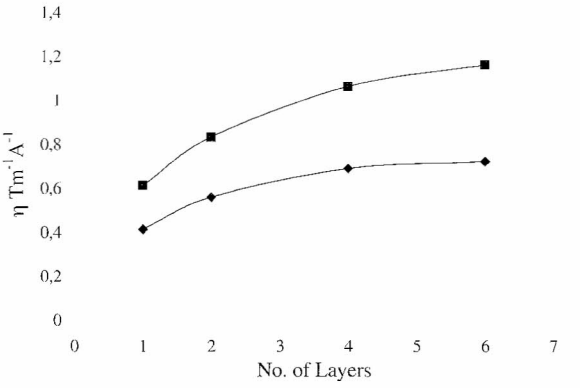

References

1. Rofe CJ, *et al.*, *J. Magn. Reson.* **B 108**, 125 (1995).
2. Callaghan PT, Stepisnik J, *et al.*, Phys. Rev. Lett. **75**, 4532, (1995).
3. Bowtell R, Robyr P, *J. Magn. Reson.* **131**, 286, (1998).
4. Carlson JW, *et al.*, *Magn. Reson. Med.* **26**, 191 (1992).

O16

A High-Gradient Permanent Magnet for the Profiling of Planar Films and Coatings

P.M. Glover, P.S. Aptaker[†], J.R. Bowler, E.Ciampi, J.L. Keddie and P.J. McDonald

Department of Physics, University of Surrey, Guildford, Surrey. GU2 5XH. UK

[†] Resonance Instruments Ltd, Unit 13, Thorney Leys Business Park, Witney. Oxon, OX8 7GE. UK

Introduction. The design, construction and preliminary application of a low-cost, permanent magnet is described. The magnet is intended for applications which require a large static gradient, such as those for which stray field imaging (STRAFI) or fringe field diffusometry are conventionally employed [1,2]. Particular features of the magnet include a field profile such that $|\mathbf{B}|$ is constant in the horizontal plane and such that $\mathbf{B}$ is horizontal at the mid-point between the poles. There is a vertical, and therefore orthogonal, strong gradient, G, in $|\mathbf{B}|$. The magnet is most suitable for the one-dimensional profiling of thin planar samples and has a more suitable geometry for this task than STRAFI based on a conventional magnet [3].

Methods. The magnet was designed using a scalar potential method. A function $\phi(x,y,z)$ satisfying $\nabla\times\mathbf{B}=\nabla^2\phi=0$ which yields the required magnetic field characteristics is found. A suitable function is $\phi(y,z)=a\sin(bz)\exp(-by)$ where a and b are constants; z is the direction across the pole pieces and y is vertical. The field is assumed constant in the x direction. The gradient is given by $G=d|\mathbf{B}|/dy=-ab^2\exp(-by)$ The magnet pole pieces are constructed from a high permeability, linear isotropic material. Their profile (given by an equipotential surface of ϕ) is $z(y)=\pm[\sin^{-1}(\sin(bw/2)\exp(by))]/2$, where w is the pole separation at y=0. The magnetic field has the property that within a large volume, the ratio $G/|\mathbf{B}|$ is constant and equal to b. It is seen that this ratio governs the shape of the pole-pieces. The constant $G/|\mathbf{B}|$ ratio within a large useable volume allows measurements at a range of gradient strengths to be carried out. Therefore, the same magnet may be used at field strengths from 0.5 T (12.5 Tm^{-1}) to 1.0 T (25 Tm^{-1}) whilst maintaining a constant $|\mathbf{B}|$ in the horizontal plane. A wire frame illustration of the optimised magnet design as constructed is shown in figure 1.

Results. The constructed magnet is used at an operating field of 0.8 T, gives a gradient of 20 Tm^{-1} and has a useable inter-pole access of 20 mm. Experimental measurements have shown that $|\mathbf{B}|$ has a deviation from uniformity equivalent to less than ±5 μm of curvature over a 5 x 5 mm area at the target field. A planar wound surface coil is used to localise a small volume of interest, usually in the centre of a sample. Although a low Q coil is desirable for an acceptable field of view, a nominal 90° pulse can be achieved in less than 1 μs whilst maintaining good sensitivity. As an example of the use of the magnet, figure 2 shows differential drying and cross-linking of alkyd resin model paint layers with and without catalytic dryers. The profiles have a nominal resolution of 6.5 μm. In an alternate study of water diffusion within and transport through human epidermis, differences in diffusion coefficient of an order of magnitude have been observed between the epidermis and the stratum corneum layers of a membrane only 50 μm thick.

Discussion. The magnet offers a low cost route to STRAFI like high resolution profiling of near-solid samples and to high gradient diffusometry. With the addition of a magnet based on this design, the owner of a benchtop spectrometer may employ a much wider range of spatially resolved techniques at a modest cost.

References.

1. Samoilenko A. A., et al, *JETP Lett.* **47**, 417-419 (1988).

2. McDonald P.J, et al, *Rep. Prog. Phys.* **61** 1441-1494 (1998).

3. Glover P.M. et al, *J. Magn. Reson.* **126**, 207-212 (1997).

Fig. 1. A wire-frame representation of the magnet showing the curved pole-pieces. The permanent magnets are positioned just behind the Swedish steel pole-piece blocks.

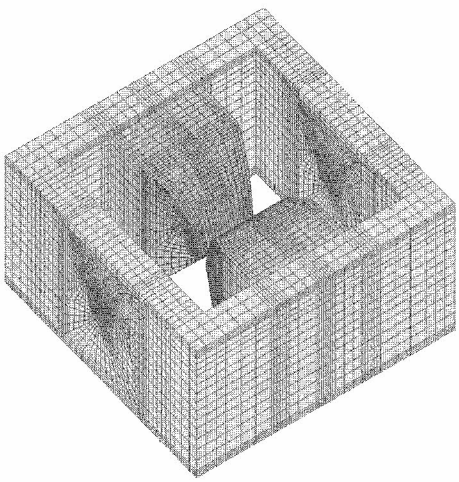

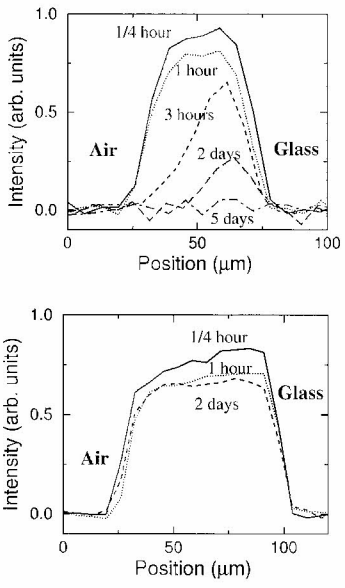

Fig. 2. The profiles through alkyd model paint layers (top) without and (bottom) with catalytic dryers. The solvent loss and subsequent cross linking may be observed. T_2 weighted profiles may be obtained from the Fourier transform of each echo from the sequence

β_x-[τ-β_y-τ-echo-]$_n$

with τ =150 μs. The profiles represent the first echo and have a nominal resolution of 6.5 μm.

O17

Development of an MRI Surrogate for Immunohistochemical Staining of Collagen Damage in Cartilage

A.C. Bageac [1], M.L. Gray [1,3], M. Zhang [1], A.R. Poole [2], D. Burstein [1]

[1]Beth Israel Deaconess Medical Center, Harvard Medical School, Boston, USA
[2]Shriners Hospital for Children, McGill University, Montreal, Canada
[3]Massachusetts Institute of Technology, Cambridge, USA

Introduction

Glycosaminoglycans (GAG) and collagen are the major components of articular cartilage that provide it with structural and functional integrity. Histological evidence indicates that both GAG loss and collagen damage occur in the pathogenesis of osteoarthritis (OA) leading to functional deficits. A non-invasive method using T_1 inversion-recovery imaging in the presence of the charged MR contrast agent $Gd(DTPA)^{2-}$ has been developed to quantify and map the distribution of GAG loss in OA [1]. However, imaging the collagen network non-invasively remains elusive. The purpose of this study was to determine whether the MR technique of magnetization transfer (MT) could potentially provide a nondestructive surrogate for immunohistochemical staining of collagen molecular damage in cartilage.

Methods

Young calf articular cartilage samples (n=3) were treated in tissue culture for four days with the cytokine IL-1β (10 ng/ml) which is known to induce GAG loss and collagen damage in cartilage. The distribution of GAG was quantified using previously standardized MR methods that employ T_1 inversion-recovery imaging in the presence of $Gd(DTPA)^{2-}$ [1]. After re-equilibration in a saline solution free of $Gd(DTPA)^{2-}$, MT was quantified as the ratio of an Ms image obtained with a saturation pulse at 12 μT and offset of 6 kHz applied for 6 s, and an Mo image with the same sequence and an offset of 10 MHz [2]. T_1, Mo and Ms images with 50 x 50 μm in-plane resolution and 250 μm thickness were obtained. T_1 and Ms/Mo maps were calculated and were matched against histological preparations of GAG loss stained with toluidine blue [3] and collagen damage stained with the COL2-3/4m antibody [4], respectively, using MATLAB software.

Results

Histology of the IL-1β-treated cartilage revealed different patterns of distribution for the toluidine blue and COL2-3/4m stains. For example, after four days of exposure to IL-1β in culture, there was almost no GAG loss but collagen damage was obvious by substantial staining with the COL2-3/4m antibody. As previously demonstrated, T1 calculated images of those samples matched the distribution of the toluidine blue stain [1]. The Ms/Mo images showed a variation in Ms/Mo distribution similar to the COL2-3/4m stain. A cluster analysis of MR and histology images showed a mainly linear distribution between Ms/Mo values and COL2-3/4m stain intensity. However, some discreet areas did not fully integrate in this linear distribution. This could be due to the non-linearity of the histology stain and/or other contributors to Ms/Mo. Currently we are investigating other small contributors to MT (i.e. GAG concentration, variations in hydration), and extending this study to determine whether the correspondence between MT and COL2-3/4m staining is robust and generalizable to other sources and interventions in cartilage.

Conclusion

Ms/Mo images of a limited set of IL-1β treated calf cartilage exhibit signal intensity patterns that match qualitatively the distribution of collagen damage as seen with the COL2-3/4m immunohistochemical stain. To our knowledge, this is the first demonstration of a correlation between MT and an immunohistochemical stain for collagen damage.

References

1. Bashir A, Gray ML, Hartke J, et al. *Magn. Reson. Med.* **41**, 857-865 (1999).
2. Gray ML, Burstein D, et al. *Magn. Reson. Med.* **34**, 319-325 (1995).
3. Poole AR. *Histochem. J.* **2**, 425-430 (1970).
4. Hollander AP, Heathfield TF, et al. *J. Clin. Investig.* **93**, 1722-1732 (1994).

O18

Non-invasive Evaluation of Engineered Cartilage Tissue Using Proton NMR Microscopy

K. Potter[1], J. Butler[2], W.E. Horton[3], and R.G.S. Spencer[2]

National Institutes of Health, [1]Section on Tissue Biophysics and Biomimetics, NICHD, Bethesda, MD 20892-5766, [2]NMR Unit, NIA, Baltimore, MD 21224-6825, [3]Dept. of Anatomy, NEOUCOM, Rootstown, OH 44272, USA.

Introduction. The goal of this work was to determine whether biochemical changes in the extracellular matrix can be staged by NMR and whether NMR measurements can be correlated with biochemical parameters. For this purpose we have developed a NMR-compatible hollow fiber bioreactor (HFBR) for studying the NMR properties of three-dimensional cartilage tissue produced by isolated chick sternal chondrocytes.

Experimental. HFBRs were inoculated with 30 million chondrocytes isolated from distal sterna of day 16 chick embryos. After inoculation the bioreactors were perfused using a pin compression pump in a 5% CO_2 / 95% air incubator. This was noted as Day 0. The culture medium for all bioreactors was supplemented with 2% serum and 10 μg/mL ascorbic acid (AA) was added twice-weekly. The following experiments were performed: (i) control experiments, (ii) daily treatment with AA, (iii) treatment with 3 μg/mL trans-retinoic acid (RA) for 1 week at Day 21, and (iv) treatment with 10 ng/mL interleukin-1B for 1 week at Day 21.

All NMR experiments were conducted on a Bruker DMX spectrometer operating at 9.4 T (400.1 MHz for ^1H). HFBRs were maintained under incubator-like conditions while in the magnet. Each image had a nominal in-plane resolution of 60 microns and a slice thickness of 2 mm. The following quantitative NMR properties were measured for HFBR tissue: water proton T_1 and T_2 values, the magnetization transfer (MT) value, and the water diffusion coefficient (D). MT was calculated from the following equation:

$$MT = [1 - M_{SO}/M_O],$$

where M_{SO}/M_O gives the ratio of image intensities acquired with and without the application of a 5 s, 12 μT saturation pulse applied 6000 Hz off-resonance. Diffusion values are reported as percentages of the free water diffusion coefficient (D_W).

After NMR imaging the tissue was extracted from the HFBR, weighed, and submitted for biochemical analysis. Dried samples were digested with papain and the glycosaminoglycan (GAG) content was determined using the dimethylmethylene blue dye binding colorimetric assay (3). The collagen content of the tissue was derived from a colorimetric assay for hydroxyproline performed after hydrolysis of the papain digest with 6 N HCl at 110°C overnight (4).

Results and Discussion. Control bioreactors produced cartilage up to several millimeters thick around each fiber after two weeks of growth. Daily doses of AA, as opposed to treatment twice weekly, accelerated the formation of mature cartilage tissue. This matrix contained comparable levels of GAGs but significantly higher levels of collagen compared to controls. In contrast, treatment with RA resulted in a significant reduction in the GAG content of the tissue, but left the collagen content of the tissue unchanged. Treatment with IL-1B resulted in higher levels of GAGs compared to control bioreactors.

When the T_1 relaxation rate (R_1) was plotted against the GAG concentration of the matrix there was a good correlation between the two parameters ($R = 0.82$, $p < 0.001$). R_1 also correlated with the collagen concentration of the matrix ($R = 0.73$, $p < 0.001$), which was consistent with results for other collagen containing tissues (5). The T_2 relaxation rate (R_2) was found to correlate the GAG concentration of the tissue ($R = 0.81$, $p < 0.001$). This result was consistent with relaxation studies of polysaccharide gels (6). The correlation with tissue collagen concentration was weak. The correlation between MT and biochemically determined collagen content was fair ($R = 0.63$, $p = 0.003$). However, a similar relationship between MT and tissue GAG content was not observed. Finally, there was good correlation between the water diffusion coefficient in the tissue and its hydration level ($R = 0.64$, $p < 0.001$). This result was consistent with that obtained for explant cartilage (7).

Conclusions. We have developed correlations between NMR measurable parameters and tissue parameters for engineered cartilage tissue. This provides a method for monitoring tissue development non-invasively. These correlations may also be used to monitor the pathophysiology of cartilage degeneration as well as to the effects of various therapeutic interventions *in vivo*.

References.

1. E. Petersen, K. Potter, J. Butler, et al., *Int J Imaging Syst Technol* 8, 285-292 (1997).
2. K. Potter, J. Butler, W. Horton, et al., *Matrix Biology* 17, 513-523 (1998).
3. R.L. Goldberg and L.M. Kolibas, *Connect Tissue Res* 24, 265-275 (1990).
4. J.F. Woessner, *Arch Biochem Biophys* 93, 440-447 (1961).
5. T.D. Scholz, et al., *Invest Radiol* 24, 893-898 (1989).
6. K. Potter, T.A. Carpenter, L.D. Hall, *Magn Reson Imaging* 12, 309-311 (1994).
7. Y. Xia, T. Farquhar, et al., *Arch Biochem Biophys* 323, 323-328 (1995).

O19

Xylem at Work: Embolism Induction and Refilling in Vessels of a Cucumber Plant

T.W.J. Scheenen, A.M. Heemskerk, P.A. de Jager, F.J. Vergeldt and H. Van As

Laboratory of Molecular Physics, Department of Biomolecular Sciences

Wageningen University, Dreijenlaan 3, 6703 HA, Wageningen, The Netherlands

Water in plants is transported over long distances from roots to shoot and leaves in the xylem. Xylem vessels in the plant stem are the conduits for water and can contain long undisrupted water columns. In strongly transpiring conditions, root cooling can induce a big pressure drop over the xylem vessels in the stem so that the water column in a vessel breaks: the induction of an embolism. Embolisms obstruct further transport of water through the vessels; the leaves transpire more water than they receive and they will wilt. Somehow, the embolisms are repaired, water uptake is restored and the leaves completely recover. At this moment the mechanism of embolism repair is hardly understood (1,2).

We present the first studies to observe the induction and refilling of embolisms in vivo in a full-grown cucumber plant by using multi-echo NMR imaging (3) and fast dynamic NMR microscopy (4). Multi-echo NMR imaging produces a series of spin echo images that is attenuated by T_2 relaxation. Fitting a one-exponential decay per pixel results in two single parameter images: an image with the amplitude at the moment of excitation and a T_2 image. Fast dynamic NMR microscopy combines Pulsed Field Gradients (PFG) for flow encoding with a Turbo Spin Echo (TSE) pulse sequence. The unique feature in our PFG TSE sequence is the fact that phase-information, imposed by the PFGs, is recalled throughout the complete TSE train. With the PFG TSE sequence we obtain a spectrum, for every pixel, of all displacements of the spins within the labelling time between the two PFGs. A model-free analysis (5) of the displacement spectrum for every pixel results in images with the following parameters: the amount of stationary water, the amount of flowing water, the volume flow, the averaged linear flow velocity and the cross-sectional area of flow.

A full-grown water-cultured cucumber plant (height ~1.50 m) was put into the gradient probe in an open access electromagnet (0.47 T). To obtain a high signal to noise ratio we twisted a small solenoid rf coil for excitation and detection directly around the plant stem (6). The water uptake of the plant was measured with a balance. The total volume flow, measured by PFG TSE, was in good agreement with the water uptake by the roots and depended strongly on day/night rhythm. Root cooling inhibited water uptake and resulted in a decrease of the cross-sectional area of flow, indicating the induction of embolisms. In one of our measurements some xylem vessels cavitated in the measured slice: some pixels in the vascular bundles in the images completely lost intensity in all images after two to three hours of cooling. The leaves of the plant at that time were wilted. When cooling was relieved, water uptake restored partially and all leaves completely recovered after one hour (still in light conditions). The visible embolisms in the images started refilling after about four hours (lights off), except from the very first embolised vessels: sixteen hours after we stopped cooling the roots, these vessels were still not refilled.

The T_2 of the tissue that surrounded vascular bundles with embolised vessels (~400 ms), decreased by about 40% at the time embolisms were visible. Assuming a model (7) in which the T_2 of vacuolised tissue depends on vacuole size and a parameter that characterises exchange with fast relaxating cytoplasm, the large decrease in T_2 cannot be explained by a decrease of cell/vacuole size alone. A higher exchange speed of water over the vacuole membrane can explain the large decrease in T_2 at the time embolisms refill. Could this increase in membrane permeability indicate a role of active water transporters (aquaporins) in the vacuole membrane?

1. Tyree, M.T., et al., *Plant Physiology*, **120**, 11-21 (1999).

2. Holbrook, N.M., et al., *Plant Physiology*, **120**, 7-10 (1999).

3. Edzes, H. T., et al., *Magnetic Resonance Imaging* **16**, 185-196 (1998).

4. Scheenen, T.W.J., et al., submitted to *Journal of Magnetic Resonance*.

5. Scheenen, T.W.J., et al., in preparation.

6. de Jager, P.A., et al., this conference

7. van der Weerd, L., et al., this conference

O20

Proton and Helium MR Microscopy of the Small Animal Lung

Laurence W. Hedlund, Gary P. Cofer, G. Allan Johnson

Center for *In Vivo* Microscopy
Duke University Medical Center, Durham, North Carolina 27710

The thorax is one of the most challenging areas of study for MR microscopy because it incorporates all the fundamental barriers for the imaging technology. Motion of the heart and lungs poses the first barrier. Limited signal from lung poses the second barrier. In our current studies, the diffusion of gas poses the third fundamental barrier. We have addressed each of these in a novel interdisciplinary effort.

Lung motion has been addressed through the development of computer-controlled scan-synchronous ventilation. Introduced in 1986 (1), the technique has been refined more recently by modifying the scan-synchronous ventilator to control the mixture and flow of hyperpolarized ^{3}He, O_2, and N_2 (2). Concentrations of these gases are individually controlled and gas mixing occurs at the start of each inspiration at a point just before the endotracheal tube. In addition to supporting delivery of normal oxygen levels with each ^{3}He breath, this design minimizes the depolarizing effect of O_2 on ^{3}He and allowed us to adjust the total signal from the ^{3}He, the tidal volume, and inspiratory oxygen level (FiO_2).

The limited signal in the lung has been addressed through use of hyperpolarized ^{3}He to image the gas spaces (3) and the use of GdDTPA to enhance the limited ^{1}H signal from the pulmonary vasculature. The signal is encoded using the sequence shown in Figure 1. After a 200–400 ms inspiration of either regular breathing gas (O_2 and N_2) for ^{1}H imaging of pulmonary vasculature or ^{3}He, O_2, and N_2 for imaging of pulmonary gas spaces, the ventilator triggers the scanner. A series of RF and gradient pulses (TR ~5 ms) are initiated during each held breath to acquire projections through either a slice-selected or non-slice-selected volume. FIDs are acquired with delay time of < 900 μs from the end of the RF excitation pulse to the first point of the FID. By keeping this "effective echo" time to a minimum and by starting the k-space trajectory at the center of k-space, diffusion effects are minimized and the sequence is inherently flow-compensated.

The RF pulse train is executed using a variable flip angle designed to minimize the view-to-view variation and maximize the recovery of the transient magnetization. For ^{3}He studies, the transient magnetization arises from the inspiration of the gas in each ventilatory cycle. For ^{1}H studies, the transient magnetization arises from incoming blood between each ventilatory cycle.

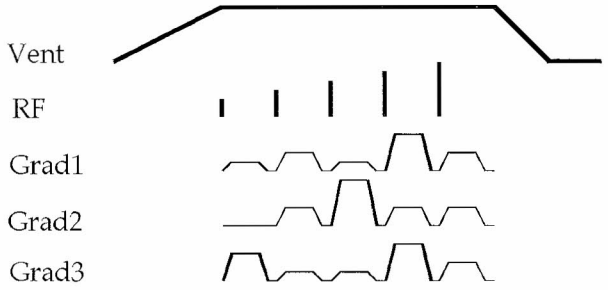

Fig. 1. Schematic of the pulse sequence for anisotropic projection encoding of the lung. The "Vent" line shows lung volume during inspiration, held breath, and expiration.

The sequence has been implemented to allow anisotropic sampling of Fourier space with anisotropy in both sampling (spatial resolution) and field-of-view. During a typical 400–800 ms held-breath period, it is possible to acquire as many as 160 views, permitting acquisition of very large arrays (512 x 512 x 64) in relatively short periods (15–30 minutes). We also used a dual-frequency birdcage coil (^{1}H: 84 mHz, ^{3}He: 64 mHz) and the same ventilation parameters to obtain, in the same session, registered ^{1}H and ^{3}He images.

By integrating these several techniques, it is now possible to produce registered ^{1}H and ^{3}He volumetric images with in-plane resolution of 100 x 100 μm in 400 μm slices.

Resolution and SNR are sufficient in both the ^{1}H and ^{3}He images to allow demonstration of significant microstructure in the live rat. By superimposing the registered gas spaces images and proton images, we are able to more clearly interpret the lung's microstructure. By following small caliber blood vessels, the very small conducting airways can be identified. Non-uniformity of gas distribution at the sub-lobar level can also be detected. This combination of techniques will support *in vivo* studies of animal models of disease, such as emphysema and asthma, at levels of resolution not previously possible.

References

1. Hedlund LW, Deitz J, Nassar K *et al.*, *Invest. Radiol.* **21**, 18-23 (1986).

2. Hedlund LW, Möller HE, Chen XJ *et al.*, *Proc. Int. Soc. Magn. Reson. Med.* **7**, 2098 (1999).

3. Johnson GA, Chen XJ, Cates G *et al.*, *Magn. Reson. Med.* 38, 66-71 (1997).

Acknowledgements

Research was supported by grants from NIH NCRR (#P41 RR05959) and NHLBI (#RO1 HL 55348). The authors would like to thank Mark Chawla, Josette Chen, Harald Möller, and Ted Wheeler for technical advice and assistance, and Elaine Fitzsimons for editorial service.

O21

^{23}Na- and ^{1}H-NMR Microimaging of Intact Plants for a Functional Study of Salt Stress

Silvia Olt, Eva Krötz[#], Ewald Komor[#], Markus Rokitta and Axel Haase
Physikalisches Institut, Universität Würzburg, [#]Pflanzenphysiologisches Institut, Universität Bayreuth

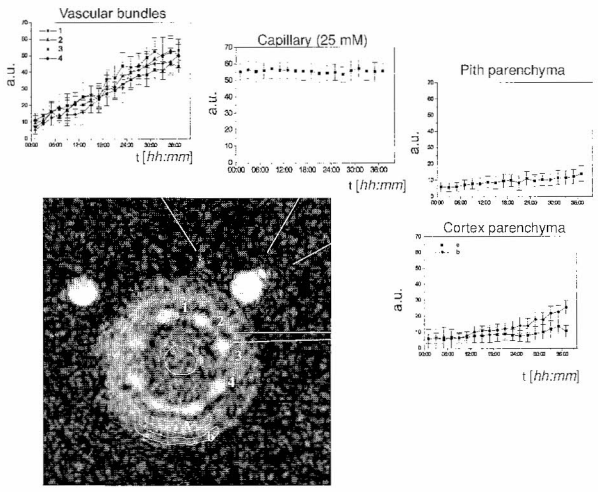

Last image of a series monitoring the sodium distribution in the hypocotyl after 39 h of NaCl incubation.Shown are mean value and standard deviation of signal intensities of the marked segments.Capillaries: 25 mM (left) and 50 mM (right). All graphics are scaled equally.

Purpose: Salinity becomes an increasing problem in irrigated soils and leads to severe limitations in crop yield. The understanding of salt stress in plants necessitates the investigation of kinetics and mechanisms of sodium uptake, exclusion and compartimentalization. Up to now, information about the sodium pools in plants have been obtained by various highly invasive methods, working only with excised tissue, dehydrated or deep frozen samples. Recently, we have described ^{23}Na-NMR-micro-imaging to map the sodium distribution in living plants without any perturbation of cell metabolism [1]. Allowing repetitive studies on single individual plants, ^{23}Na-NMR-microimaging can provide dynamical information, i.e. the time course of sodium uptake and localization. For the first time, the stress-induced reaction of the different tissue types in the hypocotyl of an intact growing plant seedling can be monitored temporally resolved.

Subjects & Methods. As plant model system for a non halophyte crop we chose six-days old seedlings of *Ricinus Communis*, grown hydroponically on top of a glass tube and aerated from below. For calibration purposes a reference capillary was added as an external standard. Experiments were performed at 11.75 T on a Bruker AMX-500 microscopy system using a double resonant ^{23}Na-^{1}H-probehead with two concentric crossed saddle shaped coils. The probehead was home-built and equipped with a climate chamber, wherein environmental conditions can be controlled. The ^{1}H -coil facilitates shimming and positioning and provides anatomic images to be correlated with the measured sodium distribution pattern.

T_1 and T_2 of ^{23}Na were measured in the cross section of the hypocotyl of a seedling grown on 200 mM NaCl. For ^{23}Na -imaging we chose a gradient echo sequence (α : 90°, TE : 3.2 ms, TR : 50 ms, FOV 10 × 10 mm², slice thickness 5 mm)

Results. T_1 and T_2 of ^{23}Na in the cross section of the hypocotyl were found to be fairly uniform over the entire stem (33.1 ± 3.0 ms and 29.5 ± 2.9 ms). Therefore, relaxation time weighting should be of no meaning in ^{23}Na-images.

Within 85 min ^{23}Na-images with an in-plane resolution of 156 µm × 156 µm were acquired of seedlings exposed to NaCl concentrations between 25 mM and 300 mM. The different tissue types in the hypocotyl could be discerned easily. Depending on the extent of salt stress, marked differences occurred in the sodium distribution pattern. SNR was between 10 and 13.

Acquiring alternately ^{23}Na- and ^{1}H-images we observed dynamical changes in the physiological response of plants after salt shock (incubation with 200 mM NaCl). The first experiment was performed after 1 h. In 19 subsequently acquired ^{23}Na-images (2 h interval) the progress of sodium-uptake of the plant was displayed in real time. The last image of the series is shown (Figure).

Conclusion. The sodium distribution in an unperturbed living plant can be visualized by ^{23}Na-NMR-microimaging, whereby the spatial resolution achieved 156 µm in-plane) allows to analyze the tissue-specific response as a function of the external NaCl concentration and the duration of incubation. An experimental time of 85 min is short compared to the time scale of the physiological response of the plant to salt stress. Thus, ^{23}Na-NMR provides temporal information sufficient for kinetic studies without a loss in spatial resolution. In conclusion, ^{23}Na-NMR-microimaging may fill the gap of *non-invasive* characterization of salt sensitive and salt tolerant crops under different environmental conditions.

References

[1] S. Olt, M. Rokitta and A. Haase, abstract ESMRMB, Geneva 1998.

O22

Characteristic Diagnosis of Hepatocellular Carcinoma by ^{19}F-MRSI of FDGal

Michiko Narazaki[1], Kazuhiro Shimokawa[2] and **Yoko Kanazawa[1]**

[1] Kyushu University, Faculty of Pharmaceutical Sciences

Present affiliation: Nihon Schering K.K. Osaka 532-0004, Japan

[2] Daikin Industries, Division of Chemistry, Settsu 566-0044, Japan

Introduction. Characteristic tumor diagnosis by monitoring regional metabolic activity with a proper NMR-pharmaceutical should be a promising field of MRSI. 2-Deoxy-2-fluoro-D-galactose (FDGal) has originally been designed as a PET-pharmaceutical for the diagnosis of liver deseases in the form of ^{18}FDGal [1]. The variation in the FDGal uptake has been the principle of differential diagnosis of hepatitis induced by CCl_4 [1] and hepatoma [2] in PET, where the proposed key reactions are the metabolism to ^{18}FDGal-1-P and to UDP-^{18}FDGal [3]. The use of ^{19}F-NMR, however, enabled us to evaluate a further metabolism to UDP-FDG, the glucose analog [4,5]. This work was designed for the cancer diagnosis by using chemical shift imaging of FDGal on the basis that the chemical shift between the FDGal group (FDGal, FDGal-1-P, and UDP-FDGal) and UDP-FDG of 8 ppm was sufficiently large for the selective observation in the NMR imaging.

Methods. FDGal was synthesized according to the method reported previously [6]. C3H male mice suspected of bearing spontaneous hepatocellular carcinoma (24 months old) and ones with transplanted MH134 on the back were used. FDGal (100 mg/kg) was injected intravenously after 4h of fasting. The tissues were excised immidiately after the MRI experiment for the pathological diagnosis and for the quantification and analysis of F-compounds by high resolution NMR. ^{19}F imaging was performed on the Varian UnityINOVA 400 at 9.4 T and an imaging probe with 38 mm ^{1}H/^{19}F tunable Litz coil from Doty Scientific. Fast spin echo with interleaved frequency selection was used for the coronal FOV of 8 x 4 cm^2 without slicing, 32 x 16 data points, T_R = 1 s, esp = 6ms and etl = 16. T_2(^{19}F) distribution was obtained from the data of modified 2-shot fast spin echo [7].

Results and Discussion. The initial uptake of FDGal as observed by the ^{19}F image in the region of liver was extremely high in the mouse suspected of HCC compared with the normal liver and MH134 tumor. Epimerization to UDP-FDG was unusually rapid at the right lobe of his liver. In the same region, dominant, high retention of FDG was confirmed on the second day of FDGal injection as in Fig. 1. These ^{19}F-MRSI data gave us sufficient information to distinguish the tissue from the normal liver and the other tumors. The part of his liver tissue was proved to be hepatocellular carcinoma by the histopathological diagnosis.

The analysis of tumor tissue including its water extracts further revealed the characteristic metabolism of HCC as follows. UDP-FDG was the dominant metabolite in HCC 24 h after FDGal injection in contrast to the other tumors such as MH134 and Sarcoma180 where further metabolism to FDG-6-P, FDM-6-P and NDP-FDM is the commonly observed pattern [8,9]. The metabolic characteristics in HCC was closer to the liver rather than the other tumors with the exception that the uptake was 5 fold higher. The high content of active hepatic cells in HCC should explain this metabolic behavior similar to the liver with much higher saturation point of related enzymes.

In the case of NMR metabolic mapping using echo signals especially in fast spin echo, tissue specific T_2 variation may obscure the quantitative information. In this study, T_2 evaluation by the method of modified 2-shot fast spin echo showed the uniform T_2 throughout the time course in the liver including HCC. Thus the present method of efficient mapping of metabolites below 1 mmol/kg was shown to be reliable.

Conclusions. Useful ^{19}F metabolic images could be constructed under a sufficiently low dose of 100 mg FDGal/kg. The characteristic diagnosis of liver tumors by FDGal-MRSI with a strong metabolic basis as shown here will find more applicability.

References

1. Fukuda, H et al. Eur. J. Nucl. Med. *11*, 444-448 (1986).
2. Fukuda, H et al. J. Nucl. Med. *34*, 780-786 (1993).
3. Ishiwata, K et al. Nucl. Med. Biol. *15*, 271-276 (1988).
4. Kanazawa, Y et al. Chem. Pharm. Bull.*36*, 4213-16 (1988).
5. Grun, BR et al. Eur. J. Biochem. *190*, 11-19 (1990).
6. Haradahira, T et al. Chem.Phrm.Bull. *32*, 3317 (1984).
7. Doi, Y et al.18th ICMRBS, (1998).
8. Umayahara, K et al. 22nd JMRM, 296 (1994).
9. Narazaki, M et al. 18th ICMRBS, IV-23 (1998).

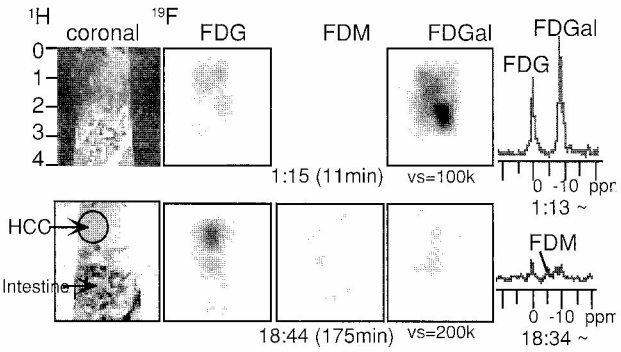

Fig.1. ^{1}H and ^{19}F images of 100 mg FDGal/kg injected male C3H mouse bearing spontaneous HCC.

O23

Ultra-fast Fluid Flow Measurement in Porous Media by MRI: Correlation Studies in a Heterogeneous System

M. Bencsik, P. Mansfield and R. Bowtell

Magnetic Resonance Centre, University of Nottingham

We have shown elsewhere [1-3] that ultra-fast spatially resolved measurement of fluid flow is possible in porous rocks in times of the order of 400 ms. In this type of experiment coherent molecular displacements are encoded as spin phase changes which are proportional to the coherent velocity. However, if an image voxel contains many pores and grains the voxel phase may not be proportional to the mean phase of the spins within the voxel [4].

We present experimental data using a glass bead phantom in which we have ensured that the voxel phase change is proportional to the voxel fluid velocity.

Analytical expressions are developed to quantify the correlation between local fluid density and fluid displacement. When the correlation discussed above is negligible our analysis shows that we may strightforwardly obtain the image flow distribution from the spin density and velocity distributions. The formula is tested against actual distributions. The analytical approach has allowed us to refine the interpretation of voxel phase change and to assess the limitations of this type of velocity measurement. This work leads naturally to new applications of NMR microscopy aimed at understanding the relationship between microscopic and macroscopic features of fluid flow in porous media.

References

1. D.N. Guilfoyle, P. Mansfield, K.J. Packer, Fluid flow measurement in porous media by echo-planar imaging. *J. Magn. Reson.* **97**, 342-358 (1992).
2. P. Mansfield, K.J. Packer, Fluid transport in porous rocks. I. EPI studies and a stochastic model of flow.*J. Magn. Reson.* **A 122**, 137-148 (1996).
3. P. Mansfield, B. Issa, Fluid transport in porous rocks. II. Hydrodynamic model of flow and intervoxel coupling.*J. Magn. Reson.* **A 122**, 149-156 (1996).
4. J. O. Seymour, P.T. Callaghan, Generalised approach to NMR analysis of flow and dispersion in porous media. *AICHE Journal* **43**(8), 2096-2111 (1997).

O24

Settling in Concentrated Suspensions

S. Altobelli, J. D. Seymour, *New Mexico Resonance*
L. Mondy, *Sandia National Laboratories*
Albuquerque, NM, USA

Phase separation in suspensions is an important practical problem with a long and interesting literature, complete with classic papers[1], use of modern techniques like NMR imaging[2,3], and interesting open questions[4]. We have developed a rapid NMR imaging based method for evaluating the primary determinant of the settling process in sedimentation, i.e., the so-called "hindered settling function" $G(\phi)$. This function describes the reduction of fall speed in a suspension of solid fraction ϕ compared to the Stokes velocity of an isolated particle. Our simple technique uses a time series of vertical profiles of liquid fraction $\rho_c = 1 - \phi$, obtained by 1-dimensional imaging, to numerically estimate the partial derivatives of ρ_c. The continuity equation in one dimension can be arranged to give

$$\frac{\partial u_c}{\partial y} = \frac{-\frac{\partial \rho_c}{\partial t} - u_c \frac{\partial \rho_c}{\partial y}}{\rho_c} \qquad [1]$$

where u_c is the continuous (liquid) phase velocity. We assume the liquid velocity is initially zero to start the calculation, then for each time step use [1] to estimate $\frac{\partial u_c}{\partial y}$, numerically integrate to get u_c, then use it in evaluating [1] for the succeeding time step. In a single batch sedimentation experiment, values of G from the initial concentration up to the maximum packing fraction are determined in this way.

When nmri-$G(\phi)$ was measured for a poly-disperse suspension, the experimental data suggested an *ad hoc* modification to the form of G that has proven useful in finite element suspension modeling. Suspensions characterized by Nmri-$G(\phi)$ have been used in studies of viscous resuspension in a vertical cylindrical Couette flow device, and settling in a container with non-uniform cross-section. In viscous resuspension, shear induced migration and gravity interact to determine the distribution of the phases, which has been measured with 2-dimensional NMR imaging. In settling experiments in a container with non-uniform cross-section, a movie-like display of NMR images shows early development of regions of pure liquid which drive the later stages of the flow, see Figure 1.

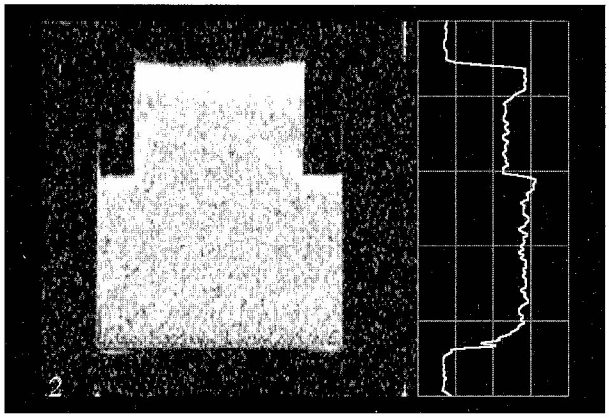

Fig. 1. 794 μm PMMA spheres sedimenting in a glycerol-water solution in a container with a step change in cross-section. Acquisition time was 36 s.

References

1. G. J. Kynch, "A theory of sedimentation" *Trans. Faraday Soc.* **48**, 166-176, (1950)
2. S. Lee, Y. Jang, C. Choi and T. Lee, "Combined effect of sedimentation velocity fluctuation and self-sharpening on interface broadening" *Phys. Fluids A* **4** (12) 2601 (1992).
3. Abbott, J. R., N. Tetlow, A. L. Graham, S. A. Altobelli, E. Fukushima, L. A. Mondy and T. S. Stephens, "Experimental observations of particle diffusion in concentrated suspensions: Couette flow," *J. Rheol.*, **35**, 773-795 (1991).
4. A. J. C. Ladd, "Hydrodynamic Screening in Sedimenting Suspensions of non-Brownian Spheres", Phys Rev Letters, 76 (8) , 1392-1395, (1996).

O25

Development of a compact MR Microscope using a 1.0 T Permanent Magnet

Tomoyuki Haishi, Yoshimasa Matsuda, Takaaki Uematsu, Katsumi Kose

Institute of Applied Physics, University of Tsukuba, Tsukuba 305-8573, JAPAN

Introduction

The limit of spatial resolution in NMR microscopy is believed to be ca. $(10\ \mu m)^3$ under a best condition: large amount of NMR sensitive nuclei (protons), narrow line width, and use of a high magnetic field (ca. 10 T). However, there are a lot of useful MR microscope applications in which spatial resolution around a hundred micron cube is sufficient. In such cases, permanent magnets have several advantages over superconducting magnets in **cost**, **maintenance**, **sample access**, **space**, and **portability**. However, because high field (ca. 1.0 T) permanent magnets using high performance magnetic material (e.g. *NdFeB* magnets) have a large temperature coefficient (–0.1 %/degree), long term drift of the resonance frequency should be overcome to obtain 3D MR microscopic images in which more than several hours of measuring time are usually required. In the present study, we have developed a compact MR microscope with a 1.0 T permanent magnet by achieving a stable field-frequency relation and acquired MR microscopic images at 50 μm in-plane pixel size and $(200\ \mu m)^3$ voxel volume in less than one hour.

Hardware And Methods

Figure 1 shows the overview of the MR microscope with a 1.0 T permanent magnet (Sumitomo Special Metals Inc., Osaka, Japan). The specification of the permanent magnet is as follows: field strength: 0.968 T (at 22 °C), gap: 61 mm, homogeneity: 12 ppm. over 20 mm dsv, magnet size: 62 cm (W) x 75 cm (H) x 75 cm (D), weight: 1,350 kg. The MRI unit is a portable system originally developed for the MR microscope with a magnetic field of a clinical MRI[1-3]. This unit consists of a TFT liquid crystal display, PC, RF modulator & detector, 3-channel gradient driver, and RF transmitter. Because the size of this unit is 54 cm (W) x 77 cm (H) x 60 cm (D) and the total weight is about 80 kg, this unit can be moved easily. All of the digital modules are assembled in the PC: a commercial DSP board (DSP6031, mtt corp., Kobe, Japan) using a TMS320C31 DSP chip for the MRI pulse programmer[4] (100 ns time resolution) and an ADC board (PC-414G3, DATEL) for data acquisition. The RF modulator & detector system has a bandwidth of 35-65 MHz. Two gradient probes (10 mm and 20 mm diam. bores) were constructed for this system.

In order to keep a field-frequency relation, two methods were applied: temperature regulation of the magnet and NMR lock. The temperature control was performed using thermal insulation with polystyrene foam slabs (30 mm thickness) and a temperature control unit consisting of a Pt temperature sensor, PID control unit, and couple of plane heaters. The nominal precision of the PID control unit was 0.1 degree. NMR lock was performed using a spin echo of the specimen itself. The frequency shift was measured with a frequency derivation of the detected signal at the echo center, and the source frequency was changed using a direct digital synthesizer board (Figure 2, FSW01, DST Inc., Japan) mounted on the ISA bus.

Experiments

Figure 3 shows the drift of the precession frequency measured every 90 seconds using the spin-echo signal when the magnet temperature was regulated at 35.0 degree. About 2 kHz drift was observed in a whole day: this result suggested that the temperature change of the magnet would be around 0.05 degree. This field drift shows that NMR lock is indispensable for image sequences which require acquisition times more than about 15 minutes, because a typical pixel bandwidth is around

200 Hz for our system.

Imaging experiments were performed to evaluate this MR microscope system. Two samples were used to obtain 2D & 3D images respectively. A celery stem (~7 mm in diameter) was used for the 2D imaging and a cherry fruit (~20 mm in diameter) was used for the 3D imaging. The pulse sequences were the conventional 2D spin-echo sequence: TR/TE = 500/24 ms, sampling rate = 20 microseconds, matrix size = 256^2, pixel size = $(50\ \mu m)^2$, slice thickness = 2 mm, NEX = 4, and the 3D gradient-echo sequence: TR/TE/FA = 100 ms/5 ms/60 degree, sampling rate = 40 μs, matrix size = 128^3, voxel size = $(200\ \mu m)^3$, NEX = 1. In these experiments, the NMR lock was not used during the sequences.

Figure 4 shows a cross-sectional image of the celery acquired with the 2D spin-echo sequence. The total acquisition time was about 8 minutes. Structures around 100 μm are clearly visualized. Figure 5 shows a cross-sectional image of cherry acquired with the 3D gradient-echo sequence. This image achieves $(200\ \mu m)^3$ voxel volume and the total acquisition time was about 27 minutes. At present, because of complexity of the system programming, we have not yet installed imaging sequences in which the NMR lock sequence runs during the data acquisition sequence. However, we could achieve higher spatial resolution if the NMR lock is successfully combined and longer image acquisition time is used.

In conclusion, we have developed a compact MR microscope using a 1.0 T permanent magnet by achieving a stable field-frequency relation. The result shows a great promise of this type MR microscope.

References

1. Kose, K, et al., *Proc. Int. Soc. Magn. Reson. Med.* 6, 1924 (1998).
2. Kose, K, et al., *Proc. Int. Soc. Magn. Reson. Med.* 7, 2036 (1999).
3. Yoshioka, H, et al., *Proc. Int. Soc. Magn. Reson. Med.* 7, 2119 (1999).
4. Kose, K, et al., *Proc. Int. Soc. Magn. Reson. Med.* 6, 2021 (1998).

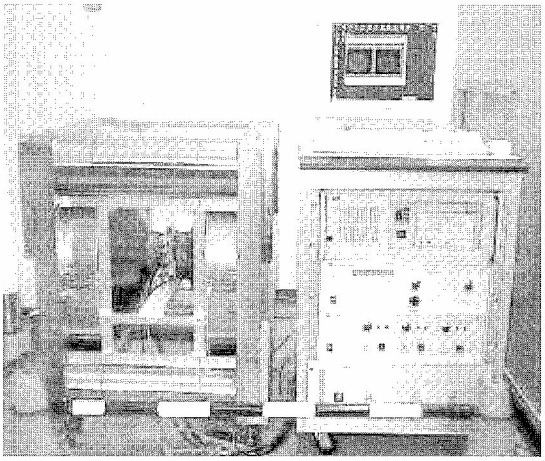

Fig. 1. Compact MR microscope with a 1.0 T permanent magnet installed within a 1 m^2 area.

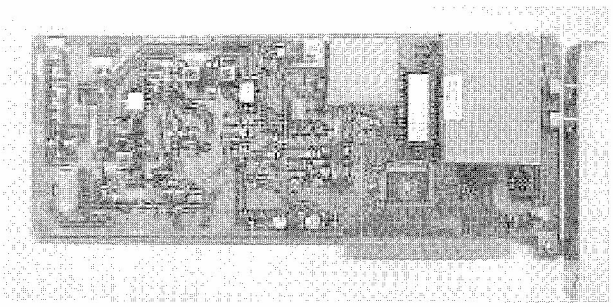

Fig. 2. Direct Digital Synthesizer for mounting on the ISA-Bus of a PC.

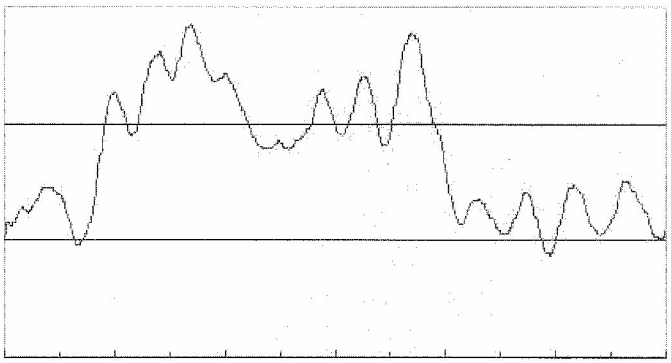

Fig. 3. Drift of precession frequency when the magnet temperature was regulated at 35.0 °C. The vertical scale divisions are 1 kHz.

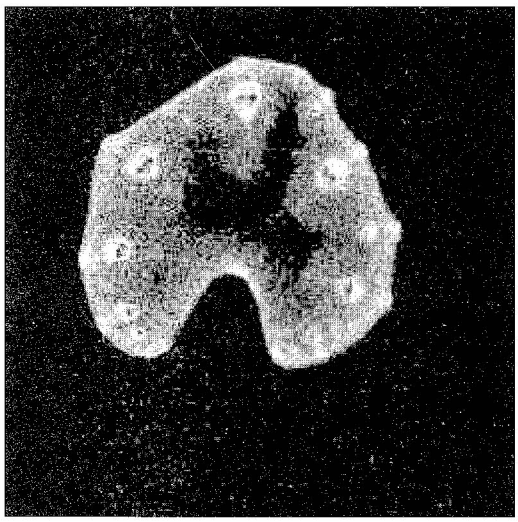

Fig. 4. 2D image of celery. FOV: 12.8 mm, 256^2 matrix, 50 µm pixels, 2 mm slice, measurement time ca. 7 min.

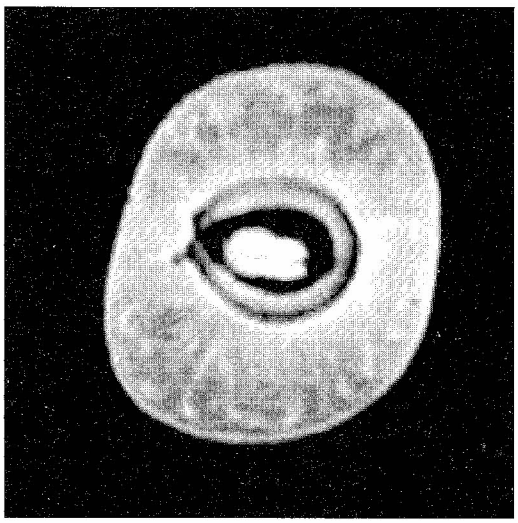

Fig. 5. Cross section taken from a 3D data set obtained from a cherry. FOV: 25.6 mm, 128^3 matrix, isotropic voxel dimension: 200 µm, measurement time ca. 27 min.

O26

Short Biplanar Gradient Coils for MR Microscopy Using Concentric Return Paths

Stephen Dodd and Chien Ho
Pittsburgh NMR Center for Biomedical Research and Department of Biological Sciences, Carnegie Mellon University, Pittsburgh, PA, 15213, USA.

Introduction

One of the main problems with MR microscopy experiments is sample preparation and access. Standard cylindrical gradient geometries provide strict limitations on the dimensions of the sample. Quadrupolar coils may be utilized for solenoidal radiofrequency (rf) coils, but these too limit sample geometry. For the study of samples on microscope slides, biplanar gradient coils are the obvious solution. Presented here is a design for a 3-axis gradient which allows easy access for microscope slide samples and for cylindrical samples and was designed specifically for use with rf microcoils. The design uses coaxial return paths similar to designs previously presented (1),(2),(3), but with a planar section forming the primary gradient generation part.

Design method

A simulated annealing algorithm was used for optimizing designs. The error function used only took into account the gradient strength at the midpoint of the coil, calculated using Biot-Savart summations. It was reasoned that once a basic coil geometry was chosen for each gradient direction, then gradient strength was of primary importance and that if the sample or rf coil was small enough, the gradient would be close to linear over the region of interest. To keep the design very simple and buildable, each half of the primary was kept to be one layer of wires with the distance between these adjustable. Shielding was attempted by adjusting the current density of the return paths through positional changes. Other parameters such as inductance and power dissipation were ignored.

Numerical Simulations

Figure 1a shows an example of an x-gradient design. The numerical simulations indicate a usable linear region (defined to be a 5% tolerance from the central value) of approximately 2 mm in diameter through the central planes of the gradient. This was considered sufficient for studies using microcoils. Similar results were obtained for the z and y gradients shown in Figures 2 and 3. The radii of the return paths were 10 mm.

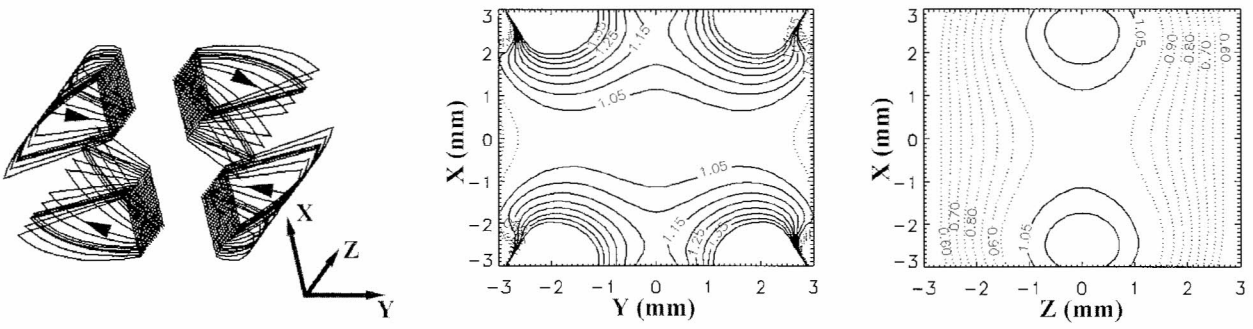

(a) (b) (c)

Figure 1 (a) example of a resultant x-gradient design. Arrows indicate the current direction in each quadrant. (b) contour plot showing deviations in field linearity from the central value in the x-y plane in levels of 5%; and (c) for the x-z plane.

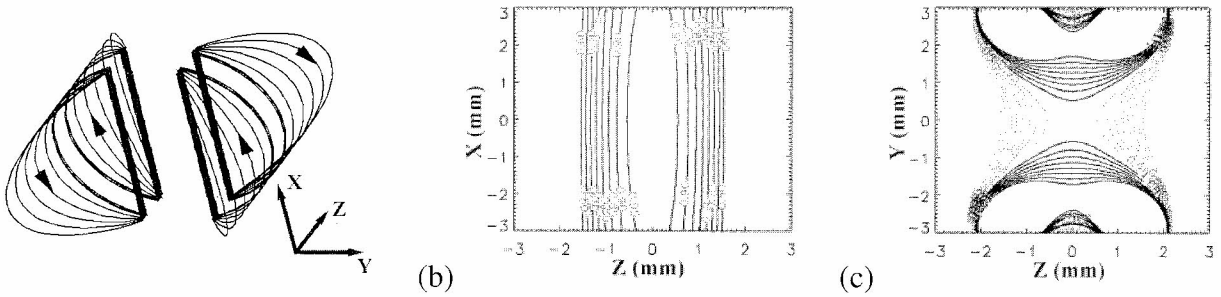

(a) (b) (c)

Figure 2 (a) example of a resultant z-gradient design. Arrows indicate the current direction. (b) contour plot showing deviations in field linearity from the central value in the x-z plane; and (c) the y-z plane.

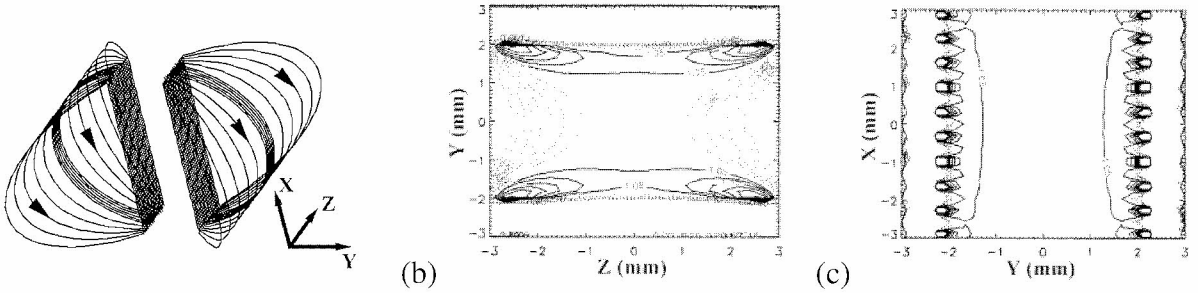

(a) (b) (c)

Figure 3 (a) example of a resultant z-gradient design. Arrows indicate the current direction. (b) contour plot showing deviations in field linearity from the central value in the y-z plane; and (c) the x-y plane.

In order to determine the effect of the shielding calculation, the resultant design was compared with one where the return paths do not spread out in a fan shape, but instead run parallel to the x-y plane, such as in Figure 4(a) for a y-gradient. The field was calculated parallel to the z-axis and at 5 mm from the return paths.

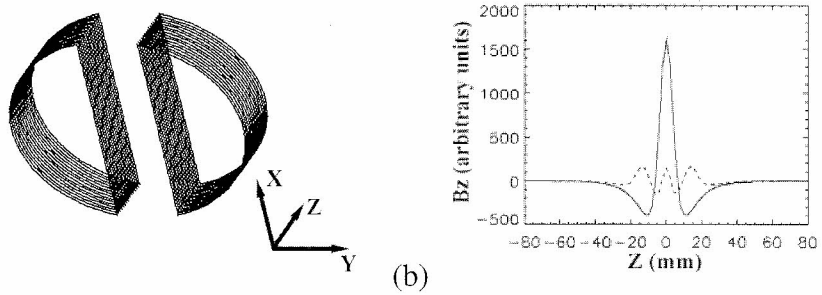

(a) (b)

Figure 4 (a) unshielded version of the y-gradient and (b) magnetic field profile 5 mm outside the return paths. The dotted line represents the shielded version. The rms value of the shielded field was 20% of the unshielded value.

It was noted that the distance between the coil halves could be adjusted somewhat and still provide a usable imaging region, leading to some leeway in the construction. It was also noted that if the central position was arbitrarily changed, then the contour plots shown above would give a linear region of at least a few hundred microns, large enough for the samples for which it will be used. This was tested at various positions up to 1 mm from the central point.

MR results

Prototype x and z gradient sets were built according to the described design except using two winding at each position of 32 AWG wire. The two gradient halves were separated by approximately 3 mm at the closest point. The initial sample used was oil contained in a 200 μm inner diameter tube. A 6 turn solenoidal coil was wound around the outer surface of this tube (500

μm diameter) using 38 AWG copper wire. 2-D images were taken using a 7T magnet equipped with a Bruker AVANCE console and using a gradient-echo sequence.

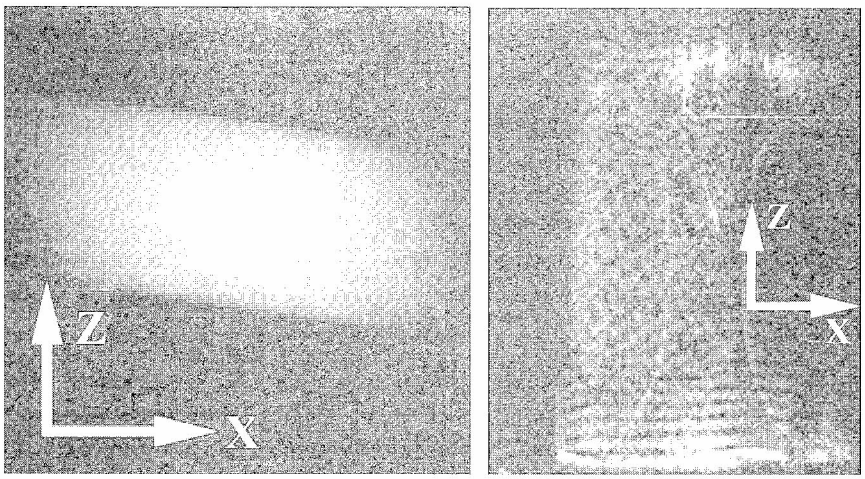

(a) (b)

Figure 5 (a) shows an image of the oil in the 200 μm tube. No distortions were observed surrounding the object, even though there is no internal structure to be seen. The z-gradient strength was estimated to be 2.0 T/m/A and the x-gradient strength was 0.7 T/m/A. (Calibration for the x-gradient was incorrect and so the tube should appear about twice as long.) It is expected that these figures would reduce somewhat with the addition of a y-gradient which would cause the distance between the gradient halves to be greater.

Figure 5 (b) shows an MR image of oil on a strip of copper in the presence of a 400 mesh copper TEM grid (bar spacing of 63 μm). Despite the foldback problems (highlighting the need for a small rf coil) seen in the image, the grid is seen to be resolved at a nominal resolution of 6 μm. Changes in the bar separation on the MR image represent show changes in gradient strength.

Possible improvements to the current prototype could include the addition of a cooling system, for which there is ample room in between the primary and the return paths. Adding more winding to the x-gradient may also be appropriate, as it will always be the furthest gradient from the sample, and is noted here to be about one third of the z-gradient strength.

Conclusions

A design for a three-axis gradient set with a planar section for the gradient generation and concentric return paths has been presented. Prototype x and z gradients were built and tested, providing high-resolution MR images with small rf coils.

Acknowledgements

The authors thank Don Williams for helpful comments. Supported by NIH research grants (RR-03631 and RR-10962) and the Whitaker Foundation.

References

1. Bowtell, R., Peters, A. Analytic approach to the design of transverse gradient coils with co-axial return paths. *Magn. Reson. Med.* 41:600-608. (1999).
2. Brey, W.W., Mareci, T.H., Dougherty, J. A field gradient coil using concentric return paths. *J. Magn. Reson. B* 112:124-130 (1996).
3. Doty, F. *et al.* Crescent gradient coils. US Patent 5,554,929 (1996).

O27

MRI with a Palm-Size Probe

Pablo J. Prado and Bernhard Blümich
Lehrstuhl für Makromolekulare Chemie, RWTH Aachen, Worringerweg 1, Aachen, D-52056, Germany.

Introduction

One-dimensional Magnetic Resonance Imaging has been accomplished using a palm-size NMR probe. The mobile scanning tool renders information in-situ in a non-destructive fashion from arbitrarily large objects. Fields of study include a wide range of heterogeneous specimens, with diverse materials such are polymers, soft tissues and porous media. Space resolution has previously been achieved employing the NMR-MOUSE [1] by lateral displacement of the probe over the sampled surface [2]. Millimeter scale resolution was associated to this process due to the dimensions of the sensitive volume.

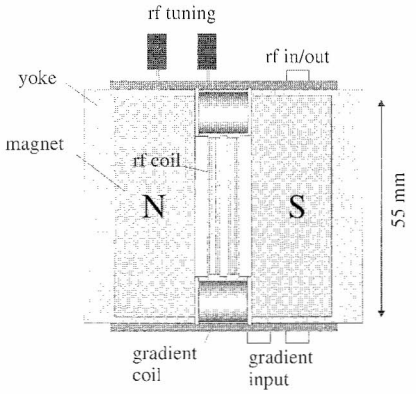

Fig. 1. Top view of the new palm-size (1.2 Kg) MRI probe. Static magnetic field at the probe's center is ~ 0.45 T. A Maxwell pair rf coil is displayed.

Magnetic field gradient coils were implemented in an NMR-MOUSE based device combining inside-out NMR and phase encoding imaging methods. A 15 mm field-of-view is attained without repositioning of the small probe (~50 x 50 x 50 mm^3). Figure 1 shows the probe configuration. Maxwell pair and self-tuned single-layer rectangular coils produce the rf field (dominantly perpendicular to $\mathbf{B}_0$) in an elongated region following the magnets gap. The benefits of this novel procedure include relaxation-time weighted profiles [3], diffusion constant assessment and the observation of dynamical processes. The acquired profile is a function of the characteristics of the sensitive volume and the system response to different heterogeneous excitation pulses.

Methods

The magnetic fields $\mathbf{B}_0$ and $\mathbf{B}_g$ generated by the permanent magnet and the gradient coils respectively were measured with a Hall probe. Figure 2 displays the contour lines for the z component of $\mathbf{B}_0$ (across the 14 mm gap) and its variation along the centre of the gap (x direction). The highly inhomogeneous polarizing field determines a proton resonance of 20 MHz at the centre of the probe and a monotonic strength decrease towards the edge of the magnets. A 4 % decrease in B_{0z} is measured over a 20 mm region in the center.

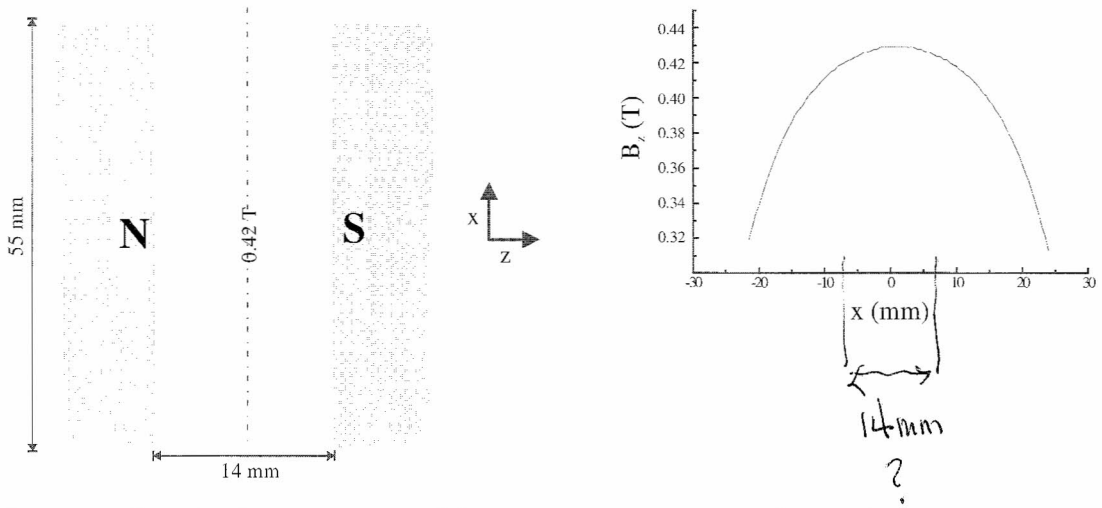

Fig. 2. Left, contour lines for the z-component of the static magnetic field. Right, parabolic-like behaviour of B_{0z} along the central region of the gap.

The additional magnetic field generated by the multi-layer 100 turn copper coils is shown in Figure 3. The gradient strength in the sensitive sector of the sample is estimated by a linear fit to these values along the probe's gap in a 20 mm region, resulting in $\delta B_{gz}/\delta x$=0.0146(2) T/m for a 1A current.

Under the current regime of the coils, the calibrated value determines a resolution of the order of 100 µm, at encoding times of ca. 100 µs. Resolution can be improved for slow decaying signals or at the expenses of reducing the field-of-view by a smaller rf excitation coil and reduced spacing between gradient coils.

Contour maps of the field produced by the imaging coils determined a non-significant variation of the field across the gap in the sensitive region. As a result of the short-lived signals in the NMR-MOUSE, a spin-echo phase-encoding technique was used for imaging. Space resolution in the read direction (static field) is not recovered due to the strength of the underlying gradients (ca. 10 T/m [2]).

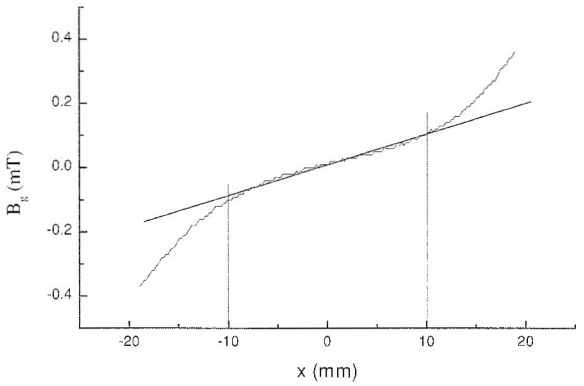

Fig. 3. z component of the magnetic field generated by the antiparallel gradient coils. The bench test current is 0.70 A. The straight line represents a linear fit to the data over the sensitive region.

Results and Discussion

Imaging tests were performed with a Bruker DSX console and Techron 7541 power amplifiers. The sensitive region of the new probe was estimated to be 15 mm along the magnets gap by displacing a thin rubber sample along the probe. A depth of over 3 mm was reached by a rectangular (7 x 27 mm^2) rf coil. The rf pulse was calibrated by using identical timing for 90° and 180° excitation and varying the power attenuation. Due to time constrains the phase encoding gradient was switched on after the second pulse and switched off before the echo acquisition. The profiles were rendered by Fourier transformation of the echo maximum. Figure 4 displays x profiles for a rubber band phantom and for an homogeneous SBR sample. In both cases the specimen is larger than the field-of-view and the resolution is estimated to be 300 µm. 64 phase encoding points were acquired and the original reciprocal-space data set was zero filled to 256 points before the Fourier transformation.

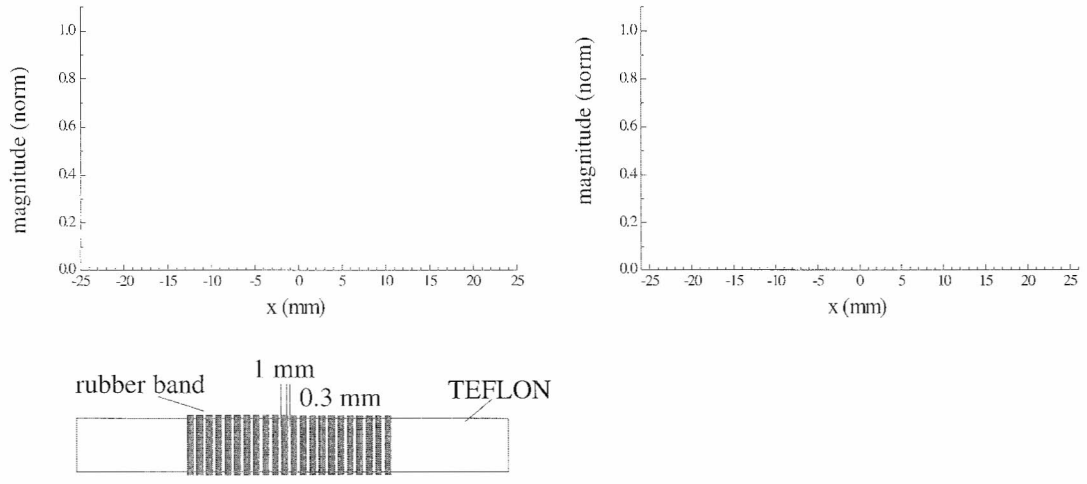

Fig. 4. 64 point (zero filled data to 256) one-dimension profiles obtained with the NMR-MOUSE. Encoding time was 100 µs. Echo time was 300 µs. Left, heterogeneous multi-turn commercial rubber band phantom (bottom) and 1D map (top). Right, uniform 20 mm SBR sample showing the shape of the sensitive region.

T_2 weighted profiles are obtained by changing the echo time (TE) and keeping the encoding time constant [3]. For full recovery between recycle delays or for constant T_1 over the sample,

$$\rho'(x, TE) = \left|FT[S(k_x, TE)]\right| = \int\int_{yz} \rho(x, y, z) \exp[-\frac{TE}{T_2(x, y, z)}] \Delta(\omega_{rf}, x, y, z, t_{pulse})\, dydz$$

$$\approx \rho(x) \exp[-\frac{TE}{T_2(x)}] \Delta(\omega_{rf}, x, t_{pulse})$$

where Δ describes the sensitive volume, ω_{rf} is the excitation frequency and t_{pulse} is the hard pulse duration.

Three natural rubber samples were prepared for this experiment. The rubbers were cut and positioned with a thin gap among them. Selected rendered profiles and the signal decay corresponding to one of the samples are plotted in Fig 5. The spin-spin relaxation time is then computed for different points along the profile.

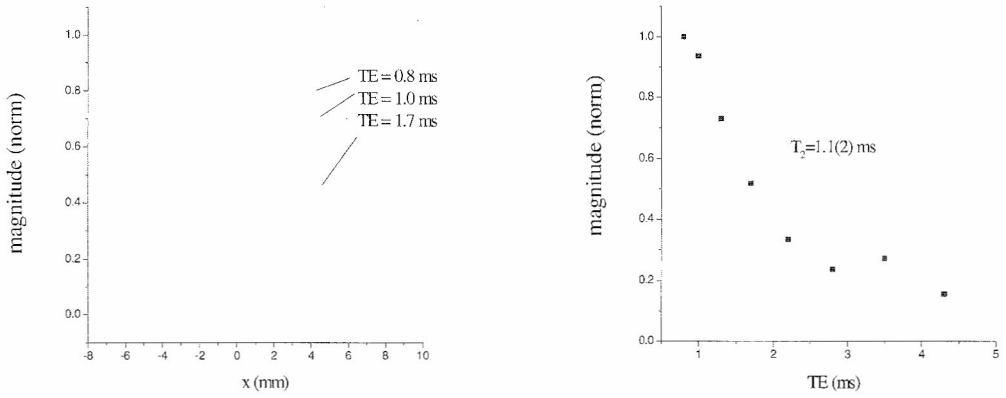

Fig. 5. Left, T_2 weighted 1D profiles of three natural rubber specimens. Right, signal decay for the left specimen. The full line corresponds to a single-exponential fit to the data.

Conclusion

A new low frequency (20 MHz) portable probe for space resolved NMR studies was built. Two gradient solenoid coils and an rf excitation probe positioned in the gap between antiparallel polarizing permanent magnets allowed for 1D maps over a 15 mm field-of-view. The weight of the scanner is about 1 Kg and can be driven by a small size NMR console.

The gradient coils produced a close to constant field gradient over the field-of-view. Due to the high inhomogeneous underlying static fields a single-point spin-echo phase encoding sequence was used for the imaging procedure. The potential of the technique was shown by the MRI measurements on heterogeneous rubber specimens, presenting spin-spin relaxation times of the order of 1 ms. T_2 contrast on the profiles was achieved by data acquisition with different echo delays and constant phase encoding time.

References

[1] Eidmann, G., et al., *J. Mag. Reson. A,* **122**, 104 (1996).
[2] Blümich, B., et al., *Mag. Reson. Imaging*, **16**, 479 (1998).
[3] Prado, P. J., et al., *J. Magn. Reson.* Sent for publication.

O28

Mapping the Refractive Index Distribution in Crystalline Lenses Using Transverse Relaxation (T_2) Imaging.

B. A. Moffat and J. M. Pope

Centre For Medical and Health Physics, School of Physical Sciences, Queensland University of Technology, GPO Box 2434, Qld, Australia, 4001.

Introduction: The inability to accommodate and focus on near objects (presbyopia) occurs in almost all humans between the ages of 40 and 50 years. It is believed that this is due to a decrease in lens power and lens elasticity. Paradoxically the lens increases in thickness and curvature which should result in an increase in power. In attempting to understand how this "lens paradox" can occur, models of lens refractive index distribution have been used (Smith et al., 1991), but only very limited experimental measurements are available to confirm the validity of these models. Previous studies have shown that both the water transverse relaxation rate (R_2) (Hills et al., 1989) and refractive index (Pierscionek et al., 1987) can be correlated with protein concentration. We have utilised these correlations, in combination with magnetic resonance microscopy (MRM) to measure refractive index distributions in the human lenses, with the aim of providing new insight into the causes of presbyopia and the "lens paradox".

Methods: We used a Carr Purcell Meiboom Gill (CPMG) pulse sequence to measure R_2 and an Abbe refractometer to measure refractive index. R_2 was measured for lens protein homogenates of different refractive indices. R_2 maps of intact human lens were acquired using a modified CPMG pulse sequence. All NMR measurements were acquired at an *in-vivo* eye temperature of 34.5 °C.

Results: In human lenses it was found that there is a distribution of single exponential R_2 constants within the lens, ranging from ~$10s^{-1}$ in the cortex to ~$60s^{-1}$ in the nucleus (Fig.1). The R_2 values measured for lens homogenates showed a strong and significant correlation ($p<0.01$) with refractive index. Therefore from maps of R_2, it was possible to calculate maps of refractive index distribution (Fig. 2).

Discussion: Significant differences in lens shape and refractive index distribution between old and young lenses were observed. Notably there is an increase in the thickness of the anterior cortex region with age. The experimental results also show that the gradient of refractive index is higher in the posterior cortex than in the anterior cortex. This differs significantly from current models used for understanding the role of a refractive index gradient in human lens optics.

Conclusion: The refractive index distribution in the human lens is extremely important for understanding the optics of the human lens. This research has shown that it is possible to measure this distribution using non-invasive MRM. The results of these measurements show subtle but potentially important differences in refractive index distribution from those currently used in models of the lens refractive index gradient. The results also provide new insight into changes in the refractive index distribution with aging. These changes may contribute to presbyopia and help to explain the "Lens paradox".

References.

Hills, B. P., Takacs, S. F. and Belton, P. S. (1989) *Molecular Physics,* **67,** 903-18.
Pierscionek, B., Smith, G. and Augusteyn, R. C. (1987) *Vision Research,* **27,** 1539-41.
Smith, G., Pierscionek, B. K. and Atchison, D. A. (1991) *Ophthalmic And Physiological Optics,* **11,** 359-69.

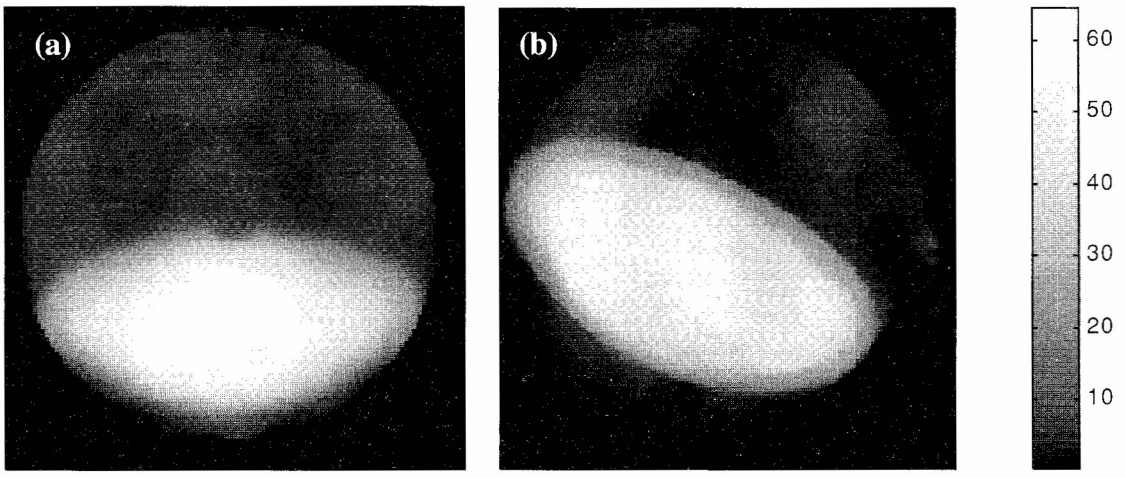

Figure 1: Transverse Relaxation Rate (R_2 (s^{-1})) maps of a human lenses, aged 14 years (a) and 86 years (b). FOV = 11mm.

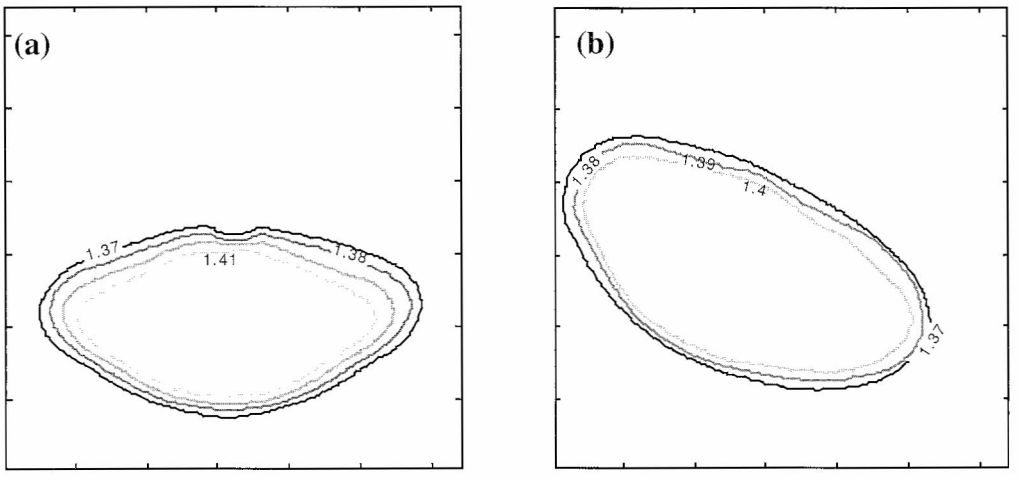

Figure 2: Refractive index contour maps of a human lenses calculated from R_2 maps, aged 14 years (a) and 86 years (b).

O29

Dynamic NMR imaging of chromatographic columns

Sally Harding[a], Herbert Baumann[b]

[a] Department of Chemistry, Swedish University of Agricultural Sciences, Uppsala, Sweden

[b] Amersham Pharmacia Biotech AB, SE 751-84, Uppsala, Sweden

Introduction

The aim of this project was to evaluate the potential of dynamic NMR microscopy to give information to aid the design of commercial chromatographic separation columns. Experimental techniques which provide insights into solvent flow characteristics through the column are desired to help relate the macroscopic column performance to the underlying transport behaviour of the solvent flow and improve rational evaluation and development of new column designs and packing techniques. Two types of chromatographic systems have been used in this study: commercially available pre packed Pharmacia 1 ml High Trap columns and syringe based columns prepared with different packing densities, manufactured by compressing the columns with varying pressures resulting in columns packed with 18.2, 22.7, and 25 µl gel/mm - for convenience these columns will be refereed to as 'colA', 'colB' and 'colC' respectively in the following text. The packing material used in both cases was based on Sepharose high performance (Sepharose HP) which is spherical highly cross linked agarose, (6%), with a particle diameter, d_p of 34 ± 10 µm. The NMR data has been interpreted in terms of the reduced Height Equivalent to a Theoretical Plate (HETP) characterising the column performance.

Methods

The NMR measurements were made using a Bruker DRX 600 MHz spectrometer equipped with a micro imaging accessory. The column was positioned in the 10 mm rf coil and de-ionised - de-gassed water was pumped through the system using a dual syringe pump. The progression of an 100 µl injection of D_2O through the column was monitored by observing vertical 2D slices using a rapid FLASH imaging sequence. This experiment was used to highlight the influence of the column inlet and outlet on band spreading effects. Images were acquired at approximately 5s intervals and subsequent images compared to the first image so that the loss in intensity due to the presence of D_2O could be visualised. Bulk PGSE measurements were made with the diffusion gradient aligned both parallel and perpendicular to the main flow direction to study the effect of flow velocity on the signal attenuation and to determine a suitable value for the diffusion time, Δ, to be used in the dynamic imaging experiments. Velocity and dispersion images were measured using a phase encoding method [1]. In each experiment 8-16 images where acquired in which the magnetic field gradient, g, used to encode for motion was successively stepped in magnitude. Typically the flow gradient duration, δ, was 0.5 ms, the strength of the flow gradient, g, was incremented from 0 to 25 G/cm, and the gradient separation time, Δ, was 200 ms. The in plane image resolution was between 40-60 µm and the imaging slice thickness was 1 mm. Velocity and dispersion maps were calculated by fitting the flow propagator obtained for each pixel in the image to a gaussian distribution. Velocity and dispersion maps were measured both parallel and perpendicular to the main flow direction, at a variety of flow rates, ranging from 0 to 2 ml/min.

Results and Discussion

Typical images of the flow of a 100 µl injection of D_2O through the column are shown in Fig. 1, which shows the inlet of the column and allows the effect of the column inlet on the band dispersion to be studied. The upwards curvature of the bands toward the edge of the column is clearly a consequence of the inlet design. The injected sample takes longer time to travel to the outer region of the column and thus lags behind the sample that flows into the central region. This band curvature remained apparent as the D_2O injection moved along the complete length of the column. The definition of reduced HETP, h, as the slope of the dependence of the band variance, σ, on migration distance, $h = \frac{1}{d_p}\frac{\partial \sigma^2}{\partial z}$, allows the HETP to be estimated directly from the imaging experiment [2]. For example at a flow rate of 0.5 ml/min for the 1 ml Hi Trap column a value of 1 ± 0.5 is obtained for h.

Analysis of the echo attenuation data from the bulk PGSE measurements in the form of Stejskal-Tanner plots showed a deviation from linear decay with q^2, as q increases and this deviation decreased with increasing Δ, see Fig. 2(a). However in the low q limit - defined as $4\pi^2 q^2 \Delta D_{ap} < 1$, the signal attenuation was linear with q^2, and can be used to calculate the effective diffusion or dispersion coefficient. The dispersion coefficient, showed a small but significant increase with increasing diffusion time Δ, for Δ values up to 200 ms. To insure that the dispersion coefficient was universal, and independent of Δ, and the flow propagator had a gaussian distribution Δ was set to 200 ms in the subsequent PGSE and imaging experiments.

The data can again be presented in the form of reduced HETP, $h_{PGSE} = \frac{2D_{ap}}{ud_p}$ and reduced velocity $v = \frac{ud_p}{D_m}$ [3, 4 and 5]

where u is the average cross sectional area velocity and D_m is the diffusion coefficient of the free solvent. The variation of h_{PGSE} with v was found to be well described by the knox equation as shown for example in Fig. 2(b).

Typical maps of velocity and dispersion for a 1 mm thick cross section through the Hi Trap column are shown in Fig 3, and typical fits of the flow propagator to the gaussian distribution are shown in Fig. 2(c). Both the maps of velocity and dispersion show strong edge effects, with a region of higher than average velocity and dispersion, approximately 1 pixel wide (40 μm or approximately one particle diameter), at the column wall, there is also a region of lower than average velocity, 4-5 pixels wide (150 μm or 4-5 particle diameters). The central region of the column, shows slight heterogeneites. This can be compared to the results reported in [6] where no radial variation in velocity across axially compressed columns was seen. The heterogenities in the velocity distribution were quantified in terms of a reduced HETP, h_{imag} which was calculated as the ratio of the variance in the velocity distribution, σ_v to the mean velocity over the column cross section, $h_{imag} = \frac{\sigma_v}{ud_p}$. For example a value of h_{imag} of 0.8 was calculated at a flow rate 2 ml/min for the Hi Trap column.

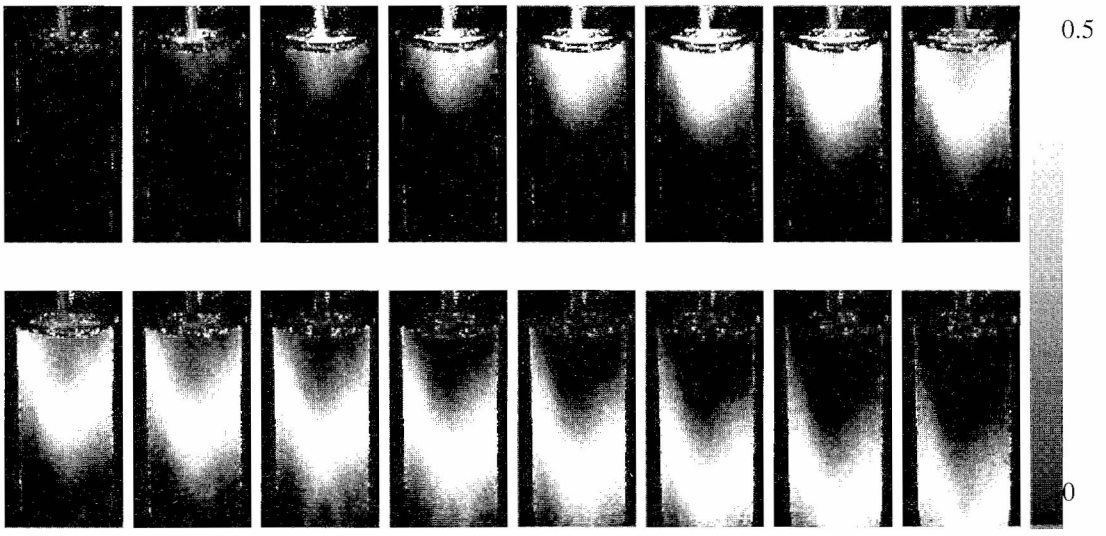

Fig. 1 NMR images of injection of D_2O passing through the 1ml Hi Trap column at a flow rate of 0.5 ml/min. The intensity scale shows the fractional loss in signal intensity relative to the first image. The images were acquired at intervals of 5.24 s. The field of view of the displayed images is 9.38 mm in the horizontal direction and 18.75 mm in the vertical direction.

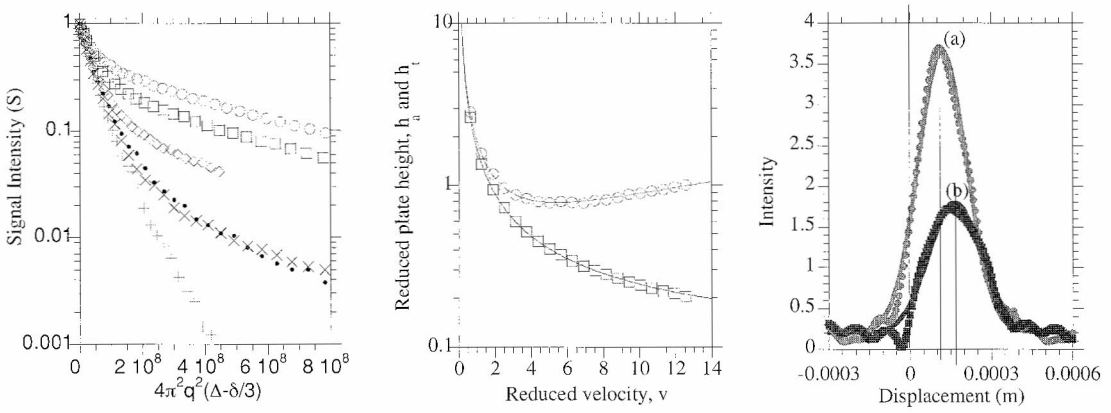

Fig. 2(a). Stejskal-Tanner plot of modulus of the echo attenuation, S as a function of $4\pi^2 q^2(\Delta - \delta/3)$ for the 1 ml Hi Trap column at flow rate of 2 ml/min using diffusion time Δ of (○) 20 ms, (□) 50 ms, (◇) 100 ms, (×) 200 ms and (+) 400 ms and (●) double PGSE with Δ of 200 ms

Fig 2(b). The axial, h_a, (○) and transverse, h_t, (□) reduced plate heights verses the reduced flow velocity for Col B and fit the knox equation. $h_a = B/v + Av^n + Cv$ (A = 0.128 ± 0.008, B=1.717 ± 0.009, C=0.0447 ± 0.001) $h_t = B/v + D$ (D = 0.084 ± 0.002)

Fig. 2(c) Dynamic displacement profile for water in two different pixels in syringe column (Col A) with a flow rate 1 ml/min. The data are taken from two individual pixels, (■) at the outer edge of the column, (velocity = 0.817 ± 0.007 mm/s, dispersion = 22.3 ± 0.8 10^{-9} m^2s^{-1}) and (●) from the middle of the column (velocity = 0.594 ± 0.003 mm/s, dispersion = 19.7 ± 0.3 10^{-9} m^2s^{-1}). Solid line shows fit to Gaussian distribution.

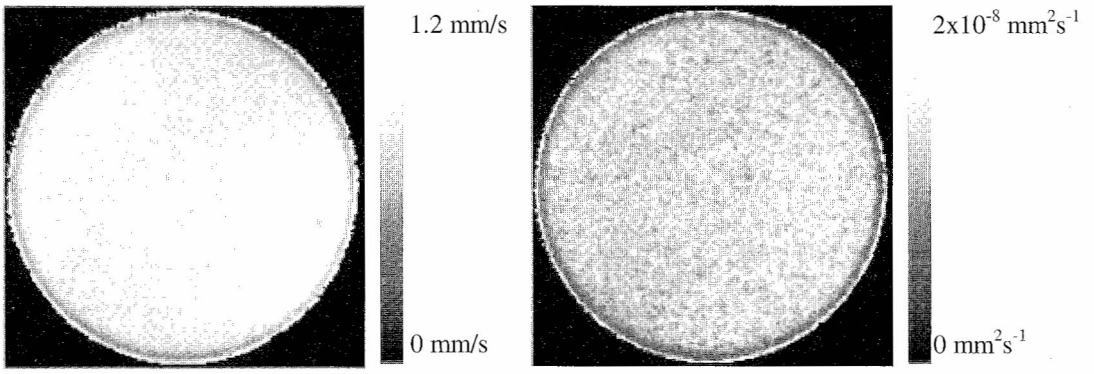

Fig 3(a) Velocity map and (b) dispersion map of horizontal cross section of 1ml Hi Trap column at a flow rate of 2 ml/min. The slice thickness is 1mm, the in plane pixel resolution is 39 μm and the PFG gradient is parallel to the flow direction

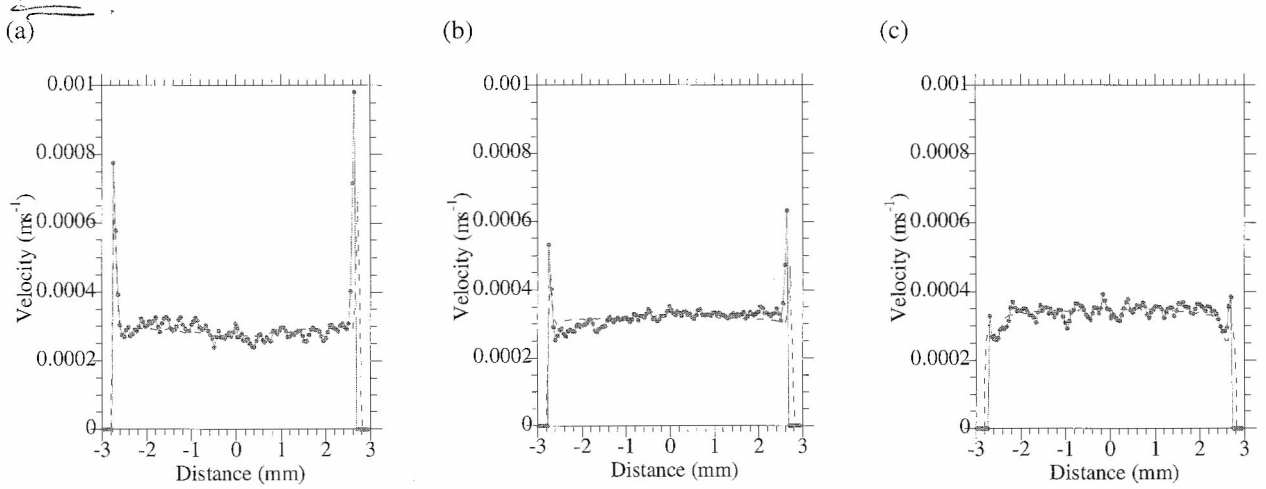

Fig. 4 (a), (b) and (c) Plots of velocity for (–●–) a single pixel row and (- - - -) the radial average value extracted from velocity of col A, B and C respectively at a flow velocity of 0.5 ml/min

Fig. 4 shows typical profiles and the radial average profile, calculated from velocity maps of the three syringe columns studied acquired at a flow rate of 0.5 ml/min . As for the Hi Trap column we see a region of higher than average velocity at the column wall, The most densely packed column shows a region of reduced velocity toward the outer region of the column. The value of h_{imag} calculated as described above at a flow rate of 0.5 ml/min for the three columns are 1.05, 0.287 and 1.405 for colA, colB and colC respectively. This shows that in terms of minimising the band spreading due to spatial heterogeneities in the velocity distribution the syringe packed with the medium packing density appears to be most efficient.

Conclusions

In this work we have demonstrated the use of NMR imaging, bulk PGSE measurements and NMR velocity imaging to study solvent flow in chromatography systems. From each of the NMR techniques employed it has been possible to make an assessment of the HETP characterising the solvent flow, over the time and length scale applicable to the particular technique. Comparison of the HETP so determined can give an indication of the varying importance of the contributions of the different mechanisms to the overall band spreading observed in chromatography.

References

[1] Callaghan, P. T. and Xia, Y., *J. Magn. Reson.*, **91**, 326 (1991).
[2] Mitchell, S. N., Hagel, L. and Fernandez, E. J., *J. Chromatography A*, 779, 73 (1997).
[3] Baumeister, E. *et. al.*, *J. Chromatography A*, **694**, 321 (1995).
[4] Tallarek, U., Bayer E., and Guiochon, G., *J. Am. Chem. Soc.*, **120** 1494 (1998).
[5] Tallarek, U., *et. al.*, *AIChE Journal.*, **42**(11), 3014 (1996).
[6] Tallarek, U., *et. al.*, *AIChE Journal.*, **44**(9), 1962 (1998).

O30

MRI 3D Velocity Mapping in a Sphere Packing: Visualization and Velocity Propagators

A.J. Sederman [1], L.F. Gladden [1], B. Manz [2]

[1]Department of Chemical Engineering, University of Cambridge, United Kingdom
[2]Fraunhofer-Institut für Biomedizinische Technik, St. Ingbert, Germany

Introduction

Phase shift MRI Velocimetry has been used to investigate the single-phase flow field in the void space created by a packing of solid spheres in a cylindrical column. A packing of spheres is investigated because of its use in fixed bed reactor technology in the chemical industry and as a model porous medium for studies of ground water remediation and oil recovery. Fully resolved 3D velocity images with high isotropic resolution equivalent to 26 and 14 voxels per sphere diameter were acquired in a packing of glass spheres of 5 mm diameter in a column of 46 mm diameter. Velocity images in 3 orthogonal directions (x, y and z) were obtained so that the velocity vector for all points in the void space could be defined. Velocity distribution in the z (superficial flow) direction shows an exponential distribution of positive z velocities as previously observed, however due to the removal of diffusion effects, the x velocity distribution was not Gaussian. A void space image was used to characterise the pore space such that flow through individual pores could be defined and the effect of void structure on the flow could be examined. Significant heterogeneities in the flow were observed. The isotropic resolution enables the production of a shear strain and shear stress map. Velocity vectors at all points allow the construction of streamlines and, by taking diffusion into account, velocity propagators, similar to those produced by PFG measurement, are acquired. The agreement between those produced from the 3D velocimetry and by PFG measurements is very good.

Method

A consolidated packing of 5 mm ballotini in a 46 mm i.d. column was filled was used in this study. A 4.7 T vertical bore magnet with a 63 mm diameter bird-cage radio-frequency coil was used. The velocity imaging sequence included slice selection in the z direction, with two phase encoding directions and a pair of velocity encoding gradients. To obtain three velocity components, phase differences in three orthogonal directions were measured acquiring a total of four 3D images. Two sets of velocity images are reported here. The higher resolution images, acquired with a field-of-view of 50×50×6.25 mm and isotropic resolution of 195 μm thereby producing a data matrix of 256×256×32 voxels were acquired for deionised, degassed water as the fluid. The images of lower resolution were acquired for flow of an 80 % glycerol in water solution; this concentration was used so that the Reynolds number characterising the flow was approximately 0.01 thereby removing the possibility of inertial effects. For these images, the field-of-view was 47×47×47 mm, yeilding an isotropic resolution of 367 μm.. The increased field-of-view in the z direction allowed streamlines to be followed over many sphere diameters. Maximum gradient strengths of 8.3 G/cm and 6.9 G/cm were used in the axial and radial direction respectively to encode the flow. An observation time, Δ, of 10 ms and flow rate of 1 ml/s were used ensuring that the motion during the observation time was small compared to the pore size and the voxel size. A zero velocity image was acquired to remove eddy current effects. The pore space was characterised and divided into individual pores using a pore space partitioning algorithm developed by Baldwin *et al.* (1996). To form the propagators, seeding points were used at every void space voxel in the top 20 slices in the image. Propagators were calculated from the flow visualisation. This corresponded to approximately 120000 seeds. The propagators were generated by incrementing the position of the seed, with the inclusion of a diffusive jump, at time intervals of 50μs and recording their displacement. Displacement propagators were also acquired experimentally for a packing of 1.0 mm ballotini with the same column-to-particle diameter ratio. An alternating PGSTE sequence was used.

Results and Discussion

Velocity images taken of water flow in the sphere packing is shown in figure 1. A shear map corresponding to τ_z is also shown. The white lines through the images show where the orthogonal images have been taken. Large areas of the bed are seen to contain almost stagnant fluid whilst there are a few high velocity channels, these are particularly prevalent at the column walls. The distribution of velocities in axial or radial directions, obtained from the distribution of velocity values for all the voxels, show that in the z direction there is an exponential tail for positive flow. These results are is similar to those obtained from PFG propagator measurements in sphere packs and in other porous media. In the x and y directions the velocity distributions are centred on and symmetrical about zero and are also found to have exponential tails to both positive and

negative velocities. This is in contrast to the distributions acquired by PFG measurements that produce Gaussian shapes. This is explained by the dominance of diffusive motion over coherent motion at low Péclet numbers (Pé). Most PFG studies have been done at low Pé to allow investigation of fluid motion over several pores. In the axial direction, where the magnitude of the coherent motion is larger, the exponential tail is still observed. Previous results have shown large heterogeneities in the flow for a single slice in the xy plane (Sederman *et al.* 1997). The heterogeneity is such that 40 % of the flow travels through only 15 % of the pores whilst many of the pores contain essentially stagnant fluid. The flow through a pore depends not only its characteristics but also on the topology of the surrounding pore space. The segregation of the pore space allows calculation of flow through pore necks and mass balances on the flow through pores confirms the quantitative nature of the technique. Despite the low Reynolds (Re) number used in this experiment evidence of inertial effects were found in some of the pores for the image taken with Re = 3 and in the direction of superficial flow. The image recorded for Re = 0.01 did not show these inertial effects. Shear strain maps are generated from the velocity maps and all 6 independent components are calculated. Figure 2 shows the shear components τ_{xy} and τ_{xz}. These are generated from the velocity maps such that

$$\tau_{xy} = \tau_{yx} = \frac{\mu}{2}\left(\frac{du_x}{dy} + \frac{du_y}{dx}\right)$$

Total stresses in the liquid and forces on the sphere surface are calculated. Large differences in the stress map are observed and areas likely for deposition and abrasion can be predicted. Displacement propagators for fluid flow in the sphere pack were acquired from the velocity image. At low Re (approximately below 1) the flow field should be totally dominated by viscous forces with inertial forces being insignificant. It therefore follows that the flow pattern is independent of pressure drop/superficial velocity as long as Re is low enough. When calculating the propagators, the input parameters including the scaling for the velocity, diffusion and ballotini size can be altered to specify the Péclet number. In this way the propagators are compared to PFG results for a packing of 1 mm spheres. Comparisons between PFG propagators and propagators from the 3D image are shown in figure 3 for average fluid displacements of 0.16 and 1.6 sphere diameters. The agreement is very good and the transition from an exponential distribution to a Gaussian distribution as the observation time is increased is seen. The propagators are calculated for a much greater range of observation times (from 1 ms to 100 s) than is possible to obtain experimentally using PFG measurements. Other advantages of this method of propagator generation is the ease of gaining extra information, such as how the starting position affects the propagators, for a very limited increase in computer time. The effect of sphere size, at constant velocity and diffusion, is observed. The propagators generated in the z direction for equivalent particle distances of 1 sphere diameter are shown sphere diameters of 5 mm and 0.5 mm for water (D=2.2e-9 m^2/s) at a superficial velocity of 0.44 mm/s. Although two peaks in the propagators are seen for both sphere sizes, the propagators look very different with the two peaks appearing much more distinctly for the larger spheres. The Péclet number for these two propagators may be equated by decreasing the diffusivity of the fluid in the 0.5 mm sphere pack by an order of magnitude. This propagator is also shown in figure 3 and is seen to be very similar to the propagator predicted for the 5 mm sphere pack with the same Péclet number. The two peaks observed correspond to fluid remaining in single pores and fluid that has passed through several pores over the observation time. The more distinct peaks seen at higher Péclet number may be attributed to the greater diffusive movement needed to move from a stagnant region to a flowing region or from a high velocity channel to a slow flowing region. For the smaller packing, therefore the two peaks from separate regions of the packing become less distinct. Propagators for different seed starting points in the packing structure and 2D propagators in the xy and xz direction have also been calculated.

Conclusions

3D velocity imaging has been used to investigate the flow field in a packing of spheres. The distribution of velocities in the absence of diffusivity effects is found to be exponential for positive z velocities and for both positive and negative velocities in the x and y directions. Heterogeneities in the flow are observed and the effect of the local pore structure on flow is investigated. Shear strain maps are produced showing forces on the solid surface during fluid flow. Propagators for a large range of observation times are calculated. These are compared to PFG measurements acquired in a packing of the same aspect ratio and agree very well over the range of observation times acquired. The effect of sphere size and Péclet number is investigated and shown to significantly change the shape of the propagators.

References

Baldwin, C.A., *et al.* J. Colloid Interface Sci., **181**, 79-92 (1996).
Sederman, A.J., *et al.* Chem. Engng. Sci., **52**, 2239-2250 (1997).

Figure 1 Velocity visualisations in 3 orthogonal planes; velocity components in the x,(a) y, (b), and z(c) directions.

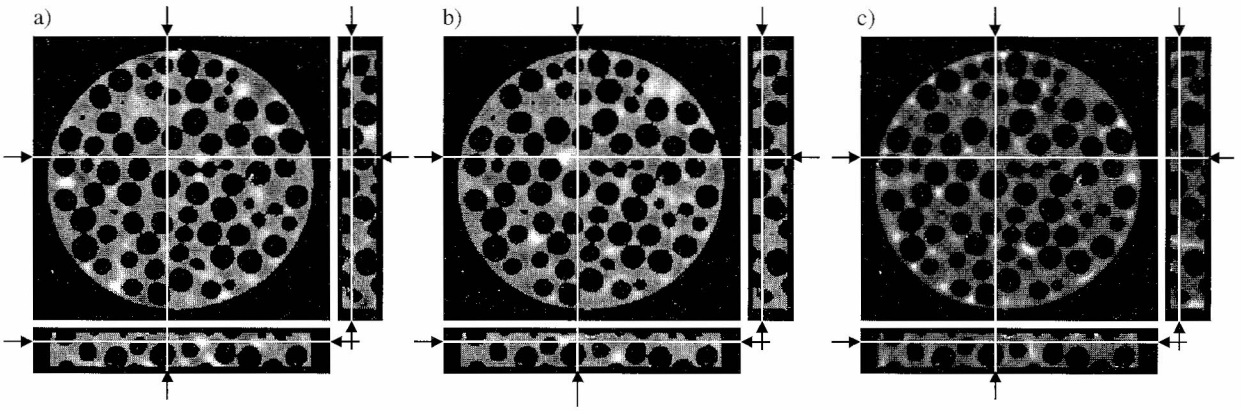

Figure 2 Shear Stress maps τ_{xy} (a) and τ_{xz} (b)

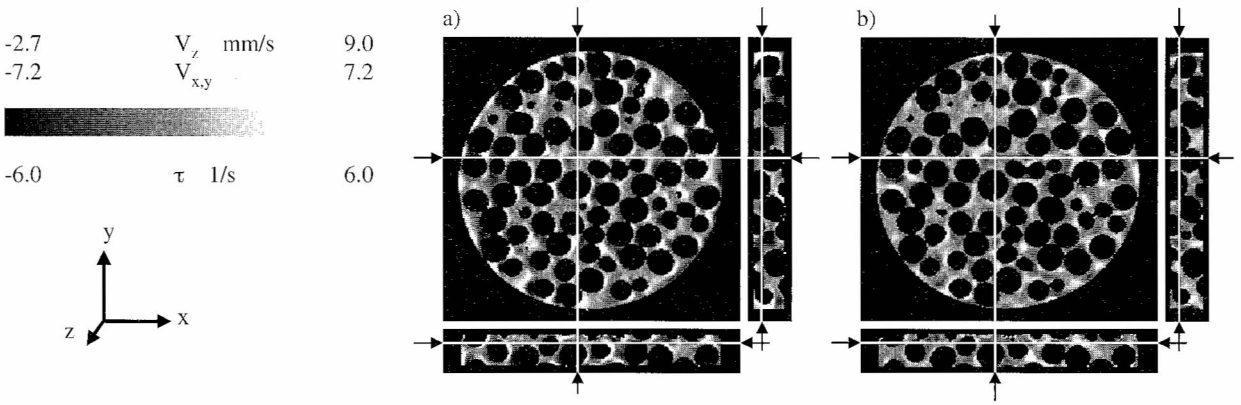

Figure 3. (a) Displacement propagators for PFG (•) and visualisation experiments (solid line) at average axial displacements of 0.16 and 1.6 sphere diameters. (b) 5 mm spheres (○) and 0.5 mm spheres (•) with diffusivity of 2.2e-9 m^2/s and 0.5 mm spheres with diffusivity of 2.2e-10 m^2/s (+) at an average axial displacement of 3 sphere diameters.

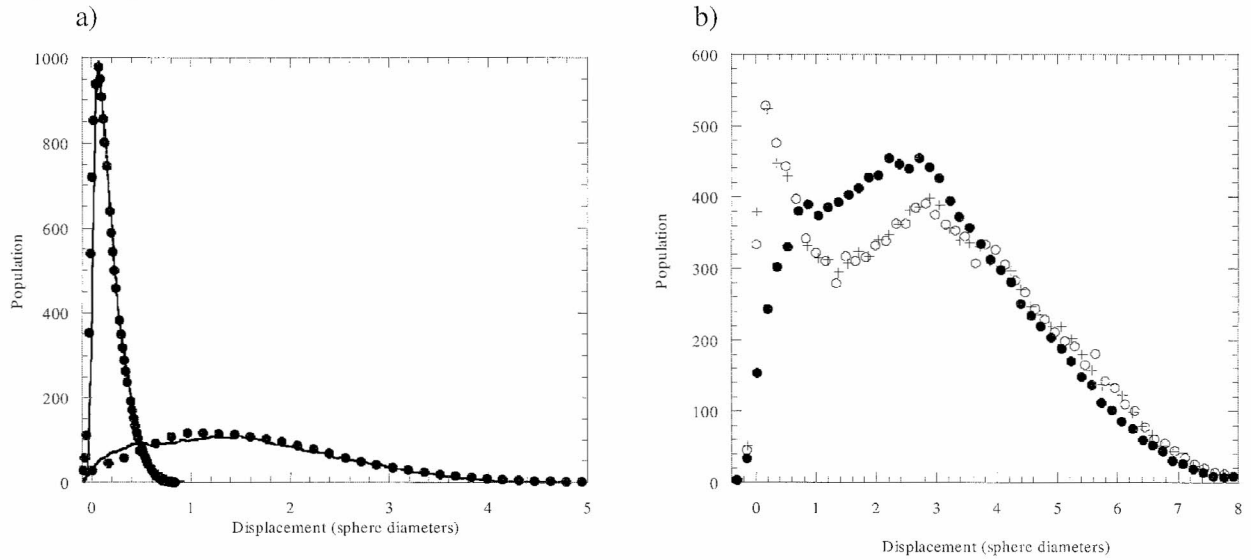

O31

Flow, Diffusion and Mass Transfer Studied by PFG-NMR

Henk Van As, Ulrich Tallarek, Tom Scheenen

Laboratory of Molecular Physics and Wageningen NMR Centre,
Department of Biomolecular Sciences, Wageningen Agricultural University,
Dreijenlaan 3, 6703 HA Wageningen, The Netherlands

Q-space imaging based on PFG-NMR has been successfully applied to study the exchange of fluid molecules between the intraparticle pore network and the interparticle void space in chromatographic columns packed with porous particles (1,2). The approach provides quantitative data about the diffusion-limited mass transfer kinetics between the intraparticle stagnant phase and the interparticle flowing fluid, in addition to the intra-particle diffusivity and the interparticle dispersive flow.

Mass transfer can be quantified by studying the amount of observed stagnant and/or flowing fluid and/or the observed averaged linear velocity of the flowing fluid as a function of the observation time Δ in a pfg-experiment. The method has been combined with turbo spin echo imaging, resulting in a fast dynamic imaging approach (3). This approach is very promising for other applications, e.g. water exchange over the walls of transport vessels in plants (wall permeability), exchange over membrane filters (artificial kindney, bioreactors), transport in the matrix of granules including immobilised micro-organisms in bioreactors, and exchange of (flowing) blood from the capillary network to surrounding cells (perfused tissue).

Complications for a reliable mass transfer quantification originate from partial volume effects, resulting in a changing averaged linear velocity of the flowing fluid as a function of the observation time Δ even in the absence of mass transfer between flowing and stationary fluid. This will be illustrated by flow profiles resulting from pressure driven and electro-osmotically driven flow in capillaries. This problem can easily be solved by summing up information from regions with pixels which are too small, as is demonstrated by results from plants. A second complication is caused by differences in relaxation behaviour between the stagnant and flowing fluid environment. If both amplitude and averaged linear flow velocity information is combined one can determine these relaxation effects in combination with the mass transfer information.

References

1. Tallarek, U, D. van Dusshoten, H. Van As, G. Guiochon, E. Bayer. *Angew. Chem. Int. Ed.* **110**, 1983-1986 (1998).
2. Tallarek, U, F. Vergeldt, H. Van As. *J. Phys. Chem. B* (in press).
3. Scheenen, TWJ, D. van Dusschoten, PA. de Jager, H. Van As, In: *Spatially Resolved Magnetic Resonance*, P. Blümler, B. Blümich, R. Botto, E. Fukushima, eds, 1998, pp. 481-488.

O32

Measurement of Mixing Effectiveness for Suspension Flow in a Kenics Static Mixer

Michael J. McCarthy and Kathryn L. McCarthy

Department of Food Science and Technology, University of California,
One Shields Avenue, Davis, CA 95616-8598 USA

Introduction. The mixing of multiple components to achieve a uniform final product is a critical step in processing for many products. Less than adequate mixing can result in inferior product performance and product failure. The effects of poor mixing can result in nonuniform soap color, poor baked product texture, taste variations, and liability issues in medicine. Over mixing results in increased costs and lower productivity.

Concentration profiles are measured using MRI to monitor and quantify mixing in a Kenics static mixer. Static mixers promote mixing without moving parts. Under laminar flow conditions, mixing will proceed by the combination of division and reorientation of the fluid streams as the material flows through each of the repetitive mixing elements. Static mixers are used in processes that require blending, reaction, dispersion, heat transfer, and mass transfer. With respect to the rate and the efficiency of mixing, there are a number of indices that can be used to describe mixedness in terms of intensity and scale when there is detailed information of the component concentrations in the equipment cross section. MRI has been used to measure the component concentrations as a function of spatial position in the cross section of the static mixer.

Methods. The mixing was performed with a 1.27 cm diameter plastic Kenics static mixer which was incorporated into a flow system. This mixer had 12 successive helical elements each with L/D of 1.0. Two fluids, both polyalkylene glycols were viscosity matched. One fluid consisted of 50% by volume polymethyl methacrylate beads of nominal diameter 200 μm. The viscosity of the fluid and the suspension were matched at 5 Pa•s. Flow rates of the two materials was ~50 mL/min.

MRI was performed on a 7T GE Omega spectrometer using a spin-echo based pulse sequence. A home built rf coil of the Alderman-Grant design was used.

Results and Discussion. Figure 1 shows the progression of mixing. Before the fluids enter the mixing elements there are significant differences in the image intensity related to differences in mobile proton density. At an L/D of 3.5 (P2), there are striations representing the spatial distribution of the two fluids. At P3 and P4, the striations remain visible. By axial position P5, the material appears homogeneous to the image resolution of 310 μm.

The extent of mixing was characterized in terms of intensity and scale of segregation. The measure of intensity was superior to the measure of scale for the pure fluid and suspension used as tes fluids. The variation coefficient gave a measure of decreasing intensity; it decreased form 0.60 to 0.28 over and L/D of 11.5. The mixing index decreased from 1.0 to 0.28.

Figure 1. Photograph of 0.5-inch ID Kenics static mixer. Positions P1 through P5 are axial locations for the MR images, which are shown below the photo.

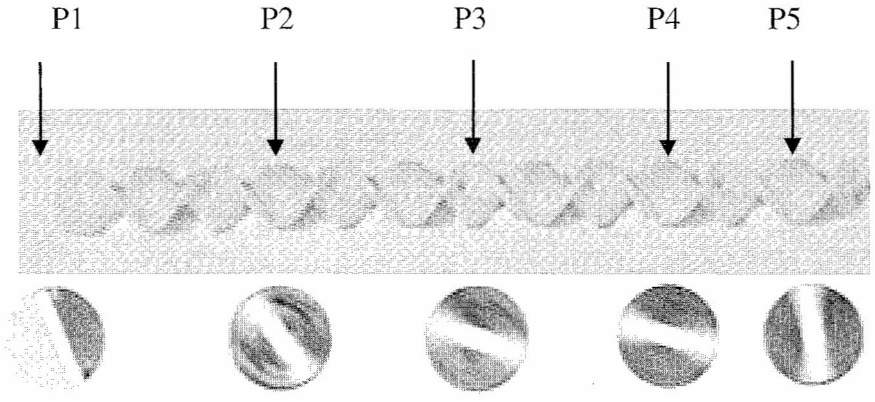

O33

Flow and Dispersion in Porous Media

Bertram Manz, Patrick B. Warren[*], Paul Alexander[†], and Lynn F. Gladden[‡]

Fraunhofer-Institut für Biomedizinische Technik,
Ensheimer Straße 48, D-66386 St. Ingbert, Germany
[*]Unilever Research Port Sunlight Laboratory,
Quarry Road East, Bebington, Wirral L63 3JW, U.K.
[†]Department of Physics, University of Cambridge, Cavendish Laboratory,
Madingley Road, Cambridge, CB3 0HE, U.K.
[‡]Department of Chemical Engineering, University of Cambridge,
Pembroke Street, Cambridge CB2 3RA, U.K.

Magnetic Resonance Imaging (MRI) and Pulsed Gradient Stimulated Echo (PGSTE) NMR experiments have been used to probe structure and dispersion of water in a model porous system formed from a packed bed of spherical particles. The structure of the pore space is characterised from the MR images by determining radial distribution functions of the pore space. The PGSTE experiments yield an average displacement propagator from which the variance of the average molecular displacement and dispersion coefficient are determined at a range of times over which the flow develops (1, 2).

A 3-dimensional MR visualisation of the packing for which NMR data are obtained is then taken as a matrix for lattice-Boltzmann simulations of the flow field, thereby enabling a direct assessment of the simulation method to quantitatively predict flow phenomena within porous media of complex geometry. By introducing normalised parameters, hydrodynamical dispersion over normalised displacement lenthscales extending over nearly four orders of magnitude is investigated and is shown to be dominated by mechanical dispersion over most of this range. Quantitative agreement between NMR measurements and the predictions of the lattice-Boltzmann simulation is obtained in all cases (3).

Axial and transverse displacement propagators of a shear thinning fluid (0.5 % w/w CMC/water) have been measured in the same model porous medium as above. There are clear differences in the propagators between Newtonian and non-Newtonian flow. In particular, the propagator characterising the transport of shear-thinning fluid comprises two populations, one of which is associated with near-stagnant fluid.

References

1. Manz, B., Alexander, P., Warren, P.B., and Gladden, L.F., *Magn. Reson. Imaging* **16**, 673-676 (1998).
2. Manz, B., Alexander, P., and Gladden, L.F., *Phys. Fluids* **11**, 259-267 (1999).
3. Manz, B., Warren, P.B., and Gladden, L.F., *AIChE J.* (in Press).

O34

Characterisation of Porous Media by NMR Imaging and Flow-Diffraction

C. De Panfilis and K.J. Packer
Department of Chemistry, University of Nottingham, Nottingham NG7 2RD, UK

A wide range of studies has been performed on structural characterisation and fluid transport in porous media with the use of the NMR technique. This is particularly suitable when dealing with opaque materials. The commonest NMR method is NMR imaging [1] which provides the fluid spin distribution function, and from this, it is possible to extract directly the spatial statistics of the medium. NMR imaging is highly limited in resolution (typically >100 μm). Barrall *et al.* [2] used the analogy between NMR imaging and diffraction to obtain the density autocorrelation function of the system (Patterson function), directly from the NMR imaging signal. This method reduces the information of a density map but improves the resolution. Even higher spatial resolution is achievable with the use of Pulsed Gradient Spin Echo (PGSE NMR), which is sensitive to the fluid spin motion. Structural information, such as pore size and spacing, become available when the host material hinders the free fluid particle diffusive motion, provided that the diffusion time is sufficiently long [3,4]. As Cory and Garroway [5] pointed out, for closed systems, the PGSE-NMR method is also capable of giving the density autocorrelation function, when the transport times are so long that the initial and final positions of the particle become uncorrelated. However this long time limit is hardly reached, because diffusive transport is very slow and the experiment is time limited. Later results by Seymour and Callaghan [6] showed that structural details are achievable with the use of flow rather than diffusion only.

In this work the echo attenuation function $E_{\Delta}(q)$ and the displacement probability $P(Z,\Delta)$ for water flowing through a bed of 0.3 mm glass beads have been measured by means of Pulsed Gradient Stimulated Echo (PGSE NMR). The encoding time Δ and the flow rates used in the experiments were chosen such that the average displacement was at least one bead diameter. The $E_{\Delta}(q)$ shows, as expected, a diffraction peak at about the inverse of the bead diameter. For longer times $E_{\Delta}(q)$ shows another peak at about the inverse of twice the bead diameter. In analogy with PGSE NMR in presence of diffusion in a closed system, these data suggest that the pore space correlation function or features closely related to it, can be accessed through the PGSE experiment with flow. The conditions leading to this possibility, are discussed and supported with the results of network modelling of fluid flow in a periodic structure. The true pore space correlation function has been determined using the Patterson function approach applied to a NMR image data set. This has been compared with the one obtained by PGSE NMR with flow. The displacement distributions $P(Z,\Delta)$ for fluid flow/diffusion in this system also show structural information and can be regarded as a product of the pore space correlation function with an evolving smooth distribution which starts as an exponential and tends to a gaussian in the longer time limit.

---

[1] P.T. Callaghan, *Principles of Nuclear Magnetic Resonance Microscopy*, Clarendon Oxford, 1991.
[2] G.A. Barrall, L. Frydman, and G.C. Chingas, *Science* **255**, 714 (1992).
[3] J. Kärger, H. Pfeiffer, and W. Heink, *J. Magn. Reson.* **51**, 1 (1983)
[4] P. T. Callaghan, A. Coy, D. McGowan, K. J. Packer, and F.O. Zelaya, *Nature* **351**, 467 (1991).
[5] D.G. Cory and A.N. Garroway, *Magn. Reson. Med.* **14**, 435 (1990).
[6] J.D. Seymour and P.T. Callaghan, *J. Magn. Reson.* A **122**, 90 (1996)

O35

NMR on Salt Water Ice

Marion I. Menzel, Song-I Han, Heike Schoof*,
Siegfried Stapf, Bernhard Blümich

Institut für Technische und Makromolekulare Chemie,
Magnetic Resonance Center (MARC), RWTH Aachen, Germany
*Helmholtz-Institut für Biomedizinische Technik, RWTH Aachen

The microscopic and macroscopic structure of sea ice has been the topic for a wide range of research activities. It is known that this structure is highly dependent on the growth rate, the temperature history, the age as well as the depth from which samples are recovered [1].

Due to an incompatibility in crystal size there are no solid solutions of salt in the ice lattice formed from aqueous NaCl-solutions. According to the phase diagram (of NaCl/ice/H_2O) an aqueous solution of NaCl (containing 3 to 3.5 % NaCl) starts to form pure ice crystals at a temperature of approx. –2°C. The remaining solution will be enriched in salt content until the eutectic is reached (-21.2°C) where two solid components, ice and precipitated NaCl•$2H_2O$ remain. At intermediate temperatures, ice and brine (in pores) coexist.[2]

The shape and size of these pores, i.e. the topology of the ice, are defined by the growth direction along the temperature gradients and depend on the growth rate and on the storage temperature (recrystallization may occur at temperatures above the eutectic). In particular because these brine pockets are a habitat for a variety of different organisms, knowledge of the size distribution and connectivity of the pore network is vital for understanding the interaction of pollution with the sea ice and its influence on the organisms which winter in the pockets.

For laboratory experiments, samples of (3 % w/w) aqueous NaCl-solution were frozen under different conditions. The absence of salts other than NaCl ensured a well defined freezing behaviour, with the pores of highest NaCl concentration (22.5 % salinity) eventually freezing at -20°C.

The wide range of pore sizes in salt-water ice makes it an ideal test-bed for combining a variety of NMR methods sensitive to restrictions in motions on various scales:

2D ^{1}H-spin density imaging reveals the distribution, size, and orientation of macroscopic pores [3]. We present images of the in-situ freezing process under rapid cooling and compare them to results for ice grown slowly under temperature controll. By NMR imaging, structures of 50 µm are resolved.

Smaller distances down to a few micrometers can be probed by measuring the propagator of water molecule displacement. Propagators for displacements of axes parallel and perpendicular to the growth axis are compared for different temperatures and encoding times Δ up to 2s. The average diffusion coefficient is found to be strongly anisotropic [4] and to decrease for longer Δ. Along with the fact that non-exponential diffusional decay curves were observed, this indicates restricted diffusion on scales of approximately 50 µm.

Finally, a comparison of T_1 and T_2 relaxation of protons is sensitive to slowed-down rotational and translational motions in dependence of the surface-to-volume ratio and the local field gradients, respectively. Thus, scales well below 1µm can be accessed. The results are compared to the relaxation behaviour of ^{23}Na ions and discussed in terms of salinity distributions within the porespace.

References

[1] Weeks, W. F., Ackley, S. F., *CRREL Rep.* **82-1** (1982).

[2] Richardson, C., Keller, E., *J. Glaciol.*, **6**, 89 (1966).

[3] Edelstein, W. A., Schulson, E. M., *J. Glaciol.*, **37**, 177 (1991).

[4] Callaghan, P. T. et al. *J. Magn. Reson.* **133,** 148 (1998).

O36

Lateral Transport of Water during Drying of Alkyd Emulsions

E. Ciampi, U. Goerke, J.L. Keddie and **P.J. McDonald**

School of Physical Sciences, University of Surrey, Guildford, GU2 5XH, Surrey, UK

Introduction

Paints and coatings are often emulsions or suspensions in which the solvent evaporates and the inevaporable dispersed phase forms a protective or decorative film. The evaporation influences film formation and hence the quality of the final coating. The scope of this paper is to study the drying of water–borne alkyd emulsions and acrylic latex dispersions. The time course of water loss of the emulsion was imaged and compared with predictions of a theoretical model. Alternate models from the literature are also discussed [1-4].

Experimental

The alkyd resin was derived from a tall-oil fatty acid, orthophtalic anhydride and pentaerythritol and was emulsified in water using nonionic surfactants (Atsurf E-3969). The acrylic latex is based on a copolymer of butyl methacrylate, methyl methacrylate and methacrylic acid. The latex dispersion was prepared using an anionic surfactanct (Nansa AS40). The drying of the alkyd emulsion and the acrylic latex dispersion was studied by spin-echo NMR imaging. A drop of the alkyd emulsion or the latex dispersion was placed on top of a glass rod in a test tube. The water evaporation rate is determined by the humidity of the air adjacent to the drop surface. The water loss of the drop was therefore studied under both static air and slowly flowing nitrogen gas for a constant exchange of air. In static air, a humidity gradient within the air column above the drop builds up. Vapour diffusion in the air column therefore controls the evaporation rate. In the alternate experiment in which the drop was exposed to flowing nitrogen gas the water evaporation is faster.

Evaporation/lateral diffusion model

The suggested model assumes a constant evaporation rate at the surface of the emulsion drop. Since the absolute water loss per area and time is the same at every point on the surface the water concentration decreases more quickly at the edges than in the middle of a convex drop. This concentration gradient drives water diffusion from the middle to the edges of the droplet. Under the assumption that the shape of the drop does not change, i.e., the volume is conserved at given position in the drop, a macroscopic flow of emulsion from the edge to the middle of drop has to take place [5].

Results

The data points in the figure show an example of the time course of water loss at different radii in an alkyd/emulsion drop (filled circles: middle of the drop to open inverted triangles: edge of the drop) in static air. The dashed line shows the average water loss. The data show a clear gradient in water loss rate across the drop. The solid lines are theoretical predictions using the evaporation/lateral diffusion model with no free parameters. The agreement between theory and experiment is very good. The model also describes the drying of emulsion drops under flowing air. However, it is less successful in describing the latex dispersions. Alternate models from the literature [2, 3], based on constant shape considerations were found to be more successful for latex.

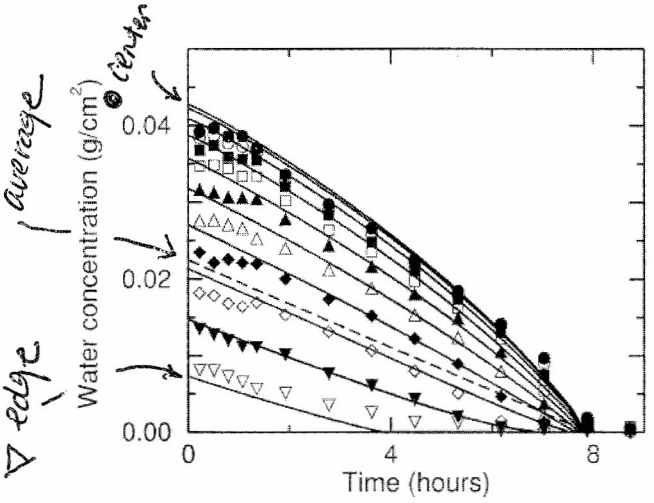

Conclusions

The lateral diffusion/evaporation model which is proposed in this paper shows good agreement with experimental results for the drying of drops of water-borne alkyd emulsion. However, the model is less successful in explaining the drying of latex dispersions. In this case it seems to be necessary to distinguish between bound and free water.

References:

[1] Winnik, M.A. et al., *J. Coatings Technol.* **68**, 39 (1996)
[2] Parisse, F. et al., *J. Phys. II France* **6**, 1111 (1996),
[3] Parisse, F. et al., *Langmuir* **8**, 3598 (1997)
[4] Deegan, R.D. et al., *Nature* **389**, 827 (1997)
[5] Crank, J., *The Mathematics of Diffusion* (Clarendon, Oxford, 1975)

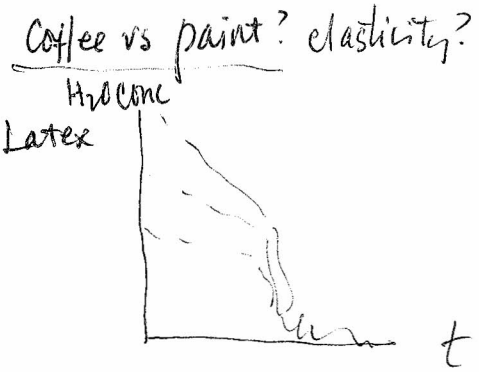

Abstracts for the Scientific Session

Poster Presentations

P1

Determination of Structure and Biomechanical Properties of Joint Cartilage by Magic Angle Sensitive Dynamic NMR Microscopy

W. Gründer, G. Hanke, U. Reibetanz, A.Werner

Universität Leipzig, Institut für Medizinische Physik und Biophysik, Liebigstraße 27, D-04103 Leipzig

Introduction

The basis of arthrotic changes of joint cartilage is the dysbalance between the stress and the ability to withstand stress. The resilience of the hyaline cartilage are determined by the matrix components. Especially the organisation of the collageneous network decide the resistance of the joint cartilage to mechanical stress. For that reason changes of the arrangement of collagen network organisation have essential influence to the development of arthrosis. The visualization of the collageneous network could improve essentially the diagnostic of early diagnostic athrotic changes and the possibility of therapeutic interventions. In the last years it was shown that high resolution MRI (NMR-microscopy) can visualize different zones of anisotropic intracartilaginar network structures. Because of the anisotropic dipolar coupling of the water molecules within zones of anisotropic collageneous network, T_2 weighted images show multilaminare internal structures of the joint cartilage, depending on the orientation of the cartilage in respect to the static magnetic field [1]. From that, informations similar to polarization light microscopy can be derived noninvasively [2]. We have shown that existence, extension and intensity of these anisotropic zones are strongly influenced by mechanical stress and that, in some equivalence to photoelastic measurements, informations about pressure distribution within joint cartilage can be derived [3]. Measuring the changes of signal intensities of the anisotropic cartilage zones a) under different orientations in respect to the magnetic field and b) during mechanical loading, we present an approach to determine the grad of network orientation and mechanical properties quantitatively.

Material and Methods

Cartilage-bone plugs (Ø 15mm and Ø 3mm) of pig and sheep knee joints were used (paired specimens of tibia/femur condyles in case of the experiments under pressure). The NMR-microscopic investigations were performed at 7 Tesla on a BRUKER AMX 300 WB spectrometer. The angle-dependent measurements were realized by application of a special designed goniometer insert. The influence of compression (up to 1,5 MPa) was determined using a home-built insert based on a hydraulic system [4]. The T_2-weighted microimages (256^2) were measured using SE sequences with TR=500 ms, TE=20 ms (slice thickness 0.5-2 mm). To get information from identical cartilage regions under pressure (and under different orientations) a digitalization and correction of the image matrix must be performed.The digitalisation was realized using a neuronal network adapted to the cartilage geometry, in this way taking into account also the non-linear deviations.

Results and Discussion

Influenced by mechanical loading the NMR microscopic visualization of the hypointense zones of anisotropic network orientation is changed. Zones of radially and tangentially oriented collageneous meshwork show drastically different behaviour under pressure.. While the radial zones becomes brighter (and vanishes) under pressure the darkness and extension of the zones of tangentially oriented collagen fibers increase. A model explaining the opposite stress reactions of the radial and tangential cartilage zones is given. Obviously because of the different biomechanical functions the orientation grad decrease in radially oriented zones while it increase in case of tangentially oriented regions. Analysing the changes of pixel intensities during loading informations about zonal different mechanical properties and pressure distribution within cartilage can be derived.

Conclusions

Based on the influence of stress to the MR visualization of zones of anisptropic collagenous network orientation biomechanical properties of joint cartilage and intracarticula pressure distributin can be determined. In contrast to photoelastizity, high resolution MRI can visualize pressure distribution within joint cartilage noninvasively ("NMR-photoelasticity").

1. Henkelmann, R. M. *et al.*, *Magn. Reson. Med.* **32**, 592 (1994).
2. Gründer, W. *et al. Magn.*, *Reson. Med.* **39**, 376 (1998).
3. Gründer, W. *et al.*, *Proc. Int. Soc. Magn. Reson. Med.* **6**, 405 (1998).
4. Gründer, W. *et al.*, *Biomed. Technik* **43**, 289 (1998).

Matrix Strain and Water Redistribution Within the Intervertebral Disc Under Non-Axial Bending Stress

Hideyuki Aoshiba [1], Yoshiaki Kusaka [1], Sinitiro Nakajima [1], Osamu Uemura [1], Yoshiteru Seo [2], Masataka Murakami [3], Yasusuke Hirasawa [1]

[1] Dept. of Orthopaedic Surg. & [2] Dept. of Physiology, Kyoto Prefectural University of Medicine, Kyoto, Japan

[3] National Institute for Physiological Sciences, Okazaki, Japan

Introduction

Viscoelastic deformation of the intervertebral disc is very important to absorb the external load applied to the vertebral column. During this deformation of the disc, there should be a concomitant intradiscal matrix strain and redistribution of water. Thus, the matrix strain in combination with water movement within the disc is a very important determinant of the viscoelasticity of the disc. We previously reported the matrix strain of the axially loaded disc by using MRI [1]. In the present study, we applied non-axial load to the bovine caudal intervertebral disc to clarify the physiological matrix strain and water movement within the disc during flexed loading of the spine.

Materials and Methods

Nine fresh bovine caudal intervertebral disc with adjacent vertebral bodies and without posterior elements were dissected. The specimens were fixed in a non-magnetic compression device which was installed in an MR imager (Biospec, Bruker) operating at 4.7 tesla. Two wedge shaped spacers with a total slope of 5 degrees were interposed between the loading blocks and the specimen. Three to 4 nylon threads (diameter 0.3mm) were inserted into the each disc in the antero-posterior direction in order to use as markers on the mid-coronal images. We acquired the first gradient echo image immediately after the beginning of a 30kg static loading and then sequentially until 180 minutes. We determined positions not only of the cross sections of nylon threads but also positions of end plates and annular lamellae on the MR images. These data obtained from all the disc were integrated on one standardized rectangular coordinate system. The plots on the coordinate were then curve fitted, and intradiscal strain was expressed as distortion of the curve. Then, sequential strain of the disc matrix was analyzed.

Results and Discussion

At 30 minutes after the beginning of loading, strain of the outer margin of the annulus fibrosus was not evident both on convex and concave side of the spine. The inner annulus fibrosus moved centrifugally on the convex side, while almost no strain of the inner annulus was observed on the concave side. Longitudinal compression of the disc was evident nearby the end plate, and thickness of the central region was relatively preserved. At 180 minutes after the beginning of loading, longitudinal compression of the disc advanced. We previously reported that there is a centripetal water movement within a axially compressed disc. This is because centrifugal expansion of the nucleus pulposus exceeds its longitudinal compression under this condition. Similar mechanism works on the disc under non-axial stress. However, intradiscal strain in this case is asymmetric, resulting in an eccentric water accumulation.

Conclusion

Non-axial bending stress of the intervertebral disc caused asymmetric strain of the disc matrix. This deformation of the disc resulted in an eccentric water accumulation within the disc.

References

[1] Uemura, O.; *et al.*, *Transactions of the 42th ORS*, 269, 1996.

P3

Uneven Strain and Water Kinetics Within the Intervertebral Disc under Compression

Osamu Uemura, Yoshiaki Kusaka*, Shin-ichiro Nakajima*, Yoshiteru Seo**

Department. of Orthopaedic Surgery, Meiji University of Oriental Medicine, Kyoto, Japan

*Department of Orthopaedic Surgery and **Physiology, Kyoto Prefectural University of Medicine, Kyoto, Japan,

Introduction. The load applied to the intervertebral disc is transformed into the kinetic energy of the intradiscal water. The intradiscal water kinetics might be controlled by the strain of the disc matrix. This mechanism is very important for absorbing mechanical stress applied to the spine.

The intervertebral disc has a water-rich region at its center called nucleus pulposus, which is surrounded by a water-tight fibrous tissue called annulus fibrosus. Therefore, the intervertebral disc is a biomechanically inhomogeneous tissue. The topographical differences in the mechanical properties of the disc could cause uneven strain of the disc matrix under compression. The aim of this study is to clarify the topographical strain and water kinetics within the compressed disc. For this purpose, we measured local strain at various points in the disc matrix and estimated water content in the nucleus pulposus by high resolution MRI.

Materials & Methods. Eleven bovine coccygeal discs were obtained. Monofilament nylon threads (0.3 mm in diameter) were inserted into the disc in the anterior-posterior direction to allow visualization of the matrix strain on MR coronal images. Three to five threads were inserted in one disc. The specimens were fixed in a non-magnetic compression device, which was positioned at the center of MR magnet (Biospec 47/40, Bruker). A 700kPa static load was applied along the major axis of the spine for 240 minutes. Mid-coronal MR images (gradient echo images and T1 calculated images) were obtained sequentially before and during compression.

Sequential changes in the disc height, disc width and the positions of markers were measured on images. The strain was observed with a total of 37 markers traced on images in the nucleus pulposus and the annulus lamellae on images in the annulus fibrosus.

The water content in the nucleus pulposus can be estimated from the T1 calculated image, based on our previous findings that the T1 relaxation time is positively correlated with the water content in the disc matrix(1).

Results. The disc height decreased and the disc width increased during compression. The uneven strain of the disc matrix was observed on MR images. In the early phase of compression, the moving distance of markers around nucleus pulposus was largest in the disc. Moreover, the horizontal strain (along the disc diameter) was greater than the longitudinal strain (along the disc height). In late phase, the longitudinal strain became dominant around the nucleus pulposus.

The water content of the nucleus pulposus increased in early phase of compression and it means that there was a temporary centripetal water flew towards the the center of the nucleus pulposus. In late phase, it decreased and the intradiscal water flew out of nucleus pulposus.

Discussion. In early phase, the effect of increase of the disc width is greater than the effect of decrease of the disc height, therefore, the volume of the nucleus pulposus increases. During this phase, the density of the solid matrix of the nucleus pulposus decrease, while that around the nucleus pulposus increases. Subsequently, the effect of the disc height decrease became dominant, resulting in a decrease in the volume of the nucleus pulposus. This uneven strain of the disc matrix apparently generates a pressure gradient within the disc that causes the centripetal water flow.

Conclusions. The uneven strain of the disc matrix was observed in the compressed disc. In the early phase of compression, it causes the centripetal water flow within the disc.

References

1. Chatani, K., et al, *Spine*, **18**: 2271-2275 (1993).

P4

Tendon Anisotropy by in vivo T_2 Relaxation with the NMR-MOUSE

R. Haken and **B. Blümich**

Institut für Technische Chemie und Makromolekulare Chemie,

Zentrum für Magnetische Resonanz, RWTH, D-52056 Aachen

The anisotropic behavior of cartilage and tendon is known in the medical community to cause the 'magic angle' phenomenon. Due to the anisotropy of the transverse relaxation rate T_2^{-1} depends on the orientation of the tendon in the magnetic field. In medical imaging measurements the orientation of the tendon is prescribed by the orientation of the human body in the magnet and can only be varied within small limits. As a consequence the 'magic angle' phenomenon may lead to a misjudgment of tendon condition. The NMR-MOUSE (mobile universal surface explorer) is a hand-held NMR sensor which has been employed to investigate the anisotropic behavior of T_2^{-1} in tendon in vitro and in vivo. It provides a tool to analyze the correlation of T_2 and the physical condition of tendon. First measurements with animal tendon and Achilles tendon of human volunteers show that the isotropic value of T_2^{-1} in tendon correlates with the state of health of the tendon. The anisotropy is a measure of the degree of molecular order of the tendon material. Its angular dependence closely follows the second Legendre polynomial. It is argued, that the anisotropy can be a measure of tendon recovery and healing after injury including rupture. Further investigations of patients with tendon dysfunction have to show in how far that this approach can be developed into a useful diagnostic tool.

T_2 Relaxation Anisotropy as a Non-Invasive Measure to Evaluate the Structural Repair of Injured Tendon Tissue

Hisatake Takamiya, Yoshiaki Kusaka, Yoshiteru Seo, Kazuya Ikoma, Masahiko Noguchi, Taketoshi Morimoto, and Yasusuke Hirasawa

Department of Orthopaedic Surgery & Department of Physiology,
Kyoto Prefectural University of Medicine, Kyoto, Japan

INTRODUCTION: It is known that the relaxation times of the oriented water molecules show anisotropy depending on the angle between the orientation and the direction of the static magnetic field. The water molecules in tendons, most of which are thought to be tightly bound with the macromolecular structure, are also highly oriented. We expect that detailed analysis of the T_2 relaxation anisotropy of the injured Achilles tendon would allow evaluation of its structural recovery. In an attempt to utilize NMR information for non-invasive evaluation of the injured tendon, we examined the relaxation anisotropy of the Achilles tendon during the healing process after injury.

MATERIALS AND METHODS: The Japanese white rabbits (mature males) were used as the materials. We made a partial incision transversely on each of the Achilles tendon under intravenous pentobarbital anesthesia. At 3, 6, 12 and 18 weeks after surgery, these rabbits were euthanized and the regenerated Achilles tendons were dissected for the following measurements. Intact Achilles tendons were served as controls. The tendon was directed parallel (0°), 35°, 75°, vertical (90°) and the magic angle (54.7°) against the static magnetic field by using our original Teflon plugs that were made to fit the NMR sample tube. Magnetic resonance measurements were obtained using an MR spectrometer (MSL-100, Bruker) operating at 2.34 Tesla. The T_2 relaxation time was measured by spin-echo pulse sequence. The repetition time of the sequence was 3.0 sec and the temperature was maintained at 25°C.

RESULTS AND DISCUSSION: Intact Achilles tendon demonstrated long and short T_2 relaxation components. Short T_2 relaxation time of the intact Achilles tendon demonstrated strong orientation dependency. With regard to healing tendon, only one fraction of T_2 relaxation time without anisotropy was recorded three weeks after surgery. The collagen fibers in the healing tendon at this stage is immature and has no structural orientation. Therefore, we suggest most of the water in this tendon may be neither bound nor oriented. In contrast, similarly to the control tendon, two fractions of T_2 relaxation times (short T_2 and long T_2) were observed in the healing tendon 6 weeks after surgery and thereafter. Although the short T_2 relaxation time was relatively prolonged and did not demonstrate anisotropy at 6 weeks, anisotropy became evident 12 weeks after surgery and thereafter with shortening of the short T_2 relaxation time. We suggest that maturation and ordering of the collagen fibers in healing tendon immobilize and align the surrounding water molecules. These changes in the state of water occurring concomitantly with structural repair of the injured tendon could explain the changes in the T_2 relaxation behavior shown in this study.

REFERENCES

1. Fullerton, G.D., et al.: *Radiology* **155**:433-435 (1985).
2. Henkelman, R.M., et al., *Magn Reson Med* **32**:592-601 (1994).
3. Takamiya, H., et al., *Trans. ORS* **23**:1017 (1998).

P6

Proton Magnetic Resonance Microimaging of Human Trabecular Bone

J. Tritt-Goc[1], N. Piślewski,[1] A. Kaflak-Hachulska,[2]
D. Chmielewski,[3] A. Górecki[3] and W. Kolodziejski[2]

[1] Institute of Molecular Physics, Polish Academy of Sciences, ul. Smoluchowskiego 17, 60-179 Poznań, Poland
[2] Medical University of Warsaw, Faculty of Pharmacy, Department of Inorganic and Analytical Chemistry, ul. Banacha 1, 02-097 Warszawa, Poland
[3] Medical University of Warsaw, Department of Orthopaedics, ul. Lindleya 4, 02-005 Warszawa, Poland.

Introduction

The MRI technique is widely used as a clinical diagnostic method and recently for characterization of porous materials such as trabecular bone [1,2,3]. For the latter purpose, the technique is particularly attractive because it is nondestructive and the same samples can be studied by other methods. The aim of our study was to acquire proton NMR images with the highest possible resolution in order to visualize the fine structure of trabecular bone *in vitro* and to find NMR parameters, which can be later used for the characterization of osteoporotic bone.

Methods

The proton NMR imaging experiments were done on a Bruker AVANCE 300 MHz WB spectrometer, equipped with a microimaging accessory. 3D Spin Echo (3D SE) and Multi-Slice Multi-Echo (MSME) pulse sequences were used for the three-dimensional (3D) microimaging and the latter for the investigation of the T_2 relaxation time spatial distribution.

Results and discussion

Two samples of trabecular bone from males, victims of car accidents were selected for MRI measurements. They are of different density and were taken out from the femur midshaft - sample 1 and from the proximal part of the femur midshaft - sample 2. Both samples were lyophilized and sterilized by the γ-radiation. The images were recorded without saturation of the samples with a proton-containing solvent. In 3D SE imaging experiment the obtained spatial resolution was ca. $(60\ \mu m)^3$ and $(78\ \mu m)^3$ for samples 1 and 2, respectively. In the MSME experiment we achieved a resolution of $(39\mu m)^2$. In the images the fine structure of trabecular bone is clearly visible indicating that the NMR microimaging can be very useful in the study of pathologic changes in the bone microarchitecture. We try to characterize the bone porosity on the basis of histogram. It follows that the intensity histogram from healthy or less porous material should be bimodal, that is consisting of two separate, nearly Gaussian peaks. This case is for sample 2. To the contrary, the histogram for substantially porous bone of sample 1 is no longer bimodal and the continuous distribution of the pixel intensities is observed. We also acquired the MSME images with various T_2 weighting. The T_2 value varied with the voxel position in this sample from 80 to 130 ms.

Conclusion

The preliminary results presented in this paper indicate that the NMR microimaging is a very promising method for the structural characterization of trabecular bone. The resolution obtained was sufficient to determine spatial distribution of the overall proton NMR signal from the organic fraction (collagen, lipids), bone mineral and tissue water. With the histogram analysis it was possible to monitor bone porosity.

References

1. Majumdar S, Genant H.K, Grampp S, J. *Bone Miner. Res.* **12**, 111(1997).
2. Wehrli F.W, Hwang S. N., Ma J., Song H. K., Ford J. C., Haddad J. G., *Radiology* **206**, 347 (1998).
3. Timonen J., Alvila L., Hirva P., Pakkanen T. T., *J. Mater. Sci.-Mater.M.* **9**, 187 (1998).

Short-TE projection reconstruction NMR microscopy of trabecular bone

Pavol Szomolanyi[1,2], Vladimír Jellúš[2], Franco Vittur[1] and Renato Toffanin[3,4]

[1] Department of Biochemistry, Biophysics and Macromolecular Chemistry, University of Trieste, Trieste, Italy
[2] Institute of Measurement Science, Slovak Academy of Sciences, Bratislava, Slovakia
[3] Laboratory of NMR Microscopy, University of Trieste, Trieste, Italy
[4] PROTOS Research Institute, Trieste, Italy

Introduction

Bone disorders such as osteoporosis lead to alterations in the trabecular bone. These alterations are characterised by a reduction of bone mass and by structural changes in architecture of bone. NMR microscopy may potentially be very useful in the *ex vivo* study of osteoporosis as non destructive technique with the ability to provide three dimensional information of the bone architecture (1). However, the trabecular width appears larger in conventional MR images, as the susceptibility effect at the bone-marrow interface causes intravoxel phase dispersion. Such an effect can be minimised if the echo-time (TE) or voxel size are reduced. The purpose of our research was to develop new NMR techniques that have a potential role in the characterisation of trabecular bone architecture. In this study we describe the use of short TE projection-reconstruction (PR) NMR microscopy for the study of trabecular bone explants.

Materials and methods

Specimens consisting of cylindrical bone plugs (∅=4 mm) were obtained from disarticulated porcine humeral heads and human femoral heads. The explants were placed in 5 mm diameter NMR tubes and examined at 7.05 T on a Bruker AM300 WB instrument, equipped with a standard microimaging accessory. All the measurements were made in air. Proton MR microimages were acquired using 3D spin-echo (TE = 3.0 ms) and gradient-echo (TE = 2.3 ms) sequences according to the PR method with constant gradient step described by Jellúš et al. (2,3). PR microimages were reconstructed off-line on a Pentium-based system by employing a convolution method. This method provided images with a voxel resolution of 50×50×150 μm. PR microimages were then compared with spin-echo and gradient-echo images obtained on the same explants by the standard Fourier transform imaging method.

Results and discussion

Projection-reconstruction (PR) refers to a family of MRI techniques that scan through *k*-space along radial trajectories rather than along the rectangular Cartesian trajectories of Fourier transform methods. One of the major advantages of the PR method is the possibility of applying short echo times for imaging short T_2 species. In the specific case of trabecular bone, short echo times were applied to minimise the phase dispersion due to the high changes in susceptibility at the bone-marrow interface. This study demonstrates that quantitative PR NMR microscopy can be used as a non-destructive tool for evaluating changes in the architecture of trabecular bone. The quality of the PR images is, in fact, significantly improved when compared to that of the images obtained by the standard FT techniques. Since the risk of bone fracture seems to be strongly related to bone microstructure, the described PR method can be a contribution towards a better understanding of bone evolution and for a more accurate prediction of risks.

References

1. Chung H.-S., Wehrli F.W., Williams J.L. et al., *J. Bone Miner. Res.* **10**, 1452-1461 (1995).
2. Jellúš V., Latta P., Budinsky L'. et al., *Proceedings of the 5th ISMRM Meeting*, pp. 1987, Vancouver, Canada (1997).
3. Jellúš V., Latta P., Budinsky L'. et al, *Proceedings of the 14th ESMRMB Meeting*, pp. 163, Brussels, Belgium (1997).

Acknowledgements. This work was supported by grants PRIN 97 (Italy) and VEGA 2/5087/99 (Slovak Republic). A postdoctoral fellowship from the Consortium for the International Development of the University of Trieste (to P.S.) is gratefully acknowledged.

In vivo Assessment of Cardiac Remodeling after Myocardial Infarction in Rats by Cine-FLASH-Magnetic Resonance Imaging – Comparison of methods

Matthias Nahrendorf[a], Frank Wiesmann[b], Karl-Heinz Hiller[a], Kai Hu[b], Christiane Waller[b], Jan Ruff[a], Axel Haase[a], Georg Ertl[b], Wolfgang R. Bauer[b]

[a] Department of Biophysics (EP5), University of Würzburg, Germany

[b] Department of Medicine, University of Würzburg, Germany

Objective. The rat infarct model has proved to offer important parallels to the process of remodeling after myocardial infarction (MI) in the human heart. Aim of the study was to test the feasability of Cine-FLASH-MRI for the assessment of cardiac morphology and function in the infarcted and noninfarcted rat heart and compare the results to established methods.

Methods. Group A: 40 female Wistar rats were subjected to left coronary artery ligation. MRI-measurements in infarcted animals were done 8-16 weeks after MI on a 7 Tesla scanner using an ECG-triggered Cine-FLASH-sequence on a 7.05 Tesla BIOSPEC 70/21 scanner. Following parameters were determined: left ventricular (LV) volumes and mass, wall thickness, MI-size, cardiac output, ejection fraction, LV diameter and circumference. Afterwards gross anatomical dimensions were measured and MI-size histologically determined (1). Group B: After MRI 8 controls and 8 rats 16 weeks post MI underwent conventional hemodynamic measurements for determination of cardiac output, LV volumes and ejection fraction by electromagnetic flowmeter (2) and pressure-volume curves (simultaneous infusion at 0.76 ml/min into LV and pressure recording, EDV is infused volume at in vivo measured end-diastolic pressure) (3). In these animals LV wet weight was determined.

Results.

	MRI		conventional method		*r*
MI-size %	18.5 ± 2		22.8 ± 2.5*		0.97
	MI	control	MI	control	
LV mass (mg)	865.1 ± 39.2	537.6 ± 19.6	865.1 ± 41.3	540.3 ± 18.4	0.97
EDV (µl)	737.0 ± 70.5	343.9 ± 8.4	671.1 ± 64.1*	262.7 ± 12.8*	0.96
SV (µl)	259.1 ± 10.4	224.4 ± 7.8	245.8 ± 13.5	221.2 ± 9.2	0.70
CO (ml/min)	82.4 ± 5.2	73.1 ± 2.9	81.9 ± 3.7	75.2 ± 2.6	0.80
EF (%)	36.7 ± 2.4	65.3 ± 1.6	41.9 ± 3.8*	84.4 ± 2.3*	0.97

Data are mean ± SEM. *r*: correlation coefficient of methods (MI plus control), * $p < 0.05$ vs. MRI of the same group, LV: left ventricular, EDV: enddiastolic volume, SV: stroke volume, CO: cardiac output, EF: ejection fraction.

Compared to the in vivo MRI-data, the maximum left ventricular circumference in the formalin fixed hearts was 5.25mm (13.3%) smaller, the diameter 1.27 mm (10.2%) smaller (mean difference). These findings were significant ($p < 0.001$ both).

Conclusion. We could show that Cine-FLASH-MRI is a valuable diagnostic tool applicable to the rat model of MI which is in agreement with existing analytical methods in determination of MI-Size, CO, LV mass and volumes. With a difference of 5% both methods of MI-size determination correlate well. There was good correlation of postmortal determined to in vivo measured EDV. The significant difference was bigger in the controls than in MI-rats (23.4% and 9.0%).

References.

1. Pfeffer MA, Pfeffer JM, Fishbein MC, Fletcher J, Spadaro J, Kloner RA, Braunwald E. Myocardial infarct size and ventricular function in rats. *Circ. Res.* **44**, 503-512 (1979).
2. Pfeffer MA, Frohlich ED. Electromagnetic flowmetry in anesthetized rats. *J. Appl. Physiol.* **33**, 137-140 (1972).
3. Fletcher PJ, Pfeffer MJ, Pfeffer MA, Braunwald E. Left ventricular diastolic pressure-volume relations in rats with healed myocardial infarction. *Circ. Res.* **49**, 618-626 (1981).

P9

An MRI View of Obesity?

M. Szayna [1], L. Polikova [2], J. Egan [3] and R.G.S. Spencer [1]

[1] NMR Unit, [2] Gene Therapy Unit, [3] Diabetes Section, NIH/National Institute on Aging, Gerontology Research Center, Baltimore, Maryland, USA

Introduction

Obesity often leads to insulin resistance and is the primary cause of type 2 diabetes mellitus. It has been shown that insulin resistance is closely associated with intra-abdominal fat rather than with total fat mass.

Diabetic Fatty Zucker rats (ZDF) are a well-established animal model for type 2 diabetes. Genetically modified Zucker rats develop obesity and eventually type 2 diabetes with age. Previous studies of ZDF rats demonstrated that the surgical removal of subcutaneous fat had no influence on insulin resistance. The present study investigate the effects of removal of fat from a different anatomical compartment, namely, the retroperitoneal region, on insulin resistance of ZDF and Wistar rats (WR).

The above studies were combined with currently carried on investigations of Exendin-4, a potential treatment for type 2 diabetes mellitus (5). Exendin-4, which is produced in the salivary glands of Gila monster lizards, is structurally similar to glucagon-like peptide-1 and shares several useful biological properties with glucagon-like peptide-1. We investigate the correlation between Exendin-4 and reduction of particular fat compartments (subcutaneous, visceral or retroperitoneal) as well as its influence on the regrowth of retroperitoneal fat after its surgical removal.

MRI has been shown to be a sensitive and accurate technique for non-invasive quantifying of regional fat distribution in experimental animals and humans (1-4). Accordingly, MRI data was used to calculate the total volume of fat as well as the subfractions in the subcutaneous, visceral (intra and retroperitoneal together) and retroperitoneal compartments.

Glucose tolerance, fat regrowth and its distribution were correlated in order to separately determine the effects of the three fat fractions under consideration on the development of obesity-induced diabetes.

Materials and methods

Surgical and experimental protocol. Retroperitoneal fat was surgically removed from 10 ZDF rats (aged 4-5 months) and 10 Wistar rats (aged 16 months). Animals were weighed, imaged, and had blood samples taken for fasting glucose levels and glucose tolerance curves one day prior to surgery (control measurements), 5 days after surgery, and monthly thereafter.

MRI and fat quantifying. MRI data was collected from Bruker 1.9 Tesla ABX Biospec. T1-weighted images were obtained using a standard two-dimensional spin-echo imaging protocol with TE=14.1 ms and TR=500 ms. Excellent contrast between fat and non-fat tissue was obtained. Imaging data was obtained throughout the entire abdominal region, with a total of 22 imaging slices of 4 mm thickness. Image processing was performed using Bruker Paravision software.

Results

A continuous increase of animal weight was observed following surgery. Most of the ZDF rats regained their control weight in approximately 4-8 weeks. MRI measurements of retroperitoneal fat agreed closely with direct assessment of the amount of fat removed. In addition, a statistical significant decrease in subcutaneous fat, as measured by MRI, was observed for all animals at a time point of 5 days after surgery

Animal weight and amount of visceral fat were each well correlated with the 15 minute glucose tolerance test and fasting plasma glucose level. One week following surgery, glucose tolerance in both WR and ZDF rats was significantly worse, and insulin levels were significantly higher, than in non-operated rats. Fifteen minutes after a glucose load, plasma glucose levels for the ZDF rats were 15.3 ± 1.9 mM/dl vs. 20 ± 2.5 mM/dl for the control group, with $P< 0.05$. In the WR, the corresponding values were 10.1 ± 0.7 mM/dl for the surgical group and 12.1 ± 1.2 mM/dl for the control group ($P< 0.05$). Four weeks after surgery, however, glucose tolerance was indistinguishable between the control and post-surgical ZDF groups. In contrast, the WR in the surgical group maintained their improved glucose tolerance.

Conclusions

These experiments demonstrate that resection of retroperitoneal fat in ZDF and WR rats with type 2 diabetes results in short term improvement in glucose tolerance. This effect persists until full regrowth of retroperitoneal fat occurs. For ZDF rats, regrowth occurs over approximately 4-8 weeks, while regrowth in WR rats takes relatively longer. It is unclear whether this difference in retroperitoneal fat regrowth rates between ZDF and WR is a species effect or an age effect.

References:

1. M. Ishikawa, K.Koga, *Magn. Reson. Imaging* **16,** 45-53 (1998).
2. J.C. Seidell, C.J.G. Bakker, K. Van der Kooy, *Am. J. Clin. Nutr.* 51, 953-957 (1990).
3. T.S. Han, I.E. Kelly, K. Walsh, R.M.E. Greene, M.E.J. Lean, *Intr. J. Obesity* **21**, 1161-1166 (1997).
4. J. Gautier, A. Mourier, E. Kerviler, A. Tarentola, A.X. Bigard, J. Villette, C.Y. Guezennec, G. Cathelineau, *J. Clin. Endocrinology & Metabolism* **83,** 1306-1311 (1998).
5. N.H. Grieg, H.W. Holloway, KA. Ore, D. Jani, Y. Wang, J. Zhou, M.J. Garant, J.M. Egan, *Diabetologia* **42**, 54-50 (1999).

P10

In vitro high resolution NMR imaging of the human cervix at 3 T for detection of early cervical carcinoma

Bence Csapó[1,2], Josef Széles[2], Csilla Balássy[2,3], Markus Klarhöfer[4], Andreas Obermair[5], Gerhard Breitenecker[6], Thomas Helbich[7], Peter Polterauer[2]

[1] Clinic of Obstetrics and Gynecology, University Medical School of Debrecen, Hungary

[2] Department of Vascular Surgery, University of Vienna, Medical School, Austria

[3] Department of Radiology at Kenézy Gy. County Hospital Debrecen, Hungary

[4] NMR-group, Department of Medical Physics, University of Vienna, Austria

[5] Department of Gynecology and Obstetrics, University of Vienna, Medical School, Austria

[6] epartment of Pathology, University of Vienna, Medical School, Department of Gynecopathology, Austria

[7] epartment of Radiology, University of Vienna, Medical School, Austria

Purpose

Investigation of the feasibility of high resolution in vitro imaging of the human cervix for the possible detection of the earliest signs of cervical malignancy using conventional histology as control.

Material and Methods

Cone biopsies of 20 female patients (ages 25-74) were acquired undergoing LLETZ (large loop excision of the transformation zone) conisation indicated by cytological findings of HSIL (highgrade squamous intraepithelial lesion) or CIN III (cervical intraepithelial neoplasm) biopsy findings. The samples, most of them marked at 12 o'clock with a single surgical suture for orientation, were placed in Fresenius solution immediately after surgery. For the duration of the NMR measurements the specimens were wrapped in foil and positioned inside a standard 50 ml centrifuge tube. The NMR measurements were carried out in a Bruker 3T whole body scanner (Bruker Medical 30/80, Bruker Medical Inc., Ettlingen, Germany) equipped with a strong gradient system (Bruker B-GA 12: inner diameter 12 cm, Gmax = 200 mT/m) and a birdcage coil with 3.5 cm maximal diameter. Images were acquired with standard 3D-Spin Echo sequences, slightly adapted for each experiment for contrast enhancement. Imaging parameters were: TR=1500 ms, TE = 60 ms, Matrix: 256 x 128 x 96, FOV: 30 x 30 x 20 mm, Acquisition time: 5 h 6 min. Data acquisition and analysis was achieved with Bruker Paravision software package. Histological workup of samples was carried out and results were compared on images of both methods.

Results:

Histology of the 20 investigated specimens showed minimal invasive carcinoma (FIGO[1] stage 1a1) in 3 cases, while in all other cases pathological changes were restricted to the epithelium (CIN I-1 case, CIN II-1 case or CIN III-15 cases).

Prospective analysis of NMR images did not enable detection of neoplastic pathology. During retrospective comparison of appropriate histological slices and MR images the localisation of minimal invasive carcinoma can be suspected.

Discussion:

NMR differentiation of cervical cancer within FIGO stage 1a has not been extensively evaluated. The infiltration of lymphocytes and local oedema are the two earliest, but not specific signs of epithelial neoplasm. These result in a increase of water signal in the affected area enabling its detection. FIGO stage 1a1 cervical carcinoma is the first, already invasive stage, where the integrity of the basal membrane of the epithelium has been broken by the multiplying tumour cells and infiltration depth is not more than 3 mm. Despite the excellent image quality and high resolution (120 x 230 x 210 µm) achieved in our experiments, the subtle pathological signs of invasivity in the three cases of early stage cervical neoplasm could only be detected with simultaneous confirmation and proof provided by the gold standard conventional histology. Reason is the poor contrast between epithelium and underlying stroma and also that in all three cases stromal invasion was only detectable to a maximal depth of about 1mm.

A FIGO stage 1a2 carcinoma however is expected to be easily identifiable due to its somewhat larger size (Infiltration of stroma is less than 5 mm from basal membrane and less than 7 mm on surface).

Conclusion:

The current work demonstrates that at high resolutions available at 3 T in vitro differentiation within cervical cancer FIGO stage 1a seems possible. Early FIGO stage 1a1 cervical carcinoma (stromal infiltration less than 1 mm) is only retrospectively detectable. Larger stage 1a1, or stage 1a2 cancers should however be well detectable, since already early stage 1a1 is localisable with the help of histologic slides.

References:

1. *TNM Classification of Malignant Tumours 5^{the} edition*, Ed.: L.H. Sobin & Ch. Wittekind, Wiley & Sons, New York, 1997

P11

Phase Contrast Angiography and Flow Measurements in the Human Finger

Josef Constantin Széles[*], Markus Klarhöfer[$], Bence Csapó[%*], Csilla Balássy[#*], Peter Polterauer[*], Ewald Moser[$&]

[*] Department of Vascular Surgery, University of Vienna, Medical School, Austria
[$] Institute for Medical Physics, University of Vienna, Austria
[%] Clinic of Obstetrics and Gynaecology, University Medical School of Debrecen, Hungary
[#] Department of Radiology at Kenézy Gy. County Hospital Debrecen, Hungary
[&] Clinical MR Unit, University Hospital of Vienna, Austria

Introduction

Diabetic neuropathy has been proven to have a strong influence on arterio-venous shunting. Through this phenomena an over-perfusion in the capillary system, a disequilibrium of the oedema-preventing mechanisms and an elevation of venous blood flow may result in the formation of the diabetic foot. Phase contrast (PC) MRI allows the visualisation of vessels and also the measurement of blood flow velocities. The aim of the presented study was to evaluate the feasibility of a 3T whole body scanner equipped with a strong gradient system to obtain PC angiographies and blood flow velocity values of the human finger with and without diabetes and apply the acquired knowledge to future examinations on the human foot.

Materials and Methods

Measurements were performed on a 3T whole body scanner (Medspec 30/80 Avance, Bruker, Germany), equipped with a strong, small bore Bruker B-GA12 gradient system (inner diameter: 12cm, max. gradient strength 200mT/m in 190μs). A 3.5cm birdcage rf coil was used for signal excitation and detection. Imaging parameters of the 3D PC sequence were: TR=50ms, TE=7ms, flip angle 30°, matrix: 256x128x64, FOV: 26x26x50mm^3. The venc value was set to 12cm/s and only the direction along the finger axis was velocity encoded. Measurement time for the full 3D dataset was 13,5min. Written informed consent was obtained from all subjects prior to examinations.

Results

Maximum intensity projections of the 3D datasets show, that the achieved resolution of about 100x200x800μm^3 is sufficient to visualise the main vessels of the finger.

Discussion

The obtained results show that PC angiography of the human finger is possible on a whole body MR system which is equipped with a strong gradient set. PC angiography methods need longer experiment times compared to time-of –flight techniques, on the other hand they offer information about flow direction and velocity which could be helpful in many medical applications.

Conclusion

The non invasive evaluation of diabetic angiopathy is a pressuring demand from medicine. The current method may supply a method for realisation of these investigations on the diabetic foot.

P12

Diffusion Tensor Imaging of Human Eye Lenses

B. A. Moffat, I. W. Turner* and J. M. Pope

Centre for Medical and Health Physics, and *Centre for Statistical Science and Industrial Mathematics, Queensland University of Technology, GPO Box 2434, Qld, Australia, 4001.

Introduction. The diffusion of water in the highly ordered long thin fibre cells of the eye lens is known to be anisotropic (Wu et al. 1993). However, to date no study has been undertaken to acquire full diffusion tensor images of eye lenses. Knowledge of water diffusion in the lens is extremely important for understanding how water and other small molecules exchange between the interior of the lens and the extra-cellular environment. Due to the diffusion anisotropy, the nature of diffusive transport within the lens can only be fully understood if the full diffusion tensor is acquired. In this study magnetic resonance microscopy (MRM) was used to measure diffusion tensors within the human lens. Analysis of the diffusion tensors provides new information on the transport of water within the human lens on a microscopic scale. This may be important for understanding the mechanisms behind degeneration of lens function with age, notably senile cataract and presbyopia.

Methods. Using a modified pulsed field gradient spin echo (PFGSE) sequence (Stejskal and Tanner, 1965), diffusion tensor maps of human lenses were acquired. From the diffusion tensors, the orientation of the principal axes and magnitude of the principal components for water diffusion within the lens could be calculated. Previously cyclic colour scales (Coremans et al., 1994) or diffusion ellipsoids (Basser et al., 1994) have been used to display the orientation of diffusion tensors in anisotropic tissues such as white matter in the brain. Although these methods are useful for showing where diffusion anisotropy exists it is not trivial to interpret the cell orientations relative to the image plane from these maps. A new approach to displaying diffusion ellipsoid results using a modified Matlab "quiver plot " is presented.

Results and Discussion. The long axes of the diffusion ellipsoids were consistently found to be parallel to the long thin fibre cells in the lens. The results show that the nature and magnitude of diffusion within the lens is not homogeneous. In the outer cortical region, the diffusion ellipsoids are highly ordered, diffusion is extremely anisotropic and relatively fast. Further into the lens cortex there is a decrease in the magnitudes of the components of the (diagonalised) diffusion tensor both parallel and perpendicular to the lens fibre cells. The perpendicular diffusion falls below our limits of measurement in a region surrounding the nucleus. The parallel diffusion also reaches a minimum in this region but well above the limits of measurement. In the nuclear region of the lens perpendicular and parallel diffusion increases to a local maximum. Anisotropy and ellipsoid order decrease in this region probably due to the known decrease in fibre cell order.

Conclusion. Diffusive transport of water and other molecules within the lens is extremely important for cell function. It is responsible for transporting in vital metabolites and removing unwanted toxins from the lens nucleus, since there is very little, if any, active transport in this region. The nature of the transport as measured in this study is unique to the lens system. The development of a barrier to diffusion in a region surrounding the lens nuclei with age (as revealed here) may be partly responsible for degeneration of lens function and contribute to presbyopia and senile cataract.

References

Basser , P.J., Mattiello, J., and LeBihan, D., MR Diffusion Tensor Spectroscopy and Imaging, *Biophys. J.* **66**:259-267 (1994).

Coremans, J., Luypaert, R., Verhelle, F., Stadnik, T., and Osteaux, M., A method for myelin fiber orientation mapping using diffusion-weighted MR images, *Magn. Reson. Imaging* **12**:443-454 (1994).

Stejskal and Tanner, Spin diffusion measurements: spin echoes in the presence of time-dependent field gradient, *J. Chem. Phys.* **42**:288-292 (1965).

Wu, J.C., Wong, E.C., Arrindell, E.L., Simmons, K.B., Jesmanowicz, A., and Hyde, J.S., In vivo determination of the anisotropic diffusion of water and the T_1 and T_2 times in the rabbit lens by high-resolution magnetic resonance imaging, *Invest. Ophthalmol. Vis. Sci.* **34**:2151-2158 (1993).

P13

Rapid Phenotyping using Magnetic Resonance Microscopy

G. Allan Johnson, **Laurence W. Hedlund,** Gary P. Cofer, Sally L. Gewalt

Center for In Vivo Microscopy, Duke University, Durham, North Carolina 27710

The utility of magnetic resonance histology has already been demonstrated in the characterization of genetic expression (1). MR histology provides three unique benefits over conventional histology: 1) it is nondestructive, 2) it provides superb soft tissue contrast, and 3) it is inherently three-dimensional. We demonstrate here the extension of these methods to the studies of whole mouse specimens by a) the use of very large three-dimensional arrays and b) the introduction of "active staining" techniques to allow for acquisition of these large arrays in reasonable scan times.

The use of three-dimensional acquisition is not new (2, 3). We have previously described the extension of these techniques to isotropic imaging for MR microscopy (4), but this previous work was constrained by the computer architecture to arrays no larger than 256^3. Spin-warp imaging sequences have been implemented on both 2.0 T and 7.1 T MR microscopes controlled by GE Signa (5X) consoles. The sequence allows acquisition of subsections of a volume of Fourier space that is shipped to a 64-bit (Silicon Graphics) workstation where the volumes as large as 1024^3 are combined and reconstructed using standard Fourier Transform methods.

The acquisition of arrays of sufficient dimension to cover a whole mouse is limited by the available signal and acquisition time. Both problems have been addressed through the use of "active stains." Specimens are perfusion-fixed with 10% buffered formalin mixed with paramagnetic species (Gd). By titrating the concentration of the mix with the animal body weight, one can effectively reduce the T1 of all tissue by more than 10-fold. This in turn allows one to acquire data with very short TR (< 50 ms), permitting the acquisition of very large arrays in relatively short times.

Figure 1 shows representative T1s for a whole mouse perfused with a 1:20 mixture of Magnevist: formalin. The T1 of all the tissues have been reduced to ~ 100 ms (@ 2.0 T) while the T2 (@ 2.0 T) of all the tissues are 0 ms. his translates to an effective gain in SNR of 5–10X when comparing "stained" vs. control specimens imaged at TR = 50 ms. Arrays of whole fixed specimens have been acquired at both 2.0 and 7.1 T, with voxel volumes ranging from 1×10^{-3} ml to 6×10^{-5} ml in acquisition times of < 30 minutes.

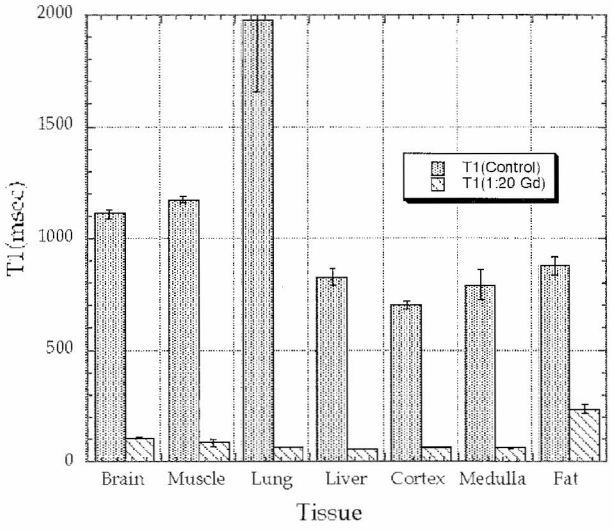

Figure 1

The ability to routinely scan large numbers of specimens and provide organ and tissue structure at microscopic resolution has application for a wide range of fields. As molecular biologists expand their genotyping research, there will be increasing need for effective phenotyping. We believe the techniques demonstrated here will provide these new approaches.

References

1. Johnson GA, Benveniste H, Black RD et al. *Magn. Reson. Quarterly* **9**, 1-30 (1993).

2. Brunner P, Ernst RR. *J. Magn. Reson.* **33**, 83-106 (1979).

3. Lai CM, Lauterbur PC. *Phys. Med. Biol* **26**, 851-856 (1981).

4. Suddarth SA, Johnson GA. *Magn. Reson. Med.* **18**, 132-141 (1991).

Acknowledgements

Research support from NIH/NCRR #P41 RR05959.

P14

Integrated Optical and Magnetic Resonance Microscopy for Cellular Research

Eric J. Ackerman, Gary R. Holtom, Paul D. Majors, **Kevin R. Minard**, and Robert A. Wind

Pacific Northwest National Laboratory, P.O. Box 999, MS K8-98, Richland, WA 99352, USA

Understanding the effects of carcinogenic chemicals and/or ionizing radiation on a cellular level is critical for safe environmental management. Particularly, since such information provides a basis for linking molecular level events with cancer development observed in tissues, animals, and humans. Over the years, MR microscopy and optical methods such as confocal and near-field microscopy have emerged as major tools used for investigating cells in a non-invasive and non-destructive way. In general, information provided by each technique is complementary. For example, with optical microscopy (OM), images with intracellular spatial resolution can be obtained in a relatively short time and cellular events can be followed using appropriate fluorescent dyes. Likewise, even without the use of exogenous contrast agents, MR microscopy can provide high-resolution images of opaque samples with contrast often better than that achieved with optical microscopy. In addition, several observable quantities (chemical shifts, spin couplings, T_1 and T_2 relaxation times, and diffusion constants) can be related to the morphological and biochemical changes that occur during cancer development. Moreover, the concentrations of specific metabolic compounds such as choline, creatine, lactate, and mobile lipids in cells can be determined, and these often change depending on tumor phenotype, size, cell proliferation status, and degree of necrosis and/or apoptosis.

If both microscopy techniques for cellular research could be combined and applied simultaneously, important advantages over each of the individual methodologies could potentially be realized. For instance, high-resolution images obtained with OM could, in principle, be used to guide micro-localized MR spectroscopy experiments. In addition, combination of MR and optical images could result in improved image contrast. Moreover, optical and MR transients observed during cellular events could be correlated. Finally, in case of rapidly fluctuating cellular events, optical information could potentially be used to trigger MRM experiments. In this context then, it is likely that integrated OM/MRM would provide information not obtainable with either approach individually, and in this regard, integrated microscopes may well be considered as the next advance in cellular microscopy instrumentation.

At the Pacific Northwest National Laboratory, integrated OM/MRM instrumentation is currently be developed for simultaneous studies of live cells in vitro. The first prototype, which combines MRM and confocal microscopy, will be used to examine oocytes from *Xenopus laevis*. These amphibian cells are intensively studied as model systems because of their unique biology and relevance to human cells. Particular interest stems from the fact that they are host to the same processes that occur in smaller cells. Moreover, *Xenopus* oocytes are ideally suited for testing the combined microscope because a single oocyte or embryo is ~100 times larger than most somatic cells, i.e., of the order of 0.2-1 mm. This large size makes it possible to perform both OM and MRM experiments on individual compartments within a single cell; thereby, facilitating testing and calibration. In this presentation, the design and construction of the microscope will be discussed and the latest results obtained with both microscopy techniques on oocytes will be presented.

A Study of the Effect of Dietary Changes on the MRM characteristics of the Seven-spot Ladybird *Coccinellae septempunctata.*

J.A. Chudek[1], I.E. Geoghegan[2], C. Lowe[1], **G. Hunter**[1], R.L. MacKay[1], M.E.N. Majerus[3], R.J. McNicol[2] and A.N.E. Birch[2].

[1] Department of Chemistry, University of Dundee, Dundee, DD1 4HN, Scotland, UK.

[2] Scottish Crop Research Institute, Invergowrie, Dundee, DD2 5DA, Scotland, UK.

[3] Department of Genetics, Downing Street, Cambridge, CB2 3EH, England, UK.

Introduction

We have already shown that magnetic resonance microimaging (MRM) is an ideal non-invasive tool to study the development of insects and the interactions between insects and their parasitoids[1-3]. During a study of the relationship between the larvae of the parasitic wasp, *Dinocampus coccinella,* and their host the Seven-spot Ladybird, *Coccinellae septempunctata,* apparently anomalous images were obtained. During laboratory studies, the insects were fed a standard artificial medium rather than their natural food, aphids. It appears that the dietary changes cause significant corresponding changes in the proton spectrum of the host insect and the intrinsic relaxation times of its tissues. While known to change some of the insects biological responses, the artificial medium previously has been considered to be a suitable food substitute for aphids during laboratory trials.

Experimental

All spectra and images were recorded on a Bruker AM 300 WB FT NMR spectrometer fitted with a Bruker Microimaging probe using a 10 mm resonator. Insects were fed either aphids (*Acyrthosiphon psium*) or an artificial medium developed by Henderson and Albrecht[4] for five days before analysis. During analysis insects were anaesthetised using CO_2. Images were acquired using a spin-echo sequence, T_1 and T_2 measurements using inversion recovery and spin echo methods respectively.

Results and Discussion

Two well defined resonances were observed in the spectrum of live specimens of *Coccinellae septempunctata* fed on aphids. In contrast, those fed on the standard artificial medium gave only a very broad resonance stretching from *circa* 6 ppm to 2 ppm.. Changing the diet from aphid to artificial and *vice versa* reversed these results. moreover T_1 is reduced when the diet is changed from aphid to artificial, whereas T_2 remains constant. Chemical shift selective images of aphid fed ladybirds clearly showed certain anatomical features, e.g. the ovaries, whereas those of the artificially fed insects not only showed completely different proton density distributions but also some features were missing altogether.

While the reason for these differences is, as yet, somewhat unclear one possible explanation is that the ladybird, on the introduction of the artificial medium, interprets the change as a signal that the aphid supply has stopped, as happens at the onset of winter, and thus commences preparing for diapause (the semi-dormant state assumed by insects during cold weather)

Conclusions

These experiments have shown that variation in the diet of the Seven-spot Ladybird, *Coccinellae septempunctata* has major effects on the NMR spectra and images of insects to an extent that artificial media cannot be regarded as a non-contributory element in insect studies. Consequently any experiments, not only magnetic resonance imaging, must in future be planned with regard to these effects.

References:

1. J.A. Chudek, *et al.* In: *Spatially Resolved Magnetic Resonance: Methods and Applications in Material Science, Agriculture and Biomedicine,* Eds. B. Blumich, P. Blumler, R. Botto and E. Fukushima, pp. 467-472 (1998).
2. J.A. Chudek, *et al., Magn. Reson. Imaging* **14**, 679-686 (1996); as a non-invasive tool to study the development of Lepidopteran Pupae. *J. Insect Physiol.* **41**, 419-424(1995).
3. B.A. Goodman, *et al., J. Insect Physiol.*, **41**, 419-424(1995).
4. S.A. Henderson, *Entomological Record Journal of Variation* **100,** 261-264 (1988).

P16

T_2 and ^1H Density Maps as Probes of Changes in the Lignin Structure of the Stems of Genetically Modified Tobacco Plants

J.A. Chudek[1], C. Halpin[2], D.W. Hopkins[3], **G. Hunter**[1], J. Metcalfe[2] and E.A. Webster[1,2]

[1]Department of Chemistry, University of Dundee, Dundee DD1 4HN, Scotland UK

[2]Department of Biological Sciences, University of Dundee, Dundee DD1 4HN, Scotland UK

[3]Department of Environmental Science, University of Stirling. Stirling FK9 4LA, Scotland UK

Introduction

Lignin is one of the most abundant classes of biological polymers, with essential structural roles in higher plants. Its relative recalcitrance to decay by micro-organisms influences the decomposition of plant material and therefore, the turnover of soil organic matter. With recent advances in understanding of the process of lignin biosynthesis, particularly the use of antisense RNA to block the activity of specific genes in the biosynthesis pathway, the possibility of tailoring lignins to particular applications, such as forage digestibility and wood pulping has been proposed. Before such developments can be exploited however, the possible ecological effects of modifications to lignin biosynthesis, such as plant material decomposition, need to be tested. In addition to contributing to the information required for informed decisions on risk assessment and disposal, such studies could provide insights into the role of the amount, composition and conformation of lignin on plant material decomposition. We have found that MRM T_2 and proton density maps clearly show differences in the nature of lignin within genetically modified cultivars of tobacco.

Experimental

Spin echo images of stems of wild and genetically modified tobacco plants were accumulated using a range of sixteen TEs on a Bruker AM300 WB FT NMR spectrometer fitted with a Bruker microimaging accessory using a 25 mm resonator. Data were worked up and fitted to T_2 and proton density maps calculated using the Bruker suite of programs ParaVision on a SGI O2 5000 workstation.

Results and Discussion

Spin echo images of the stem of wild type tobacco correlate well with the structure seen in a section cut from the same stem. This is mirrored in the T_2 and proton density maps where a ring of low T_2 and low proton density (water content) corresponds to the dark lignin band seen in the section. However, while the sections from stems of genetically modified plants are visually similar to those of the wild type stem, the intrinsic MRM maps show T_2 and proton density to be higher in the stems where the lignin has been modified. Moreover different genetic modifications affect T_2 and proton density to different degrees.

We consider that these results may be attributed to the modified lignin being more porous than that of the unmodified tobacco thus giving access to larger amounts of more mobile water. The results are consistent with data from decomposition experiments which show that stems of tobacco with these genetic modifications decompose more rapidly than does wild type tobacco. Gravimetric work has shown they also contain more water[1]

Conclusions

T_2 and proton density maps can highlight the changes induced by these modifications. The non-destructive nature of this technique will allow plants to be monitored through all stages of growth and if necessary during decomposition.

References

1. Hopkins, D.W., *et al.* unpublished data.

P17

Detection and Monitoring of Internal Browning Development in Fuji Apples Using NMRI

Juan J. Gonzalez[1]; Rosa C. Valle[2]; Serge Bobroff[3]; William V. Biasi[4]; Elizabeth J. Mitcham[4] and **Michael J. McCarthy[1]**.

[1]Department of Biological and Agricultural Engineering. University of California, Davis. USA
[2]Department of Environmental Horticulture. University of California, Davis. USA
[3]Department of Food Science. University of California, Davis. USA
[4]Department of Pomology. University of California, Davis. USA

Introduction. Internal disorders in fresh fruits and vegetables result in significant losses to growers, packers, sellers and consumers. For instance, the presence of internal browning (IB) in 'Fuji' apples results in the downgrading and/or rejection of the entire lot by produce buyers[1]. NMRI has the potential to be used as an on-line sensor for detecting defects. The development of a nondestructive imaging sensor would be beneficial to packinghouses, as it would facilitate testing of representative samples or sorting of entire lots of apples before marketing or further storage.

Purpose. The purpose of this study was to evaluate the potential of NMRI to detect, monitor and quantify IB in 'Fuji' apples during CA storage.

Methods. Nuclear Magnetic Resonance Imaging (NMRI) experiments were carried out on Fuji apples (*Malus domestica*) stored in two controlled atmospheres (CA): 3% CO_2 at 0°C and 18% CO_2 at 20°C, in order to detect and monitor the progression of internal browning (IB). Spin-echo type images were obtained with optimized echo and repetition times.

Results / Discussion. Three distinct regions were identified in the NMR images of apples with internal browning: normal, light brown and dark brown tissue. Light brown regions, more prominent in apples stored in 3% CO_2 at 0°C, had a lower signal intensity than normal tissue because of lower proton density (PD) and transverse relaxation times (T_2). Dark brown regions predominated in apples stored in 18% CO_2 at 20°C and displayed higher signal intensity than the normal tissues of apple because of higher T_2 values. We attribute this image contrast to physiological changes that occur during storage in CA that are not fully understood. Damage was monitored as it developed in the apples, since the samples remained intact during and after imaging. The NMR images of apples stored in 18% CO_2 at 20°C started to show early damage in areas located near the core after about 3 d of exposure. The IB developed rapidly thereafter. The rate of IB development and extent was proportional to the time the fruit was exposed to CO_2 and it was different for each apple. By the 9th day, all the apples imaged displayed IB as expected, since exposure to 18% CO_2 at 20°C increased the rate of development of IB[2]. After 3 d of storage the samples started to develop spike-shaped IB near the core, which spread to the cortical tissue after 7 d. The NMR images of apples obtained previous to the third week of storage in 3% CO_2 at 0°C did not show any IB development. The intensity of the signal in the core area decreased around 21d of storage, which indicated development of IB. Since the intensity decreased, it suggested that the damage started in the form of light IB, as opposed to dark IB, in which case the intensity would have increased. After 50 d, the intensity in the areas around the vascular tissues increased, whereas the region of lower intensity spread out of the core area and surrounded the areas of high intensity. After 3 months of storage, the lower, medium and high intensity areas were well defined, representing light IB, normal tissue and dark IB, respectively.

References

1. GRANT, J. et al. Calif. Agric. 50(3): 26-29 (1996).
2. VOLZ, R.K. et al. Postharvest Biol. Technol. 13, 97-107 (1997).

P18

Effect of Electric Field on Water Status in Germinating Morning Glory Seeds

Nobuaki Ishida[a], Seiichiro Isobe[a], Mika Koizumi[a], Hiromi Kano[b] and Carlton F. Hazlewood[c]

[a] National Food Research Institute, Tsukuba Science City, Ibaraki 305-8642, Japan

[b] National Institute of Agrobiological Resources, Tsukuba Science City, Ibaraki 305-8602, Japan

[c] Research Consultant International, The Woodlands TX 77393-0282, USA

Morning glory seeds in dry conditions were exposed to electric fields and then germinated. The treatment with an electric field of 500 kV/m for 60 min decreased the germination rate to 50%. ^{1}H-NMR image signal was weakened with increasing magnitude of electric field, due to an increase in the water fraction with a short relaxation time. Water movement in the morning glory seeds subjected to electric field treatments was examined by diffusion measurement with the pulse gradient stimulated-echo (PGSTE) method. Restriction in the mobility of the water was studied using the Meerwall & Ferguson's modification of the model of Tanner.

The average region containing water fraction with long relaxation times was approximately 50 μm in diameter and was surrounded by a half permeable barrier. The maximum intracellular water transport rate was 2.3 x 10^{-5} cm^2/sec. The treatment with electric field increased the water fraction which has restricted motion and caused the magnetic susceptibility of the seed to become inhomogeneous. It is thought that the membrane systems were affected by the electric polarization which led to the unusual accumulation of water and hydration of the stored macro-molecules during the imbibition process. This set of events resulted in the disruption of the membrane systems and an irregular organization of tissue structures by excessive swelling of the stored macro-molecules.

P19

Dehydration Of Multilamellar Phospholipid Model Membranes Studied On-line With ^{1}H-NMR Microimaging

Bertram Manz and **Frank Volke**

Fraunhofer-Institute of Biomedical Engineering (IBMT),
Ensheimer Straße 48, D-66386 St. Ingbert, Germany

Hydration properties of phospholipid model membranes are important to understand the selforganization, morphology, and forces acting between adjacent membrane bilayers in a multilamellar array ((Cevc and Marsh, 1987, Pampel, et al., 1998, Volke and Pampel, 1995)). Removal of water occurs during the approach of bilayers, e.g. as a pre-request for membrane-membrane fusion. There are a couple of reports showing the time dependent sorption process of water using gravimetric and spectroscopic tools ((Pampel, et al., 1998, Chen, et al., 1996, Klose, et al., 1992)).

In this study we use the NMR-Microimaging technique to get online images and profiles of the water distribution of a fully hydrated DMPC (dipalmitoyl-phosphatidyl-choline) sample during the process of temperature driven dehydration as a function of time. The lipid head group was deuterated so that the water NMR signal does not interfere with the most mobile parts of the lipid.

A 40 wt% H_2O - DMPC dispersion was homogenised using standard freeze -thawing procedures and one set of multislice images and T_2 profiles was recorded every hour using a spin-echo sequence. The T_2 corrected intensity of the water NMR signal integrated over the whole sample allows to calibrate the number of water molecules per lipid molecule (25 mol water /mol lipid for the fully hydrated sample at the start of the experiments) during the drying process.

We can clearly differentiate a fast, medium and slow dehydration process over a time period of 70 hours. The results are presented quantitatively and interpreted in relation to other studies on these systems. Furthermore, a correlation with the morphology of the multilamellar lipid-water dispersion using freeze fracture Electron-Microscopy is presented.

References

1. Cevc, G., and D. Marsh. 1987. *Phospholipid Bilayers.* John Wiley & Sons, New York.
2. Pampel, A., E. Strandberg, G. Lindblom, and F. Volke. 1998. High-resolution NMR on cubic lyotropic liquid crystalline phases. *Chem. Phys. Lett.* 287:468-474.
3. Volke, F., and A. Pampel. 1995. Membrane Hydration and Structure on a Subnanometer Scale as Seen by High Resolution Solid State Nuclear Magnetic Resonance: POPC and POPC/C12EO4 Model Membranes. *Biophys. J.* 68:1960-1965.
4. Chen, Z.-j., L. C. M. Van Gorkom, R. M. Epand, and R. E. Stark. 1996. Nuclear Magnetic Resonance Studies of Lipid Hydration in Monomethyldioleoylphosphatidyl-ethanolamine Dispersions. *Biophys. J.* 70:1412-1418.
5. Klose, G., B. König, and F. Paltauf. 1992. Sorption isotherms and swelling of POPC in H_2O and D_2O. *Chem. Phys. Lipids.* 61:265-270.

P20

NMR Study of Water Permeability of Two Transport Channels in Plasmodesmata in Plant Cells

Olga V. Volobuyeva, Genady A. Velikanov*,
Oleg A. Opanasyuk, Ludmila P. Khokhlova

Kazan State University, Kazan 420008, Russia
* Institute of Biophysics and Biochemistry, Russian Academy of Science, Kazan 420503, Russia

80-90% of plant cell occupies restrictive membrane the vacuole, the rest of volume - more compound by structure cytoplasm. All cells united by means of a mocrocappilaryes - plasmodesmata. In result forming the common structure - symplast. According to data of confocal microscopy, along external of the circular section of plasmodesmata communicating of cytoplasms of neighbour cells. The vacuoles of neighbour cells communicating by inner circular section (desmotubula).

The NMR-spectroscopy with pulsed gradient of magnetic fields and paramagnetic doping method for the investigation of water state and transport in tissue of different genotype of the winter wheat (Triticum aestivum L.) was used. The experiments have been made on the roots of 5-6 days old seedlings at rehydration after the action of the increasing water stress (weak - 0,3 MP, middle - 0,65 MP and strong - 1,5 MP). The modification of the cytoskeletal filament have been realized by the incubation of the seedlings in the solution of cytochalasin B (5 mkM, 30 min), which is the inhibitor of actin protein polymerization. The falling down of the signal amplitude in the stimulated echo has been analysed in the supposition that it may be offered in the sum of three exponents which are connected with the fraction of water with different degree of suppleness (less mobile - with coefficient of self diffusion D_1, with intermediate mobility - D_2 and the most mobile - D_3). It is supposed that these fractions are localised in different compartments of a cell.

By using of pharmacological compound that changing of water permeability (from full blockading to destruction), thus changing of degree of water self-diffusion in the cells showed that existence of self-diffusion coefficient do not able consequence of cell distribution by dimensions in root and is result of sub- and over-cell structure. At the exposition of roots in the solution of cytochalasin B in stressless conditions we have observed the increase of the mobility and the relative part of the slow fraction of water and the fraction with the intermediate degree of the mobility. After the action of the weak water stress the modification induced by cytohalasin B decreased. After the action of middle one the mobile of less moving fraction increased in more degree. The effects of cytochalasin B on the coefficients of self diffusion D_2 and D_3 in the conditions of the strong stress after-action were specific according to the cultivar. The amplitude of the diffusive modifications of the more mobile fraction D_3 corresponding probably to the water of vacuole was less for the non-resistant cultivar as compared with the more resistant ones. This is probably the evidence of the more effective mechanisms of the intracellular redistribution of water with the participation of vacuole in plants with higher adaptive potential.

P21

Imaging Membrane Permeability in Plants during Osmotic Stress

L. van der Weerd, M.M.A.E. Claessens, H. Van As

Wageningen University, Laboratory of Molecular Physics, Wageningen, The Netherlands

Introduction

The water balance in plants is of great interest for the understanding of differences in drought sensitivity and drought tolerance between various species. Maize and pearl millet plants are known to differ in drought tolerance and are used to investigate the effect of osmotic stress on the water status in the stem by means of in vivo NMR imaging. The obtained parameters T_2, proton density and Apparent Diffusion Coefficient are interpreted using a model for vacuolised plant cells based on the diffusion model of Brownstein and Tarr (1). This diffusion model assumes the spins to be confined in a volume with known geometry, i.e. the vacuole. Within this volume the magnetisation decays with a certain rate constant, T2,bulk. In addition to this bulk relaxation, relaxation occurs at the boundaries, i.e. the tonoplast membrane. When exchange of protons over the tonoplast between the vacuole and the cytoplasm is the rate limiting step (RH<<D), the observed T_2 of the vacuole can be described by a single exponential, which is dependent on the cell dimensions (R, m), the T2 value of the vacuole solution ($T_{2,bulk}$, s) and a sink strength parameter for the tonoplast (H, $m.s^{-1}$):

$$1/T_{2,obs} = H(1/R_x + 1/R_y + 1/R_z) + 1/T_{2,bulk}$$

Methods

Five-week-old water culture plants of maize and pearl millet were studied before, during and after osmotic stress, which was induced by replacing the normal root medium by a well aerated PEG-6000 medium, with a water potential of -0.35 MPa. Water uptake was measured by weighting the root medium vessel. For the T_2 measurements a multiple spin-echo imaging sequence was applied with TR=1.8 s, TE=4.6 ms, SW=50 kHz, FOV=50 mm, slice=3 mm and 64 echoes per echo train. T_2 and amplitude images were calculated after phase correction from the decay of real signal on a pixel by pixel base. Restricted diffusion was measured using a PFG-TSE sequence with •=2.4 ms and •=24 ms. Optical microscopy was used to determine the cell dimensions of the stem tissue.

Results

Under non-stress conditions the T_2 of the stem internodes varied as a function of the cell dimensions. The H parameter can be calculated from the measured T2 when the cell dimensions are known and appeared to be constant for cell volumes ranging from 2.10^4 to 2.10^6 μm^3 within the plant stem. Between the two species, however, there are differences in H. The fitted values for H are 2.8 10^{-5} and 4.0 10^{-5} $m.s^{-1}$ for maize and pearl millet respectively, assuming that $T_{2,bulk}$ is 2 s for both plants.

During osmotic stress maize showed neither changes in T_2 in the full-grown internodes nor in the shoot apical parts of the stem, though the leaves wilted and growth of the shoot apex stopped almost completely. The T_2 values in pearl millet stem tissue on the contrary decreased about 30% within 48 hours of stress. During recovery, the T2 returned to the initial values. The NMR signal density images and optical microscopy show that the cell dimensions did not change significantly during this period in both plant species. Diffusion was measured with a relatively long Δ to observe restriction effects. During osmotic stress for the pearl millet plants the apparent diffusion coefficient increased as well.

Discussion

According to Clark *et al.* (2), the T_2 of the bulk solution does not change as a function of significantly increasing concentration of osmotic solutes such as sugars. This, in combination with the unchanging cell dimensions lead to the conclusion that a change of H is the cause of the observed decrease in T2. As H represents the exchange of protons between the vacuole and the cytoplasm over the tonoplast membrane, the observed change must be caused by an increased membrane permeability for protons, most likely water (3). This conclusion is in agreement with the found increase in diffusion coefficient for pearl millet.

Conclusions

The membrane permeability as calculated from T2 data varies between different plants. During osmotic stress the membrane permeability increases in the drought tolerant pearl millet plants. We speculate that aquaporins play an important role in this increase.

References

1. Brownstein, K.R. et al., *Physical Review A* **19 (6)**, 2446-2453 (1979).
2. Clark, C.J. et al., *Journal of the science of food and agriculture* **78 (3)**, 349-358 (1998).
3. Snaar, J.E.M. et al., *Biophysical Journal* **63**, 1654-1658 (1992).

P22

Disturbance of the Ion Exchange at Membrane Pathology. A NMR Study

N. Sorokina, V. *Oslopov

Kazan Institute of Biochemistry and Biophysics , Russian Academy of Sciences;
*Kazan State Medical University, Kazan, Russia

Introduction. According to the modern approach, primary hypertension (human essential hypertension and its experimental analogue, the rats of the strain SHR with spontaneous hypertension) is based on disturbances of ion-transport function, structure and a number of other physical-chemical properties of cell membranes. The velocity changes in various ion-transport systems of cell membranes in cases of primary hypertension reflect the important pathogenetic properties of such cells[1-3].

At present the proofs of increase of passive membrane blood cells permeability for hypertension patients and SHR rats were obtained for univalent cations. These data are related with translocation velocity increase of the following ionic carriers: 1) Na^+-, K^+- unidirectional transport 2) Na^+/Na^+ counter-transport which is 2-4 times more activated at the Na^+ - Li^+ exchange. In this case it is evaluated as a ratio of the velocity of Li efflux into a Na containing medium and the velocity of Li efflux into a Na free medium .Moreover, we pay essential attention to the fact that, in cell plasma membranes of a range of tissues the system of Na^+/H^+ counter-transport (that controls a intracellular pH and can be blocked by amiloride) was identified [4]. It is known that the increase of translocation velocity of this carrier in cells is the enough reason for the activation mechanism of long-term supporting of the increased arterial pressure. At the primary hypertension the Na^+/H^+ exchange velocity increase can be caused be the following reasons: 1) an increase of proteinkinase C activity; 2) an alteration of membrane structure state controlled by proteins of membrane skeleton ; 3) an increase of contents of carrier molecules per membrane area unit. In this report we present a new method allowing us to for a find out such disturbances. This possibility is based on NMR researches of water transmembrane diffusion in red blood cells.

Results. The NMR H^1 method with pulsed magnetic field gradient (frequency 60 MHz, maximal gradient amplitude g=80 T/m) [5] was used to study erythrocyte bundles of rats of the strain SHR with spontaneous hypertension and control normal rats of the strain WKY as well as of healthy people and patients with hypertension [6]. Measurements were carried out during the first 2 h after sample extraction.

The primary information obtained by this method is a diffusive decay (DD) $A(g^2)$ - the envelope of spin-echo signals measured at different g values. DD in such complicated systems as erythrocytes, provided that the conditions of intermediate exchange when diffusion time t_d is comparable with life time in exchanging phases are fulfilled, can be presented as nonexponential function, characterized by maximal self-diffusion coefficients (SDC) pertained to extra-cellular protons, and minimal SDC, pertained to intracellular protons, where p_a^* and p_b^* are the populations of the its components respectively .

The alteration of DD $A(g^2)$ shape was observed vs extra-cellular pH (the latter varied within the range 6,55-7.4) which was displayed by the increase of the population of the intracellular component p_b^* with the decrease of erythrocyte pH for rats of the strain WKY and healthy people. In the case of the rats of the strain SHR this dependence is absent, that is obviously related with the changes of membrane permeability for protons at spontaneous hypertension. The study of DD shape dependence on a diffusion time shown, that these facts are conditioned by the changing of a proton exchange time τ from extra-cellular pH (the proton transmembrane exchange becomes slowly with decreasing of extra-cellular pH) in case healthy people and WKY rats, and by a default of a similar dependence in case of SHR

Together with NMR measurements the rate of Na^+/Li^+ counter-transport V (mkM/liter per h.) was registered in the erythrocytes of patients and healthy people using method described elsewhere [1]. There was found a distinct correlation between τ(pH) dependence and V. One should note, that the patients with $V \geq 300$ have as a rule serious forms of hypertension, and on the contrary people with $V<200$ do not as a rule suffer from primary form of hypertension . As it is shown by us, in the range of $V>300$ (corresponds unambiguously to patients) there is observed the weak dependence τ(pH), the similar behaviour of τ(pH) being observed for erythrocytes of rats of the strain SHR, and in the range of $V<150$ (healthy people) there is observed strong dependence τ(pH). This correlation implies that the change of τ(pH) dependence (its remission) points to the beginning of membrane permeability disturbances (obviously Na^+/H^+ exchange is activated [7]) of plasmalemma within the range of $150<V<300$. The Na^+/H^+ exchange contribution in the total proton exchange, registered by NMR method, was demonstrated by inhibition of this component by amiloride. This allows us to carry out the early diagnostics of membrane pathology and, consequently, to reveal predisposition of individuals to hypertension.

References

[1] M. Canessa, N. Adragna, and H. Solomon, *New Engl. J. Med.* **302**, 772-776 (1980)
[2] J.W. Woods, R. J. Falk and A.W. Pittman, *New Engl. J. Med.* **306**, 593-595 (1982)
[3] V.V. Morariu, *Rew. Rom. Phys.*, **27** 415-423 (1982)
[4] P. S. Aronson, *Ann. Rev. Phythiol.*, **42** , 545-560 (1985)
[5] R. Valiullin, V. Skirda, S. Stapf and R. Kimmich, *Phys. Rev. E* **55**, 3, 2664-2671 (1997)
[6]Y. Smirnov, V. Oslopov, N. Sorokina and A. Maklakov, *Clin. Exp. Pharm. Phys. Suppl.1*, s218-s219 (1995)
[7]W. Siffert and R. Dsing, *J. Hypertension* **26**, 04, 649-655 (1995)

P23

NMR Microscopy of Biological Samples at 600 MHz

Saebomi Park[1], Seung-Cheol Lee[3], Sungwoo Kim[2], Kwon-Soo Ha[2], Sun-Ha Kim[1], Chulhyun Lee[1], Soonchil Lee[3], Chaejoon Cheong[1]

[1] Magnetic Resonance Team, Korea Basic Science Institute, Taejon 305-333, Korea

[2] Biomolecule Research Team, Korea Basic Science Institute, Taejon 305-333, Korea

[3] Department of Physics, Korea Advanced Institute of Science and Technology, Taejon, Korea

Introduction

We have carried out microimaging experiments with a 14.1 T (600 MHz) NMR system to obtain cellular images of biological samples. A home-made probe with a newly designed rf coil and a pulse sequence which can reduce diffusion effect made it possible to obtain images with micron resolution. Cellular images of mouse follicles and geranium stem will be presented.

Method and Material

All experiments were performed on a Bruker DMX-600 spectrometer operating at 14.1 T. In these experiments we used a home-made probehead with a gradient coil which can produce a field gradient of 800 G/cm and with an rf-coil of 0.5 mm inner diameter. A half-echo pulse sequence which can reduce diffusion effect was used. The mouse follicles were isolated by a standard surgical process. The size of the follicle was around 200-240 μm in diameter. The sample was loaded in the 0.3 mm (inner diameter) tube and was fixed with agarose (1.7% concentration) containing DTPA solution (0.1% concentration). To obtain the cellular image of the geranium, we prepared a section of the stem which fitted to the tube. Both ends of the tube were sealed by mineral oil to prevent evaporation of the moisture.

Results

We obtained the proton density images and T1-weighted images of the mouse follicles with 5.6 × 5.6 × 50 μm pixel resolution. Imaging parameters were as follows: TR = 600 ms for proton density image; TR = 100 ms for T1-weighted image; TE = 2-5 ms; matrix size = 128×128; FOV = 700 μm. Distinct morphological structure of the follicle and the single cell layer of the oocyte whose diameter was 80-100 μm were apparent in these images. The cellular images of geranium stem were obtained with 2.7 × 2.7 × 100 μm pixel resolution. Imaging parameters were TR = 1500 ms, TE = 2-5 ms, matrix size = 256×256. In these images we could make a clear distinction of the cells.

Conclusion

Using a home-made probehead and high field strength, we were able to obtain cellular images of several-micron resolution which could be used in real-time cell studies.

P24

MRM Images from Biology and Materials Science

M. Gussoni [a], F. Greco [b], A.Vezzoli [a] and L. Zetta [b]

[a] Dipartimento di Scienze e Tecnologie Biomediche, Università di Milano, Milan, Italy.

[b] Istituto di Chimica delle Macromolecole, CNR, Milan, Italy.

Introduction

Peculiar aspects of Magnetic Resonance Microscopy (MRM) in different application fields have been reported[1]. They principally concern the non-destructive monitoring of a process as well as the possibility of obtaining morphologic and dynamic (flow mapping) data. The mobility of the major components of a sample, responsible for regions of different T_2, allows to get information on physico-chemical material properties. Moreover anything causing interfacial magnetic susceptibility differences in a structure (defects, voids) is detectable. Thus, on biological samples, tissues can be differentiated and flow pattern monitored; on materials, changes in dimensions, structural density, homogeneity, can be shown. Few examples from studies in progress, on samples quite different both in composition and application field will be presented.

Methods

MRM experiments were carried out on a 4.7 T Bruker AM WB spectrometer equipped with a probehead tuneable at the ^1H resonance frequency (200.13 MHz) and a gradient drive unit. A 15 mm insert was used, putting the sample in a 10mm NMR tube. Standard spin-echo (SE) and gradient-echo (GE) sequences were employed.

Results and Discussion

Applications to biological science. With respect to clinical applications, MRI of plant materials is still in its infancy[2]. Morphological images of Morning-Glory germinating seeds (23 x 23 x 3000 μm) were collected. Moreover MRM offers the unique possibility to measure flow non invasively even in complex geometry and opaque systems. Thus plant circulation was investigated by following the diffusion of D_2O into the plant germinated in pure water. Absorption of D_2O resulted in a progressive drop off of the intensity of the sequentially collected SE images, while the circulating water was released. This figure, well characterized by MRM, was assumed as a model for studying microcirculation in hollow fiber membranes, elemental units of a fiber dialyzer (an artificial kidney). Fibers with different hole diameters were imaged to prove system efficiency in regard to: i) water distribution ii) possible modification of dimension and/or structure of fiber holes after use, owing to protein deposition. This latter is a quite serious problem, as protein accumulation gives pathologies in long term dialyzed patients. Fibers, housed in glass capillaries, SE imaged at a resolution (23 x 23 x 1000 μm), higher than membrane thickness (30 μm), showed regions with not uniformly absorbed water. SE images from two fibers (before and after use respectively) were simultaneously collected at a resolution (12 x 12 x 5000 μm) lower than protein layer thickness. Nevertheless the protein-membrane interaction caused a shortening of water membrane T_2, reflected in a decrease of the signal intensity of the membrane of the used fiber.

Applications to materials science. Among polymers, elastomers, having partially liquid-like properties, create good situation for imaging[3]. The aging of a piece of styrene-butadiene natural rubber filled with carbon black was investigated. SE and GE images (86 x 86 x 5000 μm) collected at different temperatures (303K up to 363K) showed that long aging times cause the loss of elastomeric properties[4]. Structure of polymers with short T_2 can be obtained soaking them in a liquid, like water, and then imaging water distribution within them. In this case the structure of the void space is of more interest rather than the material itself[5]. Filters, different in polymer composition (cellulose diacetate, polyester, polypropylene), oversaturated with water, were SE and GE imaged to study i) water distribution; ii) efficiency in trapping water for a long time (10 days). The results accorded with data obtained by separate techniques, anyway not capable of showing spatial water distribution.

Conclusions

The reported examples emphasized the wide kind of problems that can be studied by MRM. Moreover an effort was made in trying to correlate other measurement methods to MRM, to improve our knowledge on materials.

References

1. Callaghan, P.T. *Principles of Nuclear Magnetic Resonance Microscopy.* Clarendon Press, Oxford, 1991.

2. Chudek, J.A.; Hunter, G.; *Progr. Nucl. Magn. Reson. Spectr*, **31**, 43-62 (1997).

3. Blümler, P.; Blümich, B.; *Rubber Chem.Technol., Rubber Rev.* **70**, 468-518 (1997).

4. Knoergen, M.; Heuert, U.; *et al., Angew. Makromol. Chem.* **261/262,** 123-133 (1998).

5. Miller, J.B.; *Progr. Nucl. Magn. Reson. Spectr.* **33**, 273-308 (1998).

P25

Applications of NMR Imaging to Biomaterials

R. Giesen[1], C. Chwatinski[1], D. E. Demco[1], B. Blümich[1],
A. Branderburg[2], U. Nietta[2], B. Pfeiderer[3] and A. Birkefeld[3]

[1]Institut für Technische Chemie und Makromolekulare Chemie, Rheinisch-Westfälische Technische Hochschule Aachen, Worringerweg 1, D-52074 Aachen, Germany

[2]Orthopädishe Klink, Universitätsklinikum, D-52074, Aachen, Germany

[3]Institut für Klinische Radiologie, Universität Münster, Schoßplatz 4/7, D-48149, Münster, Germany

Proton NMR dipolar filters as well as transverse relaxation filters have been employed for recording NMR images in biomaterials. The degree of local order in tissues has been investigated by these methods for intervertebral disks in the relaxed state. Dipolar-encoded longitudinal magnetization decays and double-quantum build-up curves have been recorded for the disks in order to establish the efficiencies of these filters for residual dipolar couplings. Proton NMR images encoded by the residual dipolar couplings in the intervertebral disks were determined by manipulation of the spin-echo images and double-quantum filtered images.

The same dipolar filters have been used for recording ^{1}H NMR images of silicon breast implants *in vitro*. Virgin as well as explanted silicon implants have been measured showing different residual dipolar contrast as a result of body fluid uptake and silicon degradation. The NMR images reveals differences between textured and untextured silicon materials. In the presence of axial mechanical stress ^{1}H spin-echo and dipolar-filtered images reveal the microscopic distributions of defects and local strain.

P26

High-resolution quasi-3D gel dosimetry: applications using γ-knife collimators of different sizes

A. Berg [1], A. Ertl [2], E. Moser [1]

[1] Institut für Medizinische Physik, [2] Abteilung für Neurochirurgie , University of Vienna, Austria

Introduction. Gel dosimetry by MR imaging relies on the sensitivity of the transversal relaxation time T2 on molecular mobility. By γ-irradiation a polymerization process in monomer containing gels is initiated which consequently effects correlation time. In contrast to Fricke gel dosimetry[1,2], which relies on the oxidation state of iron ions, the spatial resolution is not limited by diffusion phenomena. Since introduction of Bis-Acryl-Amid-Nitrogen Gels (BANG) based MR dosimetry[3] different investigations have been performed dealing with gel manufacturing, sensitivity, optical detection and different applications, mainly based on standard imaging on clinical MR scanners. Here we demonstrate that multi slice MR-dosimetry is possible at voxel sizes that are of an order of magnitude smaller than those reported[4]. The high spatial resolution is necessary to detect small volumes at high dose of ionizing irradiation as present in radiosurgery. We investigate dose distributions for differently sized (i.d. 4, 8, 14 mm) collimators in γ-knife irradiation and demonstrate the capability of MR-microscopy based BANG-dosimetry to detect dose steps at very small distances as present in a combined 2 step collimator (i.d. 8 and 14 mm) irradiation scheme.

Methods. The small sized sample tubes (d_{out} = 2,5 cm, length ≈ 6 cm) were delivered by MGS Research (Guilford, Conn., USA). The high spatial resolution could be achieved by a strong gradient system (d_i = 12 cm, G_{max} = 200 mT/m) and a small sized bird cage probehead on a high field (3T) whole body MR scanner (BRUKER MEDSPEC 30/80, Ettlingen, Germany). T2-weighted images are obtained by means of a CPMG 10-echo sequence (TE = 20 - 200 ms, TR = 3 s). T2 is calculated for each pixel element. A set of calibration measurements has been performed up to dose levels of 17 Gy at increments of about 2 Gy (Leksell Gamma Knife model B, Elekta Instr, Stockholm, Sweden). The relative dose distribution which is obtained from 3 differently sized collimators is investigated at pixel size of 390 μm (slice thickness = 1 mm). In case of a combined 8 mm and 14 mm collimator irradiation scheme perpendicular profiles were evaluated from corresponding profiles in T2 images at small voxel size (195 x 195 x 1000 μm^3) .

Results. The evaluation of the calibration procedures revealed a linear dependence of R2 = 1/T2 on dose D: R2 = 6.0/s + 0.48/(s Gy) D, the standard deviations for T2 being about 5 %. T2 imaging of the irradiated regions for the 4 mm collimator yielded an increased irradiated area of about 5 mm equivalent diameter whilst the 8 mm collimator offered an irradiated equivalent circle of 7.3 mm. For demonstrating the potential application to stereotactic radiosurgery a single perpendicular profile of the T2 image of the combined 8 and 14 mm collimator T2 image is transferred to dose profiles. The results are compared to Silicon diode measurements and computer simulated data (GammaPlan 5.2) provided by the gamma knife system (Fig. 1).

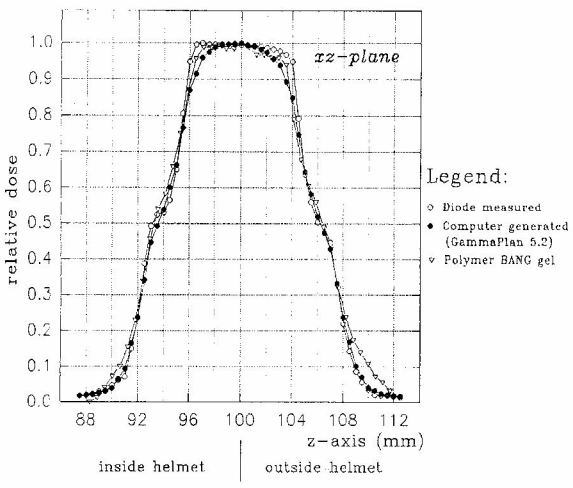

Fig.1: Energy-dose cross profiles of a γ-knife irradiated BANG sample. For comparison the simulated results of the treatment plan and Silicon diode results are shown. The steps corresponding to the differently sized 8 and 14 mm collimator can be clearly resolved.

Discussion/Conclusion. A relative accuracy in dose calibration of about 1 Gy may be achieved by means of special strong gradient and detection components on a whole body MR scanner. Along with multi echo evaluation very high spatial resolutions at tolerable noise levels are achievable in BANG dosimetry. The applicability to steep dose distributions, as present in a γ-knife two-collimator irradiation scheme, is demonstrated. Due to its ability to combine high spatial resolution and 3D information multi slice polymer dosimetry is especially suited for radiosurgery and brachytherapeutic applications[5].

References

1. Balcom BJ, Lees T J, Sharp AR, Kulkarni NS, Wagner GS, *Phys. Med. Biol* **40**, 1665 (1995).
2. Reichl B, Matthaei D, Richter J, Haase A, *Strahlenther. Onkol.* **172**(6), 312 (1996).
3. Maryanski M, Schulz R, Ibott G, Gatenby J, Xie J, Horton D, Gore JC, *Phys. Med. Biol.* **39**, 1437-55 (1994).
4. Oldham M, Baustert I , Lord C, Smith TAD, McJury M, Warrington AP, Leach MO, Webb S, *Phys. Med. Biol.* 43, 1113-1132 (1998).
5. Berg A, Schmidt W, Moser E, Proc. ESMRMB, 16th annual meeting, Sevilla, Sept. 16-19 (1999).

P27

Self-Diffusion Coefficient Maps and Visualization of the Restricted Diffusion in NMR Microscopy using B_1 Gradients

François Humbert [1], Michel Valtier [2], and Daniel Canet [2]

[1] LCPE, UMR 9992, CNRS, Université Henri Poincaré, Nancy I
405, rue de Vandoeuvre, 54600 Villers-lès-Nancy, France
[2] Laboratoire de Méthodologie RMN, UPRESA 7042
Université H. Poincaré, B.P. 239, Vandoeuvre-lès-Nancy Cedex, France

Dynamic NMR microscopy (1) using B_0 gradients, has proved to be a powerful tool not only in the biomedical field but also in the non-medical sciences including material science, food technology, fluid dynamics, and biotechnology. From a series of diffusion-weighted images, velocity and self-diffusion maps are obtained. However, for most systems of interest such as porous media and biological systems, only *apparent* diffusion coefficient (ADC) maps can be obtained essentially for three reasons : i) interaction between imaging and diffusion gradients; ii) presence of background gradients appearing at boundaries between regions of different magnetic susceptibility; iii) restricted diffusion leading to significant edge enhancement in NMR images (2). The interplay between these phenomena can cause distortion in images and numerous methods have been proposed for partially mitigating the harmful effects of features i) and ii) on the ADC determination. A method of choice to avoid these two problems is to use radio-frequency field gradients (B_1 gradients). Nevertheless, to date, the methods of measurement of spatially resolved diffusion coefficients using B_1 gradients (3) produce 1D profiles whose amplitude is not only function of the local self-diffusion coefficient but is also modulated by cosine functions of spatial coordinates. Extending our previous work (4), we show how to cancel this modulation and to obtain straightforwardly *true* self-diffusion coefficient maps (5). The feasibility and the reliability of the method are demonstrated with phantoms and systems of interest such as solvent swelled rubber, membranes and plants. Additionally, these examples exhibit a main feature of the presented method that is its ability to visualize clearly and accurately, as far as diffusion coefficients are concerned, restricted diffusion (6). For example, the spatial evolution of the self-diffusion coefficient observed experimentally in the vicinity of reflective walls is perfectly described by an appropriate theoretical model.

As shown from these results, the use of radio-frequency field gradients for obtaining self-diffusion coefficient maps represents a particularly attractive and powerful method for diffusion studies at interfaces and in heterogeneous systems such as porous media or biological tissues.

References

1. Callaghan P. T. et al., *J. Magn. Reson.* **91**, 326 (1991).
2. Callaghan P. T. et al., *J. Magn. Reson.* **A101**, 347 (1993).
3. Mischler E. et al., *J. Magn. Reson.* **B106**, 32 (1995).
4. Humbert F. et al., *J. Magn. Reson.* **134**, 245 (1998).
5. Valtier M., et al., *J. Magn. Reson.* in press (1999).
6. Humbert F., et al., *Chem. Phys. Lett.* **302**, 1 (1999).

P28

Application of B_1 Gradients in NMR Microscopy: Structural and Dynamical Study of a Water-Nonionic Fluorinated Surfactant System

François Humbert [1], Marie-Hélène Ropers [2], Marie-José Stébé [2], and Daniel Canet [3]

[1] LCPE – UMR 9992 – CNRS, Université Henri Poincaré, Nancy I, 405, rue de Vandoeuvre, 54600 Villers-lès-Nancy, France

[2] Laboratoire de Physico-chimie des colloïdes, UMR 7565, CNRS/Université Henri Poincaré, Nancy I, Faculté des Sciences, BP 239, 54506 Vandoeuvre-lès-Nancy Cedex, France

[3] Laboratoire de Méthodologie RMN, UPRESA 7042, Université Henri Poincaré, Nancy I, Faculté des Sciences, BP 239, 54506 Vandoeuvre-lès-Nancy Cedex, France

Over the two last decades, the B_0 pulsed field gradients technique has proven to be a powerful tool in the characterization of liquid surfactant systems and in particular in determining the structures of cubic liquid crystalline phases (1). In other respects, the B_1 gradient technique, considering recent advances in this field (2), should also be quite suitable for this kind of study.

We report here the use of B_1 gradients for the structural and dynamical study of a water-nonionic fluorinated surfactant $C_6F_{13}C_2H_4SC_2H_4(OC_2H_4)_2OH$ system. Beyond a reverse micellar phase, this system forms, depending on temperature and surfactant concentration, four other mesophases (3) : a phase lamellar L_α, two bicontinuous cubic phases Ia3d and Pn3m, and a sponge phase L_3. The self-diffusion coefficients of water and surfactant have been measured in the sponge and cubic phases at different temperatures and compositions. The measurements were carried out with the method described by Humbert et al. (2) using a home-made spectrometer operating at 90 MHz for protons. The B_1 gradient strength was 50 G cm^{-1}. Our results agree with other studies carried out with similar systems but by using B_0 gradients technique (4). In particular, the variation of the reduced water self-diffusion coefficient D_r with the volume fraction of surfactant exhibits a continuous change over the two phase area between the L_3 and cubic phases and, at high dilution, a limiting value of D_r of 0.65 is obtained. No significant difference is observed between the two cubic phases. All these results, combined with those obtained from small angle X ray scattering experiments, are discussed and analyzed in terms of hydration effect. A model derived of Balinov's model (4) is used to estimate the number of water molecules per oxyethylene group.

This study confirms the reliability and the potential of the B_1 gradients technique.

References

1. Lindblom G. et al., *Biochim. Biophys. Acta* **988**, 221 (1989).
2. Humbert F. et al., *J. Magn. Reson.* **134**, 245 (1998).
3. Ropers M. H. et al., *J. Phys. Chem. B* **103**, 3468 (1999).
4. Balinov B., *J. Phys. Chem.* **95**, 5931 (1991).

P29

Signal Attenuation by Self-Diffusion in Pulsed Field Gradient Heteronuclear Spectroscopy

Bernd Simon and Hartmut Oschkinat

Forschungsinstitut für Molekulare Pharmakologie,

Alfred-Kowalke Str. 4, 10315 Berlin, Germany.

The use of multiple quantum coherence in diffusion experiments is particularly attractive, because the effective gradient strength can be increased without hardware modifications. The pulse sequences to excite such coherence are composed of several pulses and free evolution intervals, and it is not always straightforward to analyze the influence of field gradients on the echo formation.

Recently, we developed a geometrical formulation, which allows the calculation of the ratios of gradient strengths and directions in different free precession intervals of a multipulse experiment for signal selection and artifact suppression [1-3]. This theory is extended to include the influence of diffusion on the signal amplitudes, following closely the approach of Stepisnik [4]. The equation for the echo attenuation in terms of an effective gradient is integrated for an arbitrary sequence of pulsed field gradients with rectangular or sine shape, leading to an expression which depends on the coherence orders and the duration, strength and separation of the individual gradients.

The formalism helps in the design of pulse sequences for diffusion experiments. As an example, we will discuss a heteronuclear quadruple quantum experiment (HQQC) [3].

References

1. Mitschang, L., Ponstingl, H., Grindrod, D. and Oschkinat, H., *J. Chem. Phys.* **102,** 3089-3098 (1994).
2. Mitschang, L., *J. Magn. Reson.* **137,** 1-9 (1999).
3. Thomas, D. J., Mitschang, L., Simon, B. and Oschkinat, H., *J. Magn. Reson.* **137,** 10-24 (1999).
4. Stepisnik, J., *Physica* **104B,** 350-364 (1981).

P30

H_2O Self-Diffusion Within Cellulose Fibres Studied Using Pulsed Gradient Nuclear Magnetic Resonance

K. V. Adams and L. F. Gladden
Magnetic Resonance Research Centre, Department of Chemical Engineering
University of Cambridge, Madingley Road, Cambridge, CB3 0HE, UK

Introduction

The self-diffusion of water within cellulose has been studied for a number of years[1-3], often using pulsed-gradient spin-echo NMR techniques. Earlier workers have developed analytical models to describe self-diffusion phenomena within cellulose in its many different forms; beads[2], fibres[1], sheets and pulps[3]. The results of the analysis by Li *et al.*[1] give two self-diffusion coefficients, one of which is dependent on the diffusion time (Δ). These diffusion coefficients correspond to motion of the 'inter' and 'intra' fibre water. However it is difficult to obtain a physical interpretation of the parameter $D(\Delta)$. In this study we investigate their results by performing analogous experiments over a much extended range of echo attenuations to fully probe the more slowly moving water molecules within the cellulose samples. We then develop a model in which there is only one free parameter, the diffusion time, Δ. In this model $D(\Delta)$ is no longer required. Finally the model is rationalised with the proposed internal structure of the cotton fibre.

Methods

All self-diffusion measurements were carried out on a Bruker Spectrospin DMX NMR spectrometer with a static magnetic field of 4.7 Tesla, corresponding to a ^1H resonance frequency of 199.96 MHz. A Bruker microimaging probe with a 5 mm radio frequency (r.f.) insert was used, giving a 90° pulse length of 3.6 μs. All experiments were performed at 294 ± 0.1 K; temperature control was achieved by means of a Eurotherm VT-2000 control system. The 13-interval alternating pulsed gradient stimulated echo (APGSTE) technique developed by Cotts *et al.*[4] was used for the diffusion measurements. The diffusion time, Δ, was varied from 20 ms to 1 s to investigate its effect on the observed diffusion characteristics. Appropriate values of gradient pulse length, δ, and gradient pulse strength, g, were chosen to give a minimum of two orders of magnitude attenuation in the signal over the range of diffusion times studied. 48 data points were acquired for each of the 12 values of the diffusion time. The cellulose fibres were soaked in deionised water for a minimum of 12 hours; excess water was removed and the samples were transferred into 5 mm o.d. glass NMR tubes and sealed.

Results

A log-attenuation plot of the experimental data did not yield a straight line, therefore the water within the cellulose fibres was not behaving as a bulk liquid. Curved log-attenuation plots are usually indicative of either more than one diffusion regime in the system or that the diffusing species are experiencing barriers to their motion over the timescale of the diffusion measurement. The initial slopes of the data corresponding to varying values of Δ coincide, however the curved parts of the data differ and their slopes appear to increase with an increase in Δ.

Discussion

Li *et al.*[1] found similar curved log-attenuation plots for water diffusing in cellulose fibres although only relatively small values of $q^2\Delta_r$, where $q^2\Delta_r = [g^2\delta^2\gamma^2(\Delta-\delta/3)]/4\pi^2$, were investigated. They suggest that a simple two-component population-weighted model should be used to fit these data, where one diffusion coefficient is dependent on the diffusion time; the term $D(\Delta)$ is required. Whilst this model appears to fit the data at low values of $q^2\Delta_r$, it consistently does not describe the shape of the curve well at greater echo attenuations. Furthermore, a self-diffusion coefficient is a physical property, in this case of water moving within the cellulose fibres, and is characteristic of the system. It cannot be dependent on diffusion time although this extra parameter appears to make the model work well. For these reasons it was decided to investigate and develop an alternative model to describe water diffusing within cellulose fibres.

The model which accurately fitted all the data corresponded to three regions with distinct diffusion coefficients associated with each within the cellulose fibres. This idea was founded from the structure of cotton fibre itself. The region with the fastest diffusion coefficient corresponds to the 'inter'-fibre diffusion as in the work of Li *et al.*[1]. This region was associated with unrestricted diffusion and did not have any dependence on Δ. Two further regions were associated with 'intra'-fibre diffusion within the primary and secondary walls of the cotton fibre respectively. These two regions allow exchange of molecules between them during the observation time of the experiment and hence show a dependence on Δ. 12 datasets each containing 48 datapoints were fitted simultaneously to give three distinct values for the diffusion coefficients for all values of Δ. This model accounts for the variation in the apparent diffusion characteristics due to changing the diffusion time, and is also consistent with a realistic physical structure of the cellulose fibre which previous models have failed to account for.

Conclusions

The pulsed-gradient NMR technique has been used to investigate the self-diffusion of water within cellulose fibres. Much greater values of $q^2\Delta_r$ were investigated than in other work, and it was found that previous models were not able to describe the shape of the log-attenuation data at these values. A new model has therefore been developed to describe the self-diffusion of water within cellulose fibres. The model described here accounts for the variation in the log-attenuation data with Δ, even at large values of $q^2\Delta_r$, and also is consistent with the known physical structure of the cotton fibre.

References

1. Li, T-Q. et al., *J. Colloid Interface Sci.* **154**, 305 (1992).
2. Ek, R. et al., *Powder Tech.* **81**, 279 (1994).
3. Li, T-Q. et al., *Langmuir* **13**, 3570 (1997).
4. Cotts, R. M. et al., *J. Magn. Res.* **83**, 252 (1989).

P31

NMR Study of Self-diffusion in the Isotropic Phase of a Nematic Liquid Crystal

M.V. Skirda*, R.V. Archipov

*Kazan Physical-Technical Institute, RAS, Kazan, Russia

Kazan State University, Kazan, Russia

Nematic liquid crystals are good model objects for the investigation of ordered systems. The processes, occurring both nearly isotropic-nematic transition and within some temperature range are of special scientific interest. Generally apparent properties of pretransitional processes are observed within narrow temperature range extremely near to the point of transitional temperature T_{IN}. The fact of existence of local order fluctuations at a high temperature is still discussing. However, some scientific groups declared about detecting of clusters at $T>T_{IN}=50K$ by NMR method according data of proton self-diffusion [1]. That scientific hypothesis deserves further proper study.

The object of this work is to quiz the general terms of article [1]. Proton self-diffusion of a law molecular weight nematic liquid crystal:

$$CH_3\text{-}(CH_2)_3\text{-}O\text{-}C_6H_6\text{-}O\text{-}C(O)\text{-}C_6H_6\text{-}(CH_2)_3\text{-}CH_3$$

is studied by NMR methods within the large temperature range ($322K<T<380K$) from $T_{IN}=322.2K$ in isotropic phase. Measurements were carried out with NMR PFG-spectrometer operating at 64 MHz for protons and high resolution Fourier-transform NMR PFG-spectrometer at 100 MHz for protons with different maximum values of pulsed gradient of magnetic field (30 T/m and 0.3 T/m consequently). The measurement errors did not exceed 5-10%. The Fourier-transform proton pulsed - gradient spin - echo NMR technique permits to measure the diffusion coefficients of the each component in the liquid complex systems without any perturbation on the studied systems, quickly and with high accuracy [2].

The typical diffusion decays are the monoexponentional shape within total temperature range and described only by one self-diffusion coefficient D_s. The important thing is absence of diffusion decay shape dependence therefore the one of value D_s on the diffusion time within range from 3 till 120 ms. The values of D_s measured with NMR-spectrometers at the various PFG values (from 0 till 30 T/m, from 0 till 0.3 T/m) correlate well to each other.

The received diffusion results have no any properties of local order fluctuations in isotropic phase of nematic within mentioned ranges of temperature and diffusion times. In other words, if clusters would even exist there their life-times are less 3ms- that is extremely minimal diffusion time used in experiment. Basically, our experimental results correlated well with conclusions of science groups majority according to them inhomogeneity in isotropic phase of nematic related with pretransitional processes can be detected in special conditions, for example in systems of controlled geometry [3,4].

References

1. E.R.Gasilova, V.A.Shevelev, S.Ya.Frenkel Dynamics of local order fluctuations and self-diffusion in the pretransitional region of nematic liquid crystal. Proton magnetic relaxation study. //4th *Russian symposium (with international attendance) "Liquid crystalline and related polymers"*, Abstract book, p.108, Moscow, RAS, 24-28.01.1999
2. James T.L., McDonald G.G. *J. Magn. Reson.* **11**, 58-61 (1973).
3. Callaghan P.T. *Principles of Nuclear Magnetic Resonance Microscopy, Oxford*: Oxford University Press, 1991.
4. Vilfan M., Lahajnar G., Zupancic I. et al., *J. Chem. Phys.* **103**, 8726-8733 (1995).

P32

Chemical-shift Selective NMR and MRI Investigations of Diffusion and Transport in Multicomponent and Multiphase Systems

Irene Bartusseck, Christian Heine, Song-I Han,
Siegfried Stapf, Peter Blümler, and Bernhard Blümich

Institut für Technische und Makromolekulare Chemie
und Magnetic Resonance Center (MARC), RWTH Aachen, Germany

Transport phenomena can generally be separated into contributions from coherent and statistical motion. The usual approach in NMR to encode displacements and to distinguish between these two contributions consists of an echo experiment where the echo is sampled after application of two, or more, magnetic field gradient pulses. Coherent motion, e.g. liquid flowing at a constant velocity, is then reflected by a gradient-dependent phase shift of the signal, while random motion (diffusion, dispersion) affects the signal intensity [1]. The spectral information of the echo is retained and can be exploited either for monitoring molecular motion of different chemical species simultaneously and for the encoding of position via a read gradient.

Conventional PGSTE and fast CPMG-PFG sequences [2], the latter allowing the determination of the full displacement propagator in less than one second, werde applied to determine the concentration-dependence of the self-diffusion-coefficient of several binary liquid mixtures in equilibrium.

If the multicomponent system is in a non-equilibrium state, i. e. macroscopic concentration or density gradients are present, the effects of interdiffusion have to be taken into account. Chemical-shift selective one-dimensional imaging of an initially layered two-component system shows the interdiffusion of the species. From the time evolution of these profiles, the concentration-dependent mutual diffusion coefficient can be computed and compared to the self-diffusion coefficients obtained in the equilibrium state.

A different case of interdiffusion is encountered for fluid ingress into porous media [3]. This situation is of particular interest in diffusion-controlled reactions such as decay processes in microporous gels which possess high biomedical and environmental relevance. The methods described above were applied to spherically symmetric systems such as liquid diffusing into a gel-stabilized drop. From the time-dependence of the one-dimensional profiles, the evolution of the diffusion front in three dimensions can be reconstructed by an inverse Abel transformation and compared to different model descriptions.

For the investigation of fast coherent motion, the available NMR tools can be optimized for short encoding times. By applying time-of-flight methods, velocity-encoded imaging and propagator measurements, a statistical description of transport processes can be combined with spatially resolved mapping the stationary velocity field. As a demonstration of these techniques, we compare flow in a thin liquid film with laminar flow in a circular pipe.

References

[1] Callaghan, P. T., *Principles of Nuclear Magnetic Resonance Microscopy*, Clarendon Press, Oxford (1991).

[2] Karlicek, R. F., Lowe, K. J., *J. Magn. Reson.* **37**, 75 (1980).

[3] Pel, L., Hazrati, K., Kopinga, K. et al., *Mag. Reson. Imaging* **16**, 525 (1998).

P33

Displacement Propagators as a Probe of the Effect of a Polymer Treatment on the Permeability of Rock

M.L. Johns [1], A.J. Sederman [1], L.F. Gladden [1], A. Wilson [2], S. Davies [2]

[1] Department of Chemical Engineering, University of Cambridge, United Kingdom

[2] Schlumberger Research, Cambridge, United Kingdom.

Introduction. Pulsed Field Gradient methods were used to investigate the effect of a commercial polymer treatment on the displacement propagators of a brine solution in a cylindrical Bentheimer sandstone rock core, with a 38.4 mm diameter. The polymer treatment is known to reduce the permeability of the rock. It is used in water-containing regions of oil reservoirs in an attempt to reduce the production of water from such reservoirs and the consequential cost of the subsequent disposal of the water. The ultimate objective of the work is to determine the exact mechanism whereby the permeability of the rock is reduced by the polymer treatment. In this respect the change in the displacement propagator, following treatment, provides valuable evidence. In addition, using a Lattice-Boltzmann model to describe the flow of the brine solution in the pore space of the rock core, the propagators were reproduced both before and after the treatment. By using various mechanisms to describe the polymer treatment in this modelling approach and subsequently comparing with the experimental data, the true mechanism of the polymer treatment was further investigated.

Method. The sandstone core was pre-saturated with brine solution and was contained in a pressurised membrane by a fluorocarbon, which constrained flow of the brine solution to an axial direction. The alternating pulsed field gradient pulse sequence, developed by Cotts *et al.* (1989), was used to determine displacement propagators for the brine solution flowing through the rock cores in an axial and hence superficial flow direction. A 4.7 T vertical bore magnet and a 63 mm diameter bird-cage radio-frequency coil were used. A maximum gradient strength of 19 G/cm was available in the axial direction to encode the flow. Displacement propagators for the brine solution were produced for a variety of observation times, Δ, ranging from 50 ms to 1 s, and two different flowrates: 5 and 10 ml/min respectively. The polymer treatment was then introduced into the rock core at a flowrate of 1 ml/min over a period of 2 hours. Brine solution was then pumped through the core until a constant pressure drop was recorded across the sample. The permeability of the core was reduced by 20% by the polymer treatment. The various displacement propagators were then re-acquired.

Results and Discussion. Before the polymer treatment, the shape of the displacement propagators is seen to evolve from an exponential shape to a Gaussian shape, centred on the average displacement, as Δ is increased. This is consistent with previous observations (e.g. Tessier *et al.* (1997)). It corresponds roughly to the transition from flow in a single pore to flow between pores. For all the propagators acquired, the average displacement was equal to within 7 % of the theoretical value, determined using the known porosity of the sample (21 %). Following treatment with the polymer, the displacement propagators acquired at short observation times show no variation from the corresponding pre-treatment propagators. However as the observation time (Δ) is increased, the post-treatment propagators show a delayed transition from an exponential shape to a Gaussian shape. At large values of Δ, the post-treatment propagators extended to higher displacements in comparison with the pre-treatment propagators, and hence the average displacement is virtually identical for corresponding pre- and post- treatment propagators. Thus despite a very modest decrease in permeability due to the polymer treatment, the change in the shape of the propagators as Δ is increased is considerable. Two hypotheses were considered for the effect of the polymer on the permeability of the core , either the polymer remains trapped in small low permeability pores or it forms a surface coating over the entire pore space. If the polymer formed a surface coating, it would be expected that all the propagators would show some variation following treatment at all values of Δ considered. However, if the polymer was trapped in virtually stagnant pores, both before and after treatment, the fluid in such pores would remain stagnant and hence the propagators would be similar at low values of Δ. However as the value of Δ is increased the fluid in such pores in the pre-treatment case would diffuse out of such pores more readily than in the after-treatment case, resulting in differences in the propagators at such large values of Δ. As more fluid is essentially stagnant and confined to a single pore following treatment in this mechanism, this results in the observed delayed transition from an exponential shape for the propagator to a Gaussian shape. This conclusion has been verified by the preliminary results from the modelling of the propagators. Allowing polymer to occupy stagnant pores produced similar variations in propagator shape as was observed experimentally. This was not the case when the polymer was allowed to coat the surface of the pore space.

Conclusions. Using pulsed field gradient techniques the effect of a polymer treatment on the permeability of sandstone rock was successfully investigated by acquiring displacement propagators both before and after the treatment. This provided useful insights into the mechanism whereby the polymer affects the permeability. The experimental data and initial modelling results suggest that the polymer preferentially occupies pores associated with stagnant flow.

References

Cotts, R.M., *et al.*, *J. Magn Reson.* **83**, 252-266 (1989).

Tessier, J.J., *et al.*, *AICHEJ* **43**, 1653-1661 (1997).

Diffusion in surface-wetting films in a two-phase saturated porous solid characterised by pulsed magnetic field gradient NMR

William M. Holmes, Robin G.Graham and Ken J.Packer
School of Chemistry, University of Nottingham, Nottingham NG7 2RD, UK

The distribution of two immiscible fluid phases within a porous solid is governed by the mutual interfacial tensions. For a strongly water-wet porous solid, saturation with both aqueous and hydrocarbon phases is expected to result in a physically continuous water phase, always in contact with the solid surface, whereas the non-wetting phase will reside in the centre of pores. At low water saturations the aqueous phase forms thin, surface-wetting films, whose shape and spatial distribution of thickness are saturation dependent.

The sample used was a strongly water-wet Fontainebleau sandstone, saturated with both 3% NaCl brine and dodecane. The diffusion of the aqueous phase within these surface wetting films was studied using pulsed field gradient NMR. For different water saturations one-dimensional displacement propagators, $P_{\Delta}(X)$, were measured at several observation times, Δ, with $X = x_{(\Delta)} - x_{(0)}$ and with x defined by the gradient used.

At high values of Sw, the water propagator has a gaussian-like distribution, as expected for 3-dimensional self-diffusion within porous solids. At lower values of Sw, the diffusion of the water takes place within surface films under conditions where the root mean squared (rms) displacements are much larger than the expected film thicknesses, thus reducing the effective dimensionality of the local diffusion process to 2-dimensional. This produces propagators with a distinctive strongly peaked shape near zero displacement. The experimental propagators P(X) are compared with two simple theoretical models, first diffusion on an isotropcally distributed array of unconnected infinite planes and second diffusion on the surface of an isolated sphere. This comparison provides unambiguous support for the quasi-two-dimensional nature of diffusion in these films. At very low water saturations (~5%) the experimental data shows deviations from the models, indicating an increased proportion of restricted water or possibly a further reduction in the dimensionality of the diffusive process associated with high-curvature features of the pore surface.

P35

Molecular Mobility Of Liquids in ZSM-5 Zeolite

Oleg Opanasyuk

Kazan State University, Kazan 420008, Russia

The molecular mobility of n-hexane, n-octane, n-decane and cyclohexane confined in ZSM-5 zeolite has been analysed by NMR technique. Concentration and temperature dependencies of free induction decays (FID), times of a longitudinal and transverse relaxation have been obtained. The free induction decays of investigated liquids reveal a nonexponential behaviour and can be decomposed onto two components. The first "liquid-like" component is exponential with the transverse relaxation times in the range from 10^{-3} up to 10^{-1} seconds. The fraction of this component decreases while a liquid concentration in the zeolite decreases. We have attributed this component to the molecules of the liquid located outside the zeolite crystalline structure. The second FID component reveals the "solid-like" nonexponential behaviour, which depends on the type of the entered liquid. This component has been attributed to the liquid molecules located inside the zeolite channels. The "solid-like" behaviour of these molecules has been confirmed by the dipolar echo observation. The other feature of this component is that it can not be approximated neither by an unique Gaussian line, nor by a superposition of such lines. From our point of view, the complex shape of this component is the consequence of the molecular mobility restrictions in the zeolite pores causing anisotropy of the molecular rotational mobility. However, at the present moment, the clear correlation between FID shapes and sizes or chemical structures of the molecules of the confined liquid has not been found.

Using the techniques of a selective separation of a NMR signal it has been found that the spin-lattice relaxation times T_1 of the molecules inside and outside the zeolite crystalline structure differ. This difference decreases while the concentration of liquid decreases. Such behaviour can be explained by the presence of the molecular exchange between the zeolite channels and the space outside the zeolite crystalline structure. The existence of such exchange in the n-hexane/zeolite and the n-octane/zeolite systems has been confirmed by using of a modified Goldman-Shen sequence. At the same time no indications of a molecular exchange have been detected in the decane/zeolite system.

To estimate the translational mobility of the molecules of liquid inside the zeolite channels in a n-octane/zeolite system with the content of a liquid 10 %, self-diffusion measurements have been carried out by a NMR PFG method. The obtained diffusion attenuations have a sharply nonexponential shape. The least self-diffusion coefficient has been evaluated from the diffusion attenuations to be of the order of 10^{-13} m^2/sec. We suppose that this coefficient is the average self-diffusion coefficient of the molecules involved in the exchange process between the zeolite channels and a the space outside the zeolite crystalline structure. Therefore this coefficient can be considered only as a rough estimation of the self-diffusion coefficient of the liquid molecules located inside the zeolite channels. The direct measurement of the self-diffusion coefficient of the liquid molecules inside zeolite micropores by the NMR PFG technique is highly complicated by the short values of the T_2 times of these molecules. The exchange kinetics experiments have been carried out to independently estimate the diffusion coefficients of the liquids in zeolite. In this experiment the zeolite sample partially saturated with the amount of the liquid sufficient to fill all micropores was filled out with the large amount of the deuterated analogue of the liquid used for the preliminary saturation. Then the sequence of $\pi/2$-pulses was applied to the sample and FID after each of them was detected. The measured FID were decomposed onto two components mentioned above and the dependencies of amplitude vs. exchange time were obtained. The obtained decreasing dependencies reveal the two stages of the exchange process. We analysed these dependencies in terms of model of diffusion in biporous system. We have attributed first stage with characteristic time about some seconds to the molecular exchange between molecules in zeolite channels and molecules of the bulk liquid inside the zeolite sample. On this stage the exchange is primary controlled by the diffusion coefficient inside the zeolite channels. After recalculating of the measured dependencies in the terms of the assumed model we have estimated this coefficient. For the system zeolite/cyclohexane/deuterated cyclohexane it is of the order of $1.5 \cdot 10^{-12}$ m^2/sec. The second stage with characteristic time about some hours correspond to the exchange between the molecules of the bulk liquid in the zeolite sample and the molecules of the bulk liquid over zeolite sample. The exchange on this stage must be controlled by the diffusion of the bulk liquid and calculated values of diffusion coefficients confirm this assumption.

P36

Detection of Fluid Flow by Profile Imaging

M. Iko Burgar

CSIRO Manufacturing Science and Technology

Gate 4 Normanby Road, Clayton VIC 3168 AUSTRALIA

The effect of molecular motion of fluid flow on NMR signal gives us the ability to detect the flow in a variety of environments by NMR imaging methods . Changing in polarization rates and spin relaxation times in particular is used to image the "velocity distribution" and "translational diffusion" of fluids. Application of these well known methods to the fluid flow in porous media is highly restrictive and time consuming. Alternative faster MRI methods have been investigated like phase sensitive imaging and profile imaging. The phase sensitive data analysis obtained by normal MRI spin echo method reveals the information on fluid velocity as well as the sense of fluid flow direction. The profile imaging of fluid flowing around obstacles reveals details essential for engineering of many industrial processes. The capacity of MRI methods to detect the local velocity with microscopic accuracy qualifies this non-destructive method to become a regular tool in material research and industrial environment. Basic limitations, short T_2 of fluids in dense porous media and long time of accumulation, guided us to explore the alternative fast selective profile detection for velocity profiles in pipes and in heterogeneous systems. This method was tested in fluid flow conditions from open tubes to tubes filled with porous material and real sandstone rocks.

P37

NMR-imaging of dead flow using a very low magnetic field

Alexandr L. Fiodorov, **Viatcheslav V. Frolov** and Konstantin V. Tiutiukin

Research Institute of Physics, St. Petersburg State University,
198904 St. Petersburg, Russia

Introduction

NMR-imaging provides a valuable information about character of a current of liquid. However, it is required to collect the rather large quantity of data. It is of no consequence if one exploits a industrial NMR-imaging hardware with strong magnetic field. However, the feature peculiar to research at weak magnetic field is a lack of sensitivity, therefore the reconstruction of flow images takes too much time, that makes impractical the method. The purpose of the research is to develop a routine method of visualization of structure of current of liquid in pipelines having a complicated configuration, in particular, the determination of domains of dead flow in models of conduits using rather simple and inexpensive hardware.

Experimental

We used simple homebuilt NMR-imaging apparatus operating with a magnetic field 7 mT. The application of the NMR-imaging to study a flow has the advantage to compensate for the basic experimental difficulty in experiments on NMR at very weak magnetic field (the low sensitivity) by utilization of preliminary polarization of a flowing liquid with remote source of magnetic field. For this purpose an inexpensive permanent magnet with bad uniformity have been used. The liquid l lie eeenin nine le $см^3$ disposed in the gap of a magnet and connected with studied system with thin pipe. It allows to avoid an appreciable relaxation of magnetization during transport of a liquid. The simplified pulse sequences on a basis of gradient echo were developed which allowed to visualize the structure of a flow without acquisition of the tax of large volume of the data.

Results

2D NMR-images of axial section of systems conducting a liquid of a various configuration was obtained in a range of velocities under various experimental conditions (different direction of reading and coding gradients, parameters of pulses). The influence of conditions of formation of the NMR-image of a flow on an appearance of the image was investigated. Stagnation domains of flow was demonstrated evidently.

Conclusion

Thus NMR at weak field provides an inexpensive and simple method of visualization of certain features of flow trough conduits of complicated configuration.

Reference

1. Frolov V. V., NMR imaging at low frequency. Extended Abstracts of the XXVII Congress AMPERE, *Magnetic Resonance and Related Phenomena.*, Kazan, Aug. 21-27, 1994. K. Salikhov (ed.). Vol. 2, p. 705.

P38

Imaging and Exchange NMR of Translational Motion

Song-I Han, Christa Chwatinski, Siegfried Stapf, Peter Blümler, Bernhard Blümich

Institut für Technische und Makromolekulare Chemie, Magnetic Resonance Center (MARC),
RWTH Aachen, Germany

Phase encoding of position by stepping of a single gradient represents one of the basic methods of NMR imaging. A pulsed gradient of the effective wave vector **k**, where $\mathbf{k} = -\gamma\int_0^{\delta}\mathbf{G}(t')dt'$ and $\mathbf{G}(t')$ denotes the gradient of length δ, is varied in equal steps to derive a signal intensity function $S(\mathbf{k})$, which is subsequently Fourier transformed to define the distribution of spin positions in a direction **r** parallel to **G**. Likewise, a pair of gradients $\mathbf{G}_1 = -\mathbf{G}_2$, defining the wave vector $\mathbf{q} = \mathbf{k}_1 - \mathbf{k}_2$, and separated by a delay Δ encodes a positional change **R** of particles during Δ and is routinely employed for the analysis of material transport such as self-diffusion and coherent flow. Combination of **k**-space and **q**-space encoding allows the spatially resolved investigation of a wide range of transport phenomena, thus correlating, for example, displacements with positions, and accelerations with velocities. The investigation of the behaviour of Newtonian and non-Newtonian fluids flowing through well-defined geometries such as cylindrical pipes represents one possible way to gain a detailed understanding of rheological properties. NMR has been shown to provide important contributions to the field of rheology due to its chemical selectivity and its applicability to opaque media [1].

One substance with particularly complex rheological behaviour is blood. Being essentially a colloidal suspension of deformable particles (erythrocytes) in a low-viscosity liquid (plasma), its properties are of special interest for biomedical problems such as treatment of venous diseases and clinical blood filtration. We present the velocity profiles of blood flowing through cylindrical tubes of diameters down to 1 mm in the parametrization $v_z(x,y)$, which shows the velocities in the flow direction as a function of the position (x,y) in the cross-section of the tube. The change from a parabolic profile to a flattened distribution indicates the cross-over towards turbulent flow at the critical Reynolds number for blood which was found to be $Re_c \approx 3000$. The same observation can be made when a volume-averaged, statistical description is obtained by measuring the particle displacement probability density, or propagator, $P(Z)$ along the flow direction. This propagator is rectangular for laminar flow but shows significant deviations in the case of turbulent flow. The flow profiles as well as the propagators are compared to corresponding results for water in cylindrical pipes and for flow in clinical hemodialyzers of 200 µm tube diameter, where exchange through permeable membrane walls alters the flow behaviour.

The determination of the correlation between position and displacement in the same directions by a simple two-pulse experiment represents a novel approach to combine imaging and displacement mapping. In a sequence containing two pulsed gradients **G** of identical area but opposite effective sign, displacements can be measured as described above. If both gradients have the same sign, the position, averaged over the mixing time Δ, is encoded by the sum of both gradients, 2**G**. The gradients, however, can in principle also be stepped independently to sample the full two-dimensional **k**-space defined by $(\mathbf{k}_1, \mathbf{k}_2)$. A two-dimensional Fourier transformation then leads to a description in position space $(\mathbf{r}_1, \mathbf{r}_2)$, the main diagonal of which contains the spatial information $\mathbf{r}_1 + \mathbf{r}_2$, while the secondary diagonal indicates displacements $\mathbf{r}_1 - \mathbf{r}_2$. Rotation of this coordinate system by 45° then renders a plot of the correlation between position and displacement [2]. The feasibility of a full two-dimensional experiment is demonstrated for a model system of water flowing through a pipe of changing cross-section. However, conventional imaging, diffusion and flow experiments with gradient pulses of matched areas can be regarded as a sampling of the diagonals of this 2D space.

The scheme can be extended by employing a larger number of gradient pulses, and higher-order correlations can be accessed by this method. We present simulations and experimental results for the case of two pairs of gradients separated by t_m, each pair being spaced by an interval Δ where $\Delta \gg t_m$. The gradient areas are matched within one pair, but are varied independently otherwise. Under these conditions, the displacements during the two intervals Δ represent averaged velocities [3], and their change during the mixing time t_m can be regarded to represent accelerated motion. As in the two-pulse case, Fourier transformation of the $(\mathbf{q}_1, \mathbf{q}_2)$ displacement space renders a description in the velocity space $(\mathbf{v}_1, \mathbf{v}_2)$, the diagonals of which represent averaged velocity and averaged acceleration, respectively [2]. As an example, the correlation of high accelerations with small velocities in the case of laminar flow due to the high shear rate near the tube wall is discussed.

References

1. Fukushima, E., *Annu. Rev. Fluid Mech.* **31**, 95 (1999).
2. Han, S.; Blümich, B., *Appl. Magn. Reson.*, submitted.
3. Callaghan, P.~T.; Manz, B., *J. Magn. Reson. A* **106**, 260 (1994).

P39 = 035

NMR on Salt Water Ice

Marion I. Menzel, Song-I Han, Heike Schoof*,
Siegfried Stapf, Bernhard Blümich

Institut für Technische und Makromolekulare Chemie,
Magnetic Resonance Center (MARC), RWTH Aachen, Germany
*Helmholtz-Institut für Biomedizinische Technik, RWTH Aachen

The microscopic and macroscopic structure of sea ice has been the topic for a wide range of research activities. It is known that this structure is highly dependent on the growth rate, the temperature history, the age as well as the depth from which samples are recovered [1].

Due to an incompatibility in crystal size there are no solid solutions of salt in the ice lattice formed from aqueous NaCl-solutions. According to the phase diagram (of NaCl/ice/H_2O) an aqueous solution of NaCl (containing 3 to 3.5 % NaCl) starts to form pure ice crystals at a temperature of approx. –2°C. The remaining solution will be enriched in salt content until the eutectic is reached (-21.2°C) where two solid components, ice and precipitated $NaCl \cdot 2H_2O$ remain. At intermediate temperatures, ice and brine (in pores) coexist.[2]

The shape and size of these pores, i.e. the topology of the ice, are defined by the growth direction along the temperature gradients and depend on the growth rate and on the storage temperature (recrystallization may occur at temperatures above the eutectic). In particular because these brine pockets are a habitat for a variety of different organisms, knowledge of the size distribution and connectivity of the pore network is vital for understanding the interaction of pollution with the sea ice and its influence on the organisms which winter in the pockets.

For laboratory experiments, samples of (3 % w/w) aqueous NaCl-solution were frozen under different conditions. The absence of salts other than NaCl ensured a well defined freezing behaviour, with the pores of highest NaCl concentration (22.5 % salinity) eventually freezing at -20°C.

The wide range of pore sizes in salt-water ice makes it an ideal test-bed for combining a variety of NMR methods sensitive to restrictions in motions on various scales:

2D ^{1}H-spin density imaging reveals the distribution, size, and orientation of macroscopic pores [3]. We present images of the in-situ freezing process under rapid cooling and compare them to results for ice grown slowly under temperature controll. By NMR imaging, structures of 50 µm are resolved.

Smaller distances down to a few micrometers can be probed by measuring the propagator of water molecule displacement. Propagators for displacements of axes parallel and perpendicular to the growth axis are compared for different temperatures and encoding times Δ up to 2s. The average diffusion coefficient is found to be strongly anisotropic [4] and to decrease for longer Δ. Along with the fact that non-exponential diffusional decay curves were observed, this indicates restricted diffusion on scales of approximately 50 µm.

Finally, a comparison of T_1 and T_2 relaxation of protons is sensitive to slowed-down rotational and translational motions in dependence of the surface-to-volume ratio and the local field gradients, respectively. Thus, scales well below 1µm can be accessed. The results are compared to the relaxation behaviour of ^{23}Na ions and discussed in terms of salinity distributions within the porespace.

References

[1] Weeks, W. F., Ackley, S. F., *CRREL Rep.* **82-1** (1982).

[2] Richardson, C., Keller, E., *J. Glaciol.*, **6**, 89 (1966).

[3] Edelstein, W. A., Schulson, E. M., *J. Glaciol.*, **37**, 177 (1991).

[4] Callaghan, P. T. et al. *J. Magn. Reson.* **133**, 148 (1998).

P40

A Sensitive RF Coil for MRI Studies on Plant Stems

P.A. de Jager, T.W.J. Scheenen, and H. Van As

Lab. of Molecular Physics, Dept. of Biomolecular Sciences, Wageningen University, Dreijenlaan 3, 6703 HA Wageningen, The Netherlands

Valuable physiological information is encoded in flow, diffusion and relaxation data of plant stems. A low field (up to 0.7 T) electromagnet is ideally suited for imaging of these parameters in plants because of the geometry and because the effect of susceptibility differences is minimal. A drawback of a low fieldstrength is the inherently low signal-to-noise ratio.

For this reason it is essential that all hardware components that determine the SNR should be chosen carefully. The best rf coil in this respect is a solenoid closely fitted around the plant stem. Inserting a full grown plant in this type of coil is clearly impossible, so each sample needs its own rf coil.

The alternatives for a solenoid are a saddle coil that can be opened from the side or a coil with a large diameter. Both have better access for the plant but a lower SNR. The third alternative the surface coil can not be used because the B_1 field homogeneity is insufficient. Although it takes some effort to fabricate a coil for each sample we have chosen this option.

First the two halves of the coilform are placed around the plant stem. A copper wire is wound in the groove of the coilform (the dimensions of the coil are optimized to obtain the maximum quality factor and filling factor). The wire is soldered to the variable tuning and matching capacitors mounted on a small board. This probe is wrapped in thin copper foil acting as a Faraday shield and carefully inserted in the 45 mm I.D. gradient probe. Finally the plant (e.g. a 80 cm Tomato plant) is placed in a vertical position in the 10 cm I.D. electromagnet and the climate chamber.

In the accompanying contributions of our group results obtained with this set-up are presented.

P41

The "TILT-Coil", a Novel RF Coil with 360 Degree Rotation

Wolfgang U. Roffmann, Stuart Crozier, Kurt Luescher, Gavin Hinds and David M. Doddrell

Centre for Magnetic Resonance, The University of Queensland, Brisbane, Australia

Introduction

It has been shown (1) that NMR Microscopy can be used to study the structural anisotropy and the orientational dependence of T_2 of biological specimens. The setup of such an experiment can be quite cumbersome in terms of sample orientation.

We have developed a RF resonator, which can be, tilted to various angles around 360 degrees without loss of Signal to Noise.

Theory

Choosing the polarization direction of a linear polarized Birdcage Resonator as the rotational axis allows us to tilt the resonator freely about the axis of B_0. The generated B_1 field of the resonator is always orthogonal to B_0. Fig 1 shows the general scheme of the "Tilt-Coil". The 90° pulse times are invariant with the rotation angle (Fig 2) and therefore by reciprocity the coil can be pivoted without loss in SNR.

Methods and Results

The "Tilt Coil" was constructed using a variable strip width pattern resulting from optimization applying inverse finite Hilbert transformation (2,3).

One of the advantages of the variable strip design is that the orthogonal mode is frequency shifted from the desired mode, preventing modal interference. Fig 3 shows images of a plant stem at 0 degrees and at 57 degrees to B_0. Note the improved resolution in the Image obtaned at 57 degrees.

Conclusion

We have demonstrated a novel RF coil for variable angle Imaging of biological specimens Such coils could also be used for other applications (eg STRAFI) and further investigations are planned.

Acknowledgements

We would like to acknowledge the help from the people of the CMR workshop, Dr. Andrew Whittake, Dr. Ian Brereton and Dr. Dieter Gross (Bruker) for helpful discussions. Support for this work is acknowledged from SPIN Systems Qld Pty Ltd under an AusIndustry Start Grant.

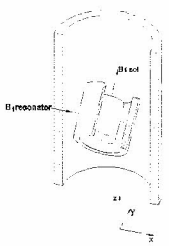

Fig. 1. General scheme of the "Tilt-Coil"

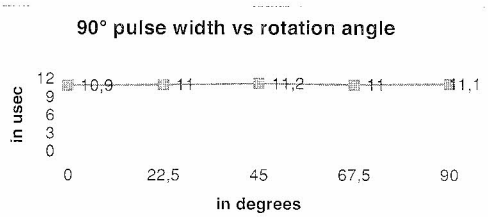

Fig. 2. 90° pulse width *vs* various tilt angles

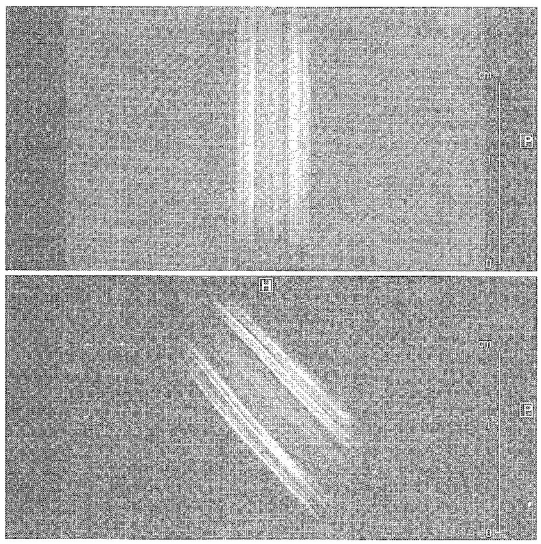

Fig. 3. sagittal images of a *cunjevoi* stem at 0 and 57 degrees to B_0

[1] Y. Xia *Mag. Res. Med.* 39:941-949 (1998).

[2] Crozier S, Forbes L, Roffmann W et al. *Concepts Magn Reson* 9:195-210 (1997).

[3] Forbes L, Crozier S, Doddrell D *Meas. Sci. Technol.* 9:1609-619 (1998).

P42

High-Temperature Imaging Probe

Ken-ichi Hasegawa [1], Yoshiaki Yamakoshi [1], Koji Saito [2]

[1] JEOL Ltd., Akishima-City, Tokyo, Japan

[2] Nippon Steel Corporation Advanced Technology Research Laboratories, Futtsu-City, Chiba, Japan

A high-temperature micro-imaging probe was developed for material science, in particular for polymer. It is very interesting subject to observe the morphology of polymer materials around the glass transition temperature, T_G. The T_G is above 400 °C, so we have designed a special high-temperature micro-imaging probe [1,2,3,4] for 400 MHz and wide-bore superconducting magnets.

Its specifications are as follows.

1. Sample tube size is 5 mm O.D.
2. Maximum sample temperature is above 500 °C.
3. Maximum field gradient strength is 240 G/cm.

We have tried SPI [5] and SPRITE [6] method at 500 °C using this probe.

Both of those two methods are very tolerant of gradient-switching time.

For example we applied large pulsed field gradients up to 240 G/cm to this probe, which made the gradient-switching time as long as 200 μsec. But the fixed phase-encoding time t_p can be shorten as short as 64 μs (method: SPI, FOV: 5 mm, points: 64)

So, the combination of high temperature and the SPI (or SPRITE) method is effective for materials science [7].

References

[1] Turner, R., Bowley, R. M., *J. Phys. E.* **19**, 876-879 (1986)

[2] Turner, R., *J. Phys. D: Appl.Phys.* **19**,L147-L151 (1986).

[3] Mansfield, P., Chapman,B., *J. Phys. E.* **19**, 540-545 (1986).

[4] Mansfield, P., Chapman,B., *J. Magn. Reson.* **72**, 211-223 (1987).

[5] Gravina,.S., Cory,.D.G., *J. Magn. Reson. B* **104**, 53-61(1994).

[6] Balcom, B.J., MacGregor, R.P., Beyea, S.D., *J. Magn. Reson. A* **123**,131-134(1996).

[7] Saito, K., Komaki. I, Hasegawa. K, *Fuel*, in press (1999).

P43

Applications of the "MP-Q" Imaging Coil

W. H. Wong, **Subramaniam Sukumar**, and Howard Hill

Varian NMR Systems,
3120, Hansen Way,
Palo Alto, CA 94304, USA

In Magnetic Resonance Microscopy images with a spatial resolution on the order of 10-100 microns are obtained. Reducing the pixel size is associated with a significant reduction in SNR. It is therefore preferable to work at high field strengths. High field vertical magnets that are used for conventional NMR spectroscopy can be readily adapted for microimaging applications. These magnets are limited to small bore sizes mainly due to cost reasons. The magnet bore size of a typical microimaging system is about 89 mm. After adding the shim and gradient coils we are left with a diameter of about 40-50 mm for the RF coil and sample. It is possible to integrate the shim/gradient coils or gradient/RF coils in order to increase the size of the imaging region. For practical reasons, a modular approach is preferred because the gradient and RF hardware can then be interchanged based on the application.

Efficient use of space inside the magnet is critical for microimaging applications particularly when it involves animal studies. The "MP-Q" coil was designed specifically with this goal in mind. The coil is designed to fit inside a 40 mm ID gradient coil. The ID of the RF coil is 30 mm and is open throughout the length of the probe to allow easy access. The most important feature of the probe is the excellent RF homogeneity as demonstrated in the Figure (right). Images from a "double saddle" coil (left) and a 12-leg birdcage coil (center) are also shown for comparison purposes. In the case of the saddle and the birdcage designs, the size of the coil had to be limited to about 26 mm (ID) because of space restrictions.

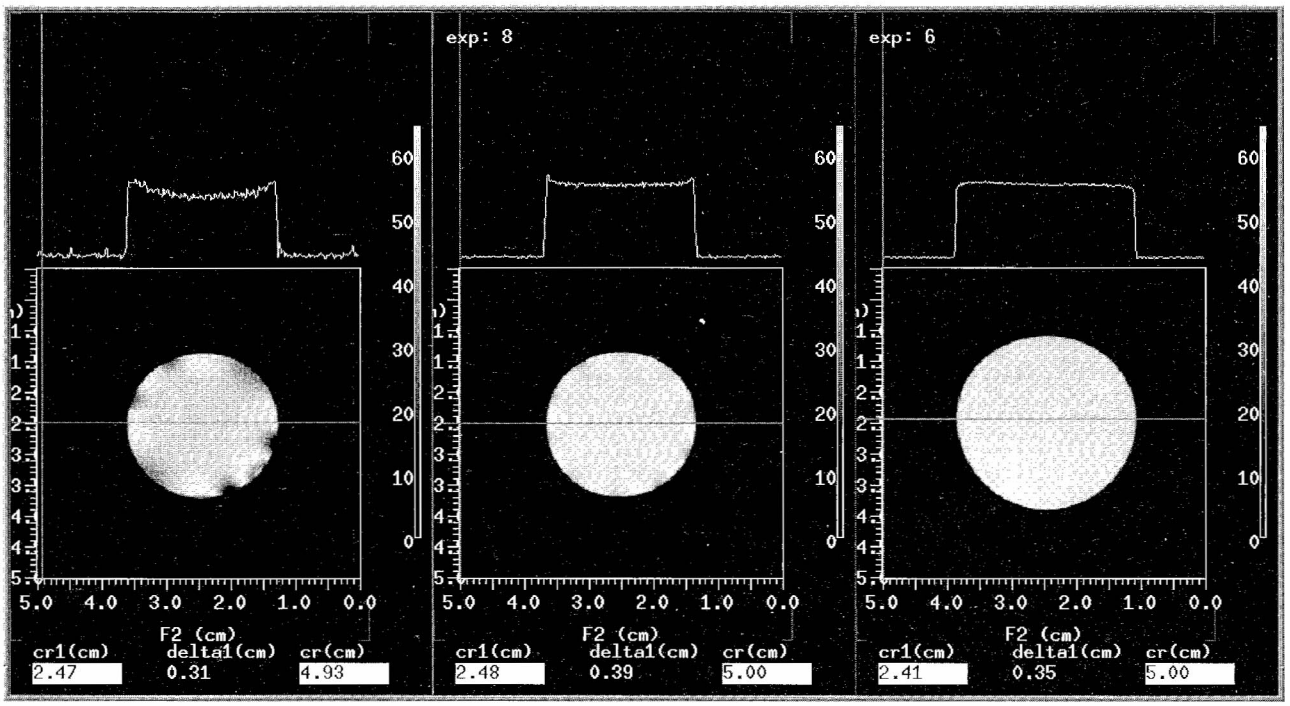

Figure: Images from a "double saddle" (left), 12-leg birdcage (center) and the "MP-Q" coil (right) to demonstrate the RF homogeneity within the coil region. Sample tubes (23 mm and 27 mm ID) containing mineral oil was used to avoid artifacts due to dielectric effects.

P44

Fabrication of NMR Microsensors for Nanoliter Sample Volumes

J. Dechow [1], A. Forchel [1], T. Lanz [2], A. Haase [2]

[1] Technische Physik and [2] Biophysik, Universität Würzburg, Am Hubland, D 97074 Würzburg, Germany,

The fabrication and characterization of microsensors for NMR spectroscopy of nanoliter sample volumes is presented. The detection of small volumes in NMR experiments is of great interest both for micro-spectroscopy of biochemical solutions as well as for NMR imaging with multi-coil arrays. In order to achieve a maximum SNR, the receiving coil has to be of the same order of magnitude as the sample itself and should be placed as close as possible to it. On the other hand, material interfaces in the nearest surrounding of the coil cause inhomogenities of the static magnetic field, leading to line broadening and poor spectral resolution. Further, microcoils fabricated by standard microelectronic techniques have a high resistance compared to conventional setups, and the *Q*-factor for the frequency of interest will decrease rapidly with the dimension of the coil.

In order to investigate the performance of a specific coil, a nl volume has to be defined and positioned in the sensitive area to avoid dominating parasitic influences of bonding wires or macroscopic contacts, for example, which may serve as receiving elements as well.

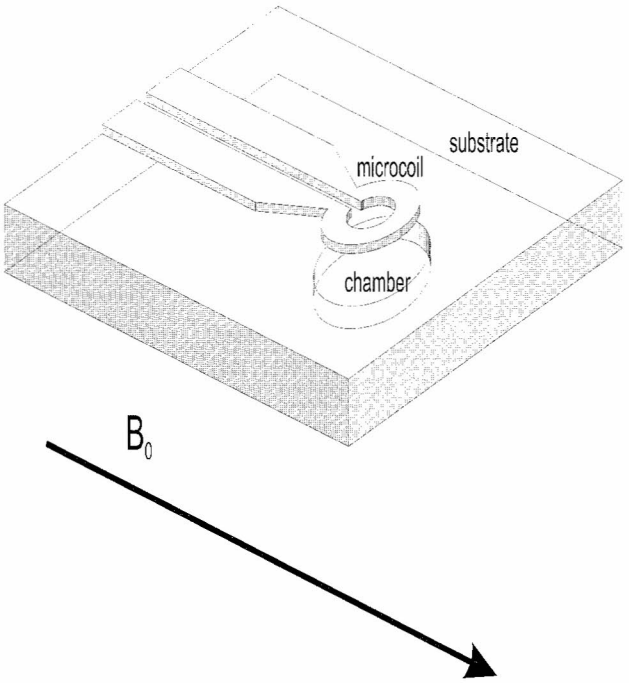

Experimental set-up with a single-turn microcoil.

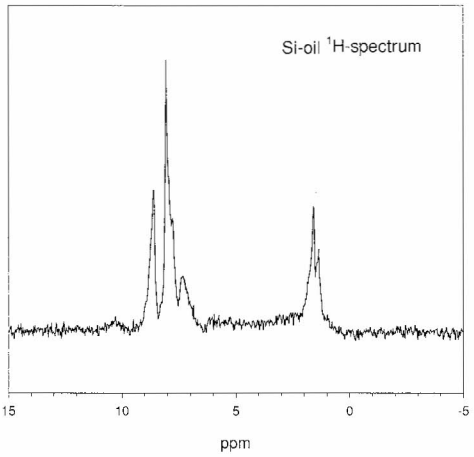

^{1}H NMR Spectrum of 100 nl pure Silicon-oil with 1200 transients from a single-turn microcoil

We fabricated microsensors both on glass and GaAs substrate. While glass is a familiar material in a NMR setup as well as in standard biochemical experiments, GaAs provides the full range of semiconductor fabrication techniques. Furthermore, the monolithic combination of the coil to a low-noise preamplifier based on a GaAs MESFET enhances the S/N of the weak NMR signal and can be used for fabrication of a full integrated NMR receiver.

All samples are fabricated on a 7 x 7 x 0.4 mm substrate. Planar coils with inner diameter from 50 µm to 600 µm are placed on its topside including a coplanar wave-guide leading to the bonding pads by using optical or e-beam lithography, lift-off, electroplating and air bridge techniques. A chamber for the liquid samples of 200-500 µm diameter is etched on the backside of the substrate, located under the coil.

Resolution Improvement on *In-Vivo* Human Skin Microscopy using a superconducting receiver coil at 1.5 Tesla

J-C. Ginefri [1], L. Darrasse [1], P. Crozat [2]

[1] U2R2M (CNRS URA 2212) and [2] IEF (CNRS UMR8622), UPS bât. 220, F91405 Orsay, France

Purpose. The use of high temperature superconducting (HTS) coil in MRI can greatly improve the quality of the images at low field[1] or in microscopy[2]. However applications with current clinical MRI systems (0.5-1.5 T) have not been yet considered. We investigate the SNR improvement provided by a small HTS surface coil for *in-vivo* human skin microscopy in a whole-body system operating at 1.5 T[3,4].

Subjects & Methods. For skin imaging, the region of interest covers a surface of a few cm^2 and a depth of a few mm and in this case, the SNR is almost entirely limited by internal coil losses if one uses a copper coil with typical Q-factor of 100. We designed a 64 MHz multi-turn HTS resonator with an average radius of 6 mm (fitted to the region of interest) and an unloaded Q higher than 30,000 at 77 K[5,6]. Using the HTS resonator, since the SNR is partially limited by the patient-induced noise, the optimum spacing depends on the loading[7] and is not zero[8]. The SNR for the HTS coil[6] and for a standard copper coil (same overall dimensions) was evaluated[7] by measuring the magnetic field per unit supplied current along the coil axis and by extracting the body-induced and coil resistance from loaded-Q. This extraction was done for various loads (anatomical regions and saline phantoms) as a function of the distance. Skin imaging was performed on a 1.5 T Signa system (GE, maximum gradient intensity of 10 mT/m) using the high-resolution insert gradient[3], modified to incorporate the HTS coil cryostat.

Results. For the copper coil, Q is about 100 whatever the load and the predicted SNR is maximum at the smallest allowed distance, 2 mm. The HTS coil Q values at 2 mm are 3084 and 1506 for the finger and calf respectively and increase to 11370 and 3576 at 6 mm. The optimum distance for the HTS coil ranges from 3 mm (calf) to 4 mm (finger) leading to predicted SNR gains in of 3.2 and 6 respectively.

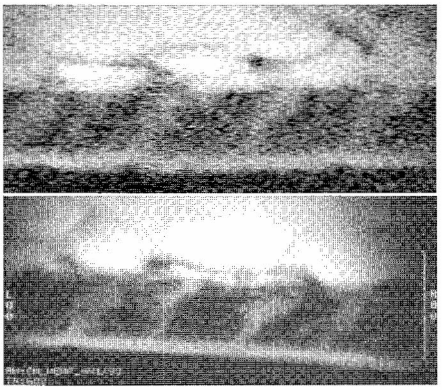

Fig. 1. Calf skin images

The *in-vivo* images of the calf skin (Fig. 1) and finger skin (Fig. 2) were performed with the copper coil (top) and the HTS coil (bottom), using a multislice spin-echo sequence:

TR/TE = 600/22 ms,

8 kHz bandwidth,

20×117×3000 μm^3 voxels,

Acquisition time; 10 min.

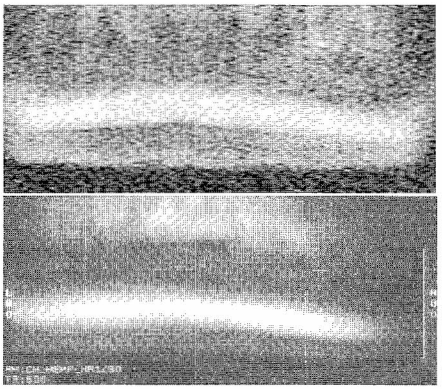

Fig. 2. Finger skin images

Discussion. We have demonstrated the first application of a HTS coil on a clinical MRI system at 1.5 T, showing highly resolved details within the skin layers. As the optimum spacing for the HTS coil is 3 to 4 mm away from the skin surface, no SNR penalty is introduced by cryogenic constraints. A significant gain in SNR, by a factor of 2, is obtained as compared to copper coils at 300 K.

Acknowledgment. We thank E Durand, O Jolivet (CIERM, CHU Bicêtre, France), Thomson-LCR. (Orsay, France).

References.

1. Van Heteren JG., et al., *Magn. Reson. Med.*, **Vol. 32**, p. 396, (1994).
2. Black RD., et al., *Science*, **Vol. 259**, p.793, (1993).
3. Bittoun J., et al., *Radiology*, **Vol. 176**, p. 457, (1990).
4. Song HK., et al., *Magn. Reson. Med.*, **Vol. 37**, p. 185, (1997).
5. Serfaty S., et al., *Magn. Reson. Med.*, **Vol. 38**, p. 687, (1997).
6. Ginefri JC., et al., proc. WOLTE 3, *J. Phys. IV.*, **Vol. 8**, p. 245, (1998).
7. Serfaty S., et al., proc. 2nd SMR meet. **Vol. 1**, p. 219, (1994).
8. Ginefri JC., et al., proc. 7th ISMRM meet. **Vol. 3**, p. 2129, (1999).

Stream Function Optimization for Gradient Coil Design

D. Tomasi
Escuela de Ciencia y Tecnologia, Universidad Nacional de General San Martin, Buenos Aires, Argentina.

Several techniques were developed in the last years in MRI to improve gradient coils [1]. Coils producing high homogeneity magnetic field gradients has been designed by the stream function method (SF), which uses an scalar stream function, S, to calculate the shape of wires, and also by the Target Field (TF) method, which gives a shielding condition and enables the design of self shielded gradient coils. Nevertheless, for restricted length coils the linearity of the field is strongly reduced in both methods due to coil truncation.

Another method, called simulated annealing (SA), has been successfully employed for developing gradient coils of restricted length [2]. Different from the TF method, discretization and restricted length are naturally taking into account in the SA method. Because the SA computing time depends strongly on the number of degrees of freedom of the annealing problem, several hours are necessary to achieve convergence. Recently a fast SA method as been proposed for the planar geometry [3]. This method uses the TF shielding condition within the SA scheme, to calculate the shape of wires. This allows a great reduction in the number of degrees of freedom of the annealing problem, and significantly decreases the computing time.

The purpose of this work is to show that, for the cylindrical geometry, S can be optimized using the Fast SA method, including an end-coil correction, which increases significantly the gradient field homogeneity.

METHOD AND RESULTS

To compensate for finite coil length we set, for the longitudinal coil, a d-length stream function defined by

$$S(z) = \sum_{i=0}^{N-1} \eta_i z^i ,$$

and for the transverse coil, $S(z,\phi) = h(z)\cos\phi$, where

$$h(z) = \begin{cases} \sum_{i=0}^{N-1} \eta_i z^i & z \le c \\ d - z & c \le z \le d \end{cases} ,$$

and η_i are N adjustable SA parameters.

At each step in the annealing algorithm, the current density, j_ϕ, that flows in the inner cylinder of radius a, is obtained from a randomly chosen S by $j_\phi = dS / dz$, while the shielding density, g_ϕ, in the outer cylinder of radius b is obtained from j_ϕ by the TF shielding condition [1]. The magnetic fields resulting from these can be calculated in the ROI, using the Biot Savart law. To perform the annealing of longitudinal and transverse gradient coils we wrote a C-code, which maximizes the homogeneity, and the efficiency of the gradient fields, and also minimizes the coil inductance.

We studied the quality of the result, as a function of the coil length, and the shielding ratio b/a.

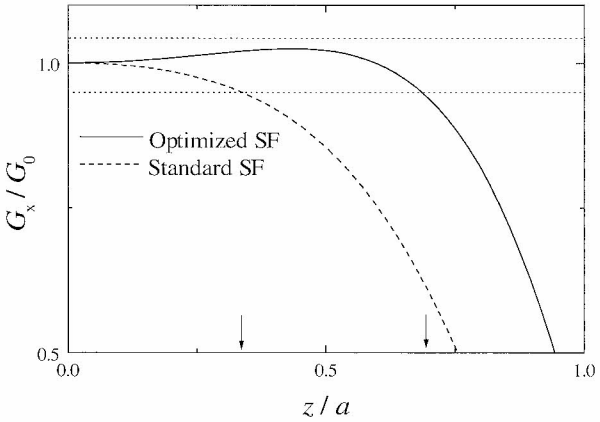

As an example, the figure above is showing the improvement in the gradient field homogeneity due to this optimization method, for a $3a$-length transverse gradient coil. As is shown by arrows in this figure, the usable FOV, defined as the region where the gradient field is 95% homogeneous, has been significantly increased by this optimization procedure, respect to the standard stream function method. The figure below shows the layout for one of the four coils forming the optimum $3a$-length transverse gradient coil

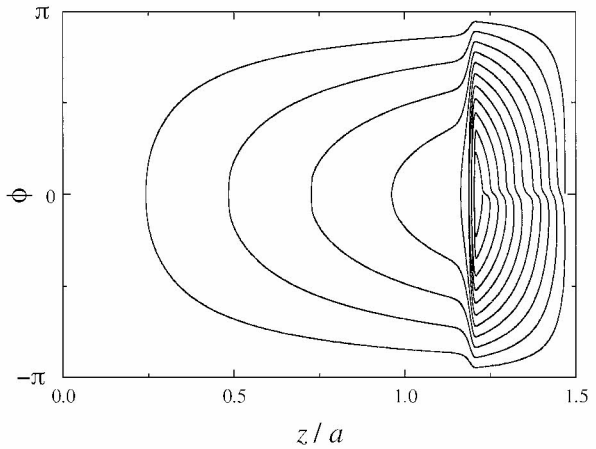

The algorithm, which runs in an standard 200MHz Pentium machine under DOS, converges to the local minimum of E in less than 30 minutes, without getting trapped in relative minima.

[1] Turner, R. Magn. Reson. Imaging. 11, 903-920, 1993
[2] Crozier, S. et al. Magn. Reson. Imaging 13, 615-620, 1995.
[3] Tomasi, D. et al. J. Magn. Reson. 1999 (in press)

P47

The NMR MOUSE: New Developments, Methods and Applications

Ralf Eymael, Kidist Hailu, Anette Wiesmath, Gisela Guthausen and Bernhard Blümich

Institute for Technical and Macromolecular Chemistry, RWTH Aachen,
Worringerweg 1, D-52056 Aachen, Germany

The NMR-MOUSE (Mobile Universal Surface Explorer) is a low field NMR device which allows for relaxation and diffusion measurements of arbitrarily large objects. It is based on the principle of inside-out NMR and can be used for scanning of surfaces. The inhomogeneous polarizing magnetic field is generated by two antiparallel permanent magnets and exhibits an approximately quadratic dependence across the magnet gap. Rf excitation is achieved by a solenoid rf-coil placed in the gap between the magnets [1,2].

NMR measurements are a powerful tool for investigation of soft materials like biological tissues and elastomers, as well as for food technology and environmental control [3]. Examples are the investigation of oil-soil mixtures and of damage in vegetables. In analogy to homogeneous magnetic field studies of elastomers, measurements with the MOUSE can be correlated to molecular dynamics and mechanical properties, such as glass transition temperature and cross link density. The longitudinal relaxation time T_1 is sensitive to deformation of the specimen and can be used for the characterization of molecular mobility. NMR measurements on different technical elastomers are correlated to mechanical relaxation methods, which are standard characterization tools in polymer technology.

New methodical approaches focus on investigations of X-nuclei in inhomogeneous magnetic fields with the NMR MOUSE. The quadratic B_0 characteristic of the MOUSE is exploited to observe flow phenomena. Furthermore, glassy polymer materials can now be studied due to a significant reduction of acoustic ringing.

References

[1] Eidmann, G. *et al.*, *J. Magn. Res.* **A 122**, 104 (1996).

[2] Guthausen, A. *et al.*, In: *Spatially resolved Magnetic Resonance* Ed.: Blümler, P. *et al.*, p. 195 (1998).

[3] Blümich, B. and Kuhn, W. (Eds.), *Magnetic Resonance Microscopy: Methods and Applications in Materials Science, Agriculture, and Biomedicine*, VCH Publishers, Weinheim, 1992.

P48

Unilateral Magnets for Remote NMR

Eiichi Fukushima and Jasper A. Jackson

New Mexico Resonance, Albuquerque, USA

Unilateral magnets are those that project a useable magnetic field to one side of the magnet rather than between elements of the magnet. We propose a unilateral magnet that projects a uniform field region in a direction for a distance that is a significant fraction of the overall cross-section of the magnet, say 25-50%.

Consider a permanent magnet in the shape of a hollow cylinder. The sketch shows a cross-section through the cylinder axis. The magnetic field on axis converges before diverging away from the ends of the magnet, providing a local maximum or a sweet spot (actually a saddle point).

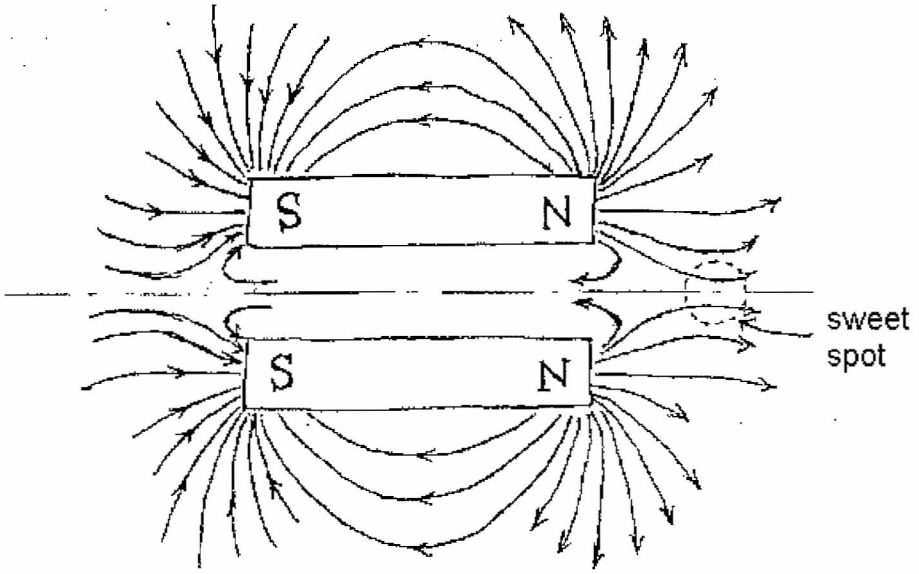

Computer simulations of a hollow tube of NdFeB that is 50 cm long with outer diameter 60 cm and wall thickness 10 cm show that the magnetic field along the axis reaches a maximum of 675 gauss, 19.4 cm past the end of the cylinder. This distance is 32% of the overall diameter of the magnet.

This magnet can be considered to be a modification of the "slab" magnets used in Schlumberger's downhole well-logger[1]. In that device, three longitudinal permanent magnet slabs, each magnetized in the same transverse direction, projected a uniform field region along but outside the borehole. The qualitative argument holds for just two slabs or, for that matter, two bar magnets magnetized in the same direction and positioned parallel to each other. Our magnet is simply a multiplicity of such bar magnet pairs arranged cylindrically to co-add the field at the same sweet spot to increase the magnetic field intensity at the spot.

Thus, this magnet, in combination with suitable NMR coils, advances the art of remote sensing NMR by increasing the combination of field strength and relative distance out to the sweet spot compared to other unilateral magnets. Several hundred gauss can be generated at approximately 1/3 of the diameter from the end, along the axis. The field homogeneity and the localization at the sweet spot are not the greatest because it is only a saddle point. However, these parameters can be improved with shim coils, additional magnet elements, and with rf coils that have different field profiles than the magnet. Finally, two of these magnets can be paired to form a "super" open architecture magnet.

Applications include "remote" sensing of materials behind barriers for reasons of extreme temperatures, toxicity, sensitivity to air, geometrical confinement for transport or storage, as well as large objects that will not fit into a magnet, including underground moisture detection.

Reference

1. Kleinberg, R. L., Sezginer, A., and Griffin, D. D., *J. Magn. Reson.* **97**, 466-485 (1992).

P49

Development of a Large-Diameter (5-cm) STRAFI Probe and Preliminary Results

P. Kinchesh[1], A.A. Samoilenko[2], **A.R. Preston**[1] and E.W. Randall[1]

[1] University of London, Queen Mary & Westfield College, Chem. Dept., London E1 4NS, UK

[2] Russian Academy of Science, Institute of Chemical Physics, Moscow,117977, Russia

Introduction

STRAFI (STRay FIeld) Imaging[(1)] is a rapidly growing technique for the study of many problems in materials science[(2)]. Typically a 1-D image is acquired from a sample less than 1cm in diameter, but for soils (and rocks) a larger sample is desirable. One of the constraints is the internal bore diameter of the magnet which is used to generate the stray field.

STRAFI is advantageous for soil imaging because the strong gradient reduces problems due to susceptibility variations arising from ferromagnetic particles and air in partially filled voids.[(3)] However samples such as soils can be very heterogeneous and friable. We wish to study the inter-grain void distribution of undisturbed material so it is important to minimise edge effects caused by compaction when a sample is extracted from the ground.

Experimental details and results

We have constructed a STRAFI probe that can take samples 5 cm in diameter and up to 8 cm long which can be rapidly installed inside a 33 cm horizontal bore imaging spectrometer (SISCO SIS-200). The sample surounded by a double-turn RF saddle coil sits inside an RF shielding box. The whole assembly is mounted on a platform that can be moved back and forth relative to the stray field by a stepper-motor driven lead-screw. A position encoder is fitted to ensure repeatability of the slice locations during multiple scans. Sample movement, RF pulsing and image acquisition are all controlled from the spectrometer console.

The theoretical gradient is 11.9 T/m at a proton resonance frequency of 111.5 MHz. Profiles are acquired by a "step and pulse" method rather than "on the fly". Sample alignment and resonant slice-flatness are sufficiently good in a 5cm diameter sample for a 40 micron thick spacer to be detected on a glass and perspex phantom. A 900 W pulse 35 μs long is needed for a 90° tip angle.

The relaxation properties of a set of highly porous ceramic samples with known pore size distributions have been studied. T1 decay curves were obtained by progressive saturation and have initially been fitted by a single exponential recovery term. A series of 40 successive repetition times were used to generate T1 values for a phantom consisting of six samples each with a narrow pore size distribution ranging from 1 to 300 microns which had been saturated with distilled water by placing in a water-filled desiccator connected to a vacuum-line for two hours. The influences of pulse-length and power on these results are being studied.

The direct relation between pore-size and relaxation time depends on a material-dependent parameter, the relaxivity, which can be derived from diffusion-coefficient measurements[(4)]. Pore-size distribution measurement by fitting a series of exponentials to a decay curve requires many more than 40 points to give a meaningful result and so the implementation of a CPMG pulse sequence is being investigated.

Acknowledgements

Thanks to the Soil Science Group of the Silsoe Research Institute for provision of samples. Work supported by BBSRC grant 68/E08576. The NMR instrumentation was provided by the University of London Intercollegiate Research Services scheme and is located at Queen Mary and Westfield College.

References

1. Samoilenko, A.A. et al., (1988), JETP Lett., 47(7), pp. 417-419
2. McDonald, P.J. et al., (1998) Rep. Prog. Phys. 61(11), pp. 1441-1493
3. Kinchesh, P. et al., (1994), Mag. Reson. Imag. 12(2), pp. 305-307
4. Slijkerman, W.F.J. et al., (1998), Mag. Reson. Imag. 16(5-6), pp. 541-544

Development of an MR Microscope Using a Portable MRI unit and a Clinical Whole-Body Magnet

Tomoyuki Haishi, Takaaki Uematsu, Yoshimasa Matsuda,
Naotaka Adachi, Katsumi Kose, Hiroshi Yoshioka*, Izumi Anno*

Institute of Applied Physics, Institute of Clinical Medicine*, University of Tsukuba, Tsukuba 305, JAPAN

Introduction

When we construct an MR microscope in clinical sites, use of a clinical MRI is a practical choice. One conceivable approach is to use a small RF coil and a high performance gradient coil system of a whole-body MRI. However, several conventional pulse sequences (e.g. short echo-time T1 weighted sequence) can not be used for a small FOV: $(\sim 10\ \mathrm{mm})^3$ because available gradient intensity is insufficient. The next approach is to use a small-bore gradient coil with a small RF coil. However, installation of such a gradient coil system to a clinical MRI is very difficult for most MRI users. Thus here we propose to use a magnetic field of a clinical MRI and a portable MRI unit, which works independently of the clinical MRI. This approach [1-3] can solve the above problems because the MRI unit can produce large field gradients using small-bore gradient coils and requires no electrical connection to clinical MRI systems.

Portable MRI Unit

Figure 1 shows the overview of the MRI unit developed in this study. This unit consists of a TFT liquid crystal display, PC, RF modulator & detector, 3-channel gradient driver, and RF transmitter. Because the size of this unit is 54 cm (W) x 77 cm (H) x 60 cm (D) and the total weight is about 80 kg, this unit can be moved easily. All of the digital modules are assembled in the PC: a commercial DSP board (DSP6031, mtt corp., Kobe, Japan) for the MRI pulse programmer (100 ns time resolution) and an ADC board (PC-414G3, DATEL) for data acquisition. The RF modulator & detector system has a bandwidth of 35-65 MHz with a built-in direct digital synthesizer module (PCK-820, DST Inc., Saitama, Japan). Two types of gradient systems were constructed and tested: a conventional gradient system for *in-vitro* specimens and a surface gradient system[4] for *in-vivo* studies.

Experiments & Results

Imaging experiments were performed with a 1.5 T whole-body magnet of a clinical MRI scanner. Water phantoms, plant stems and *in-vitro* specimens of humans and animals were used. Figure 2 shows trabecular structure of a piece of a human femur acquired *in-vitro* with a 3D gradient echo sequence (FOV: $(12.8\ \mathrm{mm})^3$, matrix size: $(64)^3$, total acquisition time: 11 hours). In conclusion, we have developed an *add-on* MR microscope which can be used with any clinical MRI and demonstrated a great promise of this system with imaging experiments.

References

1. Kose, K, et al., *Proc. Int. Soc. Magn. Reson. Med.* **6**, 1924 (1998).
2. Kose, K, et al., *Proc. Int. Soc. Magn. Reson. Med.* **7**, 2036 (1999).
3. Yoshioka, H, et al., *Proc. Int. Soc. Magn. Reson. Med.* **7**, 2119 (1999).
4. Cho, Z. H, et al., *J. Magn. Reson.* **94**, 471-485 (1991).

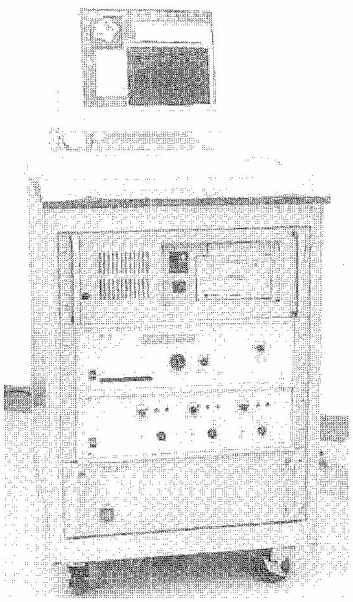

Fig.1. Portable MRI unit.

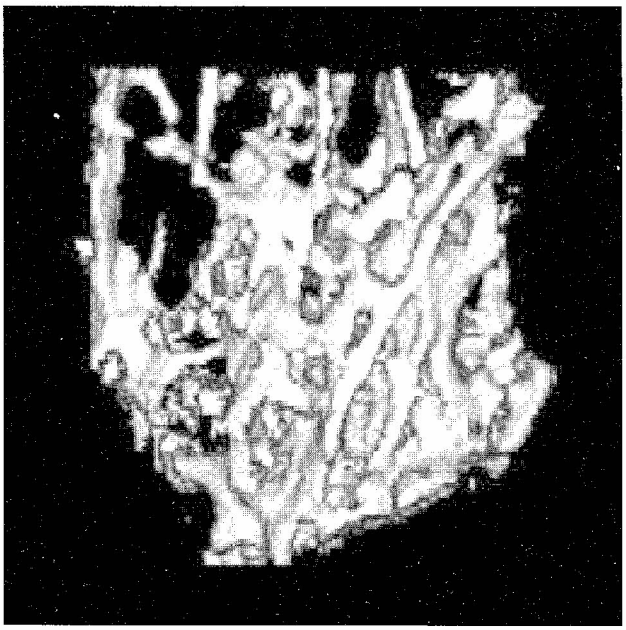

Fig.2. Trabecular structure of a piece of a human femur

P51

Quantitative Applications of Magnetic Resonance Microscopy for the Characterization of Moisture Distributions in Fibrous Substrates

Johannes Leisen, Haskell W. Beckham

Georgia Institute of Technology, School of Textile & Fiber Engineering,
Atlanta, GA, 30332-0295 USA

It is important to have exact information concerning the content and spatial distribution of moisture in textiles. Applications ranging from drying processes during manufacturing, optimized cleaning processes, wearing comfort and resistance towards the growth of microorganisms rely heavily on this information. In many cases moisture distributions in fibrous substrates can be readily obtained using standard techniques of magnetic resonance microscopy (MRM).[1,2]

The investigation of fibrous substrates such as textiles or paper generally does not pose large requirements with respect to the spatial resolution. However, the accurate quantitative determination of low moisture contents using MRM can be experimentally challenging. Moisture within common fibers typically exhibits a nonexponential T_2 relaxation behavior due to varying degrees of fiber-fluid association. This relaxation behavior is strongly dependent on the moisture content. Thus, the common approach to spin-density images fails: Data obtained with a spin-echo technique measured for various TE values cannot be interpolated to a value of TE = 0 accurately enough to obtain spin density images representing the moisture content. One approach to obtain quantitative information relies on calibrating MRM signal intensities against moisture contents determined gravimetrically. This approach has several shortcomings. Especially for the case of hydrophilic fibers such as cellulose-based fibers (i.e., cotton) the spin-echo sequence used with very short but experimentally feasible echo times will give no detectable signal for moisture contents below a critical value of 4 to 7%. Calibration of MR profiles or images to represent quantitative moisture profiles becomes highly inaccurate if moisture contents just above this threshold are considered. Moisture contents in this range and below however have to be considered when moisture uptake from humid air is investigated. Relevant information can still be obtained by comparing experimental data with model assumptions about the distribution of moisture within the sample. Correcting these model assumptions with the known experimental shortcomings established by calibrations will lead to data that are directly comparable to experimental NMR results. In cases where a low moisture content is present in conjunction with a low signal-to-noise ratio, this represents the only feasible approach.

A good filling factor of the rf coil may lead to high enough signal-to-noise ratios so that the constant-time imaging (CTI) technique[3] can be used. For this technique, the relaxation of transversal magnetization during the relevant time scale t_p is largely negligible for solvents even if they are bound to a substrate. Therefore, the CTI technique measures images and profiles where the image intensity directly represents the moisture content. However, it is necessary to correct the image intensity with respect to a background due to signals from the fibers.

We will present several examples demonstrating the application of MRM to quantitatively examine low moisture contents in fibrous materials.

1. Leisen, J. et al. In: *Spatially Resolved Magnetic Resonance*, Bluemich, B. et al. (eds.), Wiley-VCH, Weinheim, p. 265 (1998).
2. Leisen, J., et al., *Textile Chemist and Colorist*, **31**(4), 21 (1999).
3. Gravina, S.; Cory, D.G., *J. Magn. Reson. B*, **104**, 53 (1994).

P52

Investigation of Swelling and Diffusion in Organic and Non-Organic Materials by ^{1}H- and ^{2}H-NMR Imaging

Manfred Knörgen [1], Karl-Friedrich Arndt [3], Dirk Kuckling [3], Sven Richter [3], S. Peschel [2], Horst Schneider [1]

[1]Dept. of Physics and [2]Institute for Agronomy and Crop Science, Martin-Luther-Universität Halle-Wittenberg, Friedemann-Bach-Pl. 6, D-06108 Halle, Germany
[3]Institute of Physical Chemistry and Electrochemistry, Dresden University of Technology

Nuclear magnetic resonance imaging (MRI) has been used to observe the penetration of solvents into solid systems and biological objects in real-time. In opposite to the wide-spread area of objects, ranging from cherries to more solid-like nematic networks, mainly one imaging procedure based on the simple Hahn echo giving slightly T_2-weighted one- or two-dimensional pictures by Fourier Imaging (FI) was used. In any case this simple method was able to give some essential knowledge about the diffusion process not yielded by other methods.

For instance, these processes can be influenced by inhomogeneities such as surface layers[1)], cracks, which allows a fast solvent absorption in relation to the matrix[2)], anisotropy in the case of crystalline or liquid-crystalline material or a change of the type of diffusion in some regions of the sample[3)] and others. They are also influenced by membranes or skin in the case of biological tissue.

Besides others an investigation of the diffusion of a two-component solvent system (water/methanol) in poly-(N-isopropylacrylamide) (PNIPAAm)-gel is shown. This material exhibits swelling degrees $Q= M_{swollen}/M_{dry}$ up to 60 (in dependence on the temperature and the degree of crosslinking) in water[3)]. At a critical temperature T_{vpt} =34°C (volume phase transition temperature) the degree of swelling Q and also the diffusion coefficient D_{H2O} decrease rapidly by a two-step-process. During a time scale of seconds after reaching the critical temperature, the polymer matrix collapses showing a more solid-like behavior. On the other hand a shrinking process takes place for some hours. During the shrinkage process also shape changes of the samples can occur. Both processes can be visualized by MRI. In our work we investigate the influence of methanol on the swelling and diffusion processes of this system also.

An example for an anisotropic diffusion is shown by MRI of a nematic network (cross-linked nematic main-chain liquid crystal prepolymers consisting of several statistically distributed segments of methylhydroquinone, *p*-hydrobenzoic acid, itaconic acid, and sebacic acid). CD_2Cl_2 was used as solvent. The diffusion is shown by the increasing T_2 of the polymer itself. The nematic network shows an orientated fibrillar structure. The anisotropy can be seen by the more effective diffusion parallel to the chain orientation. This structure diminishes the diffusion process perpendicular to this direction.

^{2}H-MRI was used to investigate the diffusion of water from outside in a cherry due to osmotic pressure. One point of this very important agricultural problem (Why do cherries split open short before ripening?) is the determination of the area, where the water ingress takes place (through the hole skin, only at the top (near the stalk) or at the bottom). Despite the very small amount of deuterated water (ca. 2 mg in a ca. 7-g fruit) an MRI measurement was possible and the question could be answered...

1. M. Knörgen, U. Heuert, H. Menge, H. Schneider, *Angew. Makromol. Chemie* **261/262**, 123-1331 (1998).
2. P.Y. Ghi, D.J. Hill, D. Maillet, A.K. Whittaker, *Polymer* **38**, 3985-3989 (1997).
3. N. Tanaka, S. Matsukawa, H. Kurosu, I. Ando, *Polymer* **39**, 4703-4706 (1998).

P53

Magnetic Resonance Imaging Study of Water Ingress into Polyamide 4,6

Anne Pollaris, Peter Adriaensens, Victor Litvinov,* Johan Tijssen*,
Dirk Vanderzande and Jan Gelan

Institute for Materials Research, Limburg University,
Building D, Department SBG, B-3590 Diepenbeek, Belgium.
* DSM Research, P.O. Box 18, 6160 MD Geleen, The Netherlands.

Magnetic Resonance Imaging (MRI) and NMR relaxation experiments are used to study the water absorption of polyamide 4,6 (PA46) plates. Despite of the higher crystallinity, PA46 absorbs more water as compared to the polyamides 6 and 6,6 (PA6 and PA66). MRI Images clearly show a horn shaped intensity profile with a higher intensity near the surface of the plates. In PA6 and PA66 MRI only indicates mobile water near the surface of the injection moulded plates whereas in PA46 mobile water is observed over the total cross section with peaks near the surface. In the MRI images, the intensity of the ingressed water into the native plate and some pre-treated plates (annealing, scraped edges, ...), was calibrated towards the image intensity of a reference capillary filled with doped water. These experiments clearly show that pre-treating the plaques has an effect on the molecular mobility of the ingressed water.

This deviating behavior of PA46 can be explained by its very high crystallization rate, preventing the close coupling of amide groups in the amorphous phase. This results in a gradual decrease in arrangement of the amorphous phase towards the outside of the plate due to faster cooling. At the outside of the plate, the average distance between the amide groups will be larger resulting in a higher water absorption and a higher mobility (T_2) of the water molecules. During annealing the amorphous phase of PA46 shifts towards a structure typical for PA6 and PA66. The average distance between amide groups decreases, resulting in a substantial decrease of water uptake and water mobility.

P54

Diffusion of Solvents Inside Multi-Phase Polymer Systems

G. Maddinelli* and A. Ferrando**

* Enitecnologie S.p.A., San Donato, Milano, Italy

**Enichem S.p.A, Mantova, Italy

NMR imaging is a very powerful technique for investigation of diffusion phenomena inside porous materials. This feature could also be very useful in the evaluation of aggressive penetration of fluids inside bulk polymers. A typical example of such a class of products is HIPS (High Impact Polystyrene). Being a two-phases material, HIPS shows a peculiar morphology: namely a dispersed phase, formed of nearly spherical butadiene rubber particles, is contained in a hard Polystyrene (PS) matrix. The preparation of such materials resulting in different phase distributions could be very critical in order to achieve good performance of the final product. The behaviour of different HIPS materials subjected to solvent penetration was observed. In particular, the interaction of HIPS (widely used in producing refrigerator liners) with solvents used as blowing agents for polyurethanes (thermal insulators) was examined. The penetration profile of different solvents (cyclopentane and fluorinated CF11) was obtained through a series of T_1 weighted images taken dynamically during saturation of polymer cylinders. This technique allowed efficient observation of radial diffusion into the cylinders. Significant differences in diffusion rate were observed leading to correlations with the chemical and physical properties of the different materials. The diffusion regime inside HIPS cylinders was found to be Fickian (Case I). Results in terms of diffusion properties and ^{1}H and ^{13}C relaxation studies were compared and discussed: significant differences were observed and related to materials parameters.

P55

Visualization of Tensile Stress Induced Material Response at a Crack Tip in Polymers under Critical Load by NMR Imaging

Liesbet Storme [1], Peter Adriaensens [1], Victor Litvinov [2], Roel Marissen [2], Dirk Vanderzande [1], Jan Gelan [1]

[1]Limburg University Centre (LUC), Institute for Material Research (IMO), Division Organic and Polymer Chemistry, Dpt. SBG, University Campus Building D, 3590 Diepenbeek, Belgium

[2]DSM Research, P.O. Box 18, 6160 MD Geleen

The process of failure of polymers often occurs by crack growth from defects. Towards the resistance of the polymer against crack growth, toughness is an important parameter.

Magnetic Resonance Imaging (MRI) is an excellent technique to get spatially resolved information about molecular mobility and the amount of material of polymer materials.

In this study, the growth of a notch under stress for two different polymer materials is followed by MRI. The first material is an ABS (acrylonitrile-butadiene-styrene) with 28% PB (polybutadiene) rubber, the second is a PBT/PTMO (polybuteneterephthalate/ polytetramethyleneoxide) block copolymer.

Out of a series of images made as a function of the echo-time spatially resolved spin density and T_2 relaxation information is obtained. Out of this information, it can be concluded that for the ABS the molecular mobility remains unaffected while a reduced spin density appears in the shear bands. For the PBT/PTMO block copolymers it has been found that a significant change of molecular mobility occurs.

By means of a distance marker a stress-strain plot was also obtained by MRI for both materials.

P56

Critical Analysis of Network Defects and Statistical Void Densities in Cross-linked Isobutylene-Based Elastomers by NMR Imaging.

Peter Adriaensens, Anne Pollaris, Jeffery White*, Mauritz Kelchtermans**, Dirk Vanderzande and Jan Gelan

Institute for Materials Research - Limburg University - building D - Department SBG, B-3590 Diepenbeek, Belgium.

* Exxon Chemical, Baytown Polymers Centre, P. O. Box 5200, Baytown, Texas 77522.

** Exxon Chemical Europe Inc., Hermes Laan 2, B-1831 Machelen, Belgium.

The analysis of chemical and physical network heterogeneities has been carried out for synthetic isobutylene-based elastomers using ^{1}H spin-echo imaging. Spatial homogeneity was compared for isobutylene-based terpolymers cured with inorganic versus organic curatives, and unfilled materials versus those filled with carbon black. Surprising differences in the network structure were found for materials cured with an inorganic curative relative to those cured with an organic curative. Systematic comparison of solvent images and polymer images revealed the optimum experimental conditions for enhancing network density contrast or detecting micro-voids. Direct ^{1}H images of polymer spins in a fully compounded, commercial polyisobutylene-based elastomer were acquired in the absence of any swelling solvent by slightly heating. Multi-slice imaging experiments were investigated as a method to construct a three-dimensional void density matrix for elastomer compounds. Voids and void distributions (statistical calculations various slices), were found to be an important criterion to judge the mechanical performance. The ability of NMR imaging to provide data over statistically relevant sampling volumes (hundreds of mm^3) for both neat polymers and fully compounded commercial materials (carbon black filled) represents a unique advantage of MRI for material property analyses.

P57

Analysis of Local and Coherent Segmental Mobility in Elastomeric Materials by NMR Techniques

Paul Denner, Lutz Deutschbein, Sergui Zhukov, Bernd Walter
Institute of Physics, Ilmenau Technical University, D-98684 Ilmenau, Germany

Introduction

NMR spectrosopy and NMR imaging have become an indispensable tool for characterizing of segment dynamics in entangled and crosslinked elastomeric materials. The proliferation of modern pulse sequences have supplied additional information to elucidate the structure and molecular motion in inhomogeneously crosslinked polymeric systems. Important data for the refinement of structure-property relationships result from the study of local and coherent motions in the bulk. The dynamical properties of chain segments in polymers depend on a variety of parameters such as chemical structure of repeating units, the density and distribution of both chemical and physical crosslinks, but also on additional "topological" hindrances caused by aging processes and modification of curing conditions.

Methods and Materials

The proton spin relaxation was studied with a home-built n.m.r. spectrometer operating at 60 MHz (^{1}H) and a conventional BRUKER pulse spectrometer MSL 300 S. The spin locking field following a $\pi/2$-pulse of 1.8 μs was choosen in the range from 0.5 mT to 3.1 mT. Spectra were also recorded using a modified WISE experiment. Additional information is obtained by measurements of the glass transition temperatures with a PERKIN ELMER 7 Differential Scanning Calorimeter, by investigations of the dielectric relaxation behavior, and by evaluation of parameter-selective NMR-imaging data based on the longitudinal relaxation time in the rotating frame [2].

Uncrosslinked and crosslinked cis-1,4-polybutadienes and filler-free standardized Malaysian rubber samples have been studied. The polybutadiene samples (ALDRICH -cis-1,4-PB-18-137-4, T_G = 171 K, M_W = 280,000 g/mol) were crosslinked under vacuum by exposing to ionizing radiation of a ^{60}Co-gamme-source with a dose in the region from 9.6 to 520 kGy in sealed NMR tubes. The crosslink densities of three natural rubber pieces are 3.8 x 10^{-5}, 6.6 x 10^{-5}, and 9.8 x 10^{-5} mol/cm^3.

Results and Discussion

It is shown in this poster that radiation aging and the modification of curing conditions not only lead to an increasing of the crosslink density. Characteristic for these influences are too the changes of the local and coherent motional processes and the shift of the related correlation times. The situation is indeed complicated but it is describable if motional restraints and conditions for a restricted diffusion of chain defects are taken into consideration. The non-exponential relaxation behavior can be understood by two limiting cases of one and the same type of the composite diffusion process with fluctuating barriers acting as dynamical restraints. The lifetime of the fluctuating barriers strongly depends on the crosslink density. The ratio of lifetime of the fluctuating barriers and diffusion time of chain defects between crosslinks characterizes the motion of the crosslinks and the network stabilization due to radiation induced aging and curing processes.

References

[1] Barth, P.; Hafner, S.; Denner, P.; *Macromolecules* **29**, 1655 (1996).
[2] Gee, R.H.; Boyd, R.H.; *J. Chem. Phys.* **101**(9), 8028 (1994).
[3] Kremer, K.; Grest, G.S.; *J. Chem. Phys.* **92,** 5057 (1990).

The NMR dipolar-correlation effect as a potential imaging contrast parameter for material properties of polymer networks

Maciej Garbarczyk [1], Farida Grinberg [2], Rainer Kimmich [2], Winfried Kuhn [3], Stefan Jurga [1]

[1] Macromolecular Physics Dept., Institute of Physics, A. Mickiewicz University, ul. Umultowska 85, 61-614 Poznan, Poland

[2] Sektion Kernresonanzspektroskopie, Universität Ulm, 89069 Ulm, Germany

[3] IIC Innovative Imaging Corp. KG, Langental 18, 66440 Blieskastel ,Germany

In the previous works [1,2] it was reported on a special attenuation mechanism of the stimulated echo in microscopically anisotropic liquids called the "dipolar-correlation" (DCE). Due to an anisotropic molecular alignment or topological constraints molecular motions in liquid crystals, polymer melts, and polymer networks [3] tend to be strongly anisotropic on the longest time scale probed by pulsed NMR techniques. The consequence is that the secular part of the dipolar Hamiltonian is not completely averaged out and the DCE as an echo attenuation mechanism appears. It originates from modulations of effectively remaining (residual) dipolar couplings. In rubbers, severe constraints on isotropic reorientations of polymer chain are imposed by chemical cross-links. The amount and the type of cross-links as well as of special additives like reinforcing fillers strongly influence the macroscopic properties. The aim of the present work [4] is to study the influence on the DCE of the cross-link density in dry and swollen natural rubbers (NR). Another purpose is to determine the influence of the filler content on DCE.

The DCE on the stimulated echo is produced by the sequence of the three 90° pulses. Also the modified pulse sequence with additional 180° pulses in the middle of evolution intervals were used. The 180° pulses were incorporated in order to exclude effects connected with the dephasing of the spin coherences due to spin exchange.

A series of natural rubbers with different cross-link densities and different amount of reinforcing filler added was investigated. Also the samples swollen in cyclohexane and benzene were investigated. The measurements were done on a 300 MHz proton resonance frequency Bruker MSL spectrometer and the 400 MHz Bruker DSX spectrometer.

The typical attenuation curves of the stimulated echo for the dry samples reveal strong modulation with a frequency corresponding to the difference observed between the main peak and the shoulder in the proton spectra. When using the modified pulse sequence the modulations can completely be suppressed. The dipolar-correlation quotient $Q_{dc}(\tau_1)$ in natural rubbers is strongly dependent on the cross-link density, which is in agreement with the previous findings for the synthetic rubber networks (SBRs) [3]. On the contrary no influence of the carbon black content was observed. For the swollen samples no oscillations were observed. Also like in dry samples the dependence on the cross-link density was observed.

The second moment of the dipolar fluctuation $\langle\delta\Omega_d^2\rangle(P_S)$ scales in the experimental range of sulfur contents as $\langle\delta\Omega_d^2\rangle \propto (P_S)^{1.3\pm0.1} \propto N^{-1.3\pm0.1}$, where the sulfur content can be treated as the measure of the cross-link density. The exponent is nearly the same for dry and swollen samples. This result must be considered in terms of existing concepts of NMR properties of polymer networks. The value of the exponent suggests that the mesh chains in these materials are more stretched than expected for the freely jointed mesh.

The most important conclusion of this work is the strong dependence of the mean squared dipolar fluctuation on the cross-link density, both in dry and swollen samples. This also allows one to predict the DCE to be a good method for the determination of the cross-link densities. It is also promising to use the DCE as an imaging contrast parameter. Such a contrast mechanism allows one to image the material properties of polymers [5].

References

1. Kimmich, R., *NMR: Tomography, Diffusometry, Relaxometry*, Springer-Verlag, Heidelberg, 1997.
2. Grinberg F., et al., *J. Chem. Phys.* **103**, 365(1995).
3. Fischer E., et al., *J. Chem. Phys.* **109**, 846(1998).
4. Grinberg F., et al., submitted to *J. Chem. Phys.*
5. Kuhn W., et al., *Solid State NMR* **6**, 295(1996).

P59

NMR Dipolar Contrast Filters in Soft Matter

L. Gasper, M. Schneider, D. E. Demco, and B. Blümich

Institut für Technische Chemie und Makromolekulare Chemie, MARC,
Rheinisch-Westfälische Technische Hochschule, Worringerweg 1, D-52074 Aachen

Proton spectral spin diffusion as well as dipolar-encoded longitudinal magnetization decays, double- and triple-quantum NMR build-up curves are introduced for measuring site-selective residual dipolar couplings of functional groups and between functional groups in poly(styrene-cobutadiene) and synthetic polyisoprene elastomers. Nonrotating samples are considered with different cross-link density and extension ratios. Double- and triple-quantum filtered ^{1}H NMR spectra give access to chemical site-selective residual dipolar couplings. ^{1}H residual dipolar coupling contrast filters based on the above NMR methods were implemented and parameter images on heterogeneous elastomers were measured.

P60

Stray Field Imaging and Numerical Modelling of Water Ingress into Compacted Xanthan Powder

U. Goerke[*], E. Crilly[*#], P.J. McDonald[*], A.H.L. Chamberlain[#]

[*]School of Physical Sciences, [#]School of Biological Sciences, University of Surrey, Guildford, GU2 5XH, Surrey, UK

Motivation

Many polysaccharides are able to bind large amounts of water by forming a gel. It has therefore been suggested in the literature that these biopolymers are produced by microorganisms to slow down water loss during desiccation and prevent excessive water uptake when the bathing solution is very hypotonic, thus preventing damage due to water stress. This paper reports on further studies of water transport through compacted xanthan powder using stray field imaging. Previous work is reported elsewhere [1]. A theoretical model assuming vapour diffusion as well as swelling of the polymer is suggested to interpret the experimental results.

Experimental

The commercially available xanthan Keltrol F was supplied as a lyophilised powder by Keltrol-Nutrasweet. A de-acetylated form of it was kindly provided by Prof. I.W. Sutherland, University of Edinburgh [2]. The powders were compacted into glass capillaries. The top of the sample was exposed to water. The water ingress was profiled as a function of time using stray field imaging [3].

Model

At low water concentrations, water ingress is dominated by vapour diffusion in the free pore space between the xanthan grains. The vapour condensation is described by the adsorption isotherm, which was measured for both xanthan types under the assumption that the vapour and absorbed water are always in local equilibrium. In the presence of water, the xanthan forms a gel and swells. Hence the pore space is reduced. The swelling results in a shift of the water/xanthan polymer interface and in an apparent diffusion coefficient which includes the movement of the polymer matrix relative to the laboratory fixed coordinate system and the varying importance of water in polymer versus vapour in pore space diffusion. At the water interface the macromolecules dissolve. According to this model, master diffusion curves are derived by solving the Fickian diffusion equation [4] by means of a numerical integration algorithm.

Results

Trends for varying parameters are discussed and used to interpret experimental results. An example is shown in the figure. Master curves (dots) have been calculated from measured ingress profiles of xanthan powder of varying degrees of compaction. The numbers at the top of the curves represent the free void volume fraction κ. The curves for $\kappa > 0.0$ are shifted relative to abscissa and ordinate. The theoretically predicted master curves (solid lines) are calibrated to show signal intensity versus the parameter $\eta = x\, t^{-1/2}$, i.e., they were T_2- and diffusion-weighted. The theoretical curves are calculated assuming the same diffusion coefficients for all five samples and only one varying parameter κ. In particular the theoretical model successfully describes the 'foot' evident in the data at high κ due to vapour diffusion in the free void space at low water concentrations.

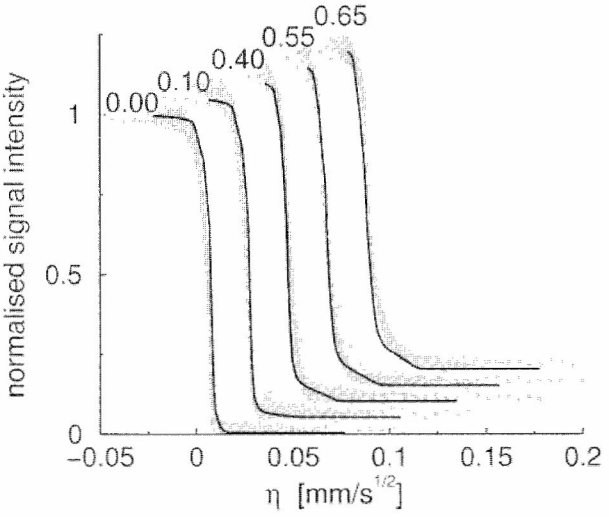

Conclusions

The model demonstrates that water vapour diffusion and swelling of the polymer matrix are essential components for water transport properties of compacted xanthan powder samples.

References

[1] Hart, T.D. et al., *Enzyme and Microbial Technology* **24**, 339-347 (1999).

[2] Shatwell, K.P. et al., *Int. J. Biolog. Macromol.* **12**, 71-78 (1990).

[3] McDonald, P.J. et al., *Reports on Progress in Physics* **61**, 1441-1493 (1998).

[4] Crank, J., *The Mathematics of Diffusion*, Clarendon, Oxford, 1975.

P61

Visualization of Moisture Transfer During Starch Molding Using SPRITE

Bryce MacMillan[a], Greg Ziegler[b], **Bruce Balcom**[a]

[a]Department of Physics, University of New Brunswick, Fredericton, New Brunswick, Canada
[b]Department of Food Science, Pennsylvania State University, University Park, Pennsylvania, USA

Starch molding is the principle forming process of many gelled confectionary products. In this process, the time alloted for drying, or stoving, determines the quality of the finished product. Superior quality requires longer stoving times, but this has a negative effect on productivity. Optimization of the drying process requires an understanding of the mechanism of moisture transfer.

Magnetic Resonance Imaging (MRI) has traditionally proven an effective tool for the study of moisture and moisture migration in food systems where the moisture content is high[1-4]. However, when the moisture content is low, such as in gelled candies, the usefulness of conventional MRI techniques is limited. A new technique, SPRITE[5], is designed to successfully image systems which produce short lived MR signals, such as low moisture foods.

We have used the SPRITE technique to measure the migration of water during the stoving process in gelled confectionary products. We have spatially mapped the moisture content inside the gel as a function of time while stoving. Additionally, we have developed a model of the drying process based on transportation of water within the gel and across interfacial boundaries. It is seen that migration of water from the gel phase to the starch plays a critical role in the drying process.

1. McCarthy, M.J. and McCarthy, KL, *J. Sci. Food Agric.*, 6, 27 (1994).

2. McCarthy, M.J. and Cheung, MK, *Annual Reports on NMR Spectroscopy*, 31, 19 (1995).

3. Schmidt, S.J. et al, *Crit. Rev. Food Sci. Nutr.*, 36, 357 (1996).

4. Hills, B., *Trends in Food Sci. & Technol.*, 6, 111 (1995).

5. Balcom, B.J., et al, *J. Mag. Res.*, A123, 131 (1996)

Supported Catalysts and Sorbents: An NMR Microscopic Visualization of Active Components and Dynamic Processes

I.V. Koptyug, R.Z. Sagdeev, L.Yu. Khitrina[1], and V.N. Parmon[1]
International Tomography Center and [1]Boreskov Institute of Catalysis, Novosibirsk 630090, Russia

Purpose. The aims of this work are to further explore the ability of NMR microimaging to visualize the spatial distribution of active components within supported catalysts and sorbents, and to study the dynamics of mass transport non-destructively and in real time during adsorption processes and supported catalysts preparation.

Methods. For adsorption studies the γ-alumina or silica gel pellets containing a hygroscopic salt ($CaCl_2$, $CuCl_2$) were prepared by soaking a pellet in the aqueous solution of the salt followed by pellet drying. In the single pellet adsorption experiments, the spin-echo technique with appropriate slice selection was used to obtain a succession of 1D profiles of water distribution along the diameter of the cylindrical pellet in the course of the adsorption process. In another set of experiments the adsorbing beds were prepared by packing the pellets in a hollow glass cylinder, and the single point imaging experiment was used to detect the 1D projection of water distribution within the bed on the cylinder axis. In the experiments with the supported Pt catalysts, the principal active component was introduced in the form of H_2PtCl_6 from a 0.02N aqueous solution. A 0.3N aqueous solution of oxalic acid ($H_2C_2O_4$) was used as a competitive sorbate in the preparation of alumina pellets with the egg-white type of active component distribution. The pellets were dried and then saturated with cyclohexane for imaging experiments. A spin-echo sequence with inversion-recovery preconditioning was employed to obtain T_1 maps of the cyclohexane. In the studies of the dynamic redistribution of hexachloroplatinate dianion, the pellet was residing in the aqueous solution containing both H_2PtCl_6 and $H_2C_2O_4$ during the entire experiment. In this case the T_1-weighted images of water were acquired. All ^1H NMR experiments were performed at 300 MHz on a Bruker Avance NMR spectrometer.

Results. In many practical applications water vapor is removed from a stream of gas by passing it through a bed comprised of porous pellets with $CaCl_2$ or other hygroscopic salt dispersed within the porous space. We were able to detect and model the evolution of the profile of adsorbed water along a cylindrcal bed taking into account the mass and heat balance in a model homogeneous medium. However, the propagation of the front of the adsorbed liquid along the bed is governed by the behavior of the individual pellets constituting the bed. Therefore, we have carried out the single pellet adsorption studies, in which we monitored the variation of the radial distributions of adsorbed water within individual cylindrical pellets in real time. It was found that the distribution of $CaCl_2$ in the alumina pellets studied has a pronounced influence on the character of water front propagation within the pellet. For uniform $CaCl_2$ distribution the sharp water front propagation resembles the non-Fikian (case II) transport, which shows that the penetration of the liquid into the dry pellet regions is the rate limiting stage of the adsorption process. In the case of the egg-shell distribution of $CaCl_2$ within the pellet, the capillary flow is much more efficient, which suggests that the latter type of distribution might have certain advantages in practical applications.

An important aspect of the preparation of supported catalysts is the type of the final macroscopic distribution of an active component within the porous support. There is a need for a non-destructive method capable of monitoring the dynamics of redistibution of the active component in the course of catalyst preparation. An indirect ^1H NMR microscopy mapping of paramagnetic ions (Cu, Fe, Cr, etc.) by monitoring the nuclear spin relaxation properties of a liquid filling the pores of a pellet can be easily performed. The studies of water vapor adsorption by alumina pellets containing paramagnetic $CuCl_2$ enabled us to visualize the redistribution of the salt upon repetitive adsorption/desorption cycles when the initial salt distribution is non-uniform. The feasibility of the similar indirect mapping of non-paramagnetic substances relies on the fact that any substance dispersed in the pore space of a support should in principle perturb the liquid-surface interaction and thereby change the relaxation times of liquids filling the pores. We have found that T_1-weighted images and T_1 maps of a liquid in the pores of an alumina pellet treated with platinum hexachloride reflect the distribution of Pt within the pellet. For some pellets the T_1 of cyclohexane increased from ca. 200 to ca. 310 ms upon impregnation. Furthermore, in the process of competitive adsorption of oxalic acid and hexachloroplatinate dianion from an aqueous solution, the sequential T_1-weighted water images revealed the dynamic transformation of the platinate distribution in the cylindrical alumina sample from egg-shell to egg-white and later to egg-yolk type, observed as a shrinking and thickening of the ring-like area of reduced water signal intensity.

Conclusions. The results of our work demonstrate that the ^1H NMR microimaging can be employed successfully to visualize the spatial distribution of active components in porous supports, and to study mass transport processes, such as water ingress during adsorption and the dynamics of supported Pt catalyst preparation.

[1] Koptyug I.V., Fenelonov V.B., Khitrina L.Yu., et al., J. Phys. Chem. B 102, 3090-3098 (1998).
[2] Koptyug I.V., Sagdeev, R.Z. Parmon V.N., et al., Proceedings of the Joint 29th AMPERE - 13th ISMAR international Conference, Berlin, 1998, pp.758-759.
[3] Koptyug I.V., Sagdeev R.Z., Khitrina L.Yu., et al., Proceedings of the Joint 18th Conference on Modern Magnetic Resonances, Poznan, 1999, p. L31.

P63

Rheoporometry - One- and Two-Dimensional q-Space Mapping of Fluids in Porous Media as a Tool to Probe Restricted Geometries

Siegfried Stapf [1,2], Ken J. Packer [1], Pierre M. Adler [3]

[1] Department of Chemistry, University of Nottingham, UK
[2] Lehrstuhl für Makromolekulare Chemie, RWTH Aachen, Germany
[3] Institut de Physique du Globe, Paris, France

In an unrestricted environment, random self-diffusion of fluid molecules takes place independently in all directions. The same is true for laminar flow, where Brownian motion in the directions perpendicular to the flow axis z does not depend on the downstream displacement, Z, if edge effects can be neglected. However, this situation changes if the flow pattern is altered by geometrical restrictions. For the flow of fluids in a porous medium, the local velocity field in combination with random self-diffusion leads to a spreading of the particle displacement probability in directions both parallel (Z) and perpendicular (X, Y) to the flow axis. Understanding how X, Y and Z are correlated at any given time and for different experimental conditions leads to important information about the topology and connectivity of the porespace sampled by the moving fluid.

The probability distribution function for displacements in an arbitrary direction $\mathbf{R}$, $P_\Delta(\mathbf{R})$, the so-called propagator, for particles in a fluid at a given encoding time Δ can be obtained from a suitable pulsed field gradient experiment by Fourier transformation of the $\mathbf{q}$-space intensity function, $S_\Delta(\mathbf{q})$ [1,2]. By independent encoding with two orthogonal gradients, one of which being parallel to the flow axis, the two-dimensional propagator $P_\Delta(X,Z)$ is obtained. Correlations between displacements X and Z for a range of encoding times Δ can be computed from the properties of this propagator [3].

A further option to investigate the decay in flow coherence is realized by refocussing the magnetization in two steps according to the scheme $\mathbf{g}_0 - \Delta_1 - \mathbf{g}_1 - (\Delta_2 - \Delta_1) - \mathbf{g}_2$, where $\mathbf{g}_0 = \mathbf{g}_1 + \mathbf{g}_2$ Thus, the joint probability density W_2 ($\mathbf{R}_1$, Δ_1; $\mathbf{R}_2$, Δ_2) for displacements $\mathbf{R}_1$ and $\mathbf{R}_2$ in time intervals Δ_1 and Δ_2, respectively, can be obtained for arbitrary directions of $\mathbf{R}_1$ and $\mathbf{R}_2$ [4].

We have measured the two-dimensional displacement probability densities $P_\Delta(X,Z)$ and $W_2(\mathbf{R}_1, \Delta_1; \mathbf{R}_2, \Delta_2)$ for water flowing through porous solids of widely differing topology such as glass bead packings, natural rock and fibers of different degree of ordering. The results are compared to numerical simulations of flow through equivalent, computer-generated systems [3] for which both encoding time Δ and self-diffusion coefficients could be varied at will over a wide range.

For all systems investigated in our study, large Z are connected with large $\langle X^2 \rangle$. The relation can be expressed by a power-law $\langle X^2 \rangle \propto Z^\gamma$ with an exponent γ which is characteristic for the porous matrix. The mutual dependence between displacements perpendicular and parallel to the flow direction is revealed in the evolution of the correlation coefficient. This coefficient $\rho_{X^2,Z}$ is found to increase for short times and to decrease for larger displacements, with a maximum at an average displacement corresponding to the characteristic length scale of the matrix [3].

Correlations between displacements in orthogonal directions can also be expected for self-diffusion within restricted geometries. Despite the fact that the measured propagator, averaged over the sample volume, is isotropic, its shape is determined by the local anisotropy of the porespace experienced by a diffusing particle [5]. However, the isotropy of the propagator allows its determination by a one-dimensional stimulated-echo experiment. The shape of the propagator is Gaussian in the limits of both short and long times [6], with a maximum deviation from a Gaussian at intermediate times. The *rms* displacement corresponding to this point is very similar to the position of the maximum of the correlation coefficient, and indeed is found to coincide with the average displacement $\langle Z \rangle$ for flow through the same system, provided a regular structure of high connectivity is investigated. Thus, structural sizes of the porous matrix can be obtained from both diffusion and flow experiments, even though the pore space is sampled in different ways by the fluid particles.

References

[1] Packer, K. J.; Tessier, J. J., *Mol. Phys.* **87**, 267 (1996).

[2] Seymour, J. D.; Callaghan, P. T., *AIChE J.* **43**, 2096 (1997).

[3] Stapf, S.; Packer, K. J.; Graham, R. G.; Thovert, J.-F., Adler, P. M., *Phys. Rev. E* **58**, 6206 (1998).

[4] Stapf, S.; Damion, R. A.; Packer, K. J., *J. Magn. Reson.* **137**, 316 (1999).

[5] Jester, C.; Loon, S. T., *Transport Porous Med.* **3**, 704 (1988).

[6] Sen, P. N.; Hürlimann, M. D., *J. Chem. Phys.* **101**, 5423 (1994).

Determining an Angle Distribution of Pore Channels in Track Membranes by NMR PFG

E.N. Vasina, V.D. Skirda
Kazan State University, Kazan, Russia

Pore characteristics of track membranes [1] such as a configuration, diameter and angle of channels to membrane surface have most important value in practice. Traditionally these parameters are determined with electron microscopy. In this work, a way for determination of an angle pore channel distribution with using a NMR with pulsed field gradient (PFG) is suggested. The idea of the way is a registration of a relative population for diffusing substance in pores whose channels are perpendicular to applied magnetic field gradient.

We used a poly(ethylene terephthalate) track membrane with pores of 0,9 μm in diameter; a number of pores in 1 sm^2 was $3{,}7 \cdot 10^7$; angle pore channel distribution was ±30° (the data of electron microscopy); the membrane thickness was about 10 μm.

A way of a sample preparation have been presented in detail in [2]. A pack of parallel track membrane films of 4×8 mm dimensions was saturated with distilled water and put between the parallel surfaces of a Teflon holder. After saturation, the pack in the holder was pressed and firmly fixed in a glass ampule with inner diameter of 5 mm. Thus, we were able to vary angle α between a magnetic field gradient direction **g** and a normal **n** to the membrane surface. Measurements were carried out with a home-built NMR-spectrometer operating at 64 MHz for protons with using the stimulated echo sequence. The sample temperature was +30°C; the measurement errors did not exceed 5-10%.

Water echo attenuations have a non-exponential shape which depends on diffusion time (t_d) and an angle between **g** and **n** (Figure 1 in [2]). The echo attenuations were recorded in a time interval from 3 up to 60 ms. In [2] we have proposed the procedure for determination of effective self-diffusion coefficient (D^*) of a diffusate in membrane pores for the same form of a sample.

At α=0°, this D^* corresponds to water molecules in pores whose channels were oriented perpendicular to surfaces of membrane films; diffusion times were such that $D^* \propto t_d^{-1}$ was satisfied (fully restricted diffusion). It have been shown in [2] that a deviation of pore channels from **n** direction must increase the D^* value and vanish its dependence upon diffusion time.

Changing α value (turning the ampule with the sample in the spectrometer unit), we registered a population p_a of a «component» with the self-diffusion coefficient D^* for which $D^* \propto t_d^{-1}$ dependence performed. The obtained in this way dependence of $p_a(\alpha)$ is presented in Figure. The α angle was varied in limits from 90° up to 0°.

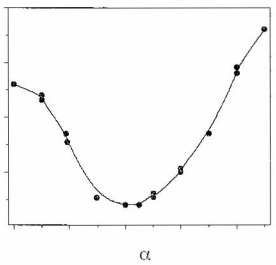

Figure. Dependence of a relative population p_a of a «component» with the self-diffusion coefficient D^* vs α, where α is an angle between applied magnetic gradient **g** and normal **n** to the membrane surface in the pack.

The presented Figure shows, when α changes from 90° to smaller values, p_a decreases and has a minimum at α=40°. This fact demonstrates that there are pores whose channels oriented to **n** even at 40°. It shows a good accordance with initial data for the average value of angle deviation for the used membrane - ±30°.

At α=0°, the increasing of p_a is caused by restricting wall effect for water diffusion between neighbor membrane films: the average distance between neighbor films (at α=0°) proved to have the same order of a magnitude (about 0,5±0,1 μm) as the pore diameter (0,9 μm).

If we write mean-squared displacements of molecules along a magnetic field gradient direction as a sum of projections on the **n** and along the membrane surface, the self-diffusion coefficient value for any α can be written as the follow expression

$$D(\alpha)=D_{\perp}(t_d)\cos^2(\alpha)+D_{||}\sin^2(\alpha),$$

where $D_{\perp}$ is a self-diffusion coefficient depending on diffusion time and a spacing between neighbor membrane films. In this case $D_{||}$ is a self-diffusion coefficient (2.7×10^{-9} m^2/s) of free water for the measurement temperature +30°C. As we have found in [2], for diffusion time on the order of a 10^{-2} s we can take $D_{\perp}$ 10^{-11} m^2/s. If we will increase α value from 0° up to 10°, according to the written expression the self-diffusion coefficient D(α) must increase to about 1 decimal order of a magnitude. Because of this fact the population p_a must decrease even at a small deviation from α=0°. However, the obtained data did not show the same behavior. We connect this result with rough surface of Teflon plates of the holder compressing the pack, as a rough Teflon surface causes some local disorder of **n** direction.

References. Fujara F. et al. *Magnetic Resonance Imaging*, Vol. 12, 245-246 (1994).
Vasina E.N. et al. *Russian Journal of Physical Chemistry*, Vol. 73, 229-234 (1999).

Velocity Mapping in Percolation Model Objects: Detection of a New Power Law

Andreas Klemm, Rainer Kimmich

Universität Ulm, Sektion Kernresonanzspektroskopie, 89069 Ulm, Germany

Purpose. We have studied flow through porous model objects fabricated on the basis of computer simulated percolation clusters. The goal was to detect laws governing transport in relation to the pore space geometry described in terms of fractal dimensions and correlation lengths. The measuring method is magnetic resonance velocity mapping with a spatial resolution corresponding to that achieved with the fabrication technique of the model objects. The NMR microscopy data were evaluated with respect to the pore space structure, velocity maps, and the percolation backbone responsible for transport properties.

Results. We report on investigations of two-dimensional model objects representing site percolation, continuous swiss-cheese and inverse swiss-cheese percolation clusters above the percolation threshold p_c . The minimum pore size is 400 µm, the overall extension of the 100 x 100 lattice point matrix is 4 x 4 cm^2. Stationary flow through the water filled pore space were generated by exerting an external pressure gradient. Velocity maps were recorded in a 4.7 T / 40 cm magnet using the Fourier Encoding Velocity Imaging (FEVI) technique.

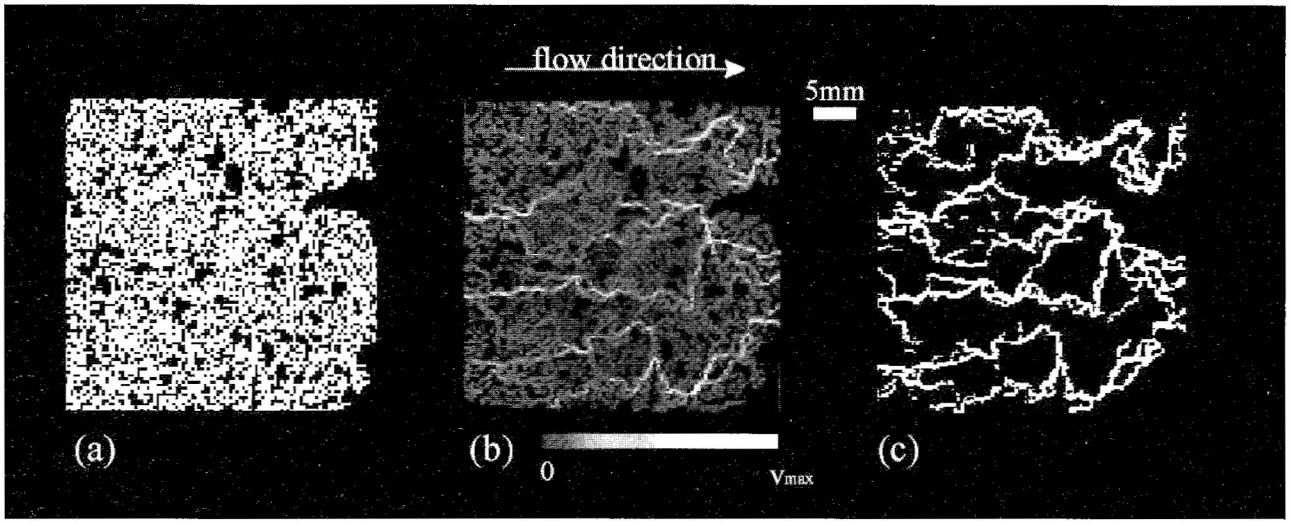

Fig. 1: **(a)** Simulation of the site percolation model: 100x100 lattice points, p-p_c=0.047, d_f=1.882. The pore space is represented by white pixels. **(b)** Experimental velocity map of the stationary liquid flow in a model object based on the simulated data in (a) (256x256 pixel; v_{max}=7.45 mm/s). **(c)** Backbone of (b), d_f=1.52.

The fractal dimension of the backbone formed by pixels with velocities greater than the velocity noise threshold (Fig. 1c) was analyzed using the sandbox algorithm. It turned out to be diminished by 0.25 ± 0.05 relative to the fractal dimension of the total pore space independently of the flow rate, the model type, and occupation probability $p - p_c \ (\leq 0.1)$. Furthermore the *volume averaged velocity,*

$$v_V(r) = \frac{1}{N_p} \sum_{i=1}^{N_p} \frac{1}{N_q} \sum_{j=1}^{N_q} v(\boldsymbol{r}_j) \quad \text{with} \quad (|\boldsymbol{r}_i - \boldsymbol{r}_j| \leq r),$$

was evaluated. A power law for the dependence on the radius of the averaging volume was detected: $v_V(r) \propto r^{-\lambda}$ (see Fig. 2).

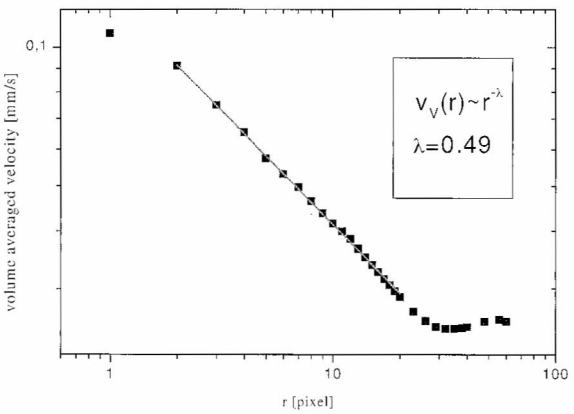

Fig. 2: Power law for the volume averaged velocity in volumes with radii below the correlation length.

References

Müller, H.-P., Kimmich, R., Weis, J. *Phys. Rev. E* **54,** 5278 (1996).

Klemm, A., Müller, H.-P., Kimmich, R., *Phys. Rev. E* **55**, 4413 (1997).

Klemm, A., Müller, H.-P., Kimmich, R., *Physica A* **266**, 242 (1999).

P66

Free Convection in Porous Media: Simulation and NMR Experiment

Markus Weber, Andreas Klemm, Rainer Kimmich

Universität Ulm, Sektion Kernresonanzspektroskopie, 89069 Ulm, Germany

Introduction: Free convection is one of the most intriguing phenomena in the field of hydrodynamics. For studies, often a Rayleigh-Bénard configuration is considered: A temperature gradient in a fluid-filled cell is directed opposite to that of gravity. In the case of good Rayleigh- and Prandtl numbers highly symmetrical Rayleigh-Bénard convection patterns are observed provided that flow is not obstructed by obstacles (1). This is in contrast to thermal convection in porous media where free flow is strongly hindered (2). The objective of the present study was to examine the patterns and the laws of convection in different percolation model objects with varying porosity.

Methods: The measuring method was NMR-Fourier encoding velocity imaging (FEVI), which permits the evaluation of two-or three-dimensional velocity maps (3). This technique is based on a spin-echo sequence modified by frequency-, phase- and bipolar gradient pulses. The experimental data were compared with finite element method (FEM) simulations of convection in identical pore space geometries. The simulations were carried out with the commercial program ANSYS/FLOTRAN.

Results: With ANSYS stationary free convection was simulated in several two-dimensional swiss-cheese and site-percolation models, the porosities of which were chosen above and below the percolation threshold p_c. Apart from velocity maps (Fig. 1a) the velocity distribution was evaluated in terms of the kinetic energy, $E_{kin} \sim v^2$. This distribution turned out to obey a power law

$$n(E_{kin}) \sim E^b_{kin}, \qquad [1]$$

where the exponent b depends linearly on the porosity p (Fig. 2). In the case of free convection in a site-percolation cluster, a phase transition was observed near p_c.

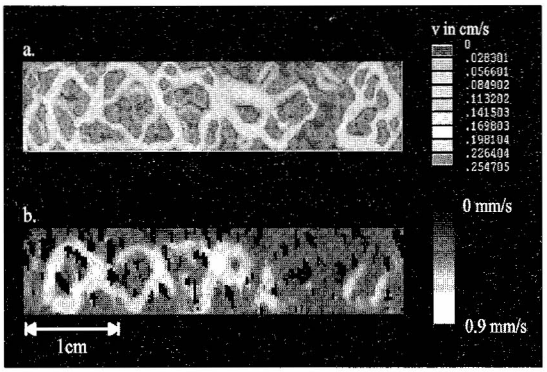

Fig. 1: Free convection in a swiss-cheese structure, p=0.79. a.) FEM-Simulation. b.) Experimental velocity map.

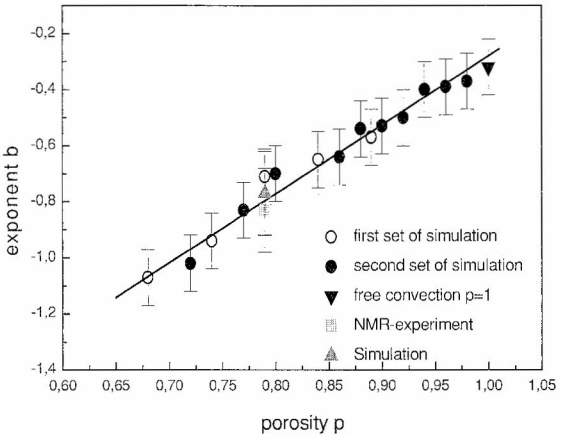

Fig. 2: Linear relationship between b and p of free convection in swiss-cheese structures.

Figure 1b shows a velocity map recorded with the FEVI technique in a 2D-swiss-cheese model object. The object was fabricated by using the simulated percolation cluster shown in Fig. 1a as template. The velocity patterns as well as the velocity distributions (see Fig. 2) are in good agreement. The power law given in Eq. 1 was also found with measurements of free convection in a fill of polystyrol granulate using a six dimensional FEVI-variant (3,4).

Conclusion: With Eq. 1, a new law for convection in porous media was found. The exponent b as a dynamic parameter of the kinetic energy distribution is linearly related to the porosity p as a static parameter. Thus predictions concerning the velocity distribution can be made for given porosities.

References

(1) J. Weis, R. Kimmich, H.-P. Müller, *Magn. Reson. Imaging* **14,** 319 (1996).

(2) A. Bejan, D. A. Nield, *Convection in porous media,* Springer Verlag, Berlin, 1992.

(3) R. Kimmich, *NMR: Tomography, Diffusometry, Relaxometry,* Springer Verlag, Berlin, 1997.

(4) A. Klemm, H.-P. Müller, R. Kimmich, *Phys. Rev. E* **55**, 4413 (1997).

P67

Visualization of the Diffusion of Cu^{2+} Ions in Dextran/K^+ Gel and Dextran/Na^+ Viscous Sol Systems by NMR Microscopy

T. Watanabe*, S. Matsukawa*, and K. Gersonde#

*Laboratory of Biomaterial Chemistry, Department of Food Science and Technology, Tokyo University of Fisheries, Tokyo 108-8477, Japan

#Fraunhofer-Institut für Biomedizinische Technik, D-66386 St. Ingbert

#Fachrichtung Medizintechnik, Universität des Saarlandes, D-66421 Homburg/Saar, Germany.

Introduction. Nowadays the absorption of heavy metal ions by biopolymers becomes attractive due to applications in environmental technology [1]. In particular dynamic aspects, such as spatially and temporally resolved sorption processes, are of importance for the design of the systems for dedicated applications. In such studies ionic biopolymers were used as sorbents. We visualize the uptake of Cu^{2+} ions by non-ionic polysaccharides, i.e., dextrans. The dextran solution forms elastic gels in the presence of K^+ ions [2], whereas it becomes a viscous solution in the presence of Na^+ ions. The diffusion of Cu^{2+} ions into K^+/dextran gels and Na^+/dextran sols has been demonstrated by NMR microscopy. Complexity of the diffusion mechanism of Cu^{2+} is not well understood.

Experimental. Dextran gels or sols were formed in glass cylinders. Then 200 µl of a 0.2 mM $CuSO_4$ aqueous solution were added carefully to the top part of the dextran system. Before and immediately after the addition of Cu^{2+} solution ^1H NMR imaging was carried out employing a Varian Unity 400 NMR spectrometer. One T_1-weighted spin-echo image and a set of 11 profiles of the signal intensity of the central slice were recorded during 13 min. This set of experiments was repeated for several hours.

Results and Discussion. Typical images reflecting the Cu^{2+} diffusion in Na^+/dextran sol are shown in Fig. 1. The high intensity band based on the water proton relaxation modified by Cu^{2+} ions proceeds downward and the band width gradually spreads with increasing time duration. Similar patterns of the intensity change of images were obtained in gels and sols. The data can not be easily interpreted on the basis of diffusion phenomena of Cu^{2+} ions expected from Fickian diffusion. Therefore, chemical reactions between dextran chains and Cu^{2+} ions have to be considered.

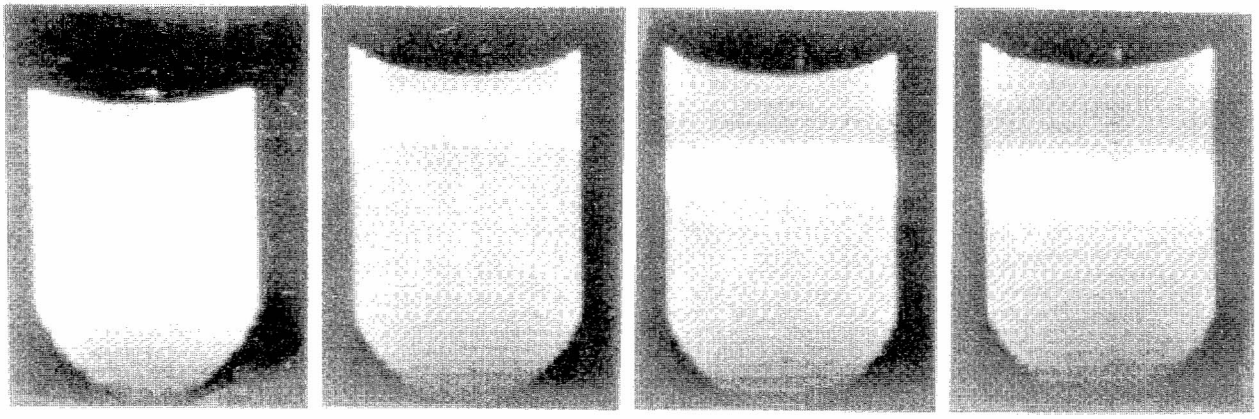

Fig. 1. ^1H NMR microimages of Cu^{2+} diffusion in Na^+/dextran sol (left to right: before and 2, 40, and 81 min after adding of Cu^{2+} solution).

References

[1] N. Nestle and R. Kimmich, *Colloids and Surfaces* A **115**, 141-147 (1996).

[2] T. Watanabe, A. Ohtsuka, P. Barth, and K. Gersonde, *Magn. Reson. Med.* **35**, 697-705 (1996).

P68

Skin Effect Imaging of Small Spheroidal Particles

Kathrin Hesse, **Günther Neue**

Physikalische Chemie, Universität Dortmund, D-44221 Dortmund, Germany

Skin Effect Imaging (SEEING-NMR) is a 2D-NMR technique that uses the steep rf gradient in electric conductors to achieve extremely high spatial resolution perpendicular to the surface. Resolutions well below 1 µm are easily obtainable by this method. Planar geometries like in surface coatings or foils lead to particularly simple solutions of Maxwells equations [1,2]. More complicated is the case of spherical metallic particles. Surfaces of constant B_1 within particles are not spherical and, hence, the relationship between depth and nutation frequencies is no longer unique. Instead, a simulation of nutation spectra is needed to derive spatial information from NMR signals.

Spheroidal particles of Al and Cu with diameters between 10 and 150 µm were studied by the Skin Effect Imaging technique. Particle sizes and size distributions are derived. The technique delivers also simultaneously information about structural defects and chemical compositions.

References

[1] Skibbe, U. Thesis, Dortmund, (1992)

[2] Neue,G., Skibbe, U., Dybowski, C., *Fresenius J Anal Chem* **349**, 112-116 (1994)

Crystallization Kinetics of Flexible Chain Polymer Confined in Pores

A.M.Zaripov, G.G. Pimenov and A.V.Filippov
Kazan State University, Department of Molecular Physics, Kazan, Kremlevskaya St., 18

Isothermal crystallization of poly(ethylene oxide) (PEO) fractions confined in cylindrical pores with the diameter 480 angstroms was studied by NMR relaxation technique. The analysis of crystallization isotherm form and temperature dependence of growing rate shows that confining in pores doesn't change the type of primary nucleation and the crystallization regime typical for the bulk polymer in the initial stage of growing.

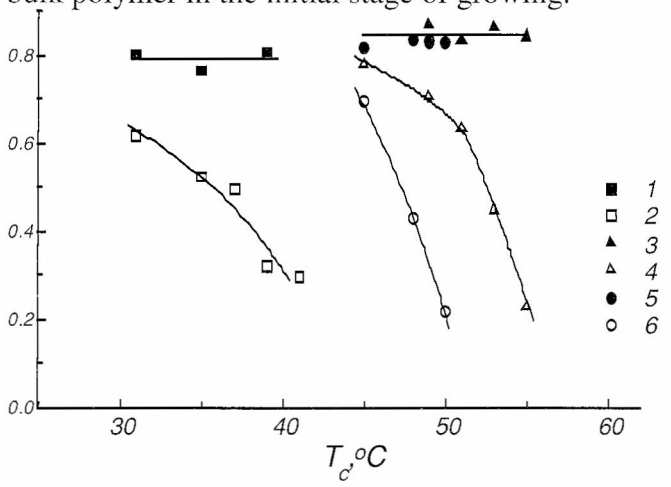

Fig.1. Dependence of $P_c(\infty)$ from T_c for PEO crystallized in bulk (1, 3, 5) and pores (2,4,6), for M=1500 (1, 2), M=40000 (3, 4), M=4000 (5, 6).

Dependence of dynamic degree of crystallinity, attained after completion of the process $P_c(\infty)$ upon the crystallization temperature T_c, was discovered (Fig.1), herewith increase of T_c lead to decrease $P_c(\infty)$. Posterior melting shows, that decrease T_c result in increase of portion of less ordered crystal phase relative to lamellar crystallites.

The change of the form of isotherms can be explained by one dimensional geometry of growing, that confirmed by the analysis of changing of transverse magnetization in the amorphous phase. Transverse relaxation decays in amorphous regions during crystallization can be described by a sum of two components, one of them was conditioned by the presence of crystal phase. The portion of this component is increased proportionally to degree of crystallinity, while relaxation times of both components remain unchanged (Fig. 2).

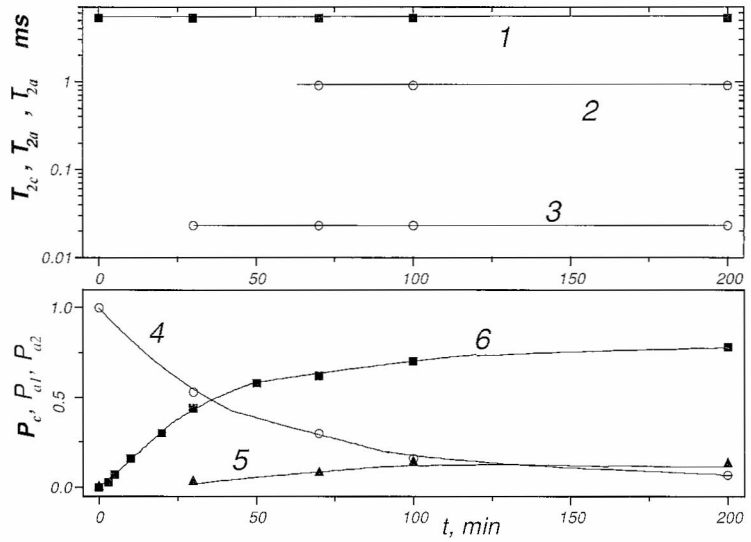

Fig.2. Dependencies of degree of crystallinity (6), populations of the transversal relaxation component of PEO with M=40000 in melt P_a (4) and in pores P_a (5), and transverse relaxation times appropriate to these components T_c (3), T_a (1), T_a (2) at 50°C.

Reference

A.V.Filippov, G.G. Pimenov, and A.M.Zaripov Crystallization kinetics of flexible chain polymer confined in pores. // Colloid Journal. (accepted for publication).

The Hardening of Portland Cement Paste and Freezing of Hardened White Cement Monitored by Single-Point Imaging

Jadwiga Tritt-Goc and **N Pi ślewski**

Institute of Molecular Physics, Polish Academy of Sciences, Smoluchowskiego 17, 60-179 Poznań, Poland

Introduction

Cement as a building material is of great importance and thus the subject of many studies by different methods among them by NMR and recently by Single Point Imaging MRI method [1,2,3]. This method is spatially suited for study of materials with very short relaxation times in the orders of microseconds. We will demonstrate the application of the SPI [4] method to noninvasive examination of water content level and its changes during the hydration process of ordinary portland cement and the possibility of this method to study the structure and pore distribution during freezing of hardened white cement.

Methods

The proton NMR imaging experiments were done on a Bruker AVANCE 300 MHz WB spectrometer, equipped with a microimaging accessory. SPI pulse sequence was used to monitor the hardening of cement paste and to follow the pore distribution during the freezing experiment. We have recorded the 1D SPI magnetization profile of cylindrical cement samples of ordinary portland cement as a function of hydration time over the period of a few weeks. The phase-encoding t_p was 80μs and phase encoding was achieved by incrementing the x gradient in 128 steps to a maximal value of 93.4 G/cm. The image was acquired with a field of view (FOV) of 2 cm and a resolution of 158μm. During the freezing process of white hardened cement a series of 1D, 2D (128×64) and bulk FID were obtained for two samples with and without superplasticizers. The T_2^* were calculated from the line width. 2D images were taken as a function of temperature (from 20 to -50^0C) with the resolution of $(100\mu m)^2$.

Results and discussion

The 1D profiles show the spatial variation of moisture content during the hardening process of the cement paste. The main feature of the profiles are the two sharp peaks at the left and right side which correspond mainly to the free water which has been displaced to the walls of the glass vial. After opening the sample this free water evaporated. We also observe an uneven distribution of the signal intensity while the sample changes its shape during hardening. A similar feature of this water distribution was also observed with 2D SPI image. In the case of white hardened cement the 2D images show the distribution of the non-frozen water in the samples. The cement and concrete is being destroyed due to the freezing of the water in the pores. First the macro and capillary pores start to freeze. Water occupying micro and meso pores (gel pores) will freeze only at very low temperature. On the basis of the images we can determine these temperatures. After adding superplasticizer the resistance to freezing grows and we observed the shift of the freezing of the macro pores from -8 (pure white cement) to -30^0 C for cement with superplasticizer.

Conclusion

We have shown the possibility of following the hydration processes of the ordinary portland cement and acquiring 2D images of a hardened white cement under freezing condition. The analysis of the images permits a distribution of the free and bound water in hydration process and permits a quantification of the nonfrozen water throughout the sample. In the latest SPI MRI method can be used to follow position based thermal changes as they take place in the cement or others materials with very short relaxation times.

References

1. Bogdan M., Balcom B.J., Bremner T.W., Armstrong R.L., *J. Magn. Reson. A* **116**, 266 (1995).
2. Beyea S.D., Balcom B.J., Bremner T.W., Prado P.J., Cross A.R., Armstrong R.L., Grattan-Bellew P.E., *Solid State Nucl. Magn. Reson.* **13**, 93 (1998).
3. Nunes T., Randall E.W., Smoilenko A.A., Bodart P., Feio G., J. Phys. D: Appl. Phys., **29**, 805 (1996)..
4. Emid S., Creyghton J.H.N., *Physica B* **128**, 81 (1985).

This work was supported by the Polish Committee for Scientific Research under project No. 2 P203B 120 14.

The Application of the FLASH - MOVIE to the Study of Polymerization of Visible Light Cured Dental Restorative Materials

John A. Chudek [1], Charles H. Lloyd [2], **Sheelagh N. Scrimgeour[1,2]**, Geoffrey Hunter[1]

[1] Chemistry Department and [2] Unit of Clinical Dental Sciences - Dental School, University of Dundee, Dundee DD1 4HN, Scotland, UK

Introduction. Visible light curing (vlc) has become the preferred method to transform dental direct restorative material from a viscous paste (in which state it is inserted into the tooth) to a rigid solid. Blue light (λ = 470 nm) will raise an α-diketone photoinitiator to an excited singlet state. By intersystem crossing this singlet state may form a triplet state. This acts as an electron acceptor to form an exciplex with an amine reducing agent and thus produces two radical-ions. An active centre is created when a free radical attacks the π bond of the monomer molecule and this is followed by rapid sequential addition of monomer. This method of polymerization has proven to be effective. It is convenient for the dentist, produces durable aesthetic restorations and is applicable to a range of material types. Research continues on improving materials and further knowledge on polymerization (both the mechanism and effect of composition) is essential.

Objective. A simple FLASH imaging experiment has been performed as a pilot to study the potential of this technique for investigating polymerization of vlc dental materials. With the curing light applied continuously and in one direction, the change in image intensity has been followed as a function of depth and time .

Experimental. A black nylon mould held a cylinder of material (12 mm x 5 mm Ø). The upper end of the cylinder was in contact with a fibre optic from the light unit to irradiate the specimen along the axis of the cylinder. Instrument: Bruker AM300WB spectrometer (7.1 T) with a standard Bruker microimaging accessory using a 25 mm saddle coil resonator. Pulse sequence: FLASH-MOVIE to produce series of images separated by time intervals of between 2 and 15 s. (10° pulse - 4ms soft hermite pulse, T_R = 0.05 s, T_E = 6.17 ms, gradient sufficient to produce an image in a $(20mm)^2$ field of view). Image: a vertical slice through the axis of the cylinder. (Slice thickness 1 mm, pixel size $(125\ \mu m)^2$). Materials: Dental resins mixtures (UDMA/TEGDMA, BisGMA/TEGDMA and DPMA/TEGDMA) and composite (diacrylate resins containing ~70% μm-size glass particles).

Results and Discussion. It was not possible to image composite. The cause may be the low resin content (30%) or the effect of its heterogeneous structure on the gradient-echo image. Imaging resin mixtures proved more successful. Images were produced for 50:50 mixtures of UDMA/TEGDMA, BisGMA/TEGDMA, DPMA/TEGDMA, and both 60:40 and 70:30 mixtures of DPMA/TEGDMA. An image could not be produced for the highest viscosity resin, 85:15 DPMA/TEGDMA. (Total elimination of air bubbles proved extremely difficult and sectioning these bubbles is a probable cause of some low intensity regions). Though the images did show considerable variation in intensity between pixels for material expected to be in an identical condition, it was possible to average intensities over rows of pixels to obtain good depth x intensity profiles. Under the prevailing imaging conditions, a fall in image intensity should be seen from the onset of polymerization, a fall which decreases in magnitude with depth (as light intensity falls). This "cure-front" should sweep into the material in time. This was seen. But, in addition, the intensity was seen to rise initially to a peak at the end in contact with the fibre optic. There are two possible causes. The exotherm raising the resin temperature (higher where the light intensity and thus reaction rate is higher) or the initial production of free radicals (the concentration of which is greatest where the light intensity is highest).

Conclusions. The MRM experiment has produced data which is not available from other techniques. This simple experiment has produced a complex result since a number of factors contribute to the image intensity. It will be possible to systematically examine each. This work has demonstrated that acceptable images of vlc dental materials can be produced by rapid imaging programmes. It is probable that FLASH imaging, particularly those sequences which have followed on from MOVIE will yield new insights into light curing.

An Analytical Calculation of the Biot Savart Law

Elisabeth de Castro Caparelli and **Dardo Gustavo Tomasi**

Escuela de Ciencia y Tecnologia, Universidad Nacional de San Martin,
Buenos Aires, Argentina

Introduction

The Biot Savart (BS) law is a very known integral equation used to calculate the magnetic field for a given current distribution. Although it has an extensive application in many branches of physics, only in elementary cases one can get analytical solutions.

Generally this integral is calculated numerically, nevertheless due to the complexity of this calculus alternatives methods have been proposed to calculate the magnetic field. An example we find in reference [1], where they have computed the magnetic field from a scalar magnetic potential expressed as a series of toroidal harmonic functions to improve the numerical code that is used to optimise toroidal magnetic devices, which are employed for fusion research. There is another example in reference [2], where they derived the magnetic field from the Maxwell equations outside of the volume conductors having axial symmetry and containing monopole current sources.

In this work we are proposing an analytical method to calculate the BS integral for a circular current distribution, obtaining an expression that describe the magnetic field for any point of the space.

Method

The method consist in expressing the Green's function of the BS integral, as the three-dimensional Fourier integration[3] and using the Fourier transform of a planar current density[3]. Next we consider the current distribution for a single loop[4] with radio R, which is suitable to use a cylindrical coordinate system. Then expanding the expression in a series of power of q ($q^2=k_x^2+k_y^2$) and making the necessary integrations, we find

$$B_r(r,z) = \frac{\mu_0 I R^2}{2} \sum_{k=0}^{\infty} (-1)^k \frac{k}{(2k)!!} r^{2k-1} z^{-(2k+1)} \Gamma[2(k+1)] \; {}_2\mathbf{F}_1\left(k+1, k+\frac{3}{2}, 2, -\frac{R^2}{z^2}\right)$$

$$B_r(r,z) = \frac{\mu_0 I R^2}{2} \sum_{k=0}^{\infty} (-1)^k \frac{(k+1)}{(2k)!!} r^{2k} z^{-(2k+3)} \Gamma[2(k+1)] \; {}_2\mathbf{F}_1\left(k+\frac{3}{2}, k+2, 2, -\frac{R^2}{z^2}\right)$$

with

$${}_2\mathbf{F}_1(a,b,c,\omega) = \sum_{m=0}^{\infty} \frac{(a)_m (b)_m}{(c)_m} \frac{\omega^m}{m!}, \quad (d)_m = \frac{\Gamma[d+m]}{\Gamma[d]}$$

Results and Conclusion

Finally we compare our result with the numerical calculation of the BS law to show the validity region of this method.

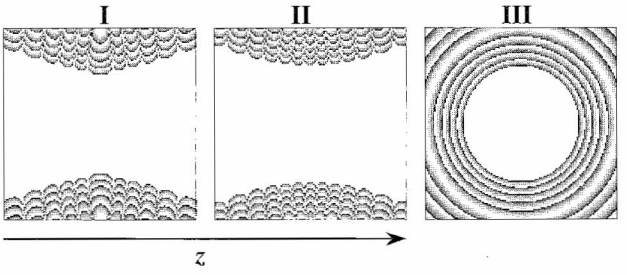

These are 2R × 2R contour maps of the difference between $B_{z,r}(r,z)$ calculated with this method and with the numerical calculation of BS. In these figures the 10% contours correspond to black-white transitions edges and a logarithmic grey scale was introduced to increase the resolution, which the white region correspond to a variation of 10 ppm between the calculations. Figure **I** shows the r-component of the magnetic field on the transversal plane of the current distribution, where we observe that at the line $z = 0$ there is a good region of concordance between the numerical and analytical calculation of BS integral (white region) at $r < 0.5R$. Figure **II** shows the z-component of the magnetic field on the same plane of figure **I,** and in this case the good region is at $r < 0.6R$. Figure **III** shows the $B_{z,r}$ on the plane $z = 0$, where we also observe that the good region is inside of $r < 0.6R$.

Hence we conclude that this method is useful to calculate the magnetic field in $r <$ R region, for example, to get a set of coil that produce a high uniform magnetic field, which is required for the magnetic resonance imaging (MRI) systems.

The advantage of this propose is to calculate and analyse the behaviour of the magnetic field at the region of interest with a good precision from simple expressions.

References

[1] Thomas Jr.,E. ,Sasser, G.E. , Knowlton, S.F. ,et al. Comp. Phys. Comm. 100, 31 (1997)

[2] Durand, D.M. Lin, J.C. IEEE Trans. on Biom. Eng. 40, 177(1997)

[3] Yoda, K. J. Appl Phys.67, 4349 (1990)

[4] Caparelli, E.C., Tomasi, D. and Panepucci, H., J. Mag. Res. Img. 9, 725 (1999)

P73

Numerical Simulations of the Signal Response for the NMR-MOUSE

F. Bălibanu, K. Hailu, R. Eymael, D.E. Demco and B. Blümich

Institute für Technische Chemie und Makromolekulare Chemie, MARC, RWTH,

Worringerweg 1, D-52074 Aachen, Germany

The spin system response has been investigated by numerical simulations in the case of an NMR experiment performed in inhomogeneous static ($\mathbf{B_0}$) and radio-frequency ($\mathbf{B_1}$) fields. The particular case of NMR-MOUSE was considered. The fields $\mathbf{B_0(r)}$ and $\mathbf{B_{1n}(r)}$ (the $\mathbf{B_1}$ component perpendicular to $\mathbf{B_0}$) were evaluated as well as the spatial distribution of the maximum NMR signal detected by the surface coil. The total NMR response to various pulse sequences was evaluated numerically for the case of an ensemble of isolated spins. The cases of two-pulse, three-pulse and Carr-Purcell Meiboom-Gill (CPMG) like pulse sequences were considered. The spatial distributions of the Hahn echoes and mixed (stimulated/Hahn) echoes were obtained. It is demonstrated that the superposition of Hahn and stimulated echoes in the CPMG pulse sequences leads to an increase in the integral intensities of the second mixed echo compared to the first Hahn echo. The simulation of the spin system response for the XY-16 pulse sequence is in a good agreement with the experiment. As a result of the superposition of the Hahn and stimulated echoes originating from different spatial regions the shape of mixed echoes are distorted. In the numerical simulations the longitudinal and transverse relaxations of nuclear magnetization are introduced in a phenomenological manner. The presence of the mixed echoes as a result of the strong distribution in the radio-frequency pulse-flip angles leads to an nonexponential decay of the CPMG echo train for longer times. Moreover, even if the intrinsic relaxation is characterized by a unique rate T_2^{-1}, the measured decay rate of the signal depends on the employed pulse sequence with different contributions from T_2^{-1} and T_1^{-1} relaxation rates. The developed numerical simulation procedure can be useful for understanding the variety of experiments performed with the NMR-MOUSE and for improving its performances.

P74

Modeling of Self-Diffusion and Relaxation Time NMR in Multi-Compartment Systems

F. Vergeldt[a], D. Hluskov[b], S. Melnikov[b], E.G. Novikov[b] and H. Van As[a]

[a]Laboratory of Molecular Physics and Wageningen NMR Centre,
Department of Biomolecular Sciences, Wageningen Agricultural University,
Dreijenlaan 3, 6703 HA Wageningen, The Netherlands
[b]Department of Systems Analysis, Belarusian State University, Minsk, Belarus

The interpretation of PFG-NMR measurements applied to biological systems containing different (sub)celluar compartments and cell-to-cell transfer is very complicated. Membranes can restrict diffusion but allow exchange and transport between compartments which can have totally different relaxation behaviour. This causes the results to be dependent on the microstructure, membrane permeability and relaxation behaviour in the different compartments. A numerical model for PFG-CPMG measurements, resulting in combined diffusion and relaxation data (1), has been presented that allows to simulate a wide range of systems and to explore temporal and spatial behaviour of the magnetization with and without the influence of gradient pulses (2). That model, however, was limited to planar membranes and so to one-dimensional diffusion behaviour.

Here we present the extension of this approach to two-dimensional systems. The extended model allows the simulation of a large variety of geometries, e.g. (concentric) cylindrical systems or ellipsoid systems, mimicing e.g. porous medium or a (variable) number of cells at variable interdistances that contain subcellular compartments. The permeability of all membranes in that system, the dimesions and the geometry (circle or ellipsoid) and the intrinsic relaxation time and self-diffusion coefficient in each compartment can be choosen independently. Using this model we simulated e.g. the difference between one- and two-dimensional diffusion models and the effect of membrane permeability on relaxation and diffusion measurements in a multi-compartment system.

The results are obtained for a matrix containing typically 100*100 points and can be presented in this matrix or integrated over (part of) this matrix. The number of gradient steps can be choosen to allow q-space imaging. The calculation time on a NT Pentium computer for a full q-space simulation with 100*100 matrix points and 100 time steps for relaxation behaviour is in the order of 10 minutes.

1. D. van Dusschoten, C.W. Moonen, P.A. de Jager, H. Van As. *Magn. Reson. Med.* **36**, 907-913 (1996).
2. E.G. Novikov, D. van Dusschoten, H. Van As. *J. Magn. Reson.* **135**, 522-528 (1998).

P75

The Effect of Finite Pixel Size and Signal-to-Noise Ratio on Quantitative Measurements in Magnetic Resonance Microscopy

Harvey H. Hensley*, John Haselgrove

Children's Hospital of Philadelphia, * Present address: Fox Chase Cancer Center

We consider the question of the quantitative determination of the area or volume of small objects in MRI, and the conditions under which it is possible to make accurate and precise measurements. The known *k*-space signal for a simple object (in two dimensions an annulus, in three dimensions a spherical shell) is computed and used to construct a simulated magnetic resonance image, which can be varied in position in the imaging field of view, and subjected to varying amounts of noise. We then count the pixels in the image whose value is greater than a given threshold in order to determine the area or volume in an automated fashion. We also address the effect of smoothing and median filters.

The MRI signal of an annulus can be calculated via the formula:

$$S(\vec{k}) = A_n + (\pi R_{out}^2 J_1(2\pi R_{out}\vec{k})/2\pi R_{out}\vec{k} - \pi R_{in}^2 J_1(2\pi R_{in}\vec{k})/2\pi R_{in}\vec{k})e^{2\pi i R_c}$$

Here $S(k)$ represents the density of the signal in *k*-space, A_n is the amplitude of Gaussian white noise, R_{in} is the inner matrix of the annulus, R_{out} the outer radius of the annulus, J_1 the first order Bessel function, and R_c the center of the annulus. Our approach automatically includes the effect of Gibbs ringing, and accurately simulates MRI partial volume effects. A similar approach is used to compute the signal from a spherical shell, using the appropriate formula.

We find that in both two and three dimensions precise and accurate measurements can be made of annuli or shells that are at least three pixels in width and radius. The random position of an annulus on the imaging matrix leads to errors of 1-2%, while systematic errors are 3-4%. We found similar results in three dimensions for the systematic errors, but found that in three dimensions the random error due to different positions is negligible. In the table below are results for calculations of annuli of different widths and radii for 100 different positions each, for the case of zero added noise, with the standard deviations and areas expressed as a fraction of the exact area.

	R=2 pixels	R=3 pixels	R=4 pixels	R=5 pixels	R=6 pixels
Width=2 pixels	0.896±.06	0.881±.05	0.890±.04	0.885±.04	0.884±.03
Width=3 pixels	0.968±.02	0.972±.02	0.971±.01	0.972±.01	0.972±.01
Width=4 pixels	0.971±.03	0.963±.02	0.967±.02	0.966±.01	0.966±.01
Width=5 pixels	0.983±.01	0.981±.01	0.982±.01	0.983±.01	0.981±.01

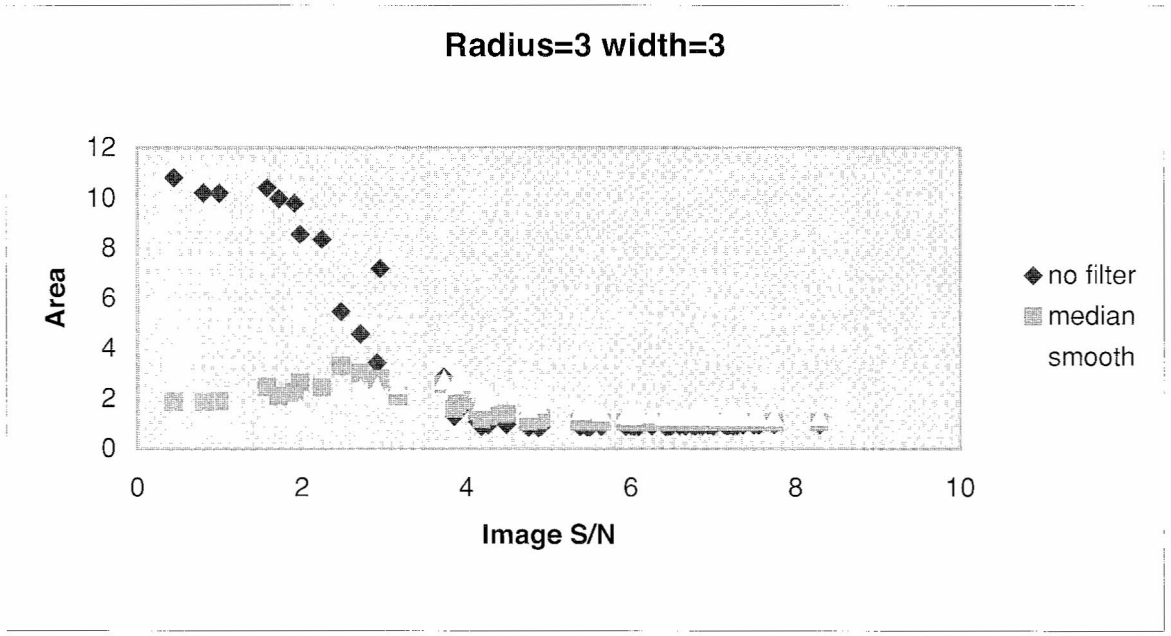

The image signal-to-noise ratio is calculated by taking the maximum pixel intensity and dividing by the standard deviation of all values which were above the threshold. The dependence of the accuracy of the measurement on signal-to-noise ratio is such that accuracy is good up to image signal-to-noise ratios of 5 or greater, then degrades and begins to diverge for signal-to-noise ratios of four or less. The effect of median and smoothing filters is minor, but median filters tend to increase both accuracy and precision, and smoothing filters tend to cause an overestimate of the area or volume.

Estimation of NMR Signal Frequency Using FIR Filters

Radomír Svoboda
Brno University of Technology, Faculty of Electrical Engineering and Computer Science, Department of Telecommunications, Purkyňova 119, 612 00 Brno, Czech Republic

1. Introduction

Due to eddy currents, the gradient magnetic field generated in tomograph does not correspond to its drive pulse exactly. This distortion can be partly eliminated by using drive pulses of a specific shape which can be derived from the time function of the instantaneous frequency of the tomograph output signal, the NMR signal, [1]. Unfortunately, this signal is distorted also by noise, which causes a computation error. The error is inversely proportional to the Signal-to-Noise Ratio, S/N. One way how to increase the S/N is to filter the NMR signal. According to the short-time spectral analysis of the NMR signal distorted by gradient field, the signal energy is mainly concentrated at frequencies less than or equal to the signal instantaneous frequency. Low-pass filters could therefore be used to increase the S/N.

2. Single-filtering method

In this method, the NMR signal is filtered only by one low-pass filter with its cut-off frequency equal to the maximal signal frequency. However, as the signal frequency decreases during the measurement, the efficiency of this filtration worsens.

3. Filters with variable parameters

The efficiency of filtration can be improved by using several low-pass filters with different cut-off frequencies. During the measurement the signal is always filtered by the one of these filters that ensures the highest possible S/N in the output. The appropriate filter is therefore selected according to both its cut-off frequency (must be higher than or equal to the signal instantaneous frequency) and its transient bandwidth (as narrow as possible). Such a set of filters can be treated as a single filter with variable parameters. FIR filters should be used because of their better stability, linear phase and other advantages.

4. Dual filtration with variable parameters

The signal of calculated instantaneous frequency of an NMR signal can be treated as a regular digital signal. Thus it can undergo digital operations such as filtration. According the short-time spectral analysis of the frequency signal, we see that the most of signal energy is concentrated at low frequencies. The effective frequency band starts at the zero frequency and ends at a frequency proportional to the steepness of the signal waveform. Thus adopting the method described in the previous paragraph on the frequency signal will further improve the measurement accuracy.

5. Discussion

standard deviation / mean value	S/N=50	S/N=20	S/N=10	S/N=3
No filtration	91,2 / 0,024	221,2 / -0,161	478,1 / 0,092	1554,6 / 0,201
Single filtration	15,8 / 0,096	45,8 / -0,048	96,3 / 0,059	261,3 / 0,246
Variable parameters	7,40 / 0,009	29,0 / -0,153	61,1 / -0,088	132,6 / 0,025
Dual filtration	2,47 / 0,051	10,56 / -0,239	11,3 / -0,094	54,1 / -1,253

Measurement errors (i.e. the difference between calculated and actual frequencies) of all three methods mentioned above for various input S/N values are shown in the table. Comparing the standard deviations, the single filtration improves the accuracy approximately 6 times, the method using a filter with variable parameters 12 times and the dual filtration even 20 times. However, due to increasing sophistication of the methods, the time consumption increases correspondingly. The measurement accuracy of the dual filtering method is comparable with that of a system using the wavelet transform [2], but in spite of that it requires less computation time and is quicker therefore.

6. Conclusion

All the methods mentioned in this report have been implemented on a PC in MATLAB and on the Motorola 96002 DSP and included in the measurement loop of the experimental tomograph at the Institute of Scientific Instruments in Brno.

References:

[1] Shaw, D.: Fourier Transform N.M.R. Spectroscopy. Elsevier Scientific Publishing Company, Amsterdam-Oxford-New York, 1976

[2] Bartušek, K, Vojta, J.: Applications of the Wavelet Transformation in NMR. 8th International IMECO Conference on Measurement in Clinical Medicine, Proc. p. 3-152 - 3-154, Dubrovník- Croatia, 1998.

turboSPI: A New MRI Technique for Imaging of Heterogeneous Materials

S.D. Beyea, **B.J. Balcom**, I.V. Mastikhin, T.W. Bremner [a], R.L. Armstrong, P.E. Grattan-Bellew [b]

MRI Research Centre, Department of Physics and [a] Materials Group, Department of Civil Engineering, University of New Brunswick, Fredericton, NB, Canada

[b] Institute for Research in Construction, National Research Council, Ottawa, ON, Canada

Nuclear magnetic resonance (NMR) signals arising from heterogeneous materials are often characterized by inherently large inhomogeneously broadened linewidths. This frequently leads to spatial distortions and resolution loss when attempting to image these materials using standard magnetic resonance imaging (MRI) methods. Pure phase encoding methods (1,2) have been shown to be successful in artifact free high resolution imaging of broad linewidth materials, however these techniques are often characterized as being "slow". The development of a new technique, which is a hybrid of the RARE (3), FLASH (4) and SPI (2) methodologies, allows fast high resolution imaging of these materials, with T2-relaxation weighting. The sensitivity, contrast and resolution characteristics of this method, called turboSPI, will be discussed, and images demonstrating the use of the method in non-destructive evaluation of composite materials will be shown.

References

1. Emid, S.; Creyghton, J.H.N.; *Physica* **128B**, 81 (1985).
2. Gravina, S.; Cory, D.G.; *J. Magn. Reson.* **104**, 53 (1994).
3. Hennig, J.; *et al.*, *Magn. Reson. Imaging* **3**, 823 (1986).
4. Haase, A. et al, *J. Magn. Reson.* **67**, 258 (1986).

P78

Structural Investigations Using the Long-Range Dipolar Field in liquid-State NMR

C. Ramanathan, S. Gutteridge and R. Bowtell

Magnetic Resonance Center, School of Physics and Astronomy,
University of Nottingham, University Park, Nottingham, NG7 2RD, UK

Introduction. NMR microimaging and diffusion measurements have conventionally been used to obtain structural information from a sample[1]. Barral et al. showed that Fourier space imaging data could also be used to measure the Patterson function of the sample[2]. Bowtell and Robyr showed that the long range magnetic dipolar field in liquids could be used to make average structure measurements[3,4]. These dipolar fields, which are usually ignored in liquid state NMR, can give rise to multiple spin echoes[5,6], transient lineshape distortions[7] and unexpected multiple quantum coherences[8,9]. The dipolar fields are usually non-local, but in the presence of a strong magnetic field gradient the dipolar field at a particular location depends primarily on the magnetization within one wavelength of the gradient modulation[3,9]. Thus it is possible to vary the localization of the dipolar fields by varying the strength of the applied gradient. In this study, we image the double-quantum CRAZED[8] signal from a phantom (a model for oriented structures) as a function of the double-quantum gradient amplitude.

Methods. Our sample consists of a 10mm NMR tube filled with water, within which were placed (randomly) a number of empty microcapillary tubes whose ends were sealed. The long capillary tubes were placed coaxially to the NMR tube. The experiments were performed on an 11.7 T microscope. The use of long coaxial cylindrical structures parallel to B_0 in combination with an MQ gradient in the same direction reduces the problem to a single dimension. As the modulation of the MQ gradient is varied in the *axial* direction, the primary effect on the image is in the *radial* direction due to the angular term in the Fourier space representation of dipolar field. The pulse sequence consists of a double-quantum CRAZED sequence using hard pulses to modulate the dipolar fields in the entire sample, followed by a standard 2D-FT spin-warp imaging sequence with a slice selective 180 degree pulse. The gradient strength was varied corresponding to spatial frequencies ($k_m = \gamma GT$) of 0.08 to 3.0 mm^{-1}. Diffusional effects were minimised by keeping the evolution time relatively short (~ 40 ms).

Results and Discussion. The figure shows representative double-quantum CRAZED images obtained with k_m = 0.08, 0.19, 0.35 and 0.93 mm^{-1}. It can be seen that the water has leaked into two of the capillaries. At very small values of k_m, the wavelength of the gradient modulation is large and dipolar field is averaged over a large distance. At intermediate values of k_m, the modulation wavelength is similar to the size of the structures present, and the dipolar fields of neighbouring structures can overlap and interfere. At larger values of k_m , the modulation wavelength is smaller than the structures present, and dipolar fields only depend on the local magnetization. Diffusional attenuation also start to be important at large k_m .

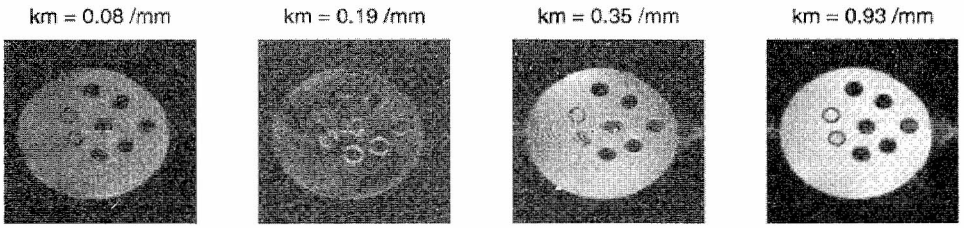

Conclusions. We have shown that the images obtained from the double-quantum CRAZED measurement are quite sensitive to the modulation wavelength of the gradient and the presence of structures in the sample. The results obtained agree well with those obtained by simulations. It should be possible to obtain the nearest neighbour distances in such oriented structures using a modification of the Hankel transform method proposed by Robyr and Bowtell[4].

References

[1] Callaghan, P.T., *Principles of Nuclear Magnetic Resonance Microscopy*, Clarendon Press, Oxford (1991).

[2] Barral G.A., Frydman L, Chingas G.C. *Science* **251**, 714 (1992).

[3] Bowtell R., Robyr P., *Phys. Rev. Lett.* **76,** 4971 (1996).

[4] Robyr P., Bowtell R., *J. Chem. Phys.* **107,** 702 (1997).

[5] Deville G., Bernier M., Delrieux J.M., *Phys. Rev. B* **19,** 5666 (1979).

[6] Bowtell R., Bowley R.M., Glover P., *J. Magn. Reson.* **88**, 643 (1990).

[7] Edzes H.T., *J. Magn. Reson.* **86**, 293 (1990).

[8] Warren W.S., Richter W., Andreotti A.H., Farmer B.T., *Science* **262**, 2005 (1993).

[9] Richter W., Lee S., Warren W.S., He Q., *Science* **267**, 654 (1995).

P79

A Single-Point Approach to Spiral Scan Magnetic Resonance Imaging

D. J. Goodyear and **B. J. Balcom**

MRI Research Centre, Department of Physics,
University of New Brunswick, Fredericton, NB, Canada

A technique for imaging semi-rigid solid materials is proposed. The technique is based on single-point ramped imaging with T_1-enhancement (SPRITE) MRI (1) with spiral k-space sampling. This method utilizes an Archimedian spiral k-space trajectory, rounded to a nearest-neighbour cartesian grid. The acquired k-space data is equally spaced, consequently eliminating the use of a regridding algorithim, leading to fast image recontruction using fast Fourier transforms. The effects of transient state behaviour on image resolution and signal/noise are discussed (2). Spiral sampling gives increased signal-to-noise compared to the basic SPRITE sequence, when imaging long-T_1 materials.

References

1. Balcom, B. J. *et al.*, *J. Magn. Reson.* **123**, 131 (1996).

2. Mastikhin, I. V. *et al.*, *J. Magn. Reson.* **136**, 159 (1999).

^{1}H Stray-Field Magnetic Resonance Imaging of Water in Different Chemical Environments: Long Hahn-Echo Train Observations

T. G. Nunes[1], E.W. Randall[2], G.Guillot[3]

[1] ICTPOL/IST, Departamento de Engenharia de Materiais, Lisboa, Portugal
[2] Chemistry Department, Queen Mary & Westfield College, London, United Kingdom
[3] CNRS URA 2212, Université Paris-Sud, Orsay, France

A new protocol for stray-field imaging was suggested, subsequently to the recording of long echo-trains (LETS) for deuterium observation in diamagnetic compounds [1]. Moreover, the fact that from coordinated heavy water in solid copper sulfate only a few echoes were recorded was explained on the basis of a dominant T_1 weighting effect on the components of the Hahn-echo train. However, in deuterated compounds, dipole-dipole interaction is much smaller than in the corresponding protonated compounds (the ratio of the square of the magnetogyric ratio is about 42) and the quadrupole electric interaction is the driving mechanism for spin-lattice relaxation (T_1D_2O~500 ms and T_1H_2O~3 s).

In the present study, we have used the LETS protocol for the observation of protonated water in the liquid, in ice, in melting ice and as coordinated water molecules in copper sulfate. One-slice STRAFI long Hahn-echo train acquisition or STRAFI-MRI one-dimensional images (profiles) were obtained. The RF pulse sequence was $[\alpha_x\text{-}(\underline{\tau}\text{-}\alpha_y\text{-}\underline{\tau}\text{-echo-})_n\text{-}D]$.The influence of the radio frequency power, the time delay $\underline{\tau}$ and the relaxation delay $\underline{D}$ on the decay of the spin-echoes is reported.

The results are discussed in terms of self-diffusion (of the order of 10^{-5} cm^2s^{-1} for the liquid and 10^{-20} cm^2s^{-1} for the solid, at 25°C and 1 atm) and spin relaxation times, and will contribute to the understanding of the mechanisms that govern the decay of Hahn-echoes, under a strong magnetic stray-field gradient.

1. Randall E.W., Nunes T. G., Guillot G. and Bodart P., *Solid State NMR* (in press).

P81

Calibration of the Gradient of the Stray Magnetic Field by Multi-Nuclear STRAFI

A.R. Preston, **E.W. Randall** and P. Kinchesh

University of London, Queen Mary & Westfield College, Department of Chemistry, London E1 4NS, England

Introduction. Self-diffusion coefficients can be measured by magnetic resonance techniques by studying the decay of the magnetisation caused by diffusion across a magnetic field gradient, G. Thus knowledge of the absolute value of G is important. The most sensitive method of measuring diffusion coefficients is the STRAFI (stray field) or fringe field method[1,2] where, typically, the large static gradient which occurs away from the central homogeneous region of a superconducting solenoidal magnet is used. Many methods have been used for measuring G but the most common one is to deduce a value by performing a calibration experiment on a material of known self-diffusion coefficient. Suitable liquids are described by Holz et al[3]. In this poster we demonstrate an alternative 'standardless' method suitable for the large gradients present in STRAFI.

In STRAFI the signal arises only from a thin slice of the sample lying at the sensitive plane of the magnet. The position of this plane is governed by the RF frequency,ω, and the gyromagnetic ratio, γ_i, of the nucleus, since shielding and coupling constants may normally be neglected. Thus for a fixed frequency an object containing several different types of nucleide will contribute to the image whenever any part of it lies in any of the relevant sensitive planes. The 1-D image is a record of the signal detected as a function of time as the sample is stepped steadily out along the B_z axis, thus profiles for different nucleides will be displaced with respect to each other[4]. The distance between these profiles equals the distance between the sensitive planes, and from the known values of γ_i the gradient can be calculated. The most suitable second nucleus to choose for a proton probe is ^{19}F, which has a gyromagnetic ratio only ~6% smaller than that of the proton. The method is analogous to the chemical shift displacement in MRI.

Method. A phantom was constructed for a 5cm internal diameter STRAFI probe[5] consisting of two discs of perspex separated by a teflon spacer. 1D profiles were acquired by stepping the phantom along the B_z axis with the coil tuned to 111.5MHz corresponding to the optimum STRAFI sensitive plane for the proton. γ_F, is less than γ_H so the fluorine sensitive plane lies at a higher field than the proton one and so as the phantom is scanned the teflon image will be recorded before the perspex one even though it is not first physically. The scale of the image can be calibrated from the known thicknesses of the phantom components and G may be calculated from the displacement, x, of the teflon image from the inner faces of the perspex sandwich, using the following:-

$$G = \frac{\omega}{x}\left(\frac{1}{\gamma_F} - \frac{1}{\gamma_H}\right)$$

Results and Discussion. The initial result 11.7±0.2 T/m agrees well with that predicted from the theoretical axial variation of B_z (11.9 T/m).

The gradient in a STRAFI diffusion experiment is the difference in field across the width of the sensitive slice and so is effectively a tangent to the axial magnetic field profile. The value calculated by our new technique is that of a chord linking the points where the two sensitive planes cut this profile. Their separation is 1.38 cm for our system. The ideal operating frequency for a STRAFI-probe is chosen so that the *lateral* variation of the field within the coil is as low as possible to minimise the curvature of the sensitive plane. The curvature of the fluorine sensitive plane will affect the precision with which its displacement from the H position can be measured.The usefulness of this method for a given magnet can be checked by repeating the experiment with the coil tuned over a range of radio frequencies. If the gradient variation is locally small then each measured chord gradient will be approximately equal to the desired tangent to the stray field curve at the optimum sensitive plane. Detailed analysis of the results for the hydrogen-fluorine system are given on the poster. We are investigating the extension of this STRAFI-method to a mononuclear system characterised by two screening constants, where the two sensitive planes become much closer.

Conclusion. The new method is a useful alternative to the diffusion method which requires a 'standard' sample for which the diffusion constant is known accurately at the temperature of the STRAFI experiment. The new method does not require matching of temperatures or great care over the purity of the specimen.

Acknowledgements. Work supported by BBSRC grant 68/E08576. The NMR instrumentation was provided by the University of London Intercollegiate Research Services scheme and is located at Queen Mary and Westfield College.

References

1. Kimmich, R. et al., *J. Magn. Reson.* **91**(1), 136-140 (1991).
2. Geil, B., *Concepts in Magn. Reson.* **10**(5), 299-321 (1998).
3. Holz, M. et al., *J. Magn. Reson.* **92**(1), 115-125 (1991).
4. Randall, E.W. et al., *J. Magn. Reson.* **117**, 317-319 (1995).
5. Kinchesh, P. et al., *Proc. 5th Int. Conf. Magn. Reson. Microsc.* (1999).

P82

Temperature Mapping via Chemical Shift Imaging

Jeffrey H. Walton[1], Juan J. Gonzalez[2], and **Michael J. McCarthy**[2]

[1]Nuclear Magnetic Resonance Facility, University of California, Davis, CA USA

[2]Department of Food Science and Technology, University of California, Davis, CA USA

Introduction. Recent outbreaks of food borne illness have dramatically highlighted the importance of achieving an adequate final temperature for ensuring food product safety. This is particularly true for packaged and individual products like bone-in chicken, hamburgers, and whole chickens. The measurement of internal temperatures in this type of product is most often achieved by using an invasive probe like a thermocouple. However, this approach is not viable for all foods and usually not rapid enough for production line use. The motivation for our work derives from a goal to develop a noninvasive temperature sensor to measure the internal temperature of a product during/after cooking.

Purpose. The goal of this work is to extend previous work [1], on the use of Nuclear Magnetic Resonance (NMR) spectroscopy to measure the internal temperature of meat during cooking, via chemical shift imaging.

Methods. Chemical shift imaging experiments were carried out on a phantom of ethylene glycol. The sample was differentially heated. The top was held at 309 K and the bottom at 302 K to avoid effects due to convection.

Results/Discussion. The difference in chemical shift of the two lines in the ethylene glycol spectrum is a well known NMR temperature standard [2,3]. The chemical shift image of the ethylene glycol phantom was exported to Matlab where the chemical shift difference was calculated on a pixel by pixel basis (shown below). Using the equation determined by Raiford *et. al.* [3] the temperature was mapped back to each pixel. Slice selection is performed such that chemical shift artifacts are minimized. In plane resolution is achieved via phase encoding in both dimensions which eliminates chemical shift "artifacts". Because the difference in chemical shift is used, a high degree of shimming is relatively unimportant.

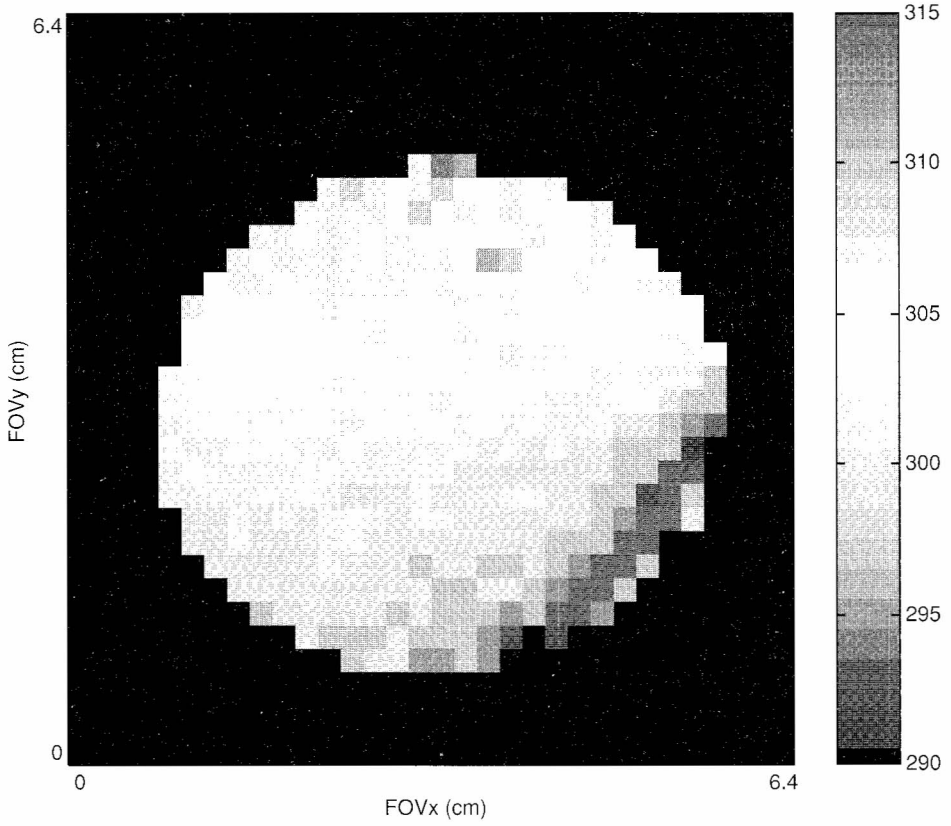

1. Walton, J. H. and McCarthy, **J. Food Proc. Eng.**, *In Press*

2. Van Geet, A. L., *Anal. Chem.*, **40**, 227 (1968).

3. Raiford, D. S., Fisk, C. L., and Becker, E. D., *Analytical Chemistry*, **51**, 2050 (1979).

Relaxation of fluorinated gases for lung imaging

V olk er C. Behr†, Dean O. Kuethe ††

† Ph ysik alisches Institut, Univers it ät W¨ urzburg, Germa n

†† Lo velace Respiratory Researc h Institute, Albuquerque, NM, USA

Gas MRI is a promising w ay to image lungs. Besides the currently popular h yperpolarized gas imaging [1], [2], it is possible to obtain useful images using thermally polarized fluorinated gases as originally proposed b y Rinck, *et al.* [3]. Fluorinated gases offer an alternative to hydrogen as well as h yperpolarized gases because their short T_1 (on the order of ms) allows for intensive av eraging. T_2 for these gases, which relax b y spin-rotation coupling, are similar to their T_1 [4], [5], [6], [7].

T o obtain data on concentration dependence SF_6, C_2F_6 and C_4F_8 gases were mixed with either pure oxygen or pure helium-4 so that the fluorinated gas fraction ranged betw een 5 and 100 % of the total. Pressure dependence experiments w ere done in the range from 162 to 4977 hPa for SF_6.

The values for T_1 of the pure gases at 292 K and atmospheric pressure in Albuquerque (840 hPa) are sho wn in the following table.

	SF_6	C_2F_6	C_4F_8
T_1 (ms)	1.67	7.90	46.78

The error for all T_1 data is 5 % or less and is mostly due to mixing and pressure measurement uncertainties.

T_1 for all the gases was found to be nearly linear in the respective fluorinated gas concentration in the mixture (see figure). F urthermore the changes in T_1 depend on the second gas in the system. This is consistent with data aquired in earlier studies [5], [8]. The decrease in T_1 with decreasing fluorinated gas fraction was muc h more rapid with helium than with oxygen.

The changes in T_1 for our range of pressures w ere almost linear whic h could be expected based on the results of Finney et al. [9] who did studies especially in the high pressure domain.

T_1 in these fluorinated gases is a function of gas fraction as well as of pressure. This faciliates choosing gas mixtures to suit the relaxation requirements for different imaging procedures.

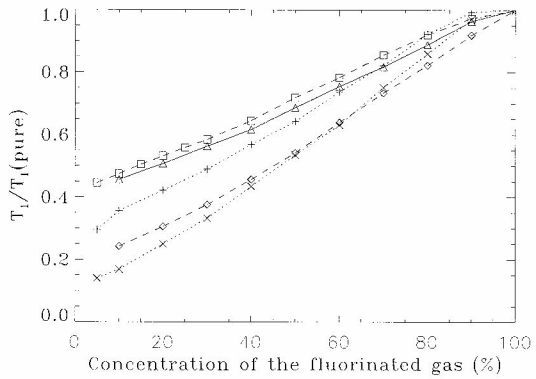

Nomalized T_1 *vs.* concen trationof thc fluorinated gas. Legend: (+) C_4F_8 and O_2, ( ) C_4F_8 and He, ( ) C_2F_6 and O_2, ( ) SF_6 and O_2, ( ) SF_6 and He

F urthermore these results agree with previous measurements of T_1 in lungs [4] so with some additional data on temperature dependence we should have a good way of estimating the relaxation of these gases in lungs under a variet y of conditions.

References

[1] Albert, M. S., *et al.*, *Nature*, , 199-201 (1994)

[2] Mugler, J. P .,III, *et al.*, *J. Magn. Reson. A nal*, (accepted, 1999)

[3] Rinck, P . A., S. B. P etersen, P . C. Lauterbur, *F ortschr. R¨ ontgenstr.* , 239-243 (1984)

[4] Kuethe, D. O., A. Caprihan, E. Fukushima, R. A. Waggoner, *Magn. Reson. Med.*, , 85-88 (1998)

[5] Mohanty, S., H. J. Bernstein, *J. Chem. Phys.*, , 461-462 (1970)

[6] Armstrong, R. L., *Magn. Reson. Rev.*, , 91-135 (1987)

[7] Lizak, M. J., M. S. Conradi, G. G. Fry, *J. Magn. R eson.*, , 548-557 (1991)

[8] Wolfe, M., E. Arndt, J. Jonas, *J. Chem. Phys.*, , No. 9, 4012-4018 (1977)

[9] Finney, R. J., M. Wolfe, J. Jonas, *J. Chem. Phys.*, , No. 9, 4004-4011 (1977)

P84

T_1 Measurements of Hyperpolarized Xenon at 85 Gauss

A. R. Cross[1], S. Breeze[2], I. Cameron[1], S. Lang[2], M. McDonald[1], I. Moudrakovski[2], C. Ratcliff[2], J. Ripmeester[2], G. Santyr[1], P. Sevigny[1], B. Simard[2] and J. Wallace[1].

[1] Carleton Magnetic Resonance Facility, Department of Physics, Carleton University, Ottawa, Canada.

[2] Steacie Institute for Molecular Science, National Research Council of Canada, Ottawa, Canada.

Introduction

Noble gases such as Helium (^{3}He) and Xenon (^{129}Xe) are capable of laser induced nuclear spin polarization 10-100,000 times greater than is achieved through Boltzmann equilibrium at room temperatures. The increased signal to noise ratio due to hyperpolarization has facilitated rapid development of MRI imaging of the lung. High quality 2D and 3D images have been produced in animals[1] and human[2] volunteers. Helium produces the best images of gas spaces since it has a long (~40s) relaxation time and very low solubility in the blood and other tissues. Xenon on the other hand readily dissolves in blood and lipid-rich substances. For this reason, there is great interest in ^{129}Xe for improved and dynamic imaging of internal organs[3]. An important factor limiting the potential enhancement of imaging with noble gases is the longitudinal relaxation rate of the hyperpolarized state. Another benefit which has great potential is the independence of the laser induced polarization to the field strength at which the polarization is observed. This removes the need for expensive high field super-conducting magnets. An added interest in low field imaging is the reduced effect of susceptibility effects at low fields[4]. For these reasons, determination of relaxation parameters at low field strengths is essential in determining the applicability of low field ^{129}Xe imaging[5,6].

Methods

At low field strengths and thus low frequencies inexpensive homebuilt spectrometer designs are adequate to detect the hyperpolarized signal. Such a design has been presented[7]. We have modified this basic design. An interface module has been added to allow pulse programming, digitization and data storage to be handled by a SMIS MR5000 console (Surrey, UK). The phase detection section was extended to quadrature with the reference frequency derived from the SMIS clock to assure synchronization. An ENI model 2100L amplifier was used to increase the RF power. Complete encasing of the probe was necessary to shield interfering signals mainly coming from computer monitors.

All measurements were performed in the fringe field of a 2T superconducting magnet at a Larmor frequency of 100 kHz (85 Gauss). Sealed glass sample tubes (1 cm diameter) coated with SurfraSil (Pierce Chemical Laboratories) were prepared with 800 mbar ^{129}Xe and 100 mbar N_2 gas and a small amount (~30 mg) of rubidium. Both natural abundance samples and 80% enriched ^{129}Xe samples were prepared. The samples were polarized (4-6%) in a 30G field at 90°C for 20 min using circularly polarized light from a 30 W diode array laser (Opto-Power, Tucson AZ) emitting at 794.6 nm. The T_1 measurements were performed using a fixed α pulse train repeated at multiple repetition times (TR). The sample was repolarized for each pulsing rate. The ratio of the intensity of successive pulses (I_{N+1}/I_N) versus TR was fit using a non-linear Marquardt fitting routine to extract both T_1 and α.

Results and Discussion

The T_1 of the natural abundance sample was found to be 760 ± 80 s with the enriched sample giving a value of 418 ± 25 s . These low field values are in agreement with the field dependent trend of measurements performed at high field (2 - 9.4T). The tip angle was 24° with a 1.2 ms pulse length in the "High"[7] output setting. The lower gamma of ^{129}Xe required more power to produce shorter pulse lengths. With the addition of the power amplifier with input attenuation, a 90° pulse of 900 μs was achieved. These initial results show that low field ^{129}Xe relaxation measurements can be performed with low cost electronics which can easily be merged with existing imaging equipment. With the spectrometer modifications performed, all of the imaging capabilities of the SMIS system are available. We are currently constructing a Helmholtz coil to be used in conjunction with our existing imaging gradients.

References

1. M. Viallon, et al., *Magn. Reson. Med.* **41**, 787-792 (1999).

2. W.G. Schreiber, et al., Proc. ISMRM, 7th Annual meeting, 2096, (1999).

3. M. S. Albert and D. Balamore, *Nuclear Instruments and Methods in Physics Research* **402**, 441-453 (1998).

4. C. H. Tseng, et al., *Phys. Rev. Lett.* **81**, 3785-3788 (1998).

5. L. Zhao and M. S. Albert, Nuclear Instruments and Methods in Physics Research 402, 454-460 (1998).

6. B. R. Patyal, et al., *J. Magn. Reson.* **126**, 58-65 (1997).

7. B. T. Saam and M. S. Conradi, *J. Magn. Reson.* **134**, 67-71 (1998).

Application of Optically Polarized ^{129}Xe to Magnetic Resonance Imaging and Spectroscopy of Microporous Materials

Igor L. Moudrakovski [a], Anivis Sanchez[a,b], Stephen Lang [a,b], Christopher I. Ratcliffe[a], John A. Ripmeester[a,b]

[a]Steacie Institute for Molecular Sciences, National Research Council, Ottawa, Ontario, K1A 0R6, Canada, [b]Carleton University, Ottawa, Ontario, K1S 5B6, Canada

Microporous materials are at the center of many industrially important applications, including heterogeneous catalysis and processes of separation and purification, and diffusion often plays a key role. For a long time now, NMR has been an important tool in the study of adsorption and diffusion, but often there are limitations because of low sensitivity. Optical pumping[1] can increase the intensity of the NMR signal by up to five orders of magnitude, thus allowing applications of new NMR and MRI experiments to materials with void space[2]. In this work we report two new applications with OP xenon, which further extend the utility of xenon NMR to the study of adsorbents and catalysts.

The first of these concerns the evaluation of diffusion properties of microporous materials. On a model system of Vycor porous glass we have shown, that optical pumping provides a vast enhancement in sensitivity, and that the diffusion of OP xenon in porous glass can be monitored with a time resolution of better than 0.1 s. The combination of 1D-imaging with the high sensitivity of laser-polarized xenon allows us to visualize the diffusion, the analysis of the data yielding the diffusion coefficient and activation barrier to diffusion.

The second application relates to the evaluation of regions with different porosity in macroscopic samples. The ^{129}Xe chemical shift of adsorbed xenon is known to be a very sensitive probe of the local environment in voids, and chemical shift imaging of ^{129}Xe promises to be an excellent tool to localizing the regions of different nature. This has been recently demonstrated with thermally polarized xenon at high pressures[3], but experimental times – tens of hours - are prohibitively long for general use. Using OP xenon we were able to produce some excellent CSI images of various adsorbents, thus confirming the utility of technique. Importantly, the time required to obtain images is also reduced drastically. We note that this is the first report on chemical shift imaging with optically polarized xenon. The experimental details of the method will be reported elsewhere.

So far, ^{129}Xe MRI images of materials have not been as spectacular as those of living organisms, however, they can reveal important new information concerning such systems.

References

1. (a) Grover, B.C.; *Phys. Rev. Lett.* 1978, **40**, 391,
   (b) Happer, W., Miron, E.; Schaefer, S., et al., *Phys. Rev. A* **29**, 3092 (1984)
2. Song, Y.-Q.; H.C. Gaede, H.C.; Pietrass, T., et al., *J. Magn. Reson., Ser. A* **115**, 127 (1995)
3. Gregory, D.M.; Gerald II, R.E.; Botto, R.E., *J. Magn. Reson.* **131**, 327 (1998)

P86

Preliminary Investigations on ^{17}O Imaging to Study Moisture Distribution and Migration in Foods

Jeffrey H. Walton[1], and **Michael J. McCarthy**[2]

[1]Nuclear Magnetic Resonance Facility, University of California, Davis, CA USA
[2]Department of Food Science and Technology, University of California, Davis, CA USA

Introduction. The most significant cause of spoilage/destabilization in foods is moisture and/or lipid migration. Proton MRI has become an important tool for monitoring moisture and lipid migration. However, for proton MRI to be successful in many foods, a significant difference between water and lipid proton NMR properties must exist. NMR properties that can generate contrast for MR are relaxation times, self-diffusion coefficients and chemical shifts. If differences do not exist in these properties, variations in proton signals cannot be associated with a specific component. The potential exists to use other nuclei to discriminate components. For the water molecule one can investigate the use of ^{2}H or ^{17}O. However due to exchange the use of ^{2}H is problematic.

Purpose. To evaluate the potential for using ^{17}O to discriminate between water and other components in foods.

Methods. We measured the T_2 of ^{17}O at 40.727 MHz (7 T) on a Bruker Biospec system. Decay rates were determined from an exponential fit to the magnitude of the FID.

Results/Discussion. Imaging the distribution of ^{17}O can be performed using either indirect or direct methods. Indirect methods measure the distribution and quantity of ^{17}O by decoupling ^{17}O from the protons and observing the effect on the T_2 weighted proton image[1]. Direct imaging of ^{17}O is difficult because ^{17}O is a quadrupolar nuclei and relaxation times are short. However, direct imaging of ^{17}O is simpler in practice than decoupling based approaches. ^{17}O imaging, using either natural abundance or minimal isotopic enrichment, can potentially address a variety of food stability issues. Prior to determining the most efficient imaging scheme, knowledge of relaxation times is imperative. We present T_2's of water, apricot, apple, kiwi, and cookie dough. ^{17}O T_2 in fruits is approximately that of tap water while T_2 in cookie dough is significantly shorter. To illustrate the potential use of a natural abundance ^{17}O imaging, the ^{17}O image (left) and a ^{1}H image (right) of a phantom of water are shown below. The ^{1}H image was produced with a gradient recalled echo sequence. The lines are deliberately saturated slices that mark the center of the gradient set. The ^{17}O image is the center slice of 3-D spin echo image. The field of view and resolution are limited by gradient strength in the ^{17}O image.

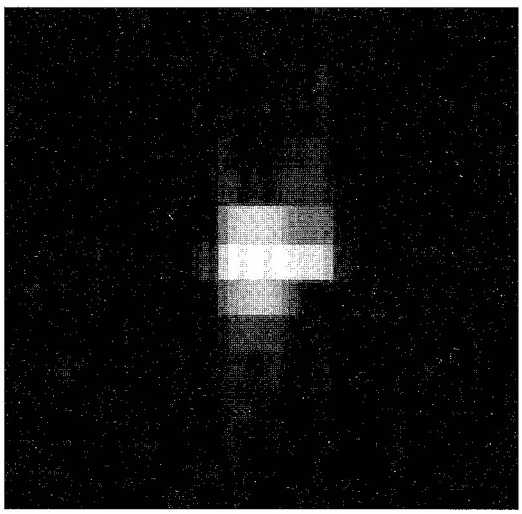

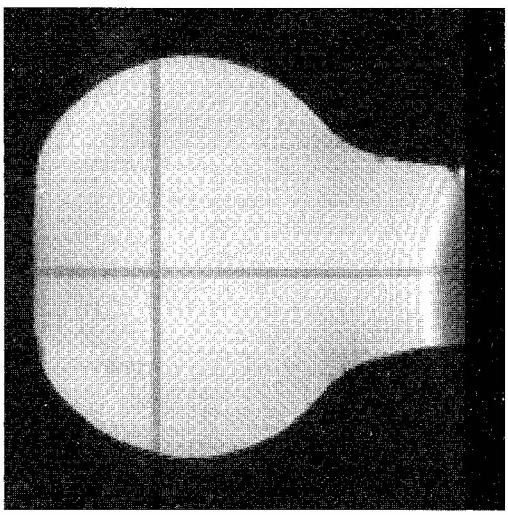

1. Reddy, R.; Stolpen, A.H.; Leigh, J.S., *J. Magn. Reson. B*, **108**, 276 (1995).

P87

Indirectly detected ^{13}C NMR imaging

M. Heidenreich, W. Köckenberger*, N. Chandrakumar, R. Bowtell*, R. Kimmich
Sektion Kernresonanzspektroskopie, Universität Ulm, Germany
*MR Centre, University of Nottingham, UK

The detection of ^{13}C NMR signals for *in vivo* spectroscopy or imaging studies is often hampered by the low sensitivity of the ^{13}C-nucleus. Nevertheless, carbon 13 resonance is of major interest for the unambiguous identification of chemical compounds permitted by the wide range of chemical shifts connected with this nucleus. Furthermore, the low natural abundance and the possibility to use isotopically enriched compounds suggests its use as NMR tracer. This opens a whole class of new experiments in analogy to radioactive tracer investigations with the advantage of noninvasive spatial resolution and chemical selectivity as concerns metabolic reaction products. A method particularly suitable for these goals is indirect ^{13}C detection via cyclic *J*-cross polarisation (*CYCLCROP*)[1].

Cyclic *J*-cross polarisation consists of three basic steps: (i) polarisation transfer $^{1}H \rightarrow {}^{13}C$ with subsequent storage of the transferred magnetisation, (ii) saturation of all non-transferred proton coherences, and (iii) reverse transfer of the carbon magnetisation. The resulting NMR-signal arises solely from protons *J*-coupled to ^{13}C. That is, ^{13}C nuclei in principle are detected with the sensitivity of a corresponding number of protons. This also refers to the repetition rate in signal accumulation sequels. Taking relaxation losses into account, the signals can be evaluated quantitatively with respect to the carbon concentration of the selected compound of interest[2]. The high ^{13}C chemical selectivity of this method is achieved by the use of Hartmann/Hahn based cross-polarisation schemes. The practical difficulties associated with this class of polarisation transfer techniques in liquids can be overcome by the use of B_1-field mismatch-compensated variants. As a variant particularly reliable and easy to adjust we suggest the *PRAWN* modification[3].

CYCLCROP ^{13}C NMR in combination with micro-imaging schemes has been used for selective mapping of compounds in heterogeneous systems[4]. A " ^{1}H-^{13}C cyclic *J*-cross polarisation PGSE" method[5] for the selective determination of the oil droplet size distribution in the creaming layers of turbid oil-in-water emulsions has been suggested. Dynamic ^{13}C tracer studies have been performed in living plant systems (*Ricinus communis* L.) for the investigation of sucrose synthesis, transport and consumption by means of indirectly detected ^{13}C imaging and spectroscopy experiments[6]. The temporal resolution for slice-selective spectra was below 2 minutes, the acquisition of a 64 × 64 image-matrix (resolution 95 μm within a 4 mm slice) required 1.5 hours of signal accumulation.

References

1. C. Kunze, R. Kimmich, *Magn. Reson. Imaging* **15**, 805 (1994).
2. M. Heidenreich *et al*, *J. Magn. Reson.* **132**, 109 (1998).
3. N. Chandrakumar, R. Kimmich, *J. Magn. Reson.* **137**, 100 (1999).
4. A. Spyros, *et al.*, *Macromolecules* **31**, 3021 (1998).
5. P. McDonald, *et al.*, *Phys. Rev. E* **59**, 874 (1999).
6. P. Blümler *et al.*,In: *Spatially Resolved Magnetic Resonance*, Wiley-VCH, Weinheim, pp.21-52 (1998).

5th International Conference on Magnetic Resonance Microscopy
Alphabetical List of Presenters and Abstract Numbers

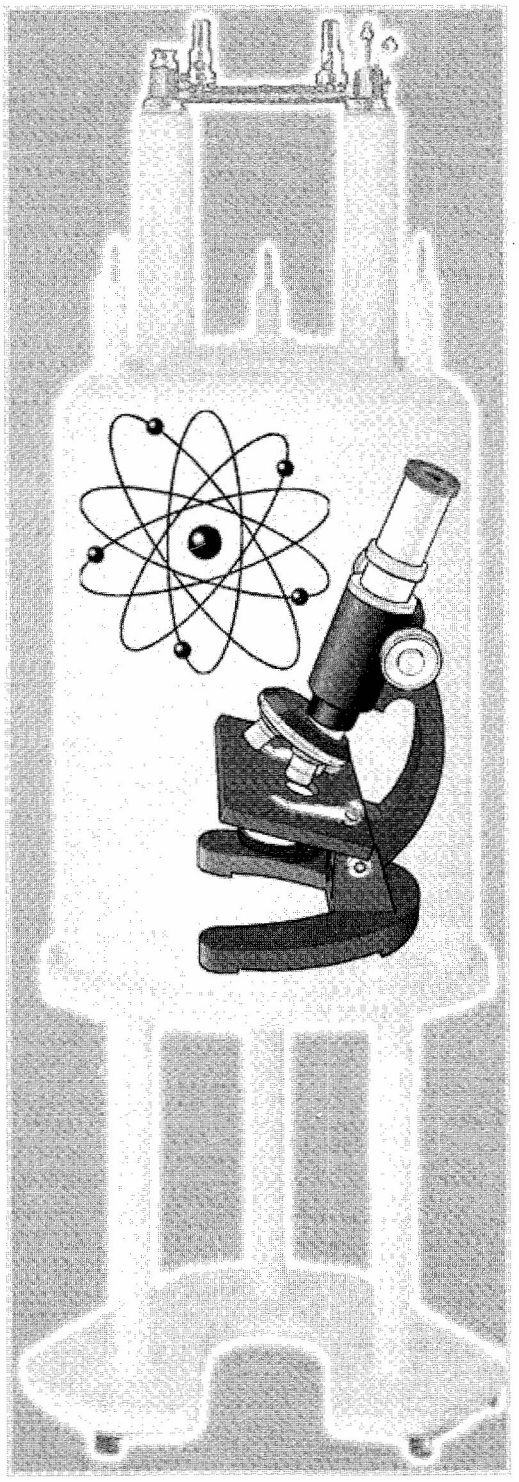

created by William E. Hull using HP ScanJet, Corel Draw, MS-Word, Adobe PhotoShop and Acrobat